Machine Learning-Based Design of Critical Raw Material (CRM)-Free Multi-Principal Element Alloys (MPEAs)

A Thesis

Submitted in partial fulfilment of the requirements for the degree

of

DOCTOR OF PHILOSOPHY

by

Swati Singh

(Roll No. 206103028)

Department of Mechanical Engineering
Indian Institute of Technology Guwahati
Guwahati, Assam, India
2025

Indian Institute of Technology Guwahati
Department of Mechanical Engineering
Guwahati – 781039

STATEMENT

The present thesis entitled, **"Machine Learning-Based Design of Critical Raw Material (CRM)-Free Multi-Principal Element Alloys (MPEAs)"** has been carried out by me under the supervision of Prof. Shrikrishna N. Joshi, Department of Mechanical Engineering, Indian Institute of Technology Guwahati, and Prof. Saurav Goel, former honorary professor, Department of Mechanical Engineering, Indian Institute of Technology Guwahati, and Professor, School of Engineering and Design, London South Bank University, UK. This work has not been submitted elsewhere for the award of any degree.

Date: September 2025

(Swati Singh)
Roll. No. 2061030286
Department of Mechanical Engineering
Indian Institute of Technology Guwahati,
Guwahati – 781039, India

Indian Institute of Technology Guwahati
Department of Mechanical Engineering
Guwahati – 781039

CERTIFICATE

It is certified that the work described in this thesis, entitled, **"Machine Learning-Based Design of Critical Raw Material (CRM)-Free Multi-Principal Element Alloys (MPEAs)"** done by **Ms. Swati Singh (Roll No. 206103028),** a Ph.D. student in the Department of Mechanical Engineering, Indian Institute of Technology Guwahati, for the award of degree of **Doctor of Philosophy** has been carried out under our supervision. This work has not been submitted elsewhere for the award of any degree.

Date: September 2025

(Prof. Shrikrishna N. Joshi)
Professor
Department of Mechanical Engineering
Indian Institute of Technology Guwahati,
Guwahati, 781039, India

Date: September 2025

(Prof. Saurav Goel)
Former Honorary Professor
Department of Mechanical Engineering
Indian Institute of Technology Guwahati,
Guwahati, 781039, India
and
Professor
School of Engineering and Design,
London South Bank University,
103 Borough Road, London
SE10AA London, United Kingdom

Dedicated to

My family

Abstract

The research community is actively exploring multi-principal element alloys (MPEAs) owing to their exceptional mechanical properties and vast compositional design space. The compositional design space becomes astronomically large, reaching approximately 10^{100} unique combinations when considering the 60 most commonly used elements with compositional resolutions as fine as 0.1%. Exploring this vast, complex design space for targeted composition is a resource-intensive exercise. Moreover, systematic discovery remains constrained by the scarcity of high-quality experimental data, the widespread practice of augmenting experimental datasets with synthetic data, the limited generalizability of existing ML models, and the continued heavy reliance on scarce raw materials in high-performance MPEA development. To address these challenges, this thesis adopts a computational approach based on the current canon of machine learning (ML) theory, robust optimization algorithms, as well as theoretical physical strategies to accelerate the design and development of novel MPEAs with reduced reliance on critical raw materials (CRMs) and critical and strategic raw materials (C&SRMs).

The research begins with the development of a robust ML framework for phase prediction in MPEAs, trained exclusively on high-quality experimental data restricted to alloys synthesized via a single route (melting and casting) to ensure consistency. Synthetic data augmentation, a common practice in the literature, was consciously avoided, and the framework was benchmarked against models trained on mixed datasets (experimental + synthetic). Comparative analysis demonstrated that while synthetic data augmentation may improve model accuracy, it compromises predictive reliability, particularly in imbalanced datasets. In contrast, models trained solely on experimental data exhibited superior robustness and generalizability, underscoring the limitations of synthetic data augmentation and providing dependable guidance for alloy design prior to time-intensive experimentation.

In the second phase of this research, mechanical property prediction was undertaken using a curated literature-derived dataset within the open-source toolkit MAST-ML. Designed for materials researchers with limited coding experience, MAST-ML allows predictive models to be built without writing code from scratch. In this work, it was applied to predict yield strength in MPEAs, marking its first systematic use for such complex alloy systems. Its predictions were benchmarked against reported literature values, and its robustness,

reproducibility, and limitations were critically assessed. Based on these insights, and recognizing the limitations of MAST-ML, a novel ML framework was developed from scratch for multi-objective optimization to simultaneously optimize yield strength (YS), ultimate tensile strength (UTS), and elongation ($\mathcal{E}$). By integrating ML regression algorithms with nature-inspired metaheuristic optimization methods, this framework enabled efficient exploration of the vast compositional space and provided, to the best of our knowledge, the first reliable ML approach for addressing the long-standing strength–ductility trade-off in MPEAs.

In pursuit of sustainability, this thesis advances a dual strategy to minimize reliance on critical raw materials (CRMs) and critical and strategic raw materials (C&SRMs) in MPEA design. The first approach established a hybrid ML–metaheuristic optimization framework that applied ML-guided chemical tuning to design high-performance CRM-free or CRM-lean MPEAs. A large computational database of Vickers hardness values for unary and binary compositions was generated using CALPHAD-based Thermo-Calc 2024a simulations. The framework successfully identified novel compositions with reduced dependence on costly elements such as Co, Nb, Ta, and W while maintaining mechanical performance, and its reliability was confirmed through experimental synthesis of a newly suggested reduced-CRM composition. This exercise led to a robust benchmarking of novel CRM-lean alloys with mechanical properties comparable to or better than those of CRM-rich alloys currently used in industries.

The second approach proposed strain engineering as a sustainable, non-ML-based physical design alternative to compositional tuning for minimizing or eliminating critical and strategic raw materials (C&SRMs). It has been shown that the change in microstructure vis-à-vis change in strain rate or cooling rate (depending on the mode of the manufacturing process) can be exploited as mechanical tools to tailor microstructural evolution and thereby tune the mechanical properties of metallic materials. A theoretical analysis of literature evidence demonstrated that strain-induced microstructural modifications, including dislocation density enhancement, ultrafine grain refinement, and the activation of twinning induced plasticity (TWIP) and transformation induced plasticity (TRIP) mechanisms, can substantially enhance mechanical performance while simultaneously reducing reliance on C&SRMs. The propagation and interaction of dislocations during plastic deformation were shown to contribute to alloy hardening through strain accumulation, while the associated

increase in stored energy drives recrystallisation and grain refinement during subsequent processing. This interplay provides a powerful framework for designing alloys with superior mechanical properties while simultaneously addressing sustainability concerns. Collectively, these findings position strain engineering as a viable pathway for the development of cost-effective, resource-efficient, and sustainable alloys aligned with global Net Zero objectives.

In conclusion, this thesis establishes a comprehensive foundation for the design and development of MPEAs by integrating high-quality experimental data, CALPHAD-generated data, advanced ML frameworks, metaheuristic optimization strategies, and physical strain-engineering approaches. The frameworks developed herein are expected to play a critical role in advancing the design of MPEAs aligned with global Net Zero priorities. Furthermore, the theories and discussions presented in this work provide important directions for achieving sustainable and resource-efficient alloys while addressing cost and supply risk challenges.

भारतीय प्रौद्योगिकी संस्थान गुवाहाटी
Indian Institute of Technology Guwahati

Acknowledgements

As another phase of life is ready to dawn with the submission of my PhD thesis, there have been numerous helping hands and genuine advice behind the successful completion of my work. First and foremost, I express my sincere gratitude and respect to my thesis supervisor(s) **Prof. Shrikrishna N. Joshi,** Department of Mechanical Engineering, Indian Institute of Technology Guwahati and **Prof. Saurav Goel**, former honorary professor, Department of Mechanical Engineering, Indian Institute of Technology Guwahati, and Professor, School of Engineering and Design, London South Bank University, UK, for their valuable guidance, constant encouragement throughout this study and untiring help, without which this research would not have attained its shape.

I extend my gratefulness to Dr. Nirmal Kumar Katiyar, Dr. Mingwen Bai, Prof. Allan Matthew and Dr. Muhammad Arshad for their valuable collaborations, guidance and support throughout this research. I am especially thankful to Dr. Mingwen Bai for the opportunity to access and utilize advanced computational tools and software under their supervision, which significantly contributed to the quality and depth of my research. Their insights and technical support played a pivotal role in shaping the outcomes of this collaborative effort.

I am highly thankful to my doctoral committee members, Prof. S. Kanagaraj, Dr. Prasenjit Khanikar, and Dr. Bulu Pradhan, for their continuous academic guidance and for checking my work progress and seminars during my Ph.D. Their valuable discussions and suggestions were truly encouraging for me.

I would like to express my sincere gratitude to Prof. Shyamanta M. Hazarika and Prof. S. Senthivelan, present and former Heads, Department of Mechanical Engineering, Indian Institute of Technology Guwahati, for providing various laboratory facilities and sanctioning funds without which completion of the work would not have been possible. I am also grateful to all the faculty members of the Mechanical Engineering department.

I would also like to thank the Ministry of Human Resource and Development (MHRD), Government of India, and Science and Engineering Research Board (SERB), Government of India for providing financial support. I sincerely thank the Indian Institute of Technology Guwahati for providing all sorts of infrastructural facilities to carry out this doctoral research work. I would also like to acknowledge the Advanced Manufacturing Laboratory, Material Science Laboratory, Central Workshop, and Central Instruments Facility of Indian Institute

of Technology Guwahati and all scientific officers and staff members for providing instruments and helping me to carry out the research work.

I also highly appreciate the technical cooperation given by Mr. Jiten Basumatary, Mr. Saiffuddin Ahmed, Mr. Sanjib Sarma, Mr. Siddhartha Kumar Saikia, Mr. Munindra Hazarika, Mr. Rajiv Kumar Gogoi, Mr. Subham Kumar Pandey, and Mr. Rishi Kumar Tisima.

I deeply acknowledge the unabated support and counseling provided by my colleagues and friends, Dr. Upasana Sarma, Dr. Sanghamitra Das, Mr. Brijesh K. Singh, Dr. Ritam Sarma, Mr. Hritaban Acharjya, Dr. Vivekananda Haldar, Dr. Debtanay Das, Dr. Samrat Tamuly, Mr. Akshay Namdeo, Mr. Dipankar Saha, Mr. Faique Shakil, Ms. Manali Sajjan, Dr. Jaspreet Kaur, Ms. Aditi Sharma, Ms. Simran Gupta, Ms. Nishi Yadav, Mr. Manoj Kumar Dhal, Mr. Amrit Pritam Rout, Mr. Manish Dalakoti, Mr. Akshay Deydar, Ms. Nayanita Kalita, Mrs. Toni Kumari, Mr. Rakesh Deore, Mr. Vishwanil Sarnaik, Mr. Umesh Melkani, Mr. Atul Kumar Gautam, Mr. Pankaj Kumar, Mr. Umesh Mishra, Mr. Akshay Kumar Soni, Mr. Evenmore Mylliem, Mr. Antash Kishor Sinha, and Mr. Suraj Goala throughout my studies.

My most sincere gratitude and appreciation go to my mother, Mrs. Kamlesh Gautam and my family for their patience, continuous encouragement, and moral support over the past difficult years. I am deeply indebted to all the other members of my family who gave me constant support and encouragement throughout my life.

There are many more persons who helped me in many more ways and whose names elude me at this moment of time. I extend my gratitude to them.

Last, but not the least, I shall always be grateful to God for providing me such an awesome dedication for research work.

Date: September, 2025

Swati Singh
(Roll No. 206103028)

TABLE OF CONTENTS

ABBREVIATIONS

Abbreviations	Term
ABR	AdaBoost Regressor
ACO	Ant Colony Optimization
AM	Amorphous phase
AUC	Area under the ROC curve
BCC	Body centered cubic
CALPHAD	CALculation of PHAse Diagrams
CCAs	Complex Concentrated Alloys
CIP	Cold Isostatic Pressing
CRM	Critical Raw Materials
CSO	Cuckoo Search Optimization
DED	Directed energy deposition
DTC	Decision tree classifier
DTR	Decision Tree Regressor
EBM	Electron Beam Melting
ECAP	Equal Channel Angular Pressing
ETR	Extra Tree Regressor (ETR)
FCC	Face centered cubic
FCC+BCC	Mixed FCC and BCC solid solution
FP	False positives
FN	False negatives
FPR	False positive rate
FSP/FSW	Friction Stir Processing/ Friction Stir Welding
GA	Genetic Algorithm
GBR	Gradient Boost Regressor
HCP	Hexagonal close packed
HIP	Hot Isostatic Pressing
HPT	High Pressure Torsion
HRSDR	High-Ratio Differential Speed Rolling
IM	Intermetallic phase
KNN	K-nearest neighbours
LENS	Laser Engineered Net Shaping
LMD	Laser Metal Deposition
L-PBF	Laser Powder Bed Fusion
MA	Mechanical Alloying
MPEAs	Multi-Principal Element Alloys
ML	Machine Learning
P/M	Powder Metallurgy

PSO	Particle Swarm Optimization
R-CRM-MPEAs	Reduced-CRM multi-principal element alloys
RFC	Random forest classifier
RFR	Random Forest Regressor
ROC	Receiver operating characteristic
SLM	Selective Laser Melting
SPD	Severe Plastic Deformation
SPS	Spark Plasma Sintering
SVM	Support vector machine
SS	Solid solution
SS+IM	Mixed solid-solution and intermetallic phase
TC	Thermo-Calc
TE	Twist Extrusion
TP	True positives
TN	True negatives
TPR	True positive rate
TRIP	Transformation induced plasticity
TWIP	Twinning induced plasticity
VEC	Valence electron concentration
WOA	Whale Optimization Algorithm
XGB	Extreme gradient boosting XGBoost
XGBR	XGBoost Regressor

NOTATIONS

English symbols	Description
c_i	Concentration of the i^{th} element
n	Total number of metallic elements in a high entropy alloy
r_i	Atomic radius of the i^{th} element,
$\bar{r}$	Average atomic radius
x_i	Pauling electronegativity
$\bar{x}$	Averaged Pauling electronegativity
$\Delta\chi$	Electronegativity difference
δ	Atomic size difference
ΔH_{mix}	Mixing enthalpy
ΔS_{mix}	Mixing entropy

LIST OF PUBLICATIONS

International Journals

1. **Swati Singh**, Mingwen Bai, Allan Matthews, Saurav Goel*, Shrikrishna N. Joshi, "Critical Raw Material-Free Multi-Principal Alloy Design for a Net-Zero Future", Sci Rep 15, 3132 (2025). Nature Scientific Reports, 2025. http://dx.doi.org/10.1038/s41598-025-87784-0. *(Related to the reported work in thesis)*

2. **Swati Singh**, Mingwen Bai, Allan Matthews, Shrikrishna N. Joshi, Saurav Goel*, "Strain engineering: A sustainable alternative to avoid using strategic and critical raw materials in developing high performance alloys", Materials Today Advances, 24, 100538, 2024. http://dx.doi.org/10.1016/j.mtadv.2024.100538 *(Related to the reported work in thesis)*

3. **Swati Singh**, Nirmal Kumar Katiyar, Saurav Goel*, Shrikrishna N. Joshi, "Phase prediction and experimental realisation of a new high entropy alloy using machine learning", Nature Scientific Reports, 2023. http://dx.doi.org/10.1038/s41598-023-31461-7 *(Related to the reported work in thesis)*

4. Dinh T. Nguyen, **Swati Singh**, Saurav Goel*, "Data mining to map nutrition value of industrial cheese produced in France", Biomaterials and Polymers Horizon, 1, 3, 2022. http://dx.doi.org/10.37819/bph.001.03.0298 *(Not related to the reported work in thesis)*

5. B. Dhindaw*, **Swati Singh**, Animesh Mandal, Ashwani Pandey, "Modelling and Experimental Characterization of Processing Parameters in Vertical Twin Roll Casting of Aluminium Alloy A356", Archives of Foundry Engineering, 20, 4, 2020. http://dx.doi.org/10.24425/afe.2020.133358 *(Not related to the reported work in thesis)*

International Conferences

1. **Swati Singh**, Saurav Goel and Shrikrishna N. Joshi, "Application of Machine Learning in Exploration of Uncharted Territory of Multi-Principal Element Alloys", International Conference on Artificial Intelligence, Machine Learning and Soft Computing (ICAIMLSC-24), Kyoto, Japan on 4th - 5th September 2024, ISSN: 1001-4055, Vol. 45 No. 3. *(Related to the reported work in thesis)*

2. **Swati Singh**, Shrikrishna N. Joshi, Saurav Goel, "Summary of Efforts in Phase Prediction of High Entropy Alloys Using Machine Learning", North-East Research Conclave (NERC-2022), IIT Guwahati, Assam, India, May 20 – 22, 2022. *(Related to the reported work in thesis)*

3. **Swati Singh**, Shrikrishna N. Joshi and Saurav Goel, "Mechanical property prediction of high entropy alloys using machine learning methodology", 2nd International Conference on Mechanical Engineering (INCOM 2024), Kolkata, India, 5th - 6th January 2024. *(Related to the reported work in thesis)*

Book Chapters

1. **Swati Singh**, Shrikrishna N. Joshi and Saurav Goel, "Mechanical property prediction of high entropy alloys using machine learning methodology", 2nd International Conference on Mechanical Engineering (INCOM 2024), Kolkata, India, 5th - 6th January 2024, pp 399-407. [Published] *(Related to the reported work in thesis)*

2. **Swati Singh**, Shrikrishna N. Joshi, Saurav Goel, "Summary of Efforts in Phase Prediction of High Entropy Alloys Using Machine Learning", North-East Research Conclave (NERC-2022), IIT Guwahati, Assam, India, May 20 – 22, 2022, pp 43-57. [Published] *(Related to the reported work in thesis)*

Invited Presentations

1. **Swati Singh**, Saurav Goel and Shrikrishna N. Joshi, "Machine learning driving the development of high entropy alloys", in First UK workshop on High-Entropy Materials organized by Henry Royce Institute, Manchester M13 9PL, UK, September 9th, 2022. *(Related to the reported work in thesis)*

2. **Swati Singh**, "Fairness in ML-Driven Sustainable High-Entropy Alloy (HEA) Discovery: Reducing Critical and Strategic Raw Materials (C&SRMs) Dependency"**,** UK-India Cooperation Towards a Fair AI Horizon Hackathon organized by Infosys Responsible AI office along with British High Commission, 5th - 6th December 2024. *(Not Related to the reported work in thesis)*

Chapter 1

Introduction

1.1. Background and Motivation

Multi-principal element alloys (MPEAs), popularly known as high entropy alloys (HEAs) or complex concentrated alloys (CCAs), were first reported by Yeh and Cantor in 2004 [1, 2]. Since then, these alloys have received critical attention due to their exceptional mechanical and functional properties, such as high-temperature strength, exceptional ductility, cryogenic fracture toughness, bio-compatibility, high electrical conductivity, and excellent catalytic and magnetic behavior, surpassing those of conventional alloys.

Initially, HEAs were defined as alloys containing at least five principal elements in equiatomic proportions [2]. The high mixing entropy in such systems was thought to stabilize single-phase solid solutions (SS), typically forming FCC, BCC, or HCP crystal structures, by suppressing the formation of intermetallic compounds [3-5]. Over time, the definition of HEAs has broadened to include multi-principal element alloys where each constituent is present in 5–35 at%, regardless of strict equiatomic ratios [5, 6]. Recent research has shown that entropy-stabilized single-phase HEAs do not always exhibit superior properties [7, 8]. Moreover, focusing solely on single-phase formation can significantly limit the exploration of the rich compositional landscape that MPEAs offer. Consequently, the definition of HEAs has evolved. Modern interpretations now include both single-phase and multi-phase alloys, with equiatomic and non-equiatomic compositions**.** This broader definition significantly expands accessible design space. Considering the 60 most commonly used elements in practical alloy design and allowing compositional variations as fine as 0.1%, the number of possible MPEA combinations is estimated to exceed 10^{177} [9]. This staggering figure highlights the immense and largely untapped potential of MPEAs compositional design space for the discovery of novel materials with tailored properties.

Moreover, it is important to distinguish between the terminologies used in the field. While the term HEAs traditionally refers to single-phase disordered solid solutions stabilized through configurational entropy, terms like MPEAs or CCAs evokes the vastness of composition space, without imposing strict constraints on types of phases present or the magnitude of configuration entropy [5]. These latter terms emphasize the versatility of alloy

design, focusing on functionality rather than rigid structural classifications. To avoid ambiguity, the term HEAs in this thesis refers broadly to both single-phase and multi-phase alloys composed of equiatomic or non-equiatomic multi-principal elements. Moreover, the terms HEAs, MPEAs, and CCAs have been used interchangeably, as they all reflect the compositional complexity and design philosophy underlying this class of materials.

Despite systematic exploration of the high-dimensional compositional space of MPEAs, only a small fraction with mechanical properties superior to those of conventional alloys has been found so far. For instance, the mechanical properties of most 3d transition metal MPEAs are comparable to those of commercial austenitic stainless steels and nickel alloys [5]. Advancing the discovery and development of novel MPEAs, as well as the integrating new functionalities, requires a deep understanding of the intricate composition–processing–structure–property relationships. A wide range of factors, including composition, synthesis routes, processing conditions, and post-treatment parameters, must be carefully optimized to obtain a high-performing MPEA composition [10]. The conventional materials discovery approach, which relies heavily on repetitive experimental trials and computational simulations, is resource-intensive, time-consuming, and inefficient [11].

In recent years, the materials science community has increasingly adopted machine learning (ML) techniques to accelerate the discovery and design of advanced materials. Numerous studies have demonstrated the use of ML algorithms for predicting phase formation [12-17], estimating mechanical properties [18-22], and identifying novel MPEA compositions [23-25]. However, despite these advances, several critical limitations continue to hinder the effectiveness and generalizability of ML approaches in the context of MPEAs, as outlined below:

(i) The scarcity of high-quality experimental data in the MPEA literature limits the effective training and validation of existing ML frameworks, thereby reducing their generalizability to unseen compositions.

(ii) There is limited consideration of the effects of synthesis routes (e.g., vacuum arc melting, powder metallurgy, additive manufacturing), their associated processing parameters (such as cooling rate, processing time, temperature, and atmosphere), and post-processing treatments during data collection for ML model development, despite their significant influence on the resulting alloy properties.

(iii) The reliance on synthetically generated data to address data scarcity and improve model accuracy raises concerns regarding the reliability of predictions. Augmenting real-world experimental data with synthetic data, a practice frequently reported in the literature, can introduce biases or unrealistic trends, thereby limiting a model's applicability to real-world scenarios.

(iv) Despite the availability of open-source toolkits developed specifically for materials informatics, their adoption remains limited in the study of advanced alloys such as MPEAs. For instance, Material Simulation Toolkit for Machine Learning (MAST-ML) provides a user-friendly interface for ML workflows without requiring researchers to write code from scratch. Yet, to the best of our knowledge, no studies have reported its application to MPEAs, with most research instead relying on custom-coded frameworks. It is important to evaluate the applicability and robustness of such toolkits in handling complex alloy systems, thereby assessing their usability, reproducibility, and potential for establishing standardized practices in the field.

(v) There is a lack of advanced multi-objective optimization frameworks capable of addressing trade-offs between key mechanical properties, such as the well-known strength–ductility dilemma. Existing studies predominantly focus on optimizing a single property in isolation, rather than simultaneously balancing multiple, and often competing, mechanical requirements.

(vi) There is an overreliance on scarce and expensive Critical Raw Materials (CRMs) and Critical and Strategic Raw Materials (C&SRMs), such as Co, Ta, Hf, V, Nb, and W, in the development of high-performance alloys, which undermines both the sustainability and scalability of the proposed compositions. To date, little efforts have been made in the MPEA literature to systematically reduce or eliminate the use of CRMs/C&SRMs during alloy design and development.

Hence, the extraction of high-quality experimental data and the development of robust predictive models that incorporates the effects of processing routes, processing parameters, and post-processing treatments are of critical importance. Equally important is the conscious avoidance of the flawed practice of augmenting or ‘polluting’ real-world datasets with synthetic data solely to inflate data size and model performance. Furthermore, the adoption of open-source toolkits such as MAST-ML, which are specifically designed to lower the entry barrier for materials researcher, has not yet been realized in the MPEA domain, representing a missed opportunity for standardization, reproducibility, and accelerated

knowledge discovery in the field. In parallel, the integration of advanced multi-objective optimization strategies is required to address trade-offs between competing properties, such as the strength-ductility dilemma, which are often overlooked in single-objective optimization studies. Finally, reducing reliance on CRMs/C&SRMs in the development of MPEAs, without compromising mechanical properties, is essential for advancing toward a more sustainable future in alloy design. These research gaps collectively form the foundation of the present study and motivate the objectives outlined in the following section.

1.2. Objectives and Scope

As outlined above, the effective application of machine learning to MPEAs is currently hindered by several interrelated challenges. First, the scarcity and inconsistent quality of experimental data in the MPEA domain present a major obstacle to building reliable ML frameworks. Second, existing ML models often overlook the critical influence of synthesis routes, processing parameters, and post-processing treatments on alloy properties, thereby restricting their capacity to capture the full composition–processing–structure–property relationships. Compounding these challenges is the widespread practice of augmenting or 'polluting' real-world experimental data with synthetic datasets, which, although intended to mitigate data scarcity, often compromises model reliability and raises concerns regarding predictive robustness and generalizability. Furthermore, the limited adoption of open-source materials informatics toolkits constrains opportunities to evaluate the usability, reproducibility, and robustness of these frameworks in the context of complex alloy systems. In addition, the lack of advanced multi-objective optimization strategies results in alloys being optimized for a single property, thereby neglecting trade-offs among competing properties and ultimately limiting real-world applicability. Finally, the continued reliance on scarce and expensive CRMs and C&SRMs in the development of high-performance MPEAs poses significant challenges to sustainability and undermines global efforts toward achieving Net Zero targets.

To address these challenges, this research focuses on developing robust ML frameworks for the design of cost-effective MPEAs with superior mechanical performance. The specific aims of this PhD project are: (i) to curate and consolidate high-quality experimental data from the literature and make it publicly accessible to advance materials informatics research; (ii) to develop a robust and reliable ML framework for predicting phase formation in MPEAs without relying on synthetically generated data, evaluate its generalizability, and

systematically investigate the key factors governing phase stability while incorporating the effects of synthesis routes; (iii) to implement and validate MAST-ML for prediction of mechanical properties in MPEAs, demonstrating its strengths and limitations for complex alloy systems; (iv) to identify novel alloys with optimally balanced mechanical properties (targeting Yield Strength (YS), Ultimate Tensile Strength (UTS), and Elongation ($\boldsymbol{\varepsilon}$) simultaneously), particularly addressing the strength–ductility trade-off through multi-objective optimization; and (v) to minimize the dependence on CRMs/C&SRMs through a dual strategy aimed at promoting the development of sustainable alloys: (a) an ML-guided chemical tuning approach to design novel, high-performance MPEAs with minimal or no reliance on expensive CRMs, without compromising mechanical properties; and (b) a non-ML-based physical design approach based on strain-engineering to reduce reliance on C&SRMs, without the need for chemical tuning.

To achieve the proposed objectives, the following key tasks were undertaken:

- Developed a robust ML framework for phase prediction, trained exclusively on high-quality experimental data encompassing 3d-transition metal HEAs, refractory HEAs, precious metal-based systems, brass/bronze-type HEAs and low-density HEAs. The curated database was restricted to alloys synthesized via melting and casting routes, thereby eliminating the influence of differing synthesis methods on phase outcomes. The framework explicitly avoided synthetic data augmentation and was benchmarked against counterparts trained on mixed datasets, demonstrating superior reliability and generalizability. It provides a generalized understanding of phase formation, enabling more efficient guidance prior to time-intensive experimentation.
- Implemented the open-source toolkit MAST–ML to predict mechanical properties of MPEAs, marking its first systematic use in the context of complex alloy systems. This involved extracting experimental data from the literature, focusing on yield strength, and employing various regression algorithms within the MAST–ML framework. A comprehensive evaluation was then conducted to assess its strengths, and limitations.
- Developed a novel ML–based framework for multi-objective optimization, designed to identify alloy candidates that simultaneously optimize yield strength (YS), ultimate tensile strength (UTS), and elongation ($\boldsymbol{\varepsilon}$), using a database derived from experimental studies. The framework combined ML regression algorithms with nature-inspired optimization methods to explore the compositional space while targeting multiple properties. This

provided an ML-based approach to effectively address the long-standing strength–ductility trade-off, which, to the best of our knowledge, had not previously been developed in the context of MPEAs.

- Established a hybrid ML-metaheuristic optimization framework for designing novel, high-performance MPEAs with minimal or no reliance on CRMs. This framework leveraged ML-guided chemical tuning to reduce dependence on expensive CRMs without compromising mechanical properties. It utilized a large computational database extracted from Thermo-calc 2024a, focusing on Vickers hardness of unary and binary compositions, to enable the identification and design of novel CRM-free or CRM-lean MPEAs.
- Investigated a non-ML-based physical design approach based on strain engineering as a sustainable strategy to reduce reliance on C&SRMs, without relying on ML-guided chemical tuning. This task involved a theoretical analysis of literature evidence, comparing the mechanical performance of various MPEAs and pure elements processed via strain-engineering against those produced through other synthesis methods. The focus was on exploring the potential of strain engineering to enhance the performance of existing materials without chemical tuning, and to enable the design of high-performance compositions with minimal or no reliance on C&SRMs.

1.3. Thesis Outline

The overall Ph.D. research has been systematically organized into the following chapters:

- ***Chapter 1*** introduces the research background, highlighting the significance of Multi-Principal Element Alloys (MPEAs), the critical need for robust machine learning (ML) models, and the pursuit of cost-effective, high-performance MPEAs free from critical raw materials (CRMs) or critical and strategic raw materials (C&SRMs). The overarching objectives and motivations driving this research have also been outlined at the end of the chapter.

- ***Chapter 2*** presents an extensive literature review beginning with an overview of MPEAs, their historical development, evolving definitions, core effects, and the vast compositional space they offer. Different approaches for exploring this landscape, including traditional trial-and-error, computational design, and machine learning have been discussed. Furthermore, a detailed examination of existing ML models employed for phase prediction, property estimation, and novel alloy discovery has also been

provided. Based on this survey, the research gaps were identified, and subsequently, a brief insight into the development of various ML frameworks for MPEA design was presented.

- ***Chapter 3*** provides an in-depth investigation into phase prediction of MPEAs by developing a robust ML framework. Experimental dataset was compiled from the literature, followed by classification of MPEAs based on observed phases. The influence of dataset balance or imbalance on classification accuracy was investigated. The importance of avoiding synthetic data augmentation has been emphasized. Various classification algorithms were compared to select the best-performing model. The selected model was validated by predicting the phase of a new composition, which was subsequently synthesized and characterized. In addition, a comparative analysis between models trained on purely experimental data and those with augmented data has been performed to demonstrate the limitations of synthetic augmentation.

- ***Chapter 4*** explores the application of the open-source toolkit MAST-ML to predict the mechanical properties of MPEAs using a literature-derived dataset, marking its first systematic use in the context of complex alloy systems. The toolkit's strengths and limitations in handling complex alloy systems has been evaluated. Predictions were critically validated against reported yield strength values from the literature. The usability and reproducibility of the toolkit were assessed. Based on the identified limitations of MAST-ML, a novel ML framework was developed from scratch for multi-objective optimization, targeting competing properties (YS, UTS and ε). The framework, which integrated ML with nature-inspired algorithms, was designed to explore the MPEA compositional space and identify alloys with an optimal balance of mechanical properties, with the aim of addressing the strength–ductility trade-off.

- ***Chapter 5*** addresses the urgent need to reduce reliance on critical raw materials (CRMs) while developing high-performance MPEAs. A three-tier classification system for CRMs severity, based on supply risk and strategic importance, was introduced. A large database of unary and binary compositions targeting Vickers hardness was generated using CALPHAD-based Thermo-Calc simulations. The development of a hybrid ML-metaheuristic optimization framework, trained on this database to identify novel multicomponent CRM-free or CRM-lean (reduced-CRM) MPEAs has been discussed.

The framework was designed to apply ML-guided chemical tuning to minimize dependence on expensive elements such as Co, Nb, Ta, and W, while aiming to maintain mechanical performance. The proposed compositions were intended to be benchmarked against CRM-rich counterparts from the literature, with the objective of achieving comparable or potentially superior hardness. Experimental validation of one such composition was conducted to evaluate the framework's reliability and demonstrate the feasibility of designing sustainable, high-performance CRM-free MPEAs.

- ***Chapter 6*** investigates strain engineering as a sustainable and non-ML-based physical design strategy for minimizing reliance on critical and strategic raw materials (C&SRMs), without the need for chemical tuning. A theoretical analysis of literature evidence, comparing the mechanical performance of MPEAs and pure elements processed via strain engineering against those produced through other processing methods, has been presented. The scientific and theoretical rationale behind strain-induced microstructural modifications, including dislocation density enhancement, ultrafine grain formation, and the activation of TWIP (twinning-induced plasticity) and TRIP (transformation-induced plasticity) mechanisms as potential pathways to enhance mechanical performance, was outlined. This study aims to position strain engineering as a transformative and resource-efficient strategy for the development of next-generation sustainable alloys aligned with Net Zero goals.

- ***Chapter 7*** summarizes the findings of the research work and presents the key conclusions of this thesis. The scope for carrying out future work in this area has also been presented.

Chapter 2

Literature Review

2.1. Introduction

This chapter presents an overview of key research activities in the field of MPEAs. It offers a critical state-of-the-art review of recent advancements in their discovery and development, tracing their historical emergence and emphasizing the exceptional properties that distinguish them from conventional alloys. The chapter also examines methodologies for designing novel MPEAs, including traditional trial-and-error experimentation, computational techniques, and machine learning-based strategies. In addition, it reviews the challenges and limitations of existing ML models developed in previous studies on MPEAs. Finally, the chapter discusses the extensive use of critical raw materials (CRMs) and critical & strategic raw materials (C&SRMs) in the development of high-performance MPEAs, highlighting the urgent need to reduce their use in pursuit of sustainable alloy design aligned with Net Zero objectives.

A comprehensive review of current research trends is presented, highlighting challenges such as limited data availability, the common practice of augmenting synthetic data to improve model accuracy, the limited generalizability of existing ML models, and the continued overreliance on CRMs/C&SRMs in MPEA development. Based on this extensive literature survey, key research gaps have been identified. The chapter concludes by outlining the specific objectives of the present work.

2.2. Brief History

The concept of combining multiple elements in equimolar or near-equimolar proportions, representing a significant departure from conventional alloy design, gained widespread recognition in 2004 and led to the development of Multi-Principal Element Alloys (MPEAs), also referred to as High Entropy Alloys (HEAs) or Complex Concentrated Alloys (CCAs) [1, 2]. This novel alloy design approach was independently proposed by Professor Jien-Wei Yeh and Professor Brian Cantor in the same year. One of the earliest examples, the Cantor alloy (CrMnFeCoNi), was described as an equiatomic multicomponent alloy and exhibited exceptional properties, making it a landmark in the development of complex concentrated alloys [1]. Around the same time, Yeh et al. developed the Al_x(CrFeCoNiCu) system, with aluminium concentrations ranging from x = 0 to 3. Following this work, the term "high-

entropy alloy (HEA)" was formally introduced [2].

2.3. Definitions

Unlike conventional alloys, which are typically based on one or two primary elements with minor additions of secondary elements, HEAs are composed of five or more principal elements in equiatomic proportions, as defined in the earliest foundational literature [1, 2]. Owing to their high configurational entropy, these equiatomic multicomponent alloys tend to form thermodynamically stable single-phase solid-solution (SS) structures, such as face-centered cubic (FCC), body-centered cubic (BCC) or hexagonal close-packed (HCP) phases [3, 26-28].

In recent years, the definition of HEAs has been broadened to include single-phase SS multicomponent alloys in which the concentration of each constituent element ranges between 5 and 35 atomic percent [5, 6]. However, numerous studies have shown that entropy-stabilized single-phase HEAs do not necessarily exhibit superior properties [12, 13]. More importantly, strict adherence to a single-phase design philosophy significantly limits the accessible compositional space. Consequently, the term 'HEA' is no longer restricted to single-phase SS alloys containing five or more principal elements. At present, a wide variety of compositions, including equiatomic quaternary systems and non-equiatomic multicomponent alloys with multi-phase microstructures, are also classified as HEAs. Notable examples include CoCrFeNi, NbMoTaW, $Fe_{50}Mn_{30}Co_{10}Cr_{10}$, TiZrHfNb, $Ta_{0.6}HfZrTi$ alloys [8, 29, 30]. For such systems with compositionally complex and multiphase characteristics, alternative terminologies such as 'compositionally complicated alloys' or 'complex concentrated alloys' (CCAs) are frequently used in the literature.

To avoid ambiguity, the term 'HEAs' in this thesis refers broadly to both single-phase and multi-phase alloys composed of equiatomic or non-equiatomic multi-principal elements. The terms HEAs, CCAs, and MPEAs are used interchangeably throughout this thesis. MPEAs exhibit a wide range of exceptional properties, including high specific strength**,** excellent ductility**,** outstanding high-temperature stability**,** high fracture toughness at cryogenic temperatures**,** bio-compatibility**,** superior corrosion and oxidation resistance**,** good electrical and thermal conductivity, as well as notable catalytic, magnetic, and even superconducting behaviors [3, 5, 31, 32]. Consequently, MPEAs have emerged as superior alternatives to conventional alloys in diverse application sectors such as defense, aerospace, nuclear energy, power generation, biomedical implants, and stealth technologies. Yeh et al. [17] identified

four key effects responsible for the extraordinary performance of MPEAs: (i) high-entropy effect, (ii) sluggish diffusion effect, (iii) severe lattice distortion effect, (iv) cocktail effect.

2.4. Four Core Effects

2.4.1. High-Entropy Effect

The high-entropy effect is a core thermodynamic principle that underpins the stability of single-phase solid solutions in MPEAs/HEAs. First introduced by J.W. Yeh, this concept explains how configurational entropy, defined as a measure of disorder due to atomic mixing, can thermodynamically favor the formation of simple solid-solution phases (such as FCC or BCC) instead of more complex and brittle intermetallic compounds [33].

In HEAs, the mixing entropy (ΔS_{mix}) increases significantly due to the near-equiatomic ratio of multiple principal elements, often five or more. This elevated entropy contributes a large negative term to the Gibbs free energy, thereby lowering its value. As a result, solid solution phases are stabilized over competing intermetallics, which typically possess lower configurational entropy [33, 34]. A high configurational entropy can also reduce the tendency for phase separation or intermetallic formation, allowing HEAs to maintain single-phase microstructures even when composed of multiple elements.

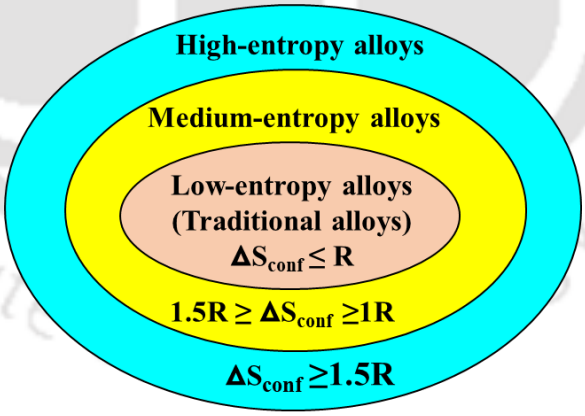

Figure 2.1. Classification of alloys based on configurational entropy of mixing (ΔS_{mix})

Based on the configurational entropy of mixing (ΔS_{mix}), which quantifies the compositional randomness within a solid solution, alloys are generally classified into three categories: low-entropy alloys (LEAs)**,** containing one or two dominant elements typical of conventional alloys; medium-entropy alloys (MEAs), composed of three to four principal elements; and high-entropy alloys (HEAs), consisting of five or more principal elements in near-equiatomic

ratios [6]. This classification is illustrated in Figure 2.1. The Gibbs free energy and configurational mixing entropy formulations, grounded in classical thermodynamics, are presented in Equations (2.1) and (2.2) [35, 36].

$$\Delta G_{mix} = \Delta H_{mix} - T.\Delta S_{mix} \quad (2.1)$$

$$\Delta S_{mix} = -R\sum_{i=1}^{n}(c_i \ln c_i) \quad (2.2)$$

where, R is the gas constant (8.314 J/mol·K), c_i is the atomic fraction of each element and n is the number of components.

2.4.2. Sluggish Diffusion Effect

The sluggish diffusion effect in MPEAs refers to their inherently reduced atomic mobility compared to conventional alloys. This phenomenon arises from the complex, disordered atomic environment created by the near-equiatomic mixture of multiple principal elements, each differing in atomic size and bonding characteristics. These variations produce diverse local atomic configurations and fluctuating lattice potential energies, which inhibit atomic movement by trapping atoms in low-energy sites or impeding them with high-energy barriers [37, 38]. As a result, diffusion-controlled processes such as grain growth and phase transformations proceed more slowly. This delayed atomic diffusion retards the growth of second-phase nuclei, thereby promoting the formation and stabilization of fine, nano-sized precipitates within a single-phase matrix. Furthermore, sluggish diffusion contributes to enhanced thermal stability, high-temperature strength, and superior creep resistance, making MPEAs particularly well-suited for demanding structural applications [39, 40].

2.4.3. Severe Lattice Distortion Effect

Severe lattice distortion in MPEAs refers to the substantial disruption of the crystal lattice arising from atomic size mismatches among the multiple principal elements. In contrast to conventional alloys, which typically contain one or two dominant elements with similar atomic radii, MPEAs incorporate several elements with varying atomic sizes, randomly occupying lattice sites. This atomic-scale irregularity induces local lattice strains and distortions throughout the material. These distortions impedes the motion of dislocations, thereby enhancing solid solution strengthening and contributing to the high strength and

hardness of MPEAs [41, 42]. Additionally, severe lattice distortion can influence phase stability and reduce atomic diffusion rates. The effect is especially pronounced in BCC-structured MPEAs, where atomic packing is less dense and more sensitive to size differences.

2.4.4. Cocktail Effect

First introduced by S. Ranganathan [34], the term 'cocktail effect' was initially used to describe concentrated alloys, such as bulk metallic glasses, and was later applied to MPEAs. It refers to the combined influence of multiple principal elements, with both direct atomic interactions and indirect effects on the microstructure contributing to unique and often unexpected properties not observed in conventional alloys.

Unlike the other core effects of MPEAs, the cocktail effect is qualitative and abstract, lacking a clear theoretical basis. Its complexity arises from the unpredictable nature of multi-element atomic interactions and the uncertain occupancies of lattice site, making it difficult to model or quantify [43]. Nevertheless, it is frequently invoked to explain the exceptional combinations of properties observed in MPEAs, such as high strength, superior corrosion resistance, and remarkable thermal stability.

2.5. Compositional Space of MPEAs

MPEAs provide access to an exceptionally broad compositional space compared to conventional alloys, as illustrated in Figure 2.2. The concept of compositional design in MPEAs extends far beyond the narrow corners occupied by conventional alloys (highlighted in blue), which typically revolve around one or two dominant elements. In contrast, MPEAs explore the central region of the phase diagram, representing multi-principal element systems where elements are present in equimolar or near-equimolar ratios.

It is estimated that over 10^{100} unique multi-principal element alloys (MPEAs) can theoretically be generated by combining the 60 most commonly used elements with compositional increments as fine as 0.1% [44]. This underscores the immense breadth of the design space available for alloy discovery and optimization. Equimolar HEAs (shown in red in Figure 2.2) occupy the center, while non-equimolar variants (shown in yellow in Figure 2.2) extend outward, still within the multi-element region [45]. This immense and largely untapped compositional landscape is often regarded as a "materials discovery treasure trove", enabling the design of novel alloys with exceptional mechanical, thermal, and chemical properties that are not accessible through traditional alloy development approaches.

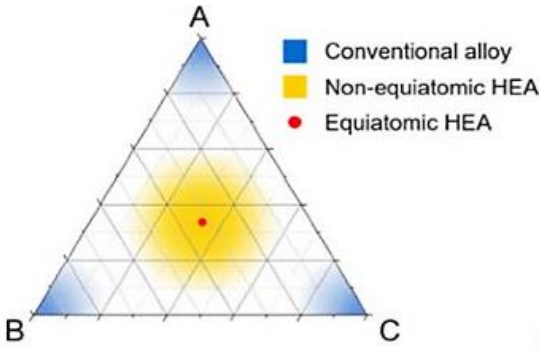

Figure 2.2. Ternary phase diagram [45] (Reproduced with permission from Springer Nature)

2.6. History and Evolution of Alloy Design

The field of alloy design has undergone a significant transformation over the past century, progressing from empirical approaches to predictive and data-driven methodologies [46]. This evolution reflects both the growing complexity of materials challenges and the rapid advancement of computational tools. The emergence of MPEAs, in particular, has highlighted the need for more efficient and scalable design strategies to navigate their vast compositional space. This section outlines the historical evolution of alloy design methods, focusing on three major paradigms: traditional trial-and-error experimentation**,** computational methods, and machine learning-driven approaches.

2.6.1. Trial-and-Error Method

Historically, alloy design has been driven by the trial-and-error approach, wherein compositions are manually varied, synthesized, and experimentally evaluated to identify desirable phases and properties [46]. This empirical method has led to landmark discoveries, such as stainless steels, superalloys, and advanced binary or ternary systems, and has occasionally revealed unexpected phases and exceptional mechanical or functional behaviors. However, as alloy systems have grown increasingly complex, particularly with the advent of MPEAs, the limitations of this approach have become pronounced. Each composition requires individual synthesis, processing, and characterization, making the method time-consuming, labor-intensive, and low-throughput. The immense compositional space of MPEAs, encompassing millions of potential combinations, makes comprehensive experimental screening impractical.

Moreover, reliance on intuition often results in biased sampling, potentially overlooking unexplored but promising regions. While trial-and-error remains vital for

empirical validation, it is no longer sufficient as a standalone discovery tool. Instead, it now serves as a targeted validation strategy, integrated with computational methods, such as CALPHAD, machine learning, and high-throughput screening, to accelerate and rationalize alloy development.

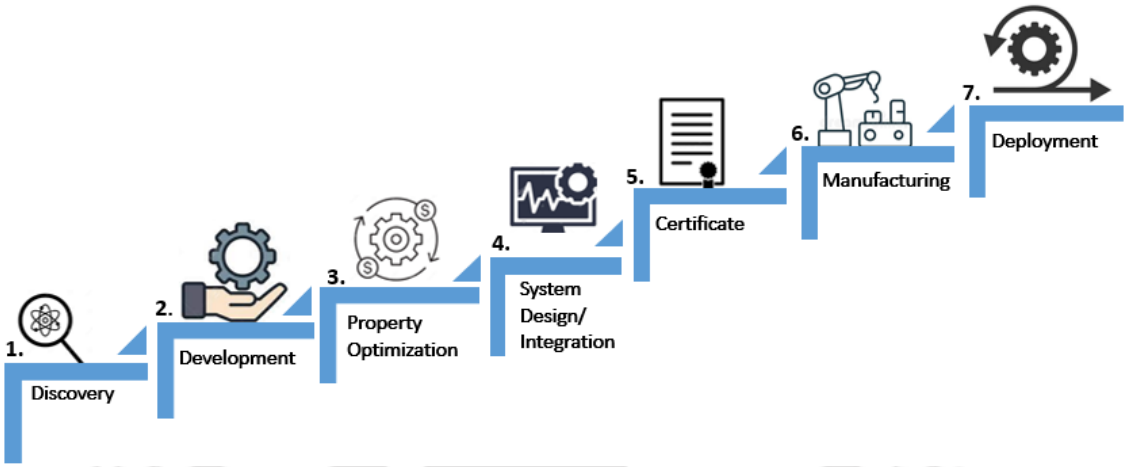

Figure 2.3. Steps involved from discovery to the deployment of a new materials in the real-world application

Despite the development of numerous MPEAs, exhibiting outstanding mechanical properties, only a small fraction of their vast compositional space has been thoroughly explored. This limited exploration is primarily due to the time- and resource-intensive nature of traditional alloy development, which relies heavily on iterative experimental methods to identify promising compositions. As shown in Figure 2.3, the conventional materials design process is a multi-stage pipeline, starting from discovery and development, through property optimization, system integration, certification, and manufacturing, to final deployment [47]. While this process has been effective in the past, it poses a major bottleneck for accelerating MPEAs research and real-world implementation, particularly given the enormous complexity and scale of the MPEA compositional landscape.

2.6.2. Computational Methods

The advent of computational approaches has significantly transformed alloy design, particularly in the exploration of complex systems like MPEAs. Techniques such as Density Functional Theory (DFT) [48, 49], Molecular Dynamics (MD) [50, 51], Monte Carlo (MC) [52], and CALPHAD (CALculation of PHAse Diagrams) [53] have been instrumental in predicting phase stability, thermodynamic behavior, and atomic-scale interactions prior to experimental validation [34].

DFT and MD simulations offer deep atomic-level insights but are hindered by high computational costs**,** modeling limitations, and uncertainties due to simplifying assumptions [54]. DFT is computationally expensive and typically restricted to small atomic systems, while MD simulations depend heavily on the accuracy of interatomic potentials, which often struggle to capture complex effects such as lattice distortion**,** configurational entropy, and the cocktail effect observed in MPEAs. Despite these limitations, computational tools remain indispensable for accelerating materials discovery, guiding experimental efforts, and narrowing the compositional space for high-throughput screening. CALPHAD, in particular, marked a shift toward predictive materials design, enabling efficient modeling of multicomponent phase diagrams and transformation temperatures. However, its performance remains constrained by the limited availability of thermodynamic databases, especially for binary miscibility gaps, intermetallic (IM) phases, and complex ternary systems [55].

2.6.3. Machine Learning

The term Machine Learning (ML) was first introduced by Arthur Samuel in 1959, defining it as a subset of artificial intelligence (AI) that enables systems to learn from data and improve their performance without being explicitly programmed [56]. Unlike traditional algorithms with predefined rules, ML systems are capable of autonomous learning, pattern recognition, and prediction, evolving as more data becomes available. Today, ML powers numerous facets of daily life, from image and speech recognition to traffic forecasting, product recommendations, autonomous vehicles, and cybersecurity applications such as spam and fraud detection [57, 58].

In recent years, the emergence of ML has marked a transformative shift in alloy design, offering a powerful alternative to traditional trial-and-error and computational methods. Its ability to efficiently analyze large, complex datasets, both experimental and computational, has opened new avenues in the prediction of material properties, phase stability, and accelerating the discovery of advanced alloys. ML drastically reduces the time and cost associated with alloy development [59].

Furthermore, the integration of ML with first-principles calculations, and materials informatics is driving the emergence of autonomous materials design frameworks, marking a paradigm shift in the field [60]. As a result, ML stands at the forefront of next-generation alloy design, offering both predictive power and the potential to uncover novel, high-performance materials that would be otherwise overlooked.

2.6.4. Types of Machine Learning Algorithms

ML algorithms can be broadly classified into three major categories based on the type of supervision and the structure of the learning task: Supervised, Unsupervised, and Reinforcement Learning. These paradigms define how models learn from data, whether through direct guidance (labels), by uncovering hidden structures, or via interaction with an environment to learn optimal actions [61].

A. Supervised Learning

As the name suggests, supervised learning involves training a model on a labeled dataset, where each input is paired with a corresponding output. The model learns to map inputs (x) to outputs (y) using a linear or non-linear function, such as y=f(x), by minimizing the prediction error between actual and predicted values. It is commonly applied to both classification tasks (e.g., predicting categorical labels such as alloy phases, FCC, BCC) and regression tasks (e.g., predicting continuous properties such as yield strength or hardness) [62]. Model performance is evaluated using metrics such as accuracy**,** precision**,** R^2 score, mean squared error (MSE) etc.

B. Unsupervised Learning

Unsupervised learning deals with data that has no predefined labels. The primary goal is to uncover hidden structures or patterns within the dataset. It is commonly used for clustering (e.g., grouping similar alloy compositions) and dimensionality reduction (e.g., reducing features for visualization using techniques like Principal Component Analysis (PCA)). This method is particularly useful for exploratory data analysis (EDA) and pre-processing in high-dimensional datasets [63].

C. Reinforcement Learning

Reinforcement learning (RL) is a feedback-driven learning paradigm where an agent learns to make optimal decisions by interacting with its environment. The agent perceives its environment, performs actions, and receives feedback in the form of rewards or penalties. The objective is to maximize cumulative reward over time by identifying the best sequence of actions. This learning paradigm operates on the principle of trial-and-error, where the agent is encouraged to adopt behaviors that lead to higher rewards (positive reinforcement) and

discouraged from actions that lead to penalties (negative reinforcement). Over time, the agent learns to avoid suboptimal actions and reinforce those that yield long-term benefits, thus evolving an ideal policy for decision-making [64].

Reinforcement learning is particularly suited for adaptive control systems, robotics and autonomous navigation, process optimization and Sequential decision-making in dynamic environments where the learning system must respond to dynamic conditions and learn through continuous interaction. Figure 2.4 categorizes various machine learning algorithms into three main types: supervised learning, unsupervised learning, and reinforcement learning, and provides examples of algorithms under each category.

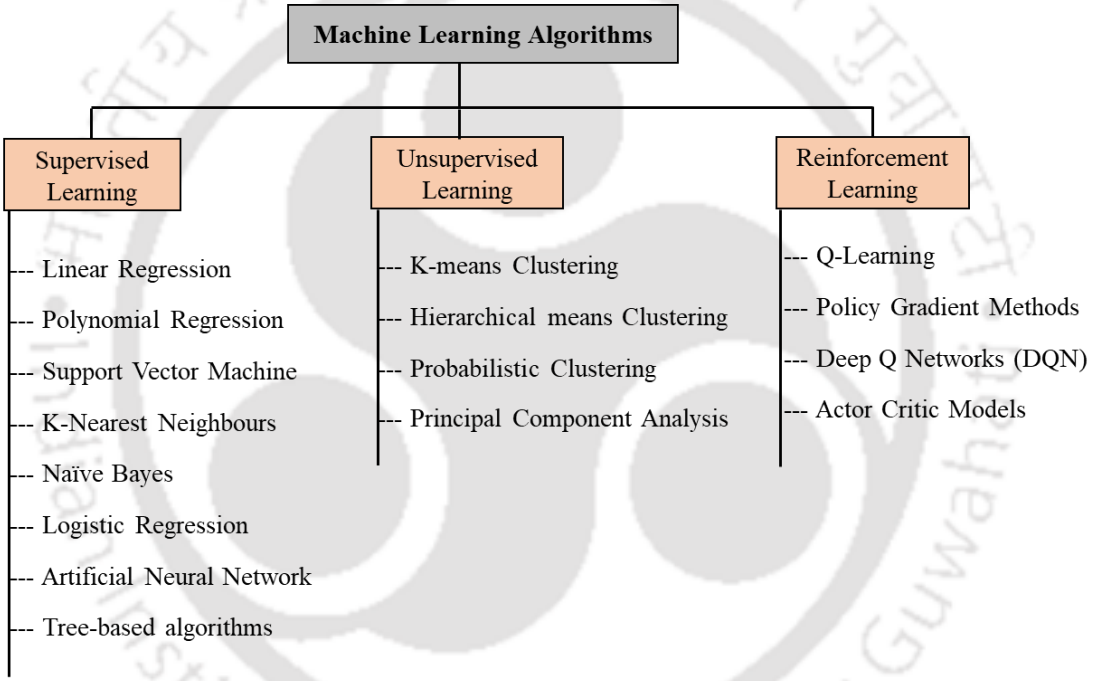

Figure 2.4. Classification of ML algorithms based on learning paradigms

Detailed descriptions of the algorithms applied to address each research objective are presented in the respective chapters.

2.7. Machine Learning Implementation in the Field of MPEAs

The field of MPEAs has witnessed a paradigm shift with the integration of machine learning. Numerous works have been reported by using various ML algorithms, such as Random Forest (RF), Support Vector Machine (SVM), Gradient Boosting Decision Trees (GBDT), Deep Neural Networks (DNN) and others, enabling rapid and accurate predictions and facilitating

the navigation of high-dimensional compositional space inherent to MPEAs through data-driven methodologies [65, 66].

This section systematically reviews the principal contributions of ML across three thematic domains: Phase Prediction, Mechanical Property Prediction, and the Discovery of Novel MPEAs with the aim of minimizing the use of critical materials (CRMs/C&SRMs). A comprehensive literature survey is detailed in the subsequent sections. The following sub-sections provide a detailed discussion of the relevant works carried out in the field of MPEAs.

2.7.1. Phase Prediction of MPEAs Using ML

Phase prediction is a critical aspect of alloy design, as phase stability directly governs the resulting microstructure and mechanical properties. Early studies relied on empirical descriptors, such as atomic size difference (δ), electronegativity difference ($\Delta\chi$), valence electron concentration (VEC), mixing enthalpy (ΔH_{mix}), and mixing entropy (ΔS_{mix}), to formulate rules for identifying phases (solid solutions, intermetallic compounds, and amorphous phases) and predicting crystal structures. These parameters describe the fundamental chemistry influencing HEA formation and provide valuable insight for phase prediction. Prominent solid-solution (SS) formation criteria include:

- Zhang et al. [67] criterion: $\delta<0.066$, $-15<\Delta H_{mix}<5$KJ/mol
- Guo et al. [68] criterion: $\delta<0.066$, $-11.6<\Delta H_{mix}<3.2$KJ/mol
- Ren et al. [69] criterion: $\delta\leq0.028$, $\Delta H_{mix}\geq -8.8$Kj/mol

Criteria for identify crystal structure of MPEAs include:

- Guo et al. [68]:
  VEC$\geq$8.0 leads to formation of FCC
  VEC<6.87 leads to formation of BCC
  6.87$\leq$ VEC <8 leads to formation of FCC+BCC
- Tsai et al. [70]: VEC range for the formation of σ phase is 6.88< VEC <7.84.
- Poletti and Battezzati [71]:
  VEC>7.5 and 1.6<e/a<1.8 for FCC,
  VEC <7.5 and 1.8< e/a <2.3 for BCC

Several other descriptors, such as Ω-parameter, ϕ-parameter, and γ-parameter [68, 72] have also been employed in phase prediction models. Note that the phase selection rules discussed

here are specific to cast HEAs, i.e., alloys produced directly from solidification without subsequent thermal treatments. Such post-solidification treatments can alter phase stability, thereby affecting the applicability of these rules. Moreover, Guo et. al. [68] highlighted that the validation of VEC rule for alloys containing non-transition metal TM (non-TM) elements remains unexplored, although its validity has been widely confirmed in HEAs composed mainly of transition metals (TM). As traditional descriptors fall short in complex systems, ML has become increasingly important. Pioneering studies by Pei et. al. [73], introduced a new thermodynamics-based rule to predict solid solutions formation (FCC, BCC, and HCP) in a high-throughput manner, using a dataset of 1252 multicomponent alloys (625 single-phase and 627 multi-phase alloys, spanning binary to multi-component systems). Although their established new rule was slightly less accurate (73%) but was physically grounded. Their ML model identified some of the most important features, like molar volume, bulk modulus, and melting temperature, which were not included in Hume-Rothery rules, achieving 93% accuracy in predicting solid solution phases. To further validate, this new rule was employed to predict solid solutions for three 9-element blocks, which was further confirmed by CALculations of PHAse Diagram (CALPHAD) calculations with high consistency (94%). A new parameter γ was defined and calculated to compare the $\Delta G_{mix,}$ for forming single phases and multi-phases, which offered much better predictability (correctly predicted 88% of FCC, 80% of BCC, and 100% of HCP single-phase alloys) than the previous criteria with an average consistency of 64%. With optimum value for α (0.2), jointly with the empirical rule lattice misfit ($\delta \leq$ ~6%), new rule increased the consistency to 81%.

Islam et. al. [15], employed neural network to classify the phase selection in MPEAs, such as single-phase solid solution (SS), amorphous (AM), intermetallic compounds (IM) by analyzing the relative importance of the five features (VEC > $\Delta\chi$ > ΔH_{mix} > δ > ΔS_{mix}) that lead to the phase selection in a dataset with 118 data of MPEAs, (with 33 AM, 64 SS, and 21 IM classes) and obtained an average generalization accuracy of 80%. Huang et. al. [12], used three machine learning models for comparison, to identify the best phase prediction algorithms in case of HEAs using 401 experimental dataset (174 Solid solution (SS), 54 Intermetallic (IM), 173 (SS+IM) mixed phase). They used the K-nearest neighbour (KNN), support vector machine (SVM) and artificial neural network (ANN) methods and observed that the ANN method showed 74.3% correctness in the phase prediction, while the other two algorithms (SVM- 64.3%, KNN- 68.6%) showing lower prediction accuracies. Chau et. al. [74], also employed SVM method to predict the phase selection of MPEAs and used Bayesian

optimization to tune the hyper-parameters. They utilized two established datasets, MPEA-118 from Islam et al. [15] and HEA-401 from Huang et al. [12]. Hyper-parameter tuning was performed to maximize the prediction accuracy efficiently in their studies and each of the classes (i.e., phases) was weighted to avoid the biased prediction in the imbalanced dataset. They obtained the mean values of cross-validation accuracy of 90.2% (not weighted) and 70.6% (weighted) for MPEA-118 and HEA-401, respectively. Similarly, Li et. al. [17] employed SVM to predict phase formation using a data set of 322 distinct as-cast MPEAs, comprising 18 single BCC, 43 single FCC, remaining 261 samples with multiple phases containing intermetallic compounds, or amorphous phase are labeled as NSP (NSP: not forming single-phase solid solution). They achieved a cross validation accuracy of over 90%. Various advanced and hybrid models were also employed. For instance, Agarwal et. al. [75] developed adaptive neuro fuzzy interface system (ANFIS) to classify HEA phases (BCC, FCC, and other multiphases), using two approaches: one considering composition as the inputs (composition-based model) and the other considering a set of six crucial parameters (parametric based model). They achieved classification accuracy of 84.21% and 80% respectively. Zhou et. al. [76], proposed a critical appraisal of the existing design rules with different ML algorithms (artificial neural network (ANN), one-dimensional convolutional neural network (CNN), and the support vector machine (SVM)) for phase designing in HEAs or compositionally complex alloys (CCAs). A total of 601 alloys, (including 165 pure AM alloys, 248 pure intermetallics, 131 pure random SS, 6 mixture of AM and intermetallic alloys, and 51 mixture of intermetallic and random SS alloys) dataset was employed for all the three models. ANN achieved a high testing accuracy of 98.9%, 97.8%, and 95.6% for predicting AM, SS, and IM phases respectively. A sensitivity matrix (which enabled the quantitative assessment of how to tune a design parameter for the formation of a certain phase, such as solid solution, intermetallic, or amorphous) was also derived and extracted based on ANN algorithm. A series of alloys out of the Fe-Cr-Ni-Zr-Cu system were experimentally developed to validate the predictions, and a good agreement was obtained.

Jaiswal et. al. [77], studied multiple ML classification algorithms in order to suitably predict the new medium entropy to high entropy alloys with solid solution phases using a dataset of 664 labeled data alloys (267 BCC alloys, 199 FCC alloys, and 198 (FCC + BCC)) of $CoCuFeNi_x$ system with a variation in Ni concentration. The analyzed data showed a change in correlation coefficient values while moving the alloy system from medium entropy

to high entropy alloy domain. VEC and T_m parameters showed higher importance in predicting FCC, BCC, and FCC + BCC phases.

Krishna et. al. [78], proposed a ML model to predict a mixture of solid solution and intermetallic (SS+IM) in multiphase alloy system with a dataset of 636 alloys (363 SS and 273 SS+IM alloys), using various ML algorithms such as Logistic Regression (LR), Decision Tree (DT), Support Vector Machine (SVM) classifier, Random Forest (RF), Gradient Boosting (GB) Classifier, and Artificial Neural Network (ANN). In their study, multiple FCC and BCC phases were considered in the category of SS (Solid Solution), and alloys with a mixture of solid solution and intermetallic phases (such as Laves, sigma, etc.), were considered in the SS+ IM category. They concluded that although the accuracy of ANN model is less in comparison to SVM, RF and GB Classifier models, but it is the only model, that can predict all the studied alloys, which are comparable to experimental result and Thermo-Calc prediction, where other models fail. Zeng et. al. [79], established high-fidelity phase selection rules based on large data (300,000 equilibrium phase data from 20 quinary families formed by the 8 elements of Al Co, Cr, Cu, Fe, Mn, Ni, and Ti using Thermo-Calc and TCHEA3 database) and five important features (by employing the eXtreme Gradient Boosting (XGBoost) method) that best delineate the single and mixed phases. Their model was validated by 155 annealing experimental data points, and then used to predict the 213 new single-phase alloys with BCC and FCC structures of the alloy families of AlCrNiFeMn and AlCrCoNiFeTi. Their established new phase selection rules, outperformed the existing phase selection rules with a success rate above 90%, and provide a powerful tool for mapping single-phase in the complex temperature-composition space of HEAs.

Choudhury et. al. [16], also utilized a very small dataset of 119 instances for phase classification and 94 samples for crystal structure classification. They observed an accuracy of 91.66% in classifying phases and 93.10% in classifying the different crystal structures. Moreover, they utilized other evaluation metrics such as precision, recall, F1_score and ROC-AUC to classify phases and crystal structure. Similarly, Mandal et. al. [80] used an experimental dataset consisting of 322 different HEAs including 258 solid solution (SS), 31 intermetallic (IM), and 33 amorphous (AM) phases. Among various algorithms, they observed both decision tree and SVM algorithms exhibited the highest accuracy of 93.84% for phase prediction along with good F1_score, recall and precision. They also studied crystal structure classification of SS phases using a dataset consisting of 194 different HEAs including 76 BCC,

61 FCC and 57 mixed BCC + FCC, and observed SVM showed the highest accuracy of 84.32%. Machaka et. al. [81] utilized a comparatively large database of 896 microstructural observations with 354 FCC, 441 BCC, and 101 dual-phase solid solutions (FCC + BCC). They employed Decision Tree (DT) and Random Forest (RF) based classifier, and observed accuracies of 73% and 85% respectively for classifying the phases into FCC, BCC, FCC+BCC and IM, along with good precision, recall, and F1_score.

Risal et. al. [82] on the other hand, utilized 598 entries (302 SS, 58 IM, and 238 SS + IM) and compared KNN, RF, SVM, and ANN algorithms for the phase prediction of HEAs with the goal of significantly improving phase prediction accuracy. They observed 92.31% accuracy with higher ROC-AUC, precision, recall and f1-scores but they used over-sampling/under-sampling method to balance out the majority and minority class data by augmenting it with synthetic data, by acknowledging that the "ML algorithms usually do not perform well for imbalanced dataset".

Lee et. al. [83], proposed a systematic deep learning approach by developing a methodology from the perspective of optimization, generation, and explanation, for enhancing the performance and identifying the key design parameters for phase prediction of HEAs (SS, SS + IM, IM, and AM). The regularized DNN model was attained (through Bayesian optimization process for overall settings related to model architecture, training, and regularization) with five hidden layers, and achieved a testing accuracy of 84.75%. They employed a conditional generative adversarial network (GAN) for generating additional HEA samples to overcome the problem of data shortage, and observed that the augmentation from generative model significantly improves the model performance (prediction accuracy of 93.17%) with unprecedented 93.17% testing accuracy for simultaneously estimating the four phases of HEAs.

Bakr et al. [84] used neural network on 775 samples of HEAs synthesized from mixed manufacturing routes (Arc-melting, sintering, SLM, and others) and obtained 93.4% of accuracy in predicting the existence of the different phases (AM, BCC, FCC, and IM). A summary of the literature discussed above is presented in Table 2.1.

Table 2.1. Summary of literature on phase prediction of MPEAs

Authors	Key findings
Zhang et. al. [13]	Investigated Hume–Rothery's rules for formation of solid-solution phases utilising Neural Network.
Qu et. al. [85]	Proposed two SVM based phase selection models; one based on composition dataset and other based on thermodynamic parameters dataset, to classify the phases in to 5 categories, BCC, FCC, HCP, IM, and other phases including tetragonal, orthorhombic, and so on. Average accuracy of 93.63% for composition inputs model, and 95.75% for feature inputs model was observed.
Mandal et. al. [80]	Analyzed various algorithms for predicting phase and crystal structure using a dataset of 322 and 194 instances of HEAs, and observed accuracy of 93.84% and 84.32% respectively.
Nong et. al. [14]	Predicted structure formation (BCC, FCC or mixed phase) utilising Back propagation artificial neural network (BP-ANN).
Tancret et. al. [86]	Predicted the formation of single-phase solid solution (SS) by integrating Hume-Rothery rules, basic thermodynamic principals, and CALPHAD method, using a Gaussian processes (GP) ML framework using database with 322 HEAs.
Islam et. al. [15]	Classified HEAs into single-phase solid solution (SS), amorphous (AM), intermetallic compounds (IM) using a dataset of 118 instance and a Neural Network, and obtained an average accuracy of 80%.
Choudhury et. al. [16]	Employed Random Forest algorithm for phase selection and crystal structure prediction, achieved accuracy of 91.66% in classifying phases and 93.10% in classifying the different crystal structures using 119 instances for phase classification and 94 samples for crystal structure classification.
Huang et. al. [12]	Predicted formation of solid solution, intermetallic or mixed solid solution and intermetallic phases using an experimental dataset of 401 instances; obtained accuracy of 74.3%, 64.3%, 68.6% for artificial neural network (ANN), support vector machine (SVM) and K-nearest neighbour (KNN) respectively.

Jiang et. al. [87]	Utilised Neural Network to find quasi-phase equilibrium for phase-field models for Al-Cu-Mg multicomponent alloy.
Chau et. al. [74]	Employed SVM to predict the phase selection of MPEAs and Bayesian optimization to tune the hyper-parameters, and obtained cross-validation accuracy of 90.2% (not weighted) and 70.6% (weighted) for existing database of 118 instances [15] & 401 instances [12] respectively.
Kaufmann & Vecchio [88]	Developed a novel high-throughput "ML-HEA" approach, coupling thermodynamic and chemical features for predicting the solid solution forming ability, using thermodynamic data from Thermo-Calc and chemical features with a random forest model, and compared with other traditional models.
Qi et. al. [89]	Predict phase formation based on binary alloy phase diagram data using random forest algorithm.
Li et. al. [17]	Employed SVM to predict phase formation in Co–Cr–Fe–Mn–Ni HEA using a data set of 322 distinct as-cast MPEAs, achieved a cross validation accuracy of over 90%. SVM model for distinguishing the single BCC, single FCC, and the remaining (NSP: not forming single-phase solid solution) phases of MPEAs.
Zhou et. al. [76]	Studied a critical appraisal of the existing design rules with different ML algorithms (artificial neural network (ANN), convolutional neural network (CNN), and support vector machine (SVM)) for phase design in HEAs or CCAs, with a dataset of 601 alloys. ANN model achieved highest accuracy of 98.9%, 97.8%, and 95.6% for predicting AM, SS, and IM phases respectively.
Qi et. al. [89]	Predicted phase formation of HEAs using a phenomenological method, solely based on the binary phase diagrams, by considering the hypothesis that the structural stability of HEA is encoded within the phase diagrams and observed a success rate of 81%.

Agarwal et. al. [75]	Developed adaptive neuro fuzzy interface system (ANFIS) for phase prediction in FCC, BCC, and multi-phase HEAs, using two approaches, one considering composition (composition-based model) as the inputs, while other considering a set of six crucial parameters (parametric based model) in the formation of HEAs and achieved accuracy of 84.21% and 80% respectively.
Wu et. al. [90]	Searched for eutectics in Al–Co–Cr–Fe–Ni HEAs using Neural Network.
Dai et. al. [91]	Implemented Logistic regression to predict phase formation in high-entropy alloys using a small dataset of 407 samples, and observed accuracy of 86%.
Zhang et. al. [92]	Employed Genetic algorithms to find the best combination of descriptors and ML models to predict phase formation in HEAs.
Al-Shibaany et. al. [93]	Implemented Deep Neural Networks (DNNs) to predict HEA phases in order to design alloy with 90% of accuracy in phase prediction.
Zhang et. al. [94]	Studied the importance of the formation enthalpy and atom-size difference in forming phases of HEAs using SVM model and extended Miedema theory.
Roy et. al. [95]	Predicted crystallographic phase for low-, medium- and high-entropy alloys using Gradient Boost classification.
Nassar et. al. [96]	Employed two Neural networks (NNs) models, one considering only the compositional data (atomic percentage) and other considering Hume-Rothery features of alloys along with compositional data to predict HEA phases and observed accuracy of 92% and 90% respectively.
Lee et. al. [97]	Utilised an ensemble of support vector machines (eSVM) comprising of multiple SVM models, generated by the bootstrap sampling method for multi-class classification, observed an accuracy of 86%.
Risal et. al. [82]	Compared KNN, RF, SVM, and ANN algorithms for the phase prediction of HEAs with the goal of significantly improving phase prediction. Observed accuracy of 92.31% and 91.21% for KNN and RF respectively, while SVM, and MLP also provided the satisfactory

	performance with accuracy greater than 90% for "Oversampled-PCA-6" dataset.
Machaka et. al. [81]	Employed Decision Tree (DT) and Random Forest (RF) based classifier on 1460 microstructural observations, and observed accuracies of 73% and 85% respectively for classifying the phases into FCC, BCC, FCC+BCC and IM.
Zeng et. al. [79]	Established high-fidelity phase selection rules based on large data, for mapping single-phase in complex temperature-composition space of HEAs. Their established new phase selection rules, outperformed the existing phase selection rules with a success rate above 90%
Lee et. al. [83]	Utilised a regularized DNN model for identifying key design parameters for phase prediction ((SS, SS + IM, IM, and AM).), achieved accuracy of 84.75%. Employed a conditional generative adversarial network (GAN) for generating additional HEA samples to overcome the problem of data shortage and observed accuracy of 93.17%.
Jin et. al. [98]	Developed a learning-based approach to predict the vast compositional space of multi-element alloys (binary alloy, ternary alloy, and HEA), while applying only the binary alloy dataset as the training set. Achieved an accuracy of 80.56% for the phase of the multi-element alloy and 84.20% accuracy for the phase of HEA.
Jaiswal et. al. [77]	Implemented Multiple ML classification algorithms to predict phases, using a dataset of 664 labeled data of $CoCuFeNi_x$ system with varying concentration of Ni, achieved testing accuracy of more than 80% for multiple algorithms
Krishna et. al. [78]	Compared Logistic Regression, Decision Tree, SVM classifier, Random Forest, Gradient Boost Classifier, and ANN algorithms to predict a mixture of solid solution and intermetallic (SS+IM) in multiphase alloy system using a dataset of 636 alloys, achieved highest accuracy of 83.02% for SVM classifier.

Observations

In literature concerning phase prediction of MPEAs/HEAs, various studies report high accuracy from their ML predictions but the fact that these accuracies often stem from combining synthetic data with experimental datasets. A dataset involving synthetic data merged into the experimental data can lead to spurious outcomes when feeding to the machine learning algorithms. An attempt like this (which is routinely done in literature) can although help achieve higher model accuracy, but it can compromise the quality of prediction, particularly, while inferring complex phases of HEAs. As acknowledged by Risal et al. [51] that the "ML algorithms usually do not perform well for imbalanced dataset" and reported 92.31% accuracy by using oversampling method to balance out the minority class data by polluting it with synthetic data. Moreover, to address class imbalance, many studies relied on over-sampling, under-sampling, or synthetic data generation using generative adversarial networks (GANs). However, the validity of synthetic data remains questionable, particularly in capturing the complexity of experimentally derived phases.

This research assumes that augmenting or polluting real-world data with synthetically generated samples is unreliable, as accuracy alone does not provide a robust measure for assessing the performance of machine learning models trained on imbalanced datasets. Precision, Recall, F1_score, ROC_AUC score are much reliable and trustworthy evaluation metrics for imbalanced datasets. Moreover, no study can be seen that targets one particular synthesis route to extract the data reliably from experimental studies which can help avoid the spurious effect of an alternative synthesis routes on the resulting phase. For instance, Bakr et al. [84] reported an accuracy of 93.4% using a neural network trained on 775 HEA samples synthesized via various methods (e.g., arc melting, sintering, selective laser melting) to predict different phases (AM, BCC, FCC, and IM). However, their model failed to predict the presence of the amorphous phase. This highlights that, despite the high reported accuracy, the model produced incorrect predictions, likely due to the omission of processing routes as input features, an important limitation given their significant influence on phase formation. Hence, care must be taken while extracting data from mixed manufacturing routes and tackling an imbalanced dataset. Additionally, ML models are often hindered by data scarcity and quality issues, lack of standardized phase formation rules, and model generalizability, all of which impact model generalizability and predictive reliability.

2.7.2. Mechanical Property Prediction and Discovery of Novel MPEAs

The mechanical properties, such as yield strength, hardness, ductility, toughness, and creep resistance, are directly influenced by complex interactions among composition, microstructure, and processing conditions. Accurate prediction of these properties is critical for alloy selection in demanding sectors like aerospace, energy, automotive, and defense. Given the limitations of exhaustive experimental testing, machine learning has emerged as a powerful alternative, offering efficient property prediction across vast compositional spaces. This section presents a comprehensive review of ML-driven approaches for predicting elastic, thermal, and mechanical properties (such as hardness, yield strength, elongation) of MPEAs.

Bundela et al. [99] utilized various regression models, including linear regression, lasso, ridge, random forest, XGBoost, and bagging regressor, to predict the microhardness of HEAs. Kim et. al. [19], proposed a combined experimental and computational approach based on in-situ neutron-diffraction (ND) characterizations, and first-principles calculations. A gradient boosting trees approach was used to investigate the elastic properties of $Al_{0.3}CoCrFeNi$. Good agreement in elastic constants was observed from ND, first-principles calculations, and ML models, confirming the elastic behavior of FCC $Al_{0.3}CoCrFeNi$, an HEA known for its high strength and excellent ductility. Furthermore, Zhou et al. [100] developed three regressor models to predict Young's modulus and hardness of novel high entropy ceramics by integrating data from previous density functional theory (DFT) calculations and experimental results.

Wen et. al. [18], conducted a study for elaborate discussion on single property prediction of materials, where they have formulated a materials design strategy combining a machine learning (ML) surrogate model with experimental design algorithms to search for HEAs with high hardness in a six component (Al-Co-Cr-Cu-Fe-Ni) HEA system. Several alloys with hardness 10% higher than the best value in the original training dataset were fabricated via only seven experiments. Moreover, $Al_{47}Co_{20}Cr_{18}Cu_5Fe_5Ni_5$ alloy, possessing the highest hardness, was predicted after the fourth iteration with 883 HV on average, which is 14% higher than the best value in the original dataset.

Rickman et. al. [24], proposed canonical correlation analysis (CCA) combined with genetic algorithms to design hard high-entropy alloys. The dataset of Vickers hardness for 82 systems from literature review was taken as input. Multiple regression was performed with canonical correlation analysis to predict the presence of BCC or FCC solid solutions or of

intermetallic phases, and to predict the Vickers hardness. Hardness was found to increase with ideal mixing entropy and decrease with valence electron concentration and mixing enthalpy. Canonical correlation analysis was used to construct a fitness function for a genetic algorithm search in a composition space of 16 metallic elements. Their model predicted the enhanced hardness with 90% confidence. Seven candidate alloys were fabricated by arc melting and hardness tested. Hardness ranged from 277HV (2.72GPa) to 1,084HV (10.63GPa); five of the alloys had hardness greater than 700HV (6.87GPa). Highest measured hardness was found for: $Co_{33}W_{07}Al_{33}Nb_{24}Cr_{03}$ = 1084 ± 37 HV.

Yang et. al. [101], constructed a ML-based alloy design system (MADS), incorporating the database establishment, model construction, composition optimization and experimental validation to facilitate the rational design of HEAs with improved hardness. A hardness prediction model based on support vector regression with radial basis kernel function (SVR-rbf) was developed with the five key features which includes the average deviation of the atomic weight (ADAW), the average deviation of the column (ADC), the average deviation of the specific volume (ADSV), the valance electron concentration (VEC), and the mean melting point (Tm). R^2_score of the model reached 0.94 for both the independent testing set and leave-one-out cross validation (LOOCV). The best performer $Co_{18}Cr_7Fe_{35}Ni_5V_{35}$ HEA exhibiting the ultra-high hardness, which is 24.8% higher than the highest one in the original dataset was obtained. Additionally, they introduced SHAP to uncover some implicit information between the key features and the hardness of as-cast alloys and found that VEC is the most significant variable, and it has positive impact on hardness when VEC < 7.5.

Bhandari et. al.[20], were the first to employ an ML model to predict the yield strength of HEAs at elevated temperatures. Their model accurately estimated the yield strengths of MoNbTaTiW and HfMoNbTaTiZr at 800°C and 1200°C with low computational cost, showing strong agreement with experimental results. The predicted value of yield strength of MoNbTaTiW and HfMoNbTaTiZr was 492 MPa and 346 MPa, respectively. Further, Klimenko et. al. [102], employed a ML approach to predict the yield strength of Al-Cr-Nb-Ti-V-Zr refractory high entropy alloys (RHEAs) in a wide range of temperatures (20–800^{O}C). They proposed a combined approach, including phenomenological rules, CALPHAD and ML, using a surrogate model based on a support-vector machine algorithm. Their model showed good accuracy at 20^{O}C and 600^{O}C (the average prediction error was 11% and 13.5%, respectively), but the error of prediction was slightly higher at 800^{O}C (worse than 20% for only two model alloys). They concluded that the content of aluminum, chromium and

zirconium have the greatest influence on the specific yield strength, while vanadium and titanium have lower effect, and an addition of niobium has a negative effect for the Al-Cr-Nb-Ti-V-Zr system. One of the predicted alloys, $Al_{13}Cr_{12}Nb_{20}Ti_{20}V_{35}$ possesses an excellent combination of strength (1295 MPa at 20^{O}C, 1113 MPa at 600^{O}C and 898 MPa at 800^{O}C) and ductility (16.8% at 20^{O}C, 5.5% at 600^{O}C and >50% at 800^{O}C).

Khakurel et. al. [103], employed ML with high throughput experimental synthesis to predict the young's modulus of compositionally complex alloys (CCAs) and achieved a significant better performance (MAE=6.15 GPa) by considering VEC in the feature sets. Multiple ML models such as four tree-based ensemble methods (Gradient Boosting, Ada Boost, Extreme Gradient Boost (or XGBoost), Random Forest (RF)), two linear based models (LASSO regression, Ridge regression), and two kernel based methods (Gaussian Process Regression and Support Vector Machine (SVM)) were used on two different sets of data; one larger dataset (154 alloys) with both the refractory and non-refractory alloys and the other smaller dataset (96 alloys) with only refractory alloys. Thus obtained 16 models, 8 for the larger dataset and 8 for smaller dataset. They concluded that among the eight ML models, Gradient Boosting model is superior in terms of accuracy and robustness and their results identified VEC, average melting temperature and difference in atomic radii as the key features that determine the young's modulus of CCAs and refractory-based CCAs. They synthesized 32 alloys in the form of thin metal plates/foils, using an arc melter and measured elastic modulus values, using the ultrasonic pulse-echo technique and compared the predicted young's modulus with the experimentally measured ones, for both the larger and smaller datasets. Finally observed that larger dataset was significantly off compared to experimentally measured young's modulus, while smaller dataset in contrast have achieved better prediction accuracy because of the quality (Homogeneous data) and relevance of the training data.

Vilalta et. al. [21], predicted the relationship between the yield stress and the stacking fault energies (SFE) landscape in HEAs. Their data contained the SFE landscape and the resulting critical yield stress (obtained from Phase-Field Dislocation Model (PFDM) simulations of dislocations moving in this energy landscape) in Ni-Co-Fe-Cr-Mn family of HEAs. They applied six different supervised ML models (K-Neighbours Regressor, Bayesian Ridge Regression, Decision Tree Regression, Gradient Boosting Regression (GBR), Kernel Ridge Regression, Gaussian Process Regression (GPR)) and one unsupervised ML model (Principal Component Analysis (PCA)). Divided the dataset randomly into 75% training and 25% testing data, and selected three different types of feature sets (prescribed statistical

features, estimated statistical features, and SFE grid) to determine which features best describe the PFDM inputs. Their best ML model was able to predict the yield stress of HEAs with varying SFE landscapes to approximately 2% error.

Bhandari et. al. [104], studied a neural network (NN) model to provide an alternative route to determine the Vickers hardness of refractory high entropy alloys (RHEAs). A dataset of 128 HEA samples after removing the redundant values was used for training the NN model (consist five hidden layers). To experimentally verify the ML model prediction, $C_{0.1}Cr_3Mo_{11.9}Nb_{20}Re_{15}Ta_{30}W_{20}$ alloy was synthesized by vacuum arc melting method; the microstructure and chemical compositions were examined using a field emission scanning electron microscope equipped with second electron (SE) and energy dispersive spectroscopy (EDS) detector and Vickers hardness was tested at five different positions on the sample using three testing loads 2000, 500, and 100 gf, for the dwell time of 15 sec. The measured Vickers hardness was found to be consistent with the NN model prediction.

Buranich et. al. [105], used complex analytical algorithms (Linear Regression (LR), Random Forest (RF) and Gradient Boosting Regressor (GBR)) to design and screen new high-entropy alloys with the proper response to mechanical and thermal processing under casting and additive manufacturing-based production for applications in mechatronics industry. The 126 different equimolar refractory based HEAs were examined for a set of thermal and mechanical properties, GBR was found to outperform (above 91% accuracy) among the developed models in the prediction. Results revealed that alloys composed of Ti, V, Nb, Hf, Ta, and W predominantly exhibited the best combination of properties (TiNbHfTaW, CrNbHfTaW and VNbHfTaW alloys demonstrated the best results for mechanical and electromechanical engineering applications).

Ren et al. [106] utilized a dataset of 205 HEA samples featuring 19 characteristics commonly employed in HEA property prediction. They implemented a tree-based machine learning model to predict hardness and integrated it with Particle Swarm Optimization (PSO) for component optimization. Due to the limited availability of real experimental data, they resorted to synthetic data through random oversampling to improve the performance of their Component Optimization Model (COM), which raises concerns about the reliability of their prediction. Their database primarily included Al, Co, Cr, Cu, Fe and Ni. Moreover, to effectively navigate the design space for alloys with high hardness, it is essential to enrich the training datasets with refractory alloys, given their inherent high-temperature stability and robust mechanical properties. However, a major impediment to the reliable application of ML

in materials science continues to be the scarcity of relevant data, particularly for HEAs/MPEAs. Roy et al. [107] addressed this issue by employing a generative adversarial network (GAN) to explore an 18-dimensional design space involving Co-Fe-Ni-Si-Al-Cr-Mo-Ti-Nb-V-Zr-Mn-Cu-Sn-Ta-Hf-W-Zn MPEAs using a limited dataset of 241 alloys. They successfully designed two new MPEAs with hardness values exceeding 941 HV.

The above-mentioned literature primarily focuses on either single-property prediction or the discovery of novel compositions through single-property optimization. Very scant studies have addressed true multi-objective optimization. Debnath et. al. [23] designed a multi-layer perceptron ANN model combined with a genetic algorithm to perform multi-objective optimization for designing iron-based HEAs with high toughness, Young's modulus, hardness, yield strength (YS), and % elongation. These properties were individually paired with ductility (%El) in three separate bi-objective optimizations, using a dataset of 600 recorded HEAs and 13 input variables. The optimization results indicated that a high Fe content (~30%) enhances strength, hardness, and modulus, but leads to a reduction in ductility (<10%). Moreover, Hastings et al. [108] developed the BIRDSHOT framework, an integrated batch Bayesian optimization system designed to accelerate multi-objective alloy discovery, targeting the Al–V–Cr–Fe–Co–Ni high-entropy alloy (HEA) space. The framework optimized three mechanical objectives simultaneously: UTS/YS ratio, hardness, and strain rate sensitivity (SRS). Using a combination of machine learning models, high-throughput synthesis, and mechanical testing, the study demonstrated rapid exploration of a high-dimensional design space, identifying Pareto-optimal alloys by evaluating only 0.15% of candidate compositions. While the approach significantly improved discovery efficiency, limitations included moderate improvement in SRS, phase prediction inaccuracies, and the exclusion of certain promising compositions due to strict pre-optimization constraints.

A summary of the literature discussed above is tabulated in Table 2.2.

Table 2.2. Summary of literature on mechanical properties of MPEAs using ML

Authors	Key findings
Menou et. al. [109]	Designed solid-solution hardened $Al_{10}Co_{17}Fe_{34}Mo_5Ni_{34}$ high-entropy alloy using Genetic algorithms, Gaussian process statistical analysis and CALPHAD.
Menou et. al. [110]	Developed solid-solution hardened BCC Al-Cr-Mn-Mo-Ti alloys by a combination of genetic algorithms, CALPHAD, Pareto optimization and data mining.
Wen et. al. [18]	Developed iterative feedback between ML and experiment to develop high-hardness alloys for Al–Co–Cr–Cu–Fe–Ni based high-entropy alloy system.
Kim et. al. [19]	Investigated elastic properties of $Al_{0.3}CoCrFeNi$ HEA using Gradient boosting trees combined with ab-initio and experiments.
Chang et. al. [25]	Utilised Neural Network to find the Al–Co–Cr–Fe–Mn–Ni composition with highest hardness.
Dai et. al. [111]	Predicted thermal and mechanical properties using a deep learning potential (DLP) for high entropy $(Zr_{0.2}Hf_{0.2}Ti_{0.2}Nb_{0.2}Ta_{0.2})C$ alloy.
Wu et. al. [90]	Searched for eutectics in Al–Co–Cr–Fe–Ni HEAs using Neural Network.
Debnath et. al. [23]	Designed ANN model for multi-objective optimization to design the iron-based HEAs with high toughness, Young's modulus, hardness, yield strength (YS) and % elongation.
Roy et. al. [95]	Predicted young's modulus for low-, medium- and high-entropy alloys using Gradient Boost regression.
Bhandari et. al. [20]	Predicted yield strength of HEAs at the desired temperature using Random Forest (RF) regressor.
Buranich et. al. [105]	Designed and screened new HEAs with proper response to mechanical and thermal processing, for applications in mechatronics industry and additive manufacturing-based production using Linear Regression (LR), Random Forest (RF) and Gradient Boosting Regression (GBR).
Li et. al. [112]	Developed a novel integration method of machine learning, a physical model and atomic simulation to obtain the optimal grain size of heterogeneous-grained CrCoFeNi HEAs, designed for achieving high yield strength.

Zhang et. al. [113]	Predicted mechanical properties of non-equiatomic CuFeNiCrCo HEAs, using Molecular dynamics (MD) simulation combined with machine learning method. Kernel-based extreme learning machine (KELM) model outperformed the others for the prediction of yield stress and young's modulus.
Bhandari et. al. [104]	Predicted hardness of refractory high entropy alloys (RHEAs) using Neural network (NN) model.
Klimenko et. al. [102]	Developed a surrogate model based on a support-vector machine algorithm to predict the strength of Al-Cr-Nb-Ti-V-Zr HEA System. Based on prediction, $Al_{13}Cr_{12}Nb_{20}Ti_{20}V_{35}$ alloy with an excellent combination of ductility and yield strength was produced.
Yang et. al. [101]	Constructed a Machine learning-based alloy design system (MADS) to facilitate the rational design of HEAs with enhanced hardness. Achieved one optimized sample with superior hardness, which is 24.8% higher than the highest hardness in the original dataset.
Li et. al. [114]	Predicted the optimum elemental composition for $Cr_xCo_yNi_{100-x-y}$ medium entropy alloy (MEA) with high strength and low cost/density using ML-based approach coupled with the high-throughput Molecular dynamic simulation.
Vilalta et. al. [21]	Studied the relationship between the stacking fault energy (SFE) fluctuations and the yield stress of an FCC HEA using ML models.
Choi et. al. [22]	Employed Artificial neural network (ANN) to predict the mechanical properties such as yield strength, microstructure, and elongation of HEA by training the model using the mole fraction and post-process information.
Zhao et. al. [115]	Designed a self-organizing algorithm (SOM) to comprehensively analyze some of the previously proposed features, and utilised some common ML algorithms, such as a k-nearest neighbour model (KNN), support vector machine model (SVM), and artificial neural network model (ANN) to find the most suitable ML model for predicting more HEAs.
Zheng et. al. [116]	Proposed a novel method to accelerate the development of ultra-strong nano-precipitated HEAs, using ML to thermodynamically confirm the alloy composition with proper volume fraction of nanoprecipitate, and

	the pre-strain aging to kinetically optimize the precipitate morphologies. A novel $Ni_{32}Co_{28}Fe_{28}Cr_3Al_3Ti_6$ (wt.%) HEA with both excellent strength and ductility was designed successfully.

Observations

Numerous studies have successfully applied ML models to predict mechanical properties such as hardness, yield strength, Young's modulus, and elasticity. Strong correlations with experimental results were observed in several cases, confirming the potential of ML-driven materials design. For example, Wen et. al. [18] and Yang et. al. [101] achieved high-accuracy property predictions and compositional optimization with only limited experimental validation, highlighting ML's efficiency in navigating vast compositional spaces. Most existing models, however, have focused on single-property prediction, primarily hardness or yield strength, often using physical features such as valence electron concentration (VEC), mixing enthalpy(ΔH_{mix}), atomic size mismatch (δ) as dominant input descriptors. Khakurel et. al. [103], demonstrated that smaller, high-quality, synthesis-specific datasets yield superior predictive performance compared to larger, heterogeneous datasets. Nevertheless, the major bottleneck remains the scarcity and uneven distribution of experimental data, particularly for underexplored compositions, which undermines model generalizability. To address data sparsity, several studies (e.g., Roy et. al. [95], Ren et al. [106]) relied on synthetic data generation or oversampling to augment sparse datasets. While these techniques support model training, they raise concerns regarding prediction reliability and the physical validity of generated compositions.

Moreover, the availability of growing datasets and increasing computational power, most studies continue to focus on optimizing a single property, an approach that fails to meet real-world engineering demands where multiple mechanical traits must be balanced simultaneously. For instance, Debnath et. al. [23] conducted bi-objective optimization, generating separate Pareto fronts for individual property pairs, but did not implement true multi-objective optimization across all relevant properties. Such approaches result in fragmented, non-integrated solutions that fall short of the comprehensive strategies required for practical, high-performance alloy discovery. Furthermore, ML models tuned for only two targets are prone to overfitting, particularly when a third property becomes critical. Narrow optimization scopes, such as fixing Fe content at 30% (Debnath et. al. [23]), further constrain

model's generalizability and restrict exploration of the broader compositional space, ultimately hindering holistic alloy design.

While Hastings et al. [108] introduced BIRDSHOT, a modern and efficient batch Bayesian optimization framework for alloy discovery, it too has notable limitations. First, it targets only the UTS/YS ratio, hardness, and strain rate sensitivity (SRS), while neglecting key properties such as elongation and fracture toughness. Second, although phase stability was predicted using CALPHAD and ML surrogates, inconsistencies between predicted and experimentally observed phases, including unexpected BCC and sigma formations, led to inefficiencies in the optimization process. Moreover, BIRDSHOT relies heavily on pre-optimization filters based on fixed physical constraints (e.g., density and thermal conductivity), which may prematurely eliminate promising compositions. Its use of SFE predictions from DFT-trained ML models, without experimental validation, introduces further uncertainty, particularly since only modest improvements in SRS were observed over successive iterations. Finally, batch Bayesian optimization, while efficient, poses the risk of batch-wise exploration bias, especially if early candidate selections lack diversity. These limitations suggest that while BIRDSHOT marks a major step forward in accelerating multi-objective materials discovery, future improvements should aim to expand mechanical property targets, including elongation and toughness, alongside YS and UTS to develop a more complete and practically applicable design framework.

2.7.3. Discovery and Design of Sustainable MPEAs Free of CRMs/C&SRMs

In literature reporting development of MPEAs, various compositions have been developed through compositional modifications of the base Cantor alloy (CoCrFeMnNi) by replacement (CrFeCoNiCu [117] and TiCrFeCoNi [118]), variation ($CrMnFeCo_xNi$ and $CrMnFeCoNi_x$ with x = 0–2 [119]), or addition of elements (CrMnFeCoNiCu [1], $CrMnFeCoNiAl_x$ [44, 120]). Furthermore, reduction-based strategies have spawned lower-order systems such as binaries, ternaries and quaternary alloys, collectively termed low and medium-entropy alloys [44]. Ten binaries, ten ternaries and five quaternaries' compositions can be made from a cantor alloy. Among two of the ten possible binaries (FeNi and CoNi), five of the ten possible ternaries (CoFeNi, CrFeNi, FeMnNi, CoCrNi and CoMnNi), and three of the five possible quaternaries (CoCrFeNi, CoFeMnNi and CoCrMnNi) are single phase FCC solid solution [121] [122]. Interestingly, equiatomic CoCrNi medium entropy alloy, shows better mechanical properties than the original Cantor alloy, which demonstrate that configurational entropy (increasing number of elements in an alloy) does not always guarantee

enhanced mechanical performance [123].

Beyond these, numerous refractory HEAs (NbMoTaW [124], Ti_xNbMoTaW (x = 0, 0.25, 0.5, 0.75, 1) [124] V_xNbMoTa (x = 0.25, 0.5, 0.75, 1.0) [125], $Nb_{40}Ti_{25}Al_{15}V_{10}Ta_5Hf_3W_2$ [126], NbMoTaW$(HfN)_x$ (x = 0, 0.3, 0.7, 1.0) [127], MoNbTaVW [128], HfNbTaZr [128], $Re_{0.1}Hf_{0.25}NbTaW_{0.4}$ [129]) and 3d transition metal HEAs (e.g., $Al_{10.3}Co_{17}Cr_{7.5}Fe_9Ni_{48.6}Ti_{5.8}Ta_{0.6}Mo_{0.8}W_{0.4}$ [130], $Al_{10.2}Co_{16.9}Cr_{7.4}Fe_{8.9}Ni_{47.9}Ti_{5.8}Mo_{0.9}Nb_{1.2}W_{0.4}C_{0.4}$ [131]) have been designed, finding applications in aerospace, gas turbines, and nuclear sectors. Other MPEAs such as $CoCrFeNiTa_x$ (x = 0, 0.1, 0.2, 0.3, 0.4, 0.5, and 0.75) [132], $CoCrFeNiNb_x$ (x = 0, 0.103, 0.155, 0.206, 0.309 and 0.412) [133] and $CoCrFeNiNb_x$ (x = 0.1, 0.25, 0.5 and 0.8) [134] have also shown a remarkable combination of high strength and ductility for their eutectic counterparts such as $CoCrFeNiTa_{0.4}$ and $CrFeCoNiNb_{0.5}$ respectively. Apart from these compositions, various MPEAs have been developed by extensively utilizing elements such as Al, Cu, Cr, Ti, V, W, Ta, Hf, Nb, Mo, Zn, Zr, Si, while certain precious metal MPEAs incorporate elements such as Ag, Pt, Au, Ru, Rh, Pd.

However, a significant number of these high-performance MPEAs incorporate critical raw materials (CRMs) or critical and strategic raw materials (C&SRMs) such as Hf, Nb, Ta, W, Pt, Pd, Ru, and Rh, elements marked as critical due to supply risks and environmental impacts [135-137]. The reliance on CRMs/C&SRMs not only generates substantial emissions during recycling processes but also imposes serious vulnerabilities in global supply chains, thereby hindering the pursuit of Net-zero ambitions. Rizzo et al. [136] emphasized the importance of having a flawless supply chain of raw materials to maintain a sustainable circular economy. This highlights the urgent need to minimize the use of CRMs and C&SRMs, reduce import dependency, and limit extensive mining, which are all crucial steps toward advancing sustainable alloy development and achieving Net-Zero goals.

Despite extensive research on performance-driven MPEAs, only one study directly addressing the sustainability challenges of high-entropy materials (HEMs) was identified. Han et al. (2024) critically reviewed these sustainability challenges in MPEAs, highlighting that many of these alloys rely heavily on CRMs such as Co, Ni, Ta, and W, which are expensive, scarce, and environmentally taxing. To improve sustainability, they proposed strategies such as utilizing scrap and waste feedstocks (secondary and tertiary synthesis), moving beyond strict equimolar compositions, exploring mixed mineral extraction processes, and designing impurity-tolerant microstructures. They advocated for a holistic sustainability-driven design

approach that integrates thermodynamic and kinetic modeling, recycling strategies, and life cycle assessment tools, ultimately outlining pathways to reduce the carbon footprint, production costs, and CRM dependency of future HEAs without compromising performance.

Notably, no study to date has integrated machine learning (ML) specifically to address sustainability, particularly with regard to reducing or eliminating critical raw materials (CRMs) or critical and strategic raw materials (C&SRMs).

Observations

Despite extensive progress in MPEAs/HEAs research, little attention has been devoted to sustainability, particularly in reducing or eliminating the use of CRMs and C&SRMs. Although various compositional modifications of the base Cantor alloy have yielded high-performance MPEAs, most continue to incorporate CRM/C&SRMs-rich elements. Even advanced alloys developed for structural and aerospace applications frequently exhibit this dependency. The existing literature also reveals a lack of integrated machine learning (ML) frameworks explicitly aimed at discovering CRM/C&SRMs-free or sustainability-oriented MPEAs. Furthermore, current MPEA databases are skewed toward CRM-heavy compositions, introducing bias into model training and predictions. Hence, there is a critical need for sustainability-aware alloy discovery frameworks capable of enabling the design of next-generation MPEAs while mitigating ecological and geopolitical risks.

Tables 2.1 and 2.2 collectively summarize the representative machine-learning approaches applied to MPEA design and optimization, detailing the input descriptors, algorithms, and reported predictive performances for both phase prediction and mechanical-property prediction. Complementing this, Section 2.7.3 highlights the critical motivation for minimizing the use of CRMs/C&SRMs in alloy development. Together, this consolidated overview establishes a clear scientific basis and rationale for the integrated data-driven frameworks developed in the present work.

2.8. Research Gaps

Despite considerable progress in applying machine learning to MPEAs, through approaches such as surrogate modeling, generative adversarial networks (GANs), and active learning, most efforts have remained focused on phase classification [12, 81, 92], prediction of mechanical properties, such as hardness, yield strength, or elastic modulus [20, 95, 104, 138, 139], and the discovery of novel alloy compositions [18] [116] without considering the

elimination of CRM/C&SRMs. However, several critical gaps continue to limit the effective design, deployment, and sustainability of MPEAs.

First, the development of robust, reliable, and generalizable ML models for phase and property prediction remains constrained by the scarcity and inconsistent quality of experimental data, as well as the limited consideration of processing-route effects on phase and property outcomes (i.e., composition–processing–structure–property relationships). This challenge is further compounded by the widespread reliance on synthetic data augmentation, which, although often employed to mitigate data scarcity, frequently compromises model reliability. Second, open-source materials informatics toolkits, which are specifically developed to support materials researchers with limited expertise in machine learning, have not been systematically employed for predicting the mechanical properties of complex alloy systems such as MPEAs. Their limited adoption has impeded efforts to establish benchmarking standards, ensure reproducibility, and promote accessibility, factors that are essential for advancing standardized practices in the field.

Moreover, the vast compositional space of MPEAs remains insufficiently explored with respect to advanced multi-objective optimization. Current efforts largely emphasize single-property optimization, neglecting the inherent trade-offs between competing properties, most notably the long-standing strength–ductility dilemma, thus restricting the practical applicability of discovered alloys. Finally, the majority of high-performance MPEAs continue to rely heavily on CRMs and C&SRMs such as Co, Ta, Hf, and V. This dependence introduces significant challenges related to material cost, supply risk, and long-term sustainability, directly conflicting with global priorities such as achieving Net Zero targets and promoting resource-efficient material design.

In summary, addressing these interconnected limitations, including data scarcity, inadequate consideration of processing-route effects on phase and property outcomes, synthetic data augmentation, limited adoption of open-source toolkits developed specifically for materials researchers, the absence of robust ML-based frameworks for multi-objective optimization, and the continued overreliance on CRMs and C&SRMs in developing high-performance MPEAs, is essential for advancing both the scientific understanding and the technological deployment of MPEAs.

2.9. Objectives of the Present Work

The primary objective of this thesis is to develop robust and generalizable machine learning frameworks for phase and mechanical property prediction, multi-objective optimization of

competing properties, and the design of CRM/C&SRMs-free or CRM/C&SRMs-lean MPEAs for a sustainable future. A key emphasis is placed on improving model generalizability by exclusively leveraging high-quality experimental datasets, restricted to alloys synthesized via a consistent route (melting and casting), without resorting to synthetic data augmentation.

The research also advances sustainability through a dual strategy: (i) an ML-guided chemical tuning approach that combines CALPHAD-generated datasets with hybrid optimization to design CRM-free or CRM-lean alloys; and (ii) a non-ML-based physical design approach via strain engineering to minimize dependence on C&SRMs.

The sub-objectives of the present work are as follows.

- To develop a phase prediction framework trained exclusively on high-quality experimental data, without the use of synthetic data augmentation, and benchmark its performance against augmented models.
- To implement MAST-ML for mechanical property prediction using experimentally-derived dataset, and critically evaluate its robustness and limitations.
- To establish a novel ML framework for multi-objective optimization of YS, UTS, and $\mathcal{E}$, thereby addressing the strength–ductility trade-off.
- To design a hybrid ML–metaheuristic framework, integrating CALPHAD (Thermo-calc)-generated data, for identifying CRM-free or CRM-lean MPEAs.
- To investigate strain engineering as a sustainable non-ML pathway for designing C&SRM-free alloys by exploiting microstructural modifications (dislocation density, grain refinement, TWIP, TRIP).

To accomplish these objectives, the present work has been structured into five stages, as illustrated in Figure 2.5.

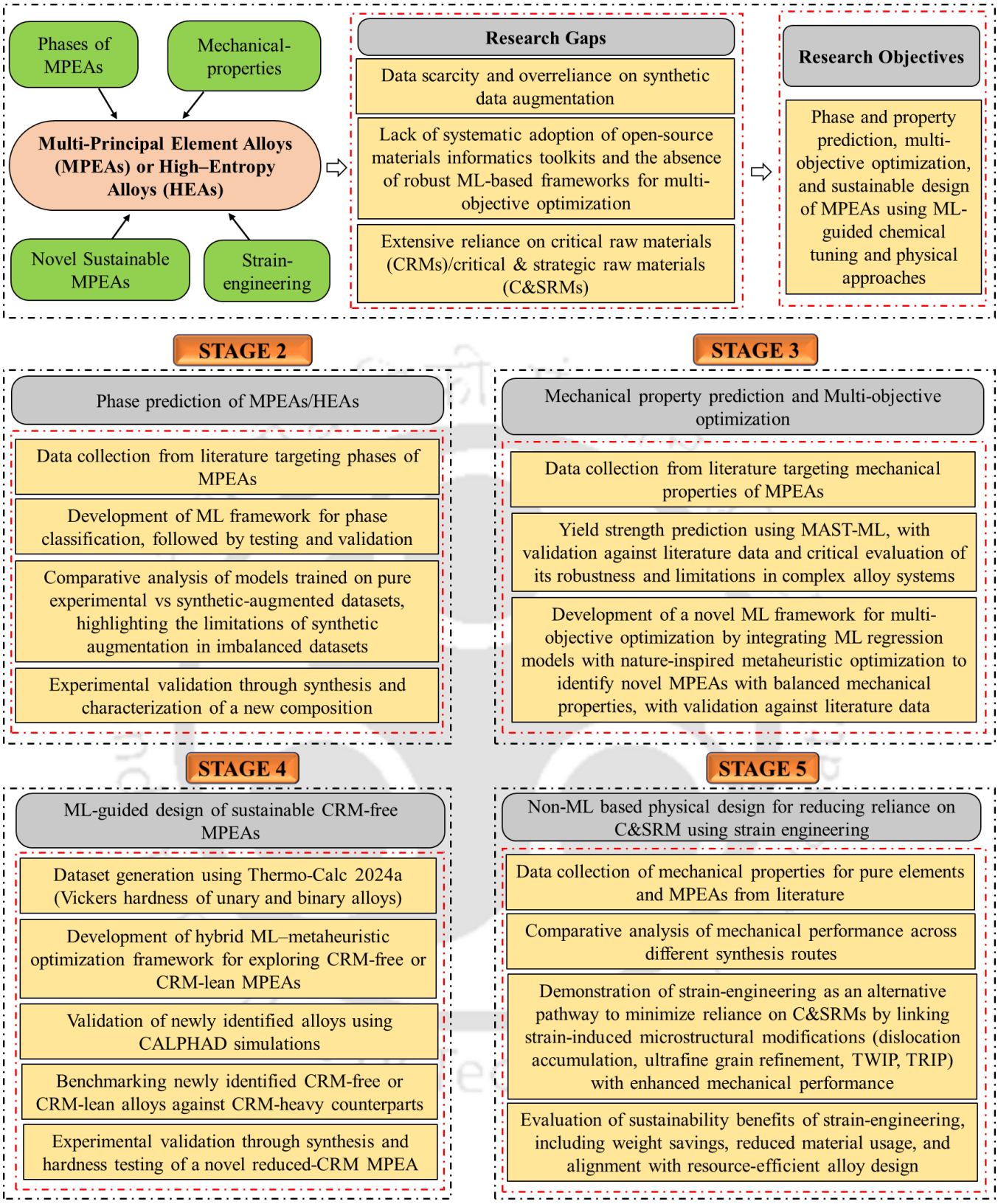

Figure 2.5. Overview of the present research work

Stage 1: Initially, a comprehensive literature survey relevant to MPEAs/HEAs has been thoroughly conducted, reviewing diverse strategies for their discovery, development, and deployment. Particular focus was placed on studies employing machine learning approaches. Based on this analysis, key research gaps were identified, forming the basis for the present work. The overall aim of this thesis is the design and development of sustainable, high-performance MPEAs using machine learning methodologies.

Stage 2: Phase prediction study has been carried out by developing a robust ML framework trained on a large experimental database curated from MPEA/HEA literature, restricted to a specific synthesis route for consistency. To analyze the effect of augmenting synthetic data, which is routinely done in literature to improve model's accuracy, two models have been compared: one trained solely on experimental data and another trained on synthetically augmented dataset. Model performance was evaluated using reliable metrics for imbalanced datasets (precision, recall, F1-score, ROC-AUC), rather than accuracy alone. The framework was further validated experimentally through the synthesis of a novel MPEA composition.

Stage 3: Building on the phase prediction efforts, a focused study was conducted to predict mechanical properties of MPEAs using a small yet high-quality experimental dataset. This work marks the first systematic application of the open-source toolkit MAST-ML, designed for materials researchers with limited or no prior ML expertise, to model complex alloy systems such as MPEAs. Predictions were validated against literature-reported data excluded from training and testing, and the toolkit's robustness and limitations were critically evaluated. Recognizing the limitations of MAST-ML, a novel ML framework was subsequently developed from scratch to perform multi-objective optimization, simultaneously balancing yield strength (YS), ultimate tensile strength (UTS), and elongation ($\mathcal{E}$) in order to address the long-standing strength–ductility trade-off. The predictions of this framework were validated against independent literature data.

Stage 4: A novel hybrid ML–metaheuristic optimization framework was developed to address the urgent need to minimize reliance on critical raw materials (CRMs) in sustainable alloy design. Given the severe scarcity of CRM-free MPEAs data in the literature, a large computational database was generated using CALPHAD-based Thermo-Calc 2024a

simulations, focusing on Vickers hardness values for unary and binary compositions. This dataset enabled the training of ML models integrated with metaheuristic algorithms to systematically explore the compositional space and identify novel CRMs-free or reduced-CRMs (CRMs-lean) MPEAs. The predicted hardness of the newly designed compositions was benchmarked against CALPHAD-evaluated values to ensure reliability of the framework. In addition, reduced-CRM alloys were systematically compared with their CRM-rich counterparts reported in the literature to evaluate the feasibility of partially or completely substituting costly elements such as Co, Nb, Ta, and W with more readily available alternatives, without compromising mechanical performance. To further validate the framework, a representative reduced-CRM MPEA was synthesized, and its Vickers hardness was measured.

Stage 5: Strain engineering was investigated as a sustainable, non-ML-based physical design strategy to minimize reliance on critical and strategic raw materials (C&SRMs), in contrast to the previous stage which employed ML-guided chemical tuning for compositional design. This approach aimed to establish a theoretical framework for enhancing mechanical properties without altering alloy chemistry or incorporating costly C&SRMs. Literature evidence was systematically analyzed to demonstrate how processing parameters, such as strain rate and cooling rate, can be exploited as mechanical tools to tailor microstructure and thereby tune performance. Strain-induced modifications, including dislocation accumulation, ultrafine grain refinement, and the activation of twinning-induced plasticity (TWIP) and transformation-induced plasticity (TRIP) mechanisms, were critically examined to understand their role in improving mechanical properties. Comparative analyses of pure elements and MPEAs synthesized via different processing routes were conducted to assess the effectiveness of this approach. Beyond mechanical improvements, strain engineering was also considered for its broader sustainability benefits, including weight reduction, reduced material consumption, and alignment with resource-efficient alloy design.

The details of the work are presented in the subsequent chapters.

Chapter 3

Development of a ML Framework for Phase Prediction in MPEAs and Experimental Validation through a Novel Alloy

3.1. Introduction

This chapter presents a robust machine learning (ML) framework for predicting the phases of MPEAs based on experimentally reported data from the literature. A new, comprehensive database was curated, encompassing ternary, quaternary, quinary, and other multicomponent alloys, including 3d transition metal MPEAs, refractory metal MPEAs, precious metal MPEAs, MPEA brass and bronze, as well as low-density MPEAs. To ensure consistency, this study exclusively focused on alloys synthesized through a single processing route, namely melting followed by casting, in order to minimize variability arising from different synthesis methods. Given that the consolidated dataset exhibited class imbalance, multiple performance metrics beyond mere accuracy were utilized, including the ROC-AUC score, Precision, Recall, and F1-score, to provide a holistic evaluation of the model's predictive capability. A novel composition was synthesized and characterized to validate the reliability of the developed framework. The proposed approach was designed to generate preliminary insights into likely phase formation prior to undertaking time-intensive experimental investigations. Furthermore, the chapter critically examines the reliability of synthetic data augmentation, which is a practice commonly observed in the literature, for phase prediction in complex alloy systems such as MPEAs.

3.2. ML Framework Developed for Predicting Phase

The ML framework developed and employed in this study for phase prediction of MPEAs involves a series of systematic steps, as presented in Figure 3.1. First, a dataset was collected from published experimental literature and subjected to preprocessing to ensure quality and consistency. The processed dataset was then divided into training and test sets using stratified sampling with an 80/20 ratio. Subsequently, various ML algorithms, including K-Nearest Neighbor (KNN), Support Vector Machine (SVM), Decision Tree (DT), Random Forest (RF), and Extreme Gradient Boosting (XGBoost), were employed for model development. These algorithms were trained on the training set and evaluated against the test set, followed by a validation step to assess their predictive performance and robustness. Finally, the best-performing model was selected to predict the phases of unseen compositions that were not the

part of either training or test sets, and a novel composition was experimentally synthesized to further examine the robustness of the model's predictive capability. Each step is discussed in detail in the subsequent sections.

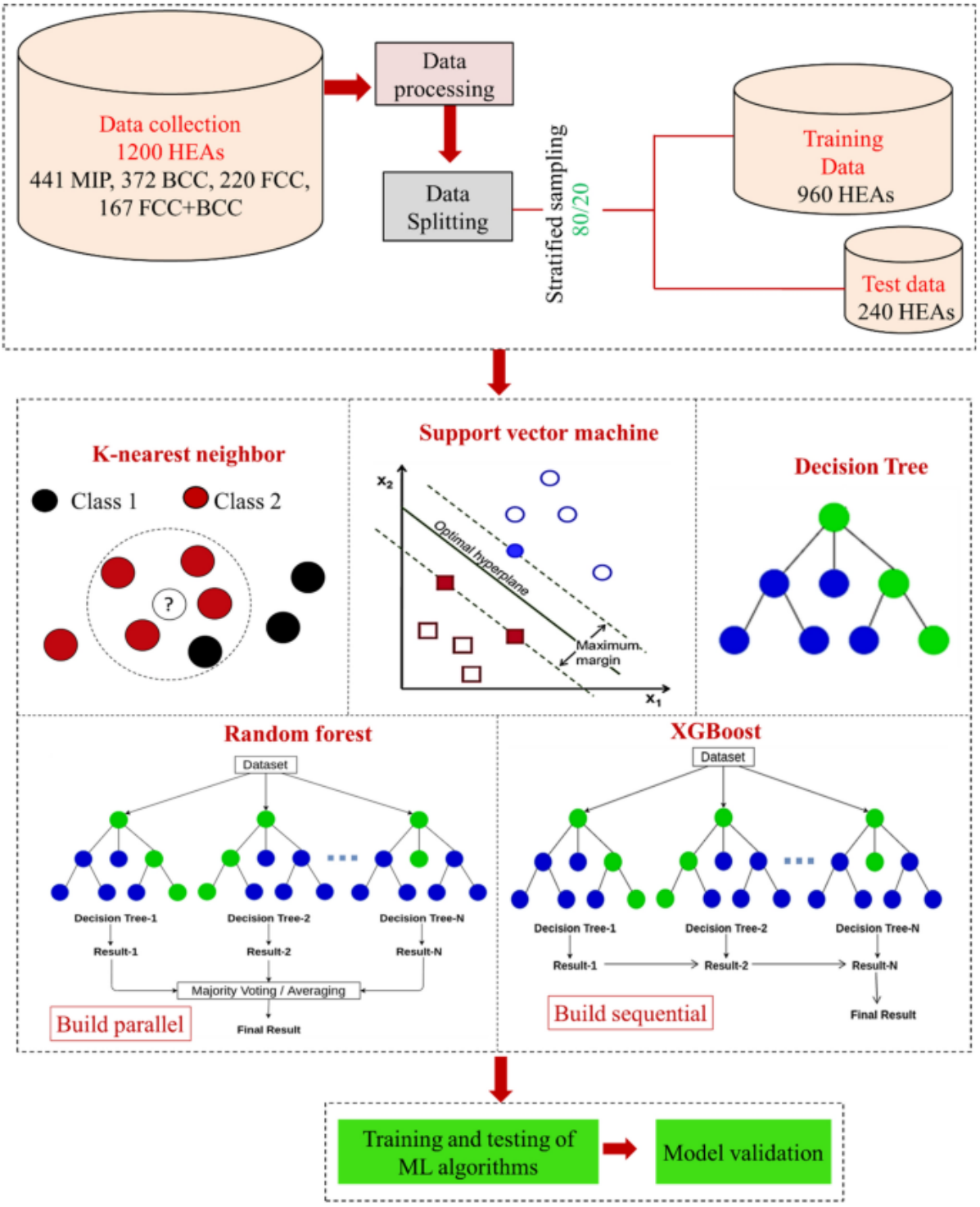

Figure 3.1. ML framework used in this study for predicting phases of MPEAs

3.3. Data Collection

Achieving homogeneity in data collection for MPEAs remains challenging due to the varying stoichiometric ratios, synthesis routes, and processing conditions adopted by different researchers. This makes it difficult to consolidate the data for meaningful comparison. In the existing literature on phase prediction of MPEAs using ML algorithms, no study has specifically focused on a particular synthesis route to reliably extract data from experimental studies. For example, Bakr et al. [84] employed a neural network on a dataset of 775 HEA samples synthesized using various manufacturing routes (arc-melting, sintering, selective laser melting, and others), achieving an accuracy of 93.4% in predicting different phases, including amorphous (AM), BCC, FCC, and intermetallic (IM) phases. However, despite achieving such a high accuracy, their model failed to correctly predict the existence of AM phase, as the effect of manufacturing methods on the resulting phase of HEAs was not considered.

In this study, a dataset of 1,200 unique MPEA compositions was extracted from the literature, focusing exclusively on melting and casting routes while excluding other processing methods [5, 81, 140]. This strategy helps avoid spurious effects introduced by alternative processing techniques on the resulting phase. The synthesis methods included induction melting, induction levitation, vacuum induction melting followed by casting, arc melting or smelting followed by casting, arc melting followed by suction casting, and electric or vacuum arc melting followed by suction casting. Alloys synthesized through other routes, such as powder metallurgy, additive manufacturing, and related methods, were excluded to avoid the influence of varying synthesis routes [10]. To provide a systematic understanding of the collected dataset, the subsequent section first outlines the taxonomy of HEAs and the phases considered in this study, followed by a detailed description of each descriptor and its significance for reliable phase prediction.

3.3.1. Taxonomy of MPEAs

Depending on the chemical nature of their constituent elements, MPEAs or HEAs can be classified into five main subfamilies:

(i) 3D transition metal high-entropy alloys (3d TM HEAs) composed of elements such as Fe, Ni, Co, Mn, Ti and Cr, which typically form face-centered cubic (FCC) solid solutions;

(ii) Refractory high entropy alloys (RHEAs), consisting of elements from groups IVB, VB and VIB of the periodic table, which generally forms body-centered cubic (BCC)

solid solutions;

(iii) Low-density high-entropy alloys, composed of lightweight elements such as Al, Be, Li, Mg, Ti, Sc, which often exhibit hexagonal closed-packed (HCP) structures;

(iv) Lanthanide-based HEAs, consisting of at least four lanthanide elements, which also tend to form HCP solid solutions; and

(v) Other HEAs, representing a diverse category that includes alloys forming multiple chemically disordered solid solutions (FCC, BCC, or HCP), ordered phases such as B2 and $L2_1$, as well as various intermetallic compounds, including σ, μ, and Laves phases (e.g., C14, C15, and C36) [141].

Drawing from the existing literature that categorizes alloy compositions according to their conformity or deviation from the ideal theory of HEA formation, a comprehensive taxonomy of HEAs is presented in Figure 3.2.

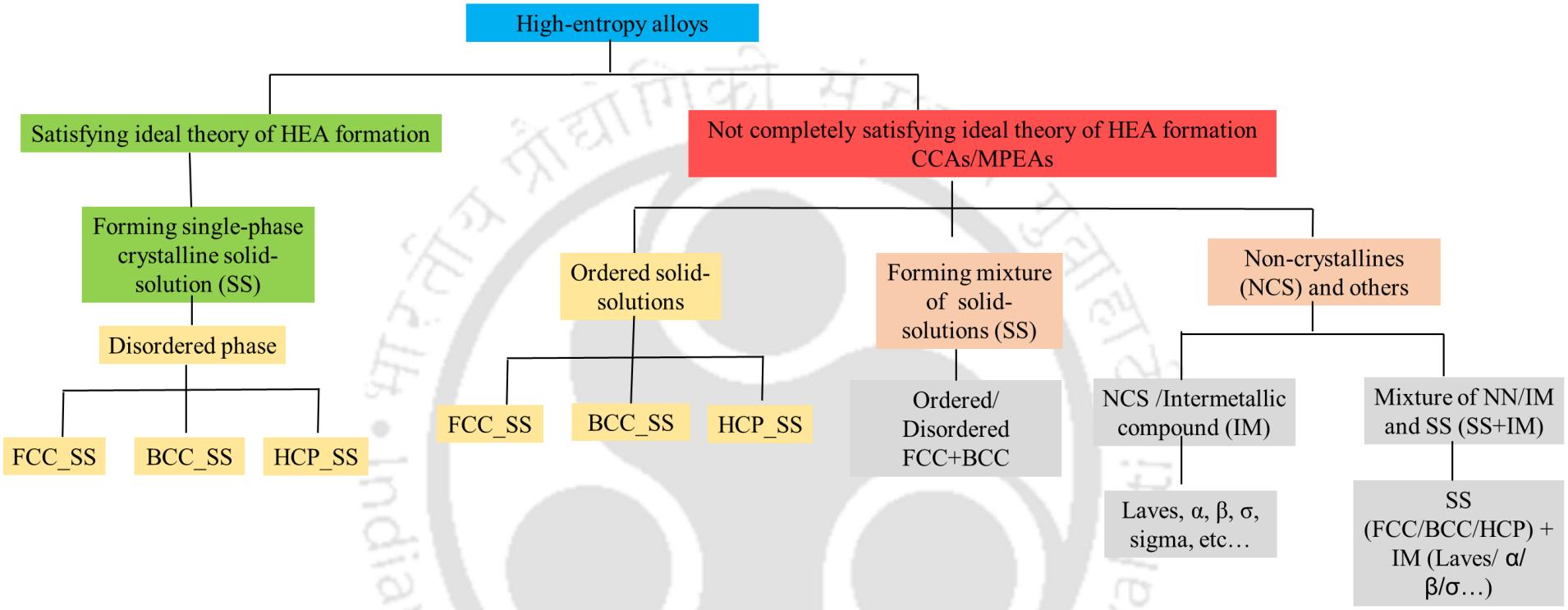

Figure 3.2. Taxonomy of HEAs based on different definitions in the existing literature

The various phases theoretically known to date in HEAs can be categorised as follows:

a. Ordered solid solution (SS) phases: HEAs consisting of a single ordered crystalline phase, such as B2 or β-ordered BCC.
b. Disordered solid solution (SS) phases: Phases exhibiting BCC, FCC, or HCP structures without long-range ordering.
c. Mixed solid solutions (Ordered + Disordered): Combinations of ordered and disordered phases such as, FCC + BCC, BCC + B2, or FCC + B2.
d. Pure Intermetallic (IM) phases: Phases including α, β, σ, μ, $L1_2$, $L2_1$, and Laves phases such as C14, C15, and C36.
e. Intermetallic + solid solution (IM + SS) phases: Coexisting intermetallic and solid solution phases, such as BCC + C14 Laves, BCC1 + BCC2 + C15 Laves, BCC + β-ordered BCC, FCC + CoMo2Ni-type IM, FCC + IM combinations.

To facilitate phase prediction, the identified phases were clustered into four broader categories. Specifically: categories (a) and (b) were grouped as single-phase solid solution (SS), category (c) was designated as mixed solid solutions (MSS), and categories (d) and (e) were combined and labeled as a mixture of intermetallic phases (MIP), as shown in Figure 3.3. Based on the most frequently reported phases in the literature, the database used in this study included four phase types: FCC, BCC, FCC + BCC, and MIP (mixture of intermetallic phases). Due to the limited availability of data corresponding to the HCP solid solution phase, it was excluded from the present study.

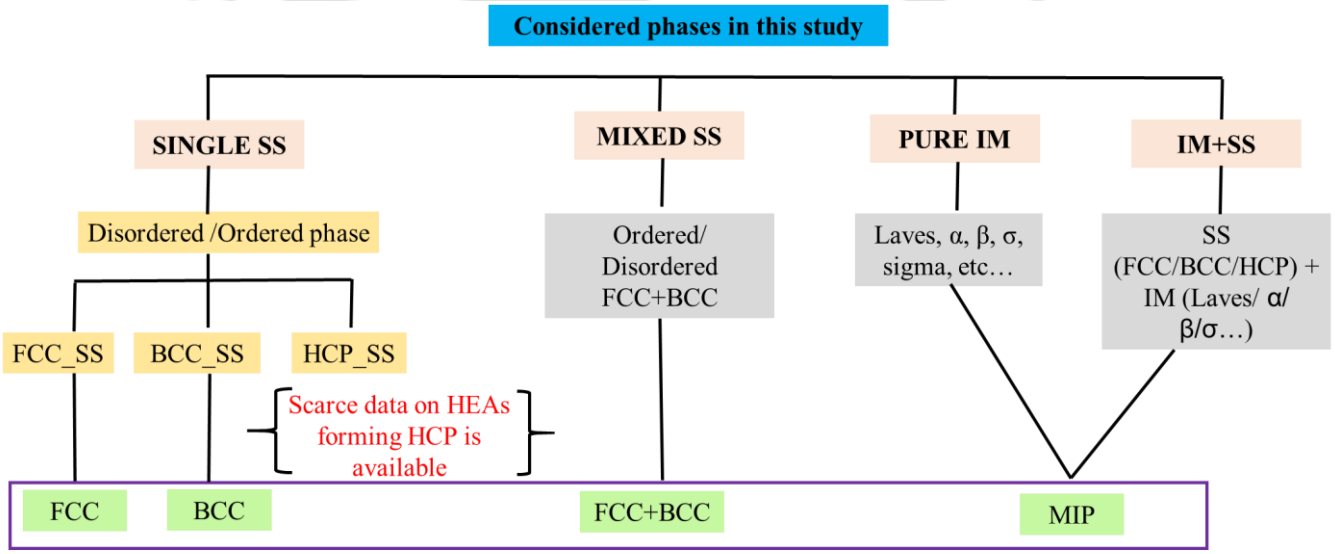

Figure 3.3. Classification of HEA phases with the emphasis on four phases considered in this study

The complete dataset was labelled in four categories: FCC, BCC, FCC + BCC, and MIP (see Figure 3.3). Alloys exhibiting a single-phase ordered or disordered FCC structure, or multiple FCC phases (e.g., FCC1 + FCC2) were grouped under the 'FCC' category. Similarly, alloys with a single-phase ordered or disordered BCC structure, or multiple BCC phases (e.g., BCC1 + BCC2) were included in the 'BCC' category. Mixtures of FCC and BCC phases were considered in the 'FCC + BCC' category. Compositions containing pure IM compounds, such as Laves, α, β, or sigma phases, or mixtures of solid solution and intermetallic phases (e.g., FCC + IM, FCC + BCC + α, BCC + IM, FCC + α + β, BCC + Laves etc.) were categorized as 'MIP'. Amorphous phases were not considered in this analysis.

3.3.2. Description of Collected Database

The curated database comprises 1,200 unique alloy entries, distributed as follows: 441 MIP, 372 BCC_SS, 220 FCC_SS, and 167 mixed FCC+BCC phases. During dataset compilation, an initial cleaning step, including duplicate removal and consistency checks, was performed to ensure data integrity. All compositions extracted from the literature were synthesized via melting and casting routes, and no duplicate alloys were retained in the final dataset (see Figure 3.4).

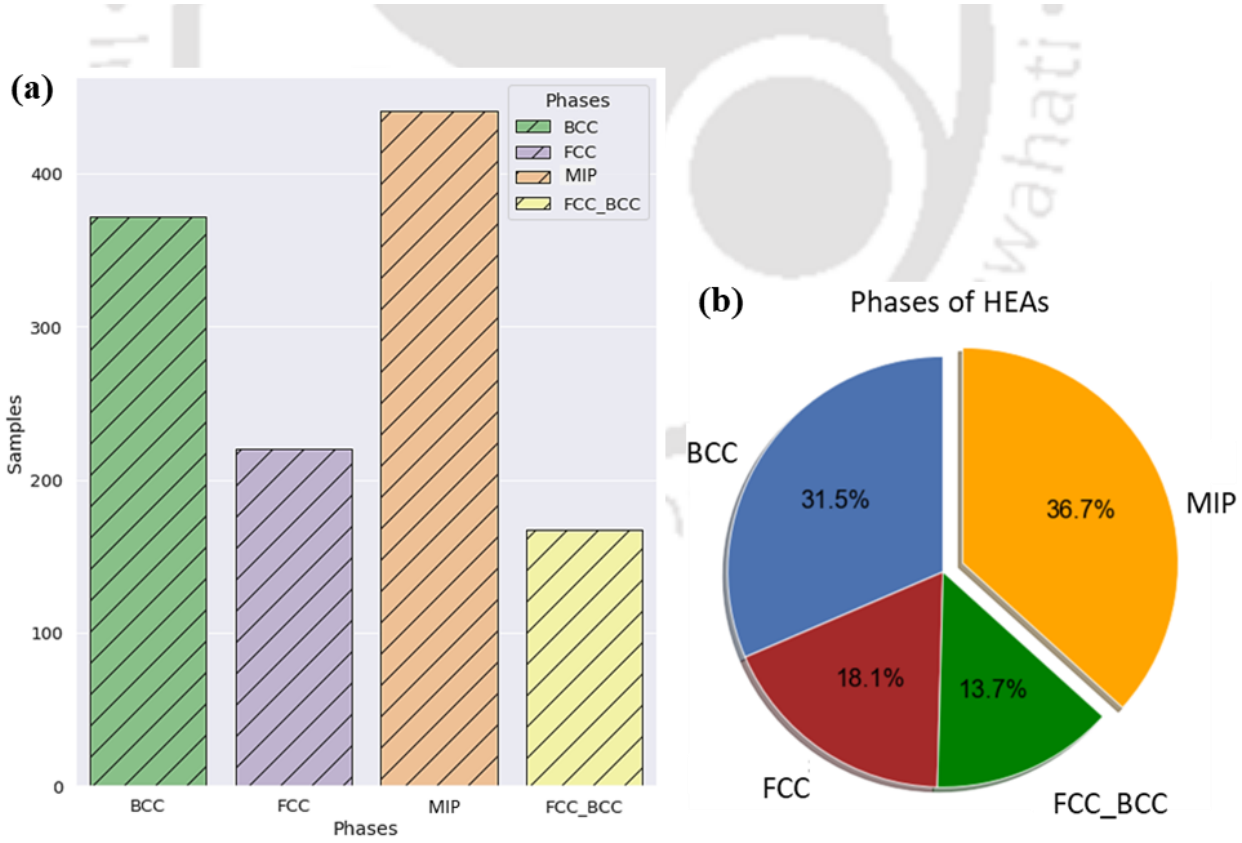

Figure 3.4. HEA dataset showing the (a) numbers, and (b) percentages of different phases of HEAs such as MIP, BCC_SS, FCC_SS, and FCC+BCC in the dataset

Depending on the number of instances belonging to each class, a dataset can typically be recognized as **balanced** (when the number of instances available from each class is equal) or **imbalanced** (when the number of instances available from each class is different) for a classification problem. In the case of an imbalanced dataset, the class with the highest and least number of instances is known as the majority and minority class, respectively. The present database, which includes HEAs developed via only melting and casting routes, has been identified as imbalanced. The impact of this imbalance on the performance of ML models is explicitly discussed in Section 3.8.

The dataset contains a total of 35 different input feature variables (including the chemical composition and fundamental physical parameters) and one target variable i.e., the resulting phase for each composition of MPEA. To provide an overview of the dataset, a representative snapshot of the imported data is presented in Table 3.1. The complete dataset is provided as an excel sheet in Supplementary 3s. Chemical composition comprising 30 elements (Al, Co, Cr, Fe, Ni, Cu, Mn, Ti, V, Nb, Mo, Zr, Hf, Ta, W, C, Mg, Zn, Si, Re, N, Li, Sn, Be, B, Ag, Pt, Y, Pd, Au) and five physical parameters that are crucial for phase prediction of MPEAs were taken in to consideration. The range of compositional and physical parameters (minimum, maximum, average and standard deviation values) are tabulated in Table 3.2.

Table 3.1. Representative snapshot of the imported dataset, illustrating the structure and key descriptors considered for phase prediction in this study

	Alloy	Al	Co	Cr	Fe	Ni	Cu	Mn	Ti	V	...	Pd	Au	dHmix	dSmix	Atom.Size.Diff	Elect.Diff	VEC	Phases considered	Actual phase	References
0	Al0.5NbTaTiV	0.111111	0.0	0.0	0.0	0.0	0.0	0.0	0.222222	0.222222	...	0.0	0.0	-8.395062	13.145944	3.737505	0.049616	4.555556	BCC	BCC	https://doi.org/10.1016/j.proeng.2012.03.043
1	Al0.75MoNbTiV	0.157895	0.0	0.0	0.0	0.0	0.0	0.0	0.210526	0.210526	...	0.0	0.0	-9.351801	13.332806	3.863332	0.232765	4.684211	BCC	BCC	https://doi.org/10.3390/e16020870
2	Al0.25MoNbTiV	0.058824	0.0	0.0	0.0	0.0	0.0	0.0	0.235294	0.235294	...	0.0	0.0	-4.041522	12.708370	4.003399	0.243217	4.882353	BCC	BCC	https://doi.org/10.3390/e16020870
3	Al0.25NbTaTiV	0.058824	0.0	0.0	0.0	0.0	0.0	0.0	0.235294	0.235294	...	0.0	0.0	-4.816609	12.708370	3.832440	0.050176	4.647059	BCC	BCC	https://doi.org/10.1016/j.proeng.2012.03.043
4	Al0.2MoTaTiV	0.047619	0.0	0.0	0.0	0.0	0.0	0.0	0.238095	0.238095	...	0.0	0.0	-3.356009	12.569175	4.017794	0.244333	4.904762	BCC	BCC	https://doi.org/10.4028/www.scientific.net/MSF...
5	Al0.3NbTa0.8Ti1.4V0.2Zr1.3	0.060000	0.0	0.0	0.0	0.0	0.0	0.0	0.280000	0.040000	...	0.0	0.0	-4.860000	13.460000	4.500000	0.110000	4.340000	BCC	BCC	https://doi.org/10.1007/s11837-014-1066-0
6	Al0.5CrNbTi2V0.5	0.100000	0.0	0.2	0.0	0.0	0.0	0.0	0.400000	0.100000	...	0.0	0.0	-10.960000	12.228981	6.018492	0.046861	4.600000	BCC	BCC	https://doi.org/10.1016/j.matlet.2016.11.030
7	Al0.5MoNbTiV	0.111111	0.0	0.0	0.0	0.0	0.0	0.0	0.222222	0.222222	...	0.0	0.0	-7.012346	13.145944	3.932393	0.237835	4.777778	BCC	BCC	https://doi.org/10.3390/e16020870
8	Al0.6MoTaTiV	0.130435	0.0	0.0	0.0	0.0	0.0	0.0	0.000000	0.217391	...	0.0	0.0	-8.015123	13.242325	3.904515	0.235771	4.739130	BCC	BCC	https://doi.org/10.4028/www.scientific.net/MSF...
9	Al1.5MoNbTiV	0.272727	0.0	0.0	0.0	0.0	0.0	0.0	0.181818	0.181818	...	0.0	0.0	-13.818182	13.254639	3.669956	0.219191	4.454545	BCC	BCC	https://doi.org/10.3390/e16020870

10 rows × 39 columns

Table 3.2. Range of composition (atomic weight %) and physical parameters used in this study

Variant	Minimum	Maximum	Average	Deviation
Al	10	100	33.55	24.86
Co	10	99.99	21.58	10.84
Cr	10	100	21.67	11.86
Fe	10	99.99	22.57	10.8
Ni	10	99.99	22	9.64
Cu	10	100	25.76	19.8
Mn	10	89.3	23.8	11.96
Ti	10	100	30.26	21.67
V	10	100	30.23	24.07
Nb	11.11	100	26.2	16
Mo	10	100	29.65	23.98
Zr	10	100	23.9	13.44
Hf	11	100	26.09	21.35
Ta	10	99	23.52	13.1
W	10	90	27.7	19.75
C	10	100	38.5	25.34
Mg	10	71.9	34.88	14.82
Zn	10	52.6	30.79	14.5
Si	10	100	34.63	26.6
Re	10	10	10	NaN
N	19	35	32.33	6.53
Li	10	50	24.75	15.27
Sn	10	99	37.51	25.33
Be	16.7	16.7	16.7	NaN
B	15.4	98.4	50.57	35.32
Ag	16.7	16.7	16.7	NaN
Pt	20	20	20	NaN
Y	11.8	20	16.4	4.01
Pd	20	40	30	14.14
Au	16.7	16.7	16.7	NaN
ΔH_{mix} (kJ/mol)	-166.38	14.82	-8.61	8.65
ΔS_{mix} (J/K. mol)	1.609	19.05	12.99	1.905

δ (δ*100)	0.056	69.93	5.48	3.29
Δχ	0.015	3.92	0.171	0.253
VEC	2.0	10.4	6.74	1.54

3.3.3. Crucial Physical Parameters Included in the Collected Database

Among all physical parameters (atomic size difference (δ), electronegativity difference (Δχ), valence electron concentration (VEC), thermodynamic rule (mixing enthalpy (ΔH_{mix}) and mixing entropy (ΔS_{mix})), and others (Ω-parameter, ϕ-parameter, and γ-parameter)) proposed for guiding the design of stabilizing phases of HEAs, only five crucial parameters (ΔH_{mix}, ΔS_{mix}, δ, Δχ, VEC) were considered for this study, as these are widely accepted and easy to compute. Empirical relations observed in high entropy alloys literature suggest that an HEA (solid-solution phase) formation becomes plausible when δ<6.6% and 11.6 < ΔH_{mix} < 3.2 kJ/mol. When δ is large (δ>6.6%) and ΔH_{mix} is noticeably negative (ΔH_{mix} = -12.2 kJ/mol) [68], it leads to an amorphous phase instead of a crystalline phase. Intermetallic compounds tend to form in the intermediate range in terms of δ and ΔH_{mix}, or it overlaps largely with those for solid solutions and amorphous phase. Furthermore, for the identification of crystal structure in various solid solution forming HEAs, the effect of VEC was formulated and the threshold value were found to be as below:

- BCC when VEC < 6.87,
- FCC when VEC > 8.0 and
- Mixed phase (BCC+FCC) when VEC is in between 6.87 and 8.0.

The criterion proposed by Zhang et al. [142] was almost the same for δ (δ < 6.6%), although the range of ΔH_{mix} differed slightly (-15 < ΔH_{mix} < 5 kJ/mol). A joint plot and swarm plot of the consolidated dataset were made (see Figure 3.5) to visualize and examine whether the HEA instances in the database satisfy the established empirical rules.

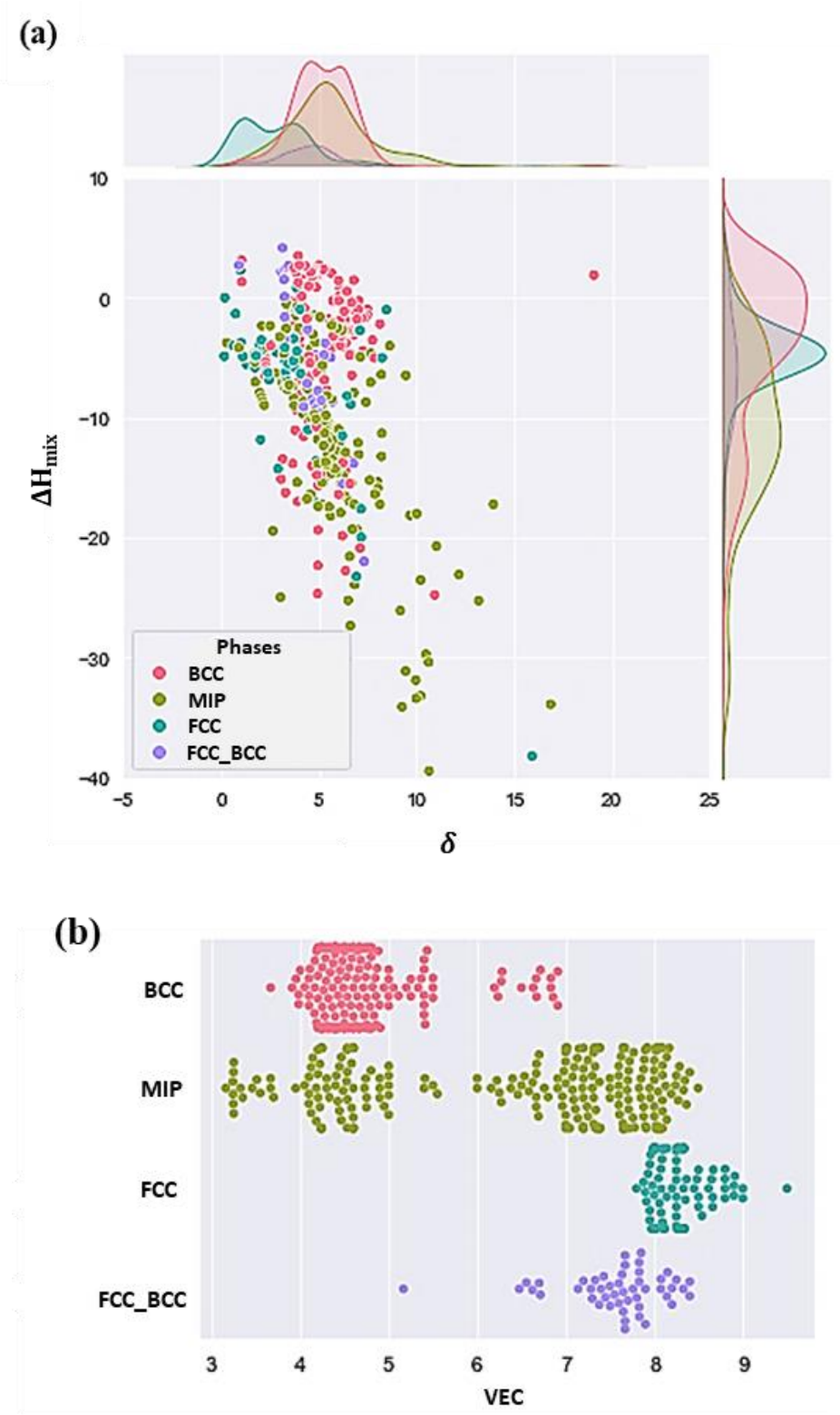

Figure 3.5. (a) Joint plot of ΔH_{mix} and (δ) for the collected dataset, (b) swarm plot showing the role of VEC in phase selection among BCC, FCC, MIP, and FCC+BCC structures, each satisfying the HEA criteria defined by empirical rules in the literature

As shown in Figure 3.5, the current database is satisfying these empirical phase-selection rules, with the joint plot of (ΔH_{mix} –δ) and a swarm plot of VEC values for four different phases of HEAs. The ΔH_{mix} for the available HEAs in the dataset was calculated using Miedema's rule [143], while ΔS_{mix}, δ, $\Delta\chi$, VEC were computed following the method proposed by Guo et al. [144].

Other parameters, such as geometric parameter (γ), still awaits support from more experimental data and the complete information is still missing from the current HEA literature. Accordingly, the five key physical parameters that are primarily responsible for determining the crystal structure in HEAs were considered in this study. The mere requirement of these five theoretically accessible parameters to guide alloy design underscores the simplicity and practicality of the developed methodology, thereby enabling more efficient and effortless development of HEAs in the future.

3.3.4. Evaluation of Correlations Among Five Physical Parameters

To visualize the correlation among features as a sanity check for identifying redundant features, a Pearson correlation matrix of five physical parameters (ΔH_{mix}, ΔS_{mix}, δ, $\Delta\chi$, VEC) governing the formation of HEAs was drawn using the seaborn library in python (see Figure 3.6). Two features that are strongly positively correlated (i.e., when they move in tandem) or negatively correlated (i.e., when they are inversly related) can lead to the problem of multicollinearity, which significantly reduces model performance and increases the standard error. Thus, it is suggested to eliminate one of the features if a strong correlation exist between them [145, 146]. However, as shown in Figure 3.6, no strong positive or negative correlation was observed between any pair of these independent features. Consequently, all five physical parameters were retained for further analysis without elimination.

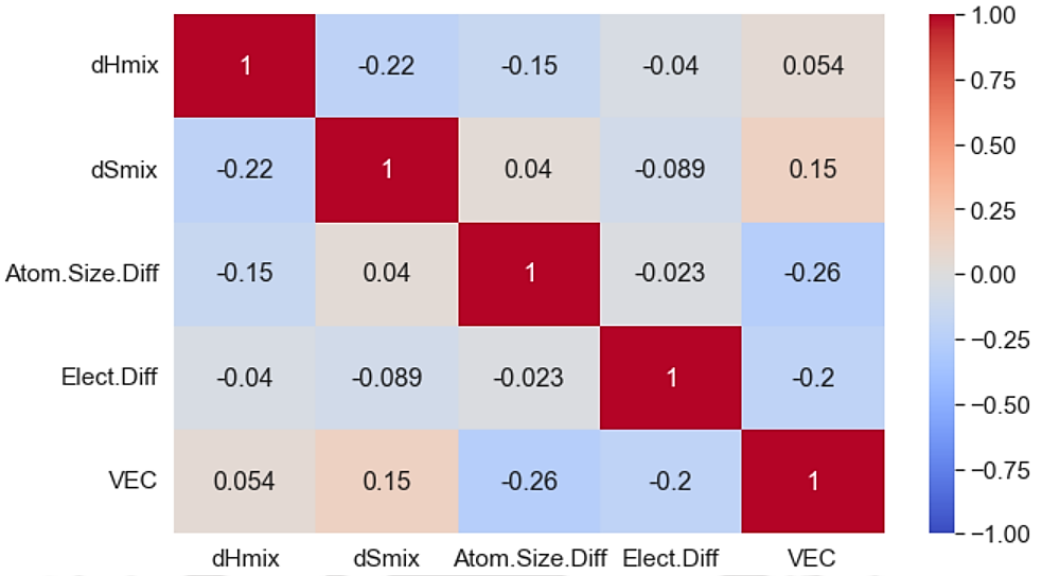

Figure 3.6. Heatmap illustrating the Pearson correlation coefficients among the five key parameters influencing HEA formation

3.4. Data Processing

The data processing described in this section was performed after initial cleaning of the curated database, as detailed in Section 3.3.2, where duplicate or inconsistent entries were removed and compositional consistency was ensured. Before feeding the data into the ML algorithms, several statistical processing steps were performed to enhance the reliability of predictions [147, 148]. The categorical phase data was encoded into numeric values as follows: MIP = 0, BCC = 1, FCC = 2, and FCC + BCC = 3. Outlier detection was used to identify and remove outliers (anomalies) from the database. To address missing values (NaN), various imputation methods were employed, including simple imputation with different strategies (mean, median, and constant), KNN imputation and MICE (Multiple Imputations by Chained Equations) imputation. Feature scaling was performed on each set of imputed data to normalize the data into a finite range, using robust scalar imported from scikit-learn library. The robust scaling formula can be expressed as [147]:

$$X_{\text{robust}} = \frac{X - X_{\text{median}}}{X_{75} - X_{25}} \tag{3.1}$$

where X is an input variable, X_{median} is the median of X, X_{75} is the 75th quantile and X_{25} is the 25th quantile of X. The difference between 75^{th} quantile and 25^{th} quantile is also known as interquartile range (IQR). The dataset was subsequently divided into training (80%) and testing (20%) subsets to enable model development and performance evaluation.

3.5. Brief Description of Employed ML Algorithms

3.5.1. K-Nearest Neighbors (KNN)

The KNN algorithm searches for the nearest neighbors by measuring the distance between the two points [149, 150], as shown in Figure 3.7, and is expressed as:

$$d(q, x_i) = \sum_{f \in F} w_f \delta\left(q_f, x_{i_f}\right) \tag{3.2}$$

for classifying an unknown input variable (q) one needs to know the existing input variable (x_i) in F and the weight factor (w_f) for each feature. Based on this distance, the k nearest neighbors is selected, and the class of q is determined from the voting of the nearest neighbors as mentioned below:

$$\text{Vote}\ (y_i) = \sum_{c=1}^{k} \frac{1}{d(q, x_c)\rho} 1(y_i, y_c) \tag{3.3}$$

this returns 1 if the class labels matches or 0 if does not match. The vote assigned to class y_i by neighbor x_c is the inverse of their distance, *i.e.*, $1(y_i , y_c)$.

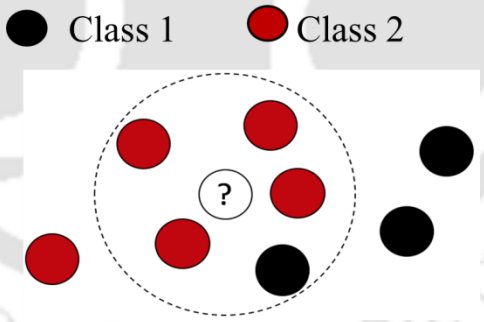

Figure 3.7. Schematic of K-Nearest Neighbours algorithm

The KNN algorithm makes predictions by searching for similar instances based on the specified value of k, using the Euclidean distance metric. In this study, important hyperparameters of the model, such as k (n_neighbors = 5), and the distance metric (euclidean), were set to their default values.

3.5.2. Support Vector Machine (SVM)

The SVM classifier searches for the hyper plane that best separates different classes by maximizing the margin, defined as the distance between the nearest data points from different

classes [151, 152], as shown in Figure 3.8. The closest data points that define these margins are known as support vectors. Important hyper-parameters of the model, such as the Regularization parameter (C = 1.0), and kernel function ('rbf', radial basis function), were set to their default values in this study.

The decision function is expressed as follows:

$$f(x) = w.x + b \tag{3.4}$$

$$\min_{\mathbf{w},\xi} \left\{ \frac{1}{2} \| \mathbf{w} \|^2 + C \sum_{i=1}^{N} \xi_i \right\} \tag{3.5}$$

Subject to: $y_i(\mathbf{w} \cdot \mathbf{x_i}) \geqslant 1 - \xi_i, \xi_i \geqslant 0$ (3.6)

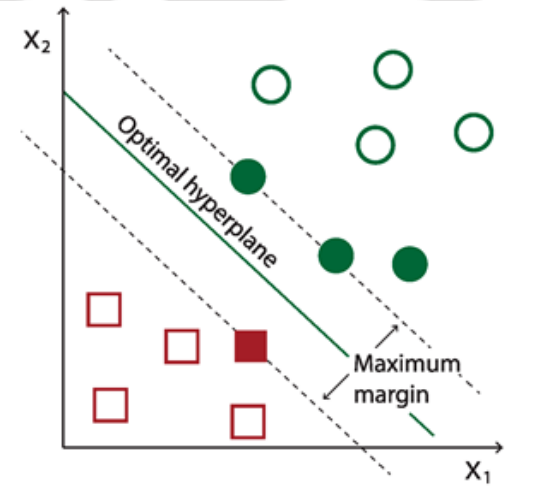

Figure 3.8. Schematic of Support Vector Machine algorithm

3.5.3. Decision Tree Classifier (DTC)

A decision tree classifier splits the dataset into root node, sub-node and leaf-node by calculating the information gain, i.e., the change in entropy after dividing a dataset based on attributes, which helps to determine the order of features in various nodes of a decision tree (quality of splitting) [153, 154]. Information gain is calculated as expressed below:

$$H(Y \mid X) = H(X,Y) - H(X) \tag{3.7}$$

where $H(Y \mid X)$ is the conditional entropy, $H(X)$ is the entropy of random variable X, and $H(X,Y)$ is the joint entropy, calculated as follows:

$$H(X,Y) = -\sum_{i,j} p(x_i, y_j) \log_2 p(x_i, y_j) \tag{3.8}$$

It is based on the branching method to match all the possible outcomes based on the consequences of our decisions. Criterion= 'gini' for Gini impurity, max_depth=None, and min_sample_split=2, are some of the important hyper-parameters of DTC, set by default. The schematic of decision tree algorithm is presented in Figure 3.9.

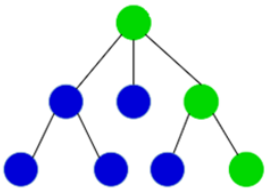

Figure 3.9. Schematic of Decision Tree algorithm

3.5.4. Random Forest Classifier (RFC)

Random forest algorithm is an ensemble of various decision trees, builds on different samples, and takes majority voting for classification (see Figure 3.10). It uses Bootstrap Aggregating or Bagging method. In a random forest classifier, ensembles of various decision trees (base learners) are considered such as $h_1(x), h_2(x), \ldots, h_J(x)$, and majority of votes is taken to calculate *f(x)* such that the loss function is minimized [155, 156]. Loss function is expressed as below:

$$L(Y, f(x)) = I(Y \neq f(x)) = \begin{cases} 0, \text{ if } Y = f(x) \\ 1, \text{ otherwise} \end{cases} \quad (3.9)$$

Voting is based on $f(x) = \arg\ max \sum_{j=1}^{J} I\big(y = h_j(x)\big)$ (3.10)

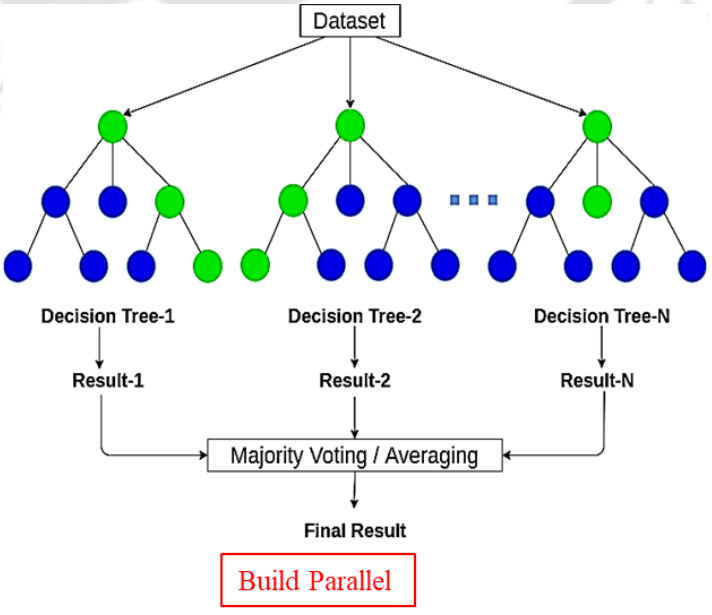

Figure 3.10. Schematic of Random Forest algorithm

Some important hyper-parameters such as: n_estimators=100, criterion= 'gini', max_depth=None, and min_sample_split=2, are set by default for the present study.

3.5.5. Extreme Gradient Boosting (XGBoost)

XGBoost is an ensemble learning algorithm that employs parallel tree boosting, where a single weak model is improved by combining it with several other weak models to produce a collectively strong model [151, 157], as shown in Figure 3.11. The objective function is expressed as:

$$\text{obj}\ (\theta) = \sum_i^n\ l(\hat{y}_i, y_i) + \sum_k^K\ \Omega(f_k) \tag{3.11}$$

The term $l(\hat{y}_i, y_i)$ represents the loss function, which measures the difference between predicted output and the actual output, where y_i is the actual output, and $\hat{y}_i$ is the predicted output given by $\hat{y}_i = \sum_k^K\ f_k(x_i), f_k \in F$. x_i is the input variable and $\Omega(f_k)$ is regularization term that helps to avoid overfitting by penalizing the complexity of the model. XGBoost is trained additively, where one tree is optimized and added each at a time. Learning_rate = 0.30, max_depth = 6, and n_estimators = 100 are default hyper-parameters used in this study.

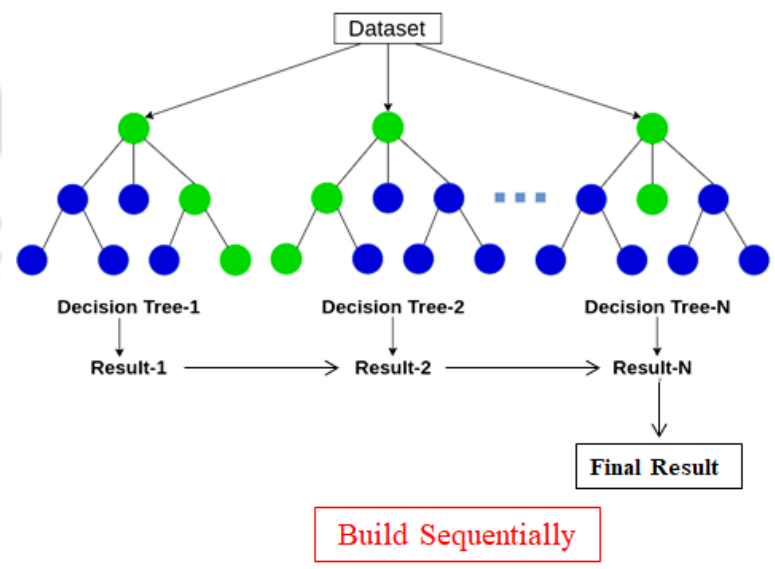

Figure 3.11. Schematic of XGBoost algorithm

3.6. Model Training and Testing

All five of the above-mentioned ML algorithms were trained on the training data and tested on the test data, and their performance was evaluated using various evaluation metrics. While

accuracy is a well-accepted measure for evaluating classification problems, it can be misleading in case of imbalanced datasets such as the one addressed in this study. Therefore, alternative evaluation metrics were explored to appropriately assess the performance of ML models, as accuracy alone is not considered reliable.

3.6.1. Evaluation Metrics for Imbalanced Data Classification

Various evaluation metrics, such as Precision, Recall, F1-score, and ROC-AUC, available in the scikit-learn module (version 1.1.1) [158] in python (version 3.9.12), are widely recognized as robust measures for imbalanced data classification [159]. A detailed description of these metrics is provided in Table 3.3. Precision measures the fraction of predicted positive cases that are actually true positives (TP), whereas Recall reflects the model's ability to correctly identify all true positives (TP). The F1-score calculates the harmonic mean of Precision and Recall [160, 161].

Table 3.3. Evaluation metrics and their statistical definition used for an imbalanced multiclass classification problem

Evaluation Metric Terms	**Description**
True Positive (TP)	TP is the total number of right predictions when the actual class was positive.
True Negative (TN)	TN is the total number of right predictions when the actual class was negative.
False Positive (FP)	FP is the total number of wrong predictions when the actual class was positive.
False Negative (FN)	FN is the total number of wrong predictions when the actual class was negative.
Accuracy	$\frac{TP+TN}{TP+TN+FP+FN}$
Precision	Precision tells how many of the correctly predicted classes actually turned out to be positive.
Recall	Recall, on the other hand, make sure that positive observations are not being missed.

F1-score	F1-score is the harmonic mean of precision and recall, gives a combined idea about both metrics, calculated as follows: $$\text{F1-Score} = \frac{2 \times (\text{Recall} \times \text{Precision})}{(\text{Recall} + \text{Precision})}$$
True Positive Rate (TPR)	$\text{TPR} = \frac{\text{TP}}{\text{TP+FN}}$
False Positive Rate (FPR)	$\text{FPR} = \frac{\text{TN}}{\text{TN+FP}}$

The receiver operating characteristic (ROC) curve is a probability curve typically plotted for binary classification tasks at different threshold values [158, 162]. It can be extended to multiclass classification using the 'one-vs-one' and 'one-vs-rest' strategies [158, 163]. In this study, the 'one-vs-rest' strategy was employed to compute the AUC score by calculating area under the ROC curve for each class against the rest, and then averaging across all classes. The ROC_AUC score provides a summary measure of a classifier's performance by quantifying the area under the ROC curve, which is generally considered a more reliable indicator of model's performance for imbalanced datasets. The ROC_AUC score ranges from 0 to 1, where 1 indicates the perfectly correct classifier and 0 indicates a perfectly incorrect classifier.

3.7. Comparison of Model Performance Using Various Metrics

The effectiveness of five vanilla (base) models, namely V-KNN, V-SVM, V-DTC, V-RFC, and V-XGB, was evaluated and compared using all the aforementioned evaluation. Here, the term 'vanilla' (or base) refers to models trained with their default hyperparameters, without any tuning, and using only the curated experimental dataset from literature. This approach was adopted to establish a baseline for performance, which will later be compared against models trained on an augmented dataset (i.e., experimental + synthetic data). Such a comparison is intended to highlight that, although synthetic data augmentation may lead to apparent improvements in accuracy, it does not necessarily yield reliable predictions in the context of materials development.

Table 3.4. Performance of vanilla models using various evaluation metrics

Algorithms		Simple Imputer with different strategy			MICE Imputer	KNN Imputer
	Metrics	Mean	Median	Constant		
Vanilla KNN (V-KNN)	Accuracy	68.75	68.75	68.75	68.75	68.75
	F1-score, Precision, Recall	0.6876, 0.6894, 0.6875	0.6876, 0.6894, 0.6875	0.6876, 0.6894, 0.6875	0.6876, 0.6894, 0.6875	0.6876, 0.6894, 0.6875
	ROC-AUC, 10-fold CV score	0.9453, 0.8341	0.9453, 0.8341	0.9453, 0.8341	0.9453, 0.8341	0.9453, 0.8341
Vanilla SVM (V-SVM)	Accuracy	71.25	71.25	71.25	71.25	71.25
	F1-score, Precision, Recall	0.7113, 0.7189, 0.7125	0.7113, 0.7189, 0.7125	0.7113, 0.7189, 0.7125	0.7113, 0.7189, 0.7125	0.7113, 0.7189, 0.7125
	ROC-AUC, 10-fold CV score	0.9117, 0.8762	0.9055, 0.8750	0.9053, 0.8750	0.8846, 0.8747	0.9052, 0.8739
Vanilla DTC (V-DTC)	Accuracy	79.17	79.58	77.50,	79.58	8042
	F1-score, Precision, Recall	0.7959, 0.7960, 0.7958	0.7958, 0.7959, 0.7958	0.7750, 0.7753, 0.7750	0.7916, 0.7916, 0.7917	0.8043, 0.8049, 0.8042
	ROC-AUC, 10-fold CV score	0.7947, 0.7818	0.8129, 0.7772	0.8173, 0.7841	0.836, 0.7828	0.8275, 0.7819
Vanilla RFC (V-RFC)	Accuracy	83.834	82.5	82.25	82.91	84.5
	F1-score, Precision, Recall	0.8214, 0.8205, 0.8225	0.8215, 0.8132, 0.8203	0.8203, 0.8231, 0.8250	0.8359, 0.8347, 0.8450	0.8172, 0.8264, 0.8167
	ROC-AUC, 10-fold CV score	0.9566, 0.9251	0.9546, 0.9238	0.9550, 0.9242	0.9349, 0.9315	0.9522, 0.9272

Vanilla XGB (V-XGB)	Accuracy	0.8250	0.8250	0.8250	0.8250	0.8250
	F1-score, Precision, Recall	0.8215, 0.8232, 0.8250	0.8215, 0.8232, 0.8250	0.8215, 0.8232, 0.8250	0.8215, 0.8232, 0.8250	0.8215, 0.8232, 0.8250
	ROC-AUC, 10-fold CV score	0.9455, 0.8998	0.9455, 0.8998	0.9455, 0.8998	0.9453, 0.9074	0.9455, 0.8998

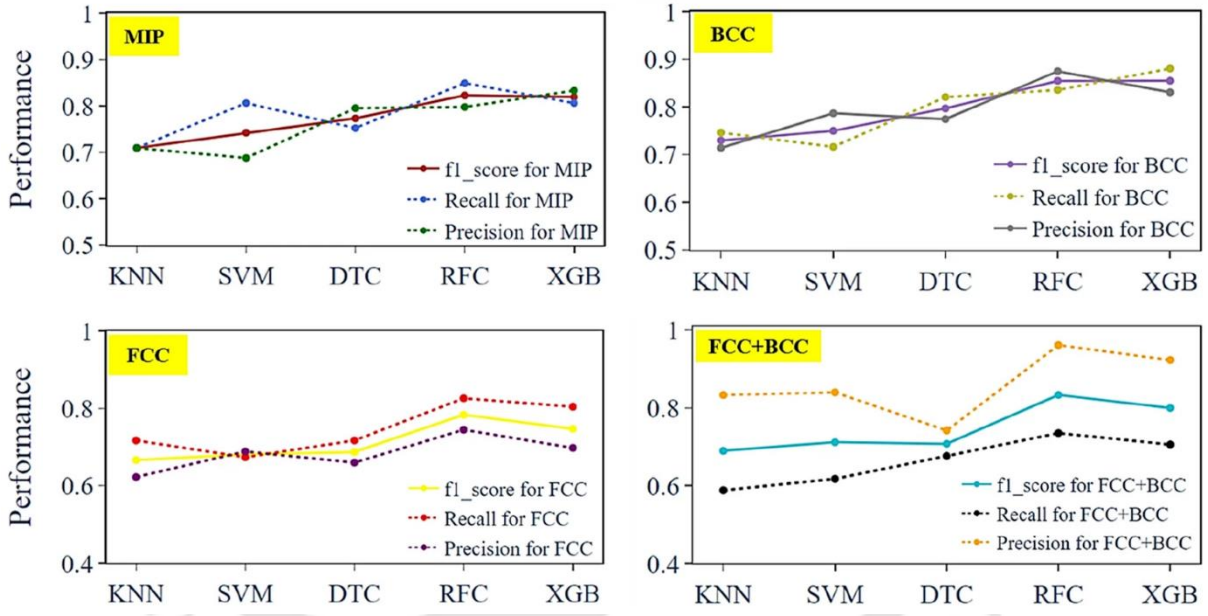

Figure 3.12. F1-score, Recall and Precision for four distinct phases of HEAs for five vanilla models

Table 3.4 presents the performance of all five vanilla models across five different imputers: Simple imputer (SI) with mean, median and constant strategies; KNN imputer; and MICE imputer, evaluated using various performance metrics. For each model, five iterations were performed, and the average values are reported. No significant differences in the model performance were observed across these imputers. Among these models, Vanilla-RFC (V-RFC) demonstrated the best overall performance, achieving an average accuracy of 84%, a ROC-AUC score of 0.9649, a 10-fold cross-validation mean score of 0.9315, and higher values of Precision, Recall and F1-score compared to the others (see Figure 3.12).

3.8. Synthetic Data Augmentation

In this study, V-RFC exhibited better performance compared to the other models. However, in the existing literature on phase prediction of HEAs using ML approaches, several studies have reported even higher accuracies than those obtained through our methodology. To improve performance, Hyper-parameter Tuning of Random Forest Classifier (HT-RFC) was performed, which resulted in a modest increase of approximately 3% in test accuracy, reaching 87.49%. Nevertheless, literature reports even higher classification accuracies. For instance, Risal et al. [82] achieved an accuracy of 91.21% for an oversampled Random Forest Classifier, along with higher ROC-AUC, Precision, Recall and F1-scores. However, it should be noted that these improvements were achieved by mixing experimental data with synthetic data, raising concerns about the reliability of such models. Specifically, over-sampling techniques were used in their study to address class imbalance by augmenting the dataset with synthetic samples, acknowledging that "ML algorithms usually do not perform well for imbalanced datasets".

Various other studies have similarly employed over-sampling and under-sampling methods, either by supplementing minority classes with synthetically generated samples to match the majority class in case of over-sampling method or by reducing the majority class to match the minority class in case of under-sampling method. Some researchers have also utilized generative adversarial network (GAN) for generating synthetic alloys to avoid the biasness in the dataset. However, whether a synthetically generated alloy can be definitively regarded as a high entropy alloy remains controversial.

In our consideration, augmenting or 'polluting' real-world experimental data with synthetic samples to balance the dataset and improve accuracy is not a reliable approach, for two main reasons. First accuracy alone is not the most robust metric for evaluating classifier performance on imbalanced data, as its effectiveness has been questioned by several authors recently [164-168]. Second, the definition of what qualifies as a high entropy alloy remains controversial, making it uncertain whether the generated samples truly represent HEAs.

This consideration formed the primary basis of the present investigation, as synthetic data is not regarded as fully comparable to experimental data and therefore cannot be considered a prudent alternative. Accordingly, the SMOTE-Tomek links resampling method was applied to the dataset to generate synthetic samples, thereby inflating the dataset size and improving model accuracy. The models trained on this augmented dataset were then compared against all five vanilla models and HT-RFC (i.e., hyper-parameter tuned RFC) model to evaluate the reliability their predictions.

3.8.1. SMOTE-Tomek Links Resampling for Data Augmentation

SMOTE-Tomek links resampling method was applied to the original experimental dataset of 1,200 instances, to inflate dataset size. This approach differs from other existing over-sampling and under-sampling methods. It generates synthetic samples for the minority class using SMOTE and removes samples from the majority class that are closest to minority class using Tomek links [169]. In this study, the augmented dataset consisted of 1,392 entries, including 1,200 original instances and 192 synthetic samples generated using the SMOTE-Tomek links method.

3.8.2. Performance Comparison of Models Trained on Pure Experimental vs. Augmented Data

Figure 3.13 presents a bar-chart comparing the performance of all ML models tested in this study, including five vanilla models (V-KNN, V-SVM, V-DTC, V-RFC, V-XGB), the hyper-parameter tuned Random Forest Classifier (HT-RFC), and the SMOTE-TOMEK link augmented Random Forest Classifier (ST-RFC). The performance is illustrated using three key metrics: average test accuracy (peach bars), ROC-AUC score (light green bars), and 10-fold cross-validation score (light purple bars). Among all models, ST-RFC achieved the highest average accuracy of 92%, consistent with trends reported in the literature for synthetic data augmentation methods. However, while ST-RFC demonstrated improved accuracy, its reliability remains questionable, since the enhancement results from augmenting experimental data with synthetic samples. Therefore, the performance of the ST-RFC model was further evaluated using a confusion matrix to analyze its relaibility in predicting each individual phase, and it was compared against that of the V-RFC model.

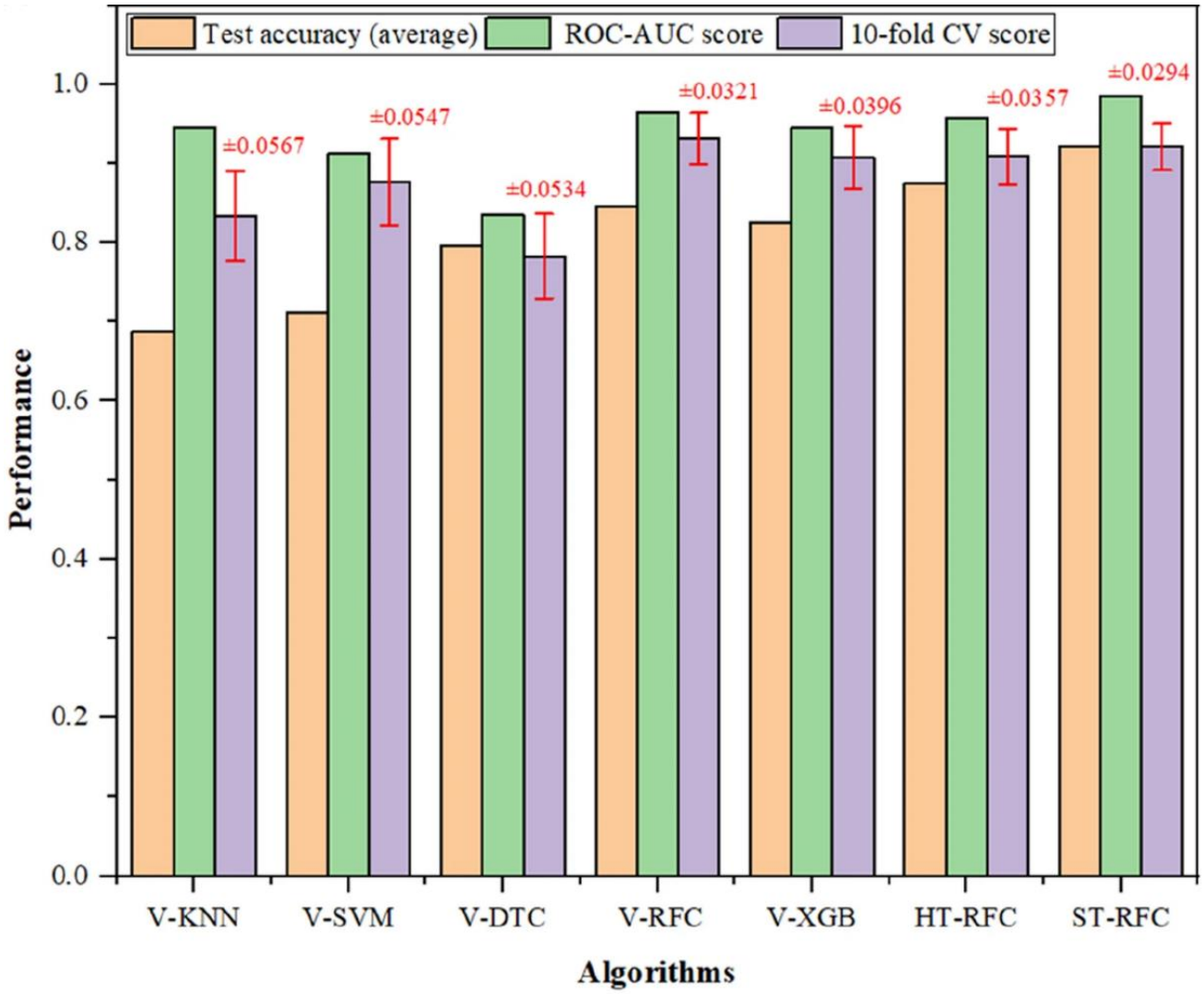

Figure 3.13. Performance comparison of V-KNN, V-SVM, V-DTC, V-RFC, V-XGB, HT-RFC, and ST-RFC models using accuracy (multiply by 100 for % value), ROC_AUC score,10-fold cross-validation score and its standard deviation (values shown in red color)

Confusion Matrix-Based Comparison of V-RFC and ST-RFC

A confusion matrix is a useful tool for visualising a classifier's performance, where an $n \times n$ matrix (where n is the number of classes) provides detailed insights into correctly and incorrectly classified instances. Two 4×4 confusion matrices were generated: one for the V-RFC model using the original dataset (1200) based on test data comprising 240 HEA samples (93 MIP, 67 BCC, 46 FCC, and 34 FCC + BCC), and another for ST-RFC model using the augmented dataset (1,392 samples) based on test data comprising 279 HEA samples (78 MIP, 67 BCC, 40 FCC, and 94 FCC + BCC), as shown in Figure 3.14. It can be observed that, in the ST-RFC model, the number of samples in the minority class increased while maintaining the stratified ratio among classes. Although the number of incorrect predictions decreased in the case of ST-RFC model compared

to the V-RFC model, the reliability of the ST-RFC model remains questionable due to the uncertainty associated with synthetic samples, which cannot guarantee the formation of a true high-entropy alloy. Therefore, a comparison between vanilla models with SMOTE-Tomek links models (trained on the augmented dataset) was further performed based on ROC curves and their AUC scores.

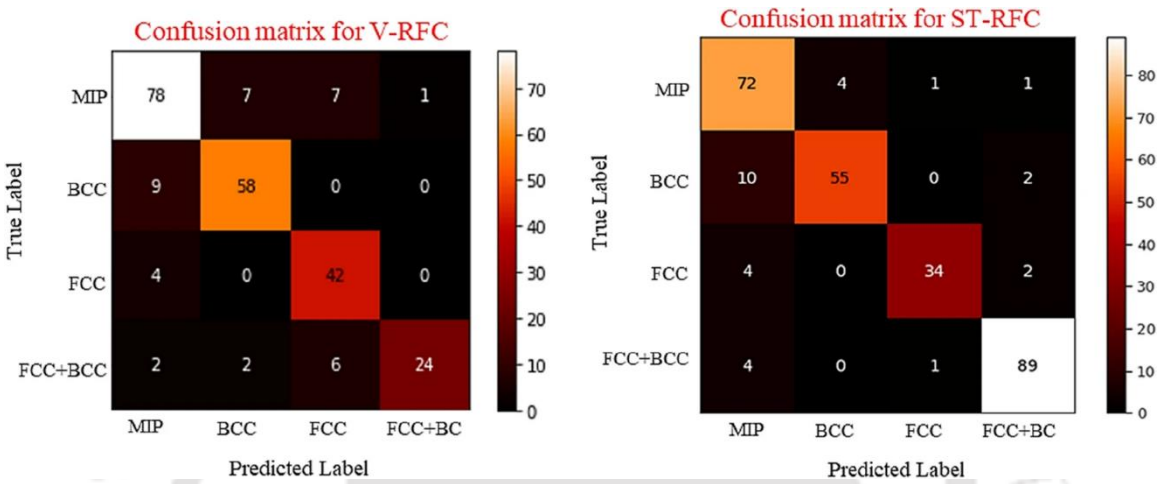

Figure 3.14. Confusion matrix comparing the performance of V-RFC, and ST-RFC for each distinct phase

ROC-AUC Score-Based Comparison

The ROC curves and their corresponding AUC scores for all five vanilla models (trained on original dataset), and SMOTE-Tomek links models (trained on augmented dataset) were plotted, as shown in Figure 3.15(a) and 3.15(c). The ROC-AUC scores of all ST-models were higher than those of the vanilla models.

The best performing models i.e., V-RFC and ST-RFC were selected, and the AUC score for each individual phase (MIP, BCC, FCC, and FCC + BCC) evaluated using the test data from the original dataset (240 HEAs) and the augmented dataset (279 HEAs), as depicted in Figure 3.15(b) and 3.15(d). It can be observed that although the overall ROC-AUC of the ST-RFC model was approximately 3% higher than the vanilla model (V-RFC), both models exhibited comparable AUC scores across all phases except for the FCC + BCC phase. The higher AUC score for the FCC + BCC phase in the ST-RFC model can be attributed to the increased number of instances for this minority class, which was expanded from 34 instances to 94 instances through synthetic data augmentation, thereby, making it the majority class in the augmented dataset.

Thus, our claim was reinforced by comparing the confusion matrices and ROC-AUC scores of the models trained on both the original and augmented datasets. Since these metrics provide deeper insights and are regarded as reliable indicators of classification performance, this study asserts that augmenting data solely to increase model accuracy is not a dependable practice. Therefore, the present work is particularly relevant in light of the aforementioned issues.

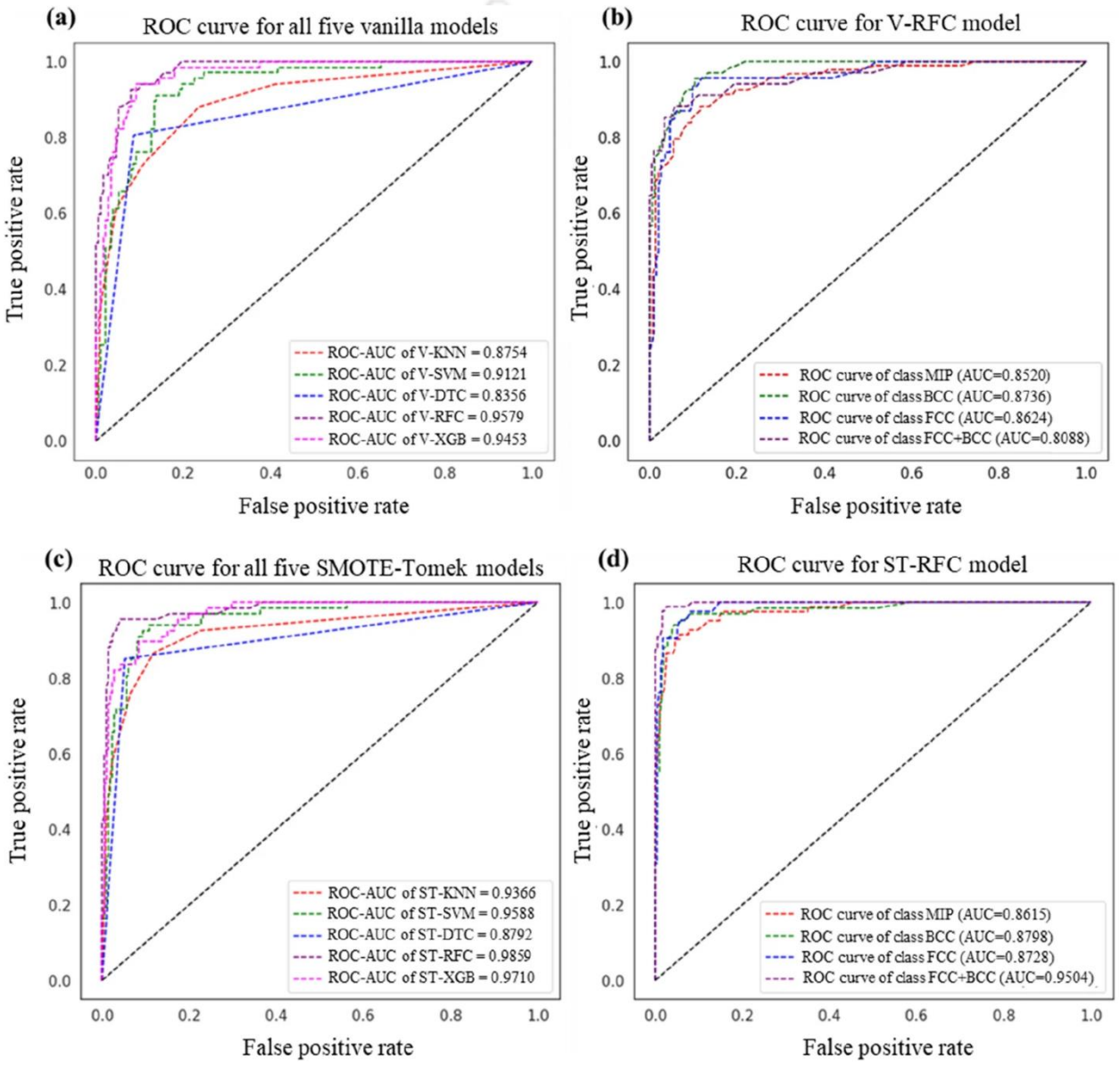

Figure 3.15. ROC-AUC scores for (a) five vanilla (base) models, (b) AUC score of each phase for the best vanilla model i.e., V-RFC model, (c) for all five SMOTE-Tomek links augmented model, (d) AUC score of each phase for the best SMOTE-Tomek links augmented model i.e., ST-RFC model

3.9. Validation of the Best Performing V-RFC Model

The predictive capability of the V-RFC model was validated in two stages: first, by predicting the phases of compositions reported in literature that were not part of either training or test datasets; and second, by predicting the phase of a novel composition, which was subsequently synthesized experimentally and characterized.

3.9.1. Validation Using Unseen Data from Literature

To evaluate the reliability and generalizability of the V-RFC model, the phases of five recently developed alloys, including two refractory HEAs [124], one 3d-transition metal HEA [170], and two precious metal HEAs [171], were predicted and compared with experimental reports, as summarized in Table 3.5. The physical parameters corresponding to these HEAs were calculated using the chemical formulae described in the earlier sections.

Table 3.5. Validation of V-RFC model performance for unseen compositions (not used in training or test datasets)

Alloys	Physical parameters					V- RFC Predicted phases	Actual phases
	ΔH_{mix} (kJ/mol)	ΔS_{mix} (J/K.mol)	VEC	$\Delta\chi$	δ		
Refractory HEAs [124]							
$Ti_{0.5}$NbMoTaW	−3.06	13.15	5.33	0.361	2.6	BCC	BCC
TiNbMoTaW	−3.04	13.38	5.2	0.356	2.75	BCC	BCC
3d transition metal HEAs [170]							
$Al_{0.5}$CrCuNiV	−6.01	13.15	5.43	0.133	4.39	*MIP*	FCC+ 2BCC+ ordered B2 phase
Precious metal HEAs [171]							
PdPtRhIrCuNi	−2.56	14.89	9.82	0.161	3.71	FCC	FCC
AuPdAgPtCuNi	−2.22	14.89	10.49	0.236	5.39	FCC	FCC

The V-RFC predictions matched the experimentally reported phases, demonstrating good consistency between model output and experimentally reported phases, except for the $Al_{0.5}$CrCuNiV, as illustrated in Table 3.5. In the case of $Al_{0.5}$CrCuNiV 3d-transition metal HEA [170], the model predicted the MIP phase (shown in italic font). Experimentally, this alloy was reported to consist 1FCC + 2BCC + ordered B2 phase, forming a complex multiphase structure. As explained in section 3.3, the ML models used in this study considers mixtures of multiple solid solutions or intermetallic

phases under the MIP category. Thus, based on this consideration, it can be inferred that the V-RFC model prediction is correct for all unseen compositions. However, the model is limited in identifying the number and types of phases present in complex multiphase HEAs. A list of such complex multiphase HEAs from the literature (not included in the training or test datasets) is tabulated in Table 3.6.

Table 3.6. High-entropy alloys (that were not the part of train-test set) correctly predicted as MIP using V-RFC model as per considered assumption

Alloy	V-RFC predicted phases	Actual phase	References
CoCrCuFeMnNiTiV	MIP	FCC+BCC+IM	[172]
Al0.2Co1.5CrFeNi1.5Ti	MIP	Gamma (FCC) + η (Ni, Co)$_3$Ti	[173]
$Ti_{20}Zr_{20}Hf_{20}Nb_{20}Cr_{20}$	MIP	BCC + 2 Laves (Cr_2Nb and Cr_2Hf)	[174]
$Ni_{44.8}(FeCoCr)_{40}(AlTi)_{15}Hf_{0.2}$	MIP	FCC+ordered FCC phase ($L1_2$)	[67]
AlTiCrFeNiCu	MIP	BCC1+BCC2+Fe2Ti	[175]
AlCoCrFeNiTi0.4	MIP	A2 (disordered BCC)+B2 (ordered BCC)+Laves	[176]
AlCoCrFeNb0.25Ni	MIP	BCC + (Laves + bcc)	[177]

3.9.2. Validation by Predicting Phase of a Novel MPEA

To further validate the predictive capability of the V-RFC model, a new alloy composition, **$Ni_{25}Cu_{18.75}Fe_{25}Co_{25}Al_{6.25}$**, was proposed. A detailed description of this novel composition including compositional and physical parameters details are presented in Table 3.7. The V-RFC model was fed with these details, and it predicted that this new HEA would stabilize as FCC phase at room temperature. Figure 3.16 compares various HEAs for the test dataset (240 alloys) with the newly proposed HEA composition ($Ni_{25}Cu_{18.75}Fe_{25}Co_{25}Al_{6.25}$). The orange dot represents the reported experimental phase of the HEA for the test data while the blue triangles represent the V-RFC prediction, and the red asterisk represents the new composition.

Table 3.7. Detailed description of newly proposed HEA

Novel high-entropy alloy **($Ni_{25}Cu_{18.75}Fe_{25}Co_{25}Al_{6.25}$)**				
Chemical composition (wt %)				
Ni	**Cu**	**Fe**	**Co**	**Al**
0.25	0.1875	0.25	0.25	0.0625
Calculated physical parameters				
ΔHmix (kJ/mol)	ΔSmix (J/K.mol)	VEC	$\Delta\chi$	δ
0.2656	12.689	9	0.07178	3.5973

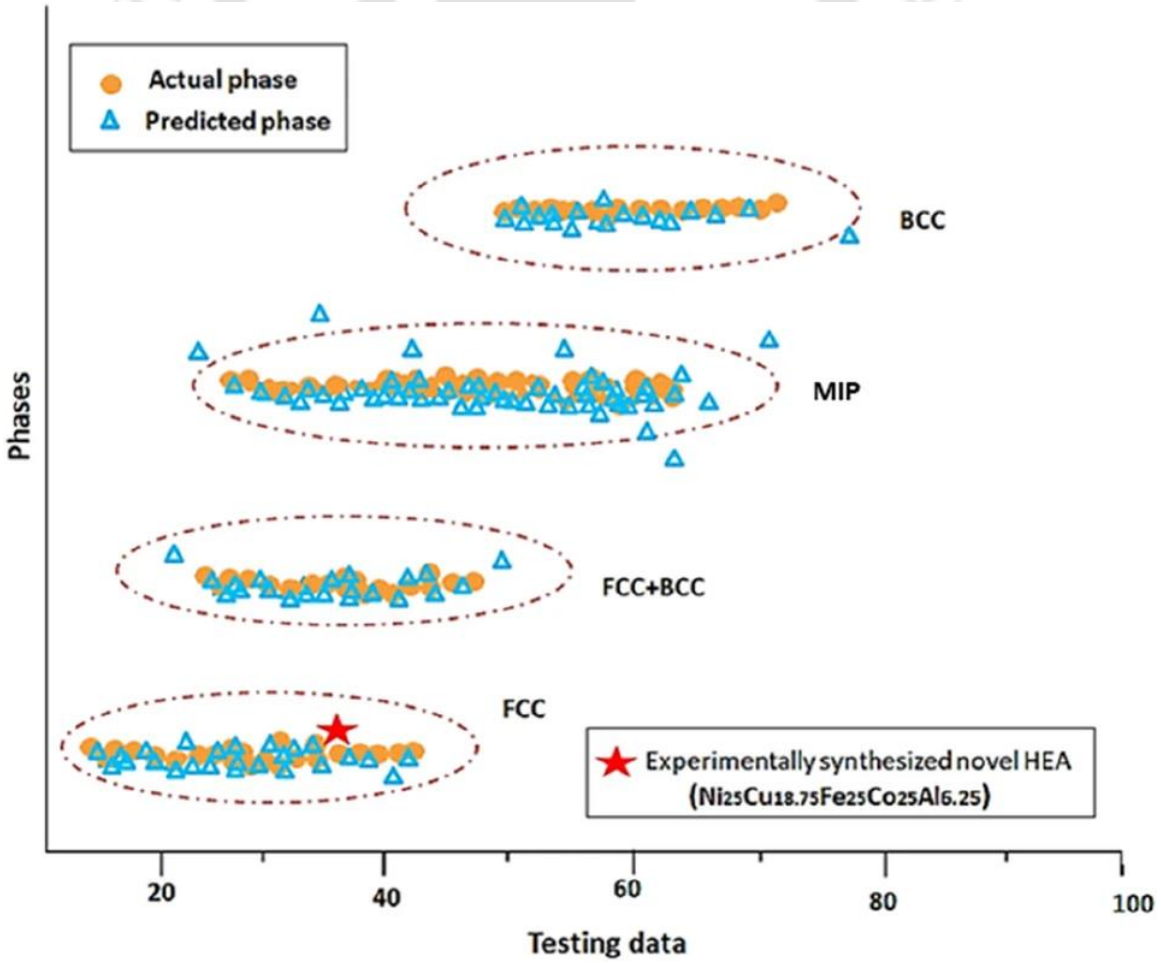

Figure 3.16. Phase prediction of novel HEA composition $Ni_{25}Cu_{18.75}Fe_{25}Co_{25}Al_{6.25}$ (shown in red asterisk), along with 240 test data

3.9.3. Experimental Synthesis and Characterisation of Novel HEA

Various metal buttons of Ni, Cu, Fe, Co and Al elements (purities> 99.99%) were purchased from Thermofisher Scientific®. All elemental metals with the proposition $Ni_{25}Cu_{18.75}Fe_{25}Co_{25}Al_{6.25}$ were melted together by vacuum arc melting under inert gas (high purity Ar) environment, see Figure 3.17. The formed ingot was melted and solidified multiple times to ensure chemical homogeneity, and then the HEA button was vacuum sealed in a quartz tube, homogenized at 1000°C for 10 hours, and then quenched into water for stabilizing high-temperature phase.

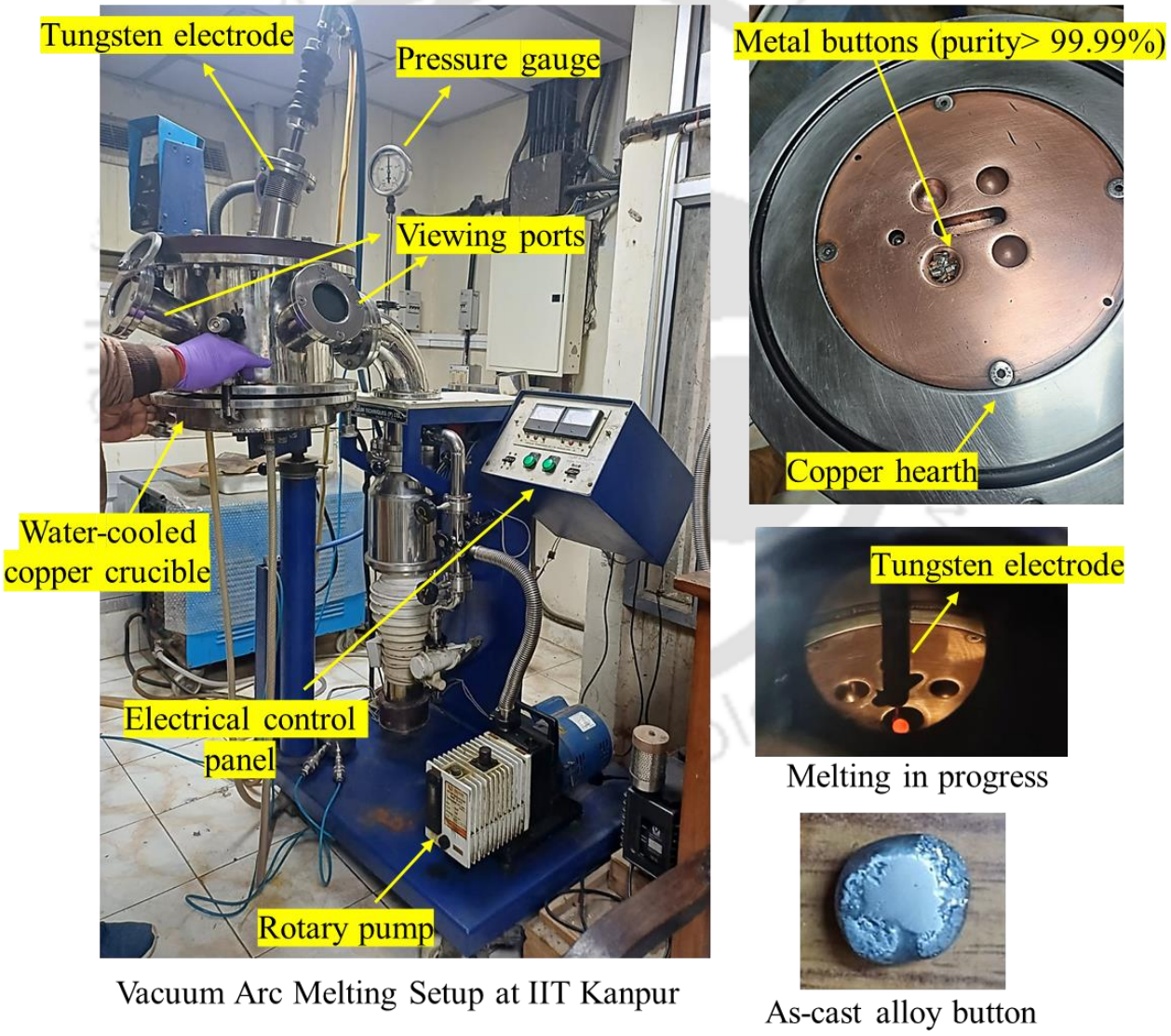

Figure 3.17. Vacuum arc melting setup at IIT Kanpur, and the sample prepared using it; (Courtesy: Dr. Nirmal Kumar Kaiya and Prof. Saurav Goel)

XRD Characterization

X-ray diffraction (XRD, Broker D8) was used to identify the phase of $Ni_{25}Cu_{18.75}Fe_{25}Co_{25}Al_{6.25}$ alloy, with the wavelength Cu Kα (λ =1.54056 Å) at a step size of 0.02° recorded with angles (*2θ)* in the range of 20-100° (see Figure 3.18). The Bragg's peaks (111), (200), (220), (311), and (222), belong to the lattice planes of FCC phase, while no other peaks corresponding to ordered structure were detected (see Figure 3.18), indicating that this new HEA resides in a crystalline FCC structure.

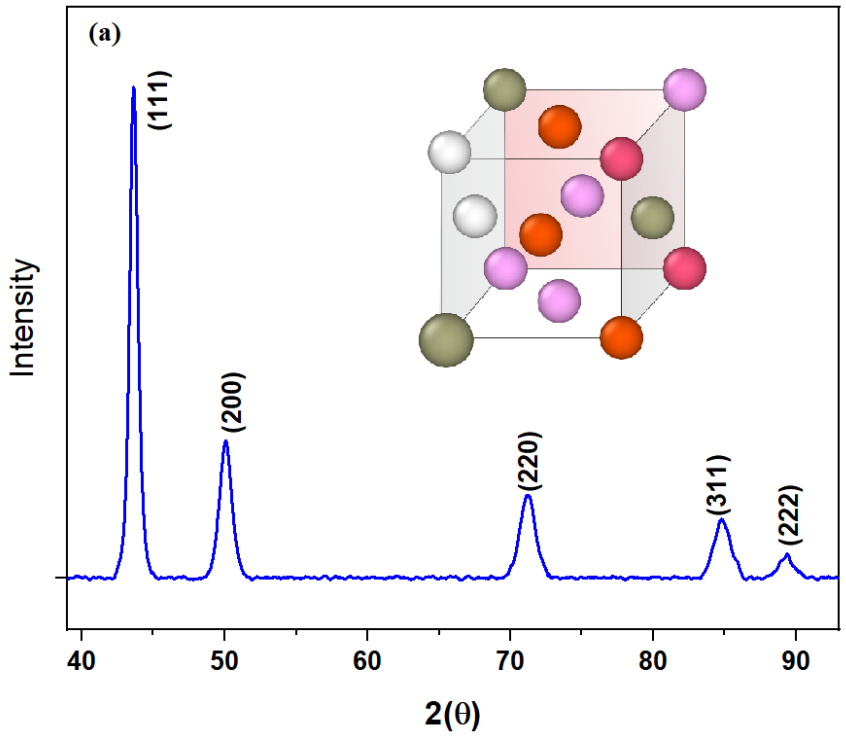

Figure 3.18. XRD analysis of newly synthesized HEA ($Ni_{25}Cu_{18.75}Fe_{25}Co_{25}Al_{6.25}$). Peaks (111), (200), (220), (311), and (222) correspond to FCC structure

A remarkable agreement between V-RFC model prediction and experiment can be seen for this new composition of HEA. It can be inferred that the V-RFC model is reliable and robust in predicting phases of novel compositions of HEAs as simple solid solution (FCC, BCC, FCC + BCC) and MIP (Mixture of intermetallic phases) with higher reliability of phase prediction, where MIP denotes the presence of either pure IM compounds such as α, β, σ, L12, L21, C15, C15, C36 Laves or mixture of IM + SS phases (FCC + IM, FCC + BCC + α, BCC + IM, FCC + α + β, BCC + Laves, BCC1 + BCC2 + C15 Laves, BCC + β-ordered BCC, FCC + CoMo2Ni-type IM, FCC + IM etc.). However, this method is limited in exactly interpreting the number and types of phases present in a complex multiphase HEA, which it

usually predicts as MIP phase, but it is robust for predicting solid-solution phases.

3.10. Comparison of Present Study with Existing Literature

The recently published literature was critically assessed and compared against the present study based on various evaluation metrics, as shown in Figure 3.19. Scant literature was found to focus on alternative evaluation metrics such as ROC-AUC, Precision, Recall and F1-score. The proposed RFC model in this study, evaluated through ROC-AUC score, tenfold cross-validation, confusion matrix, Precision, Recall, and F1-score, demonstrated satisfactory performance in predicting phases of HEAs as solid-solution phases (BCC, FCC, FCC + BCC) or MIP (denoting either pure intermetallic compounds (IM : such as α, β, σ , L12, C14, C15, C36 Laves, and others) or mixture IM + SS phases such as FCC + IM, FCC + BCC + α, BCC + IM, FCC + α + β, BCC + Laves, BCC1 + BCC2 + C15 Laves etc.)) for a large imbalanced dataset of HEAs synthesized solely via melting and casting routes, without augmenting or polluting experimental data with synthetically generated samples.

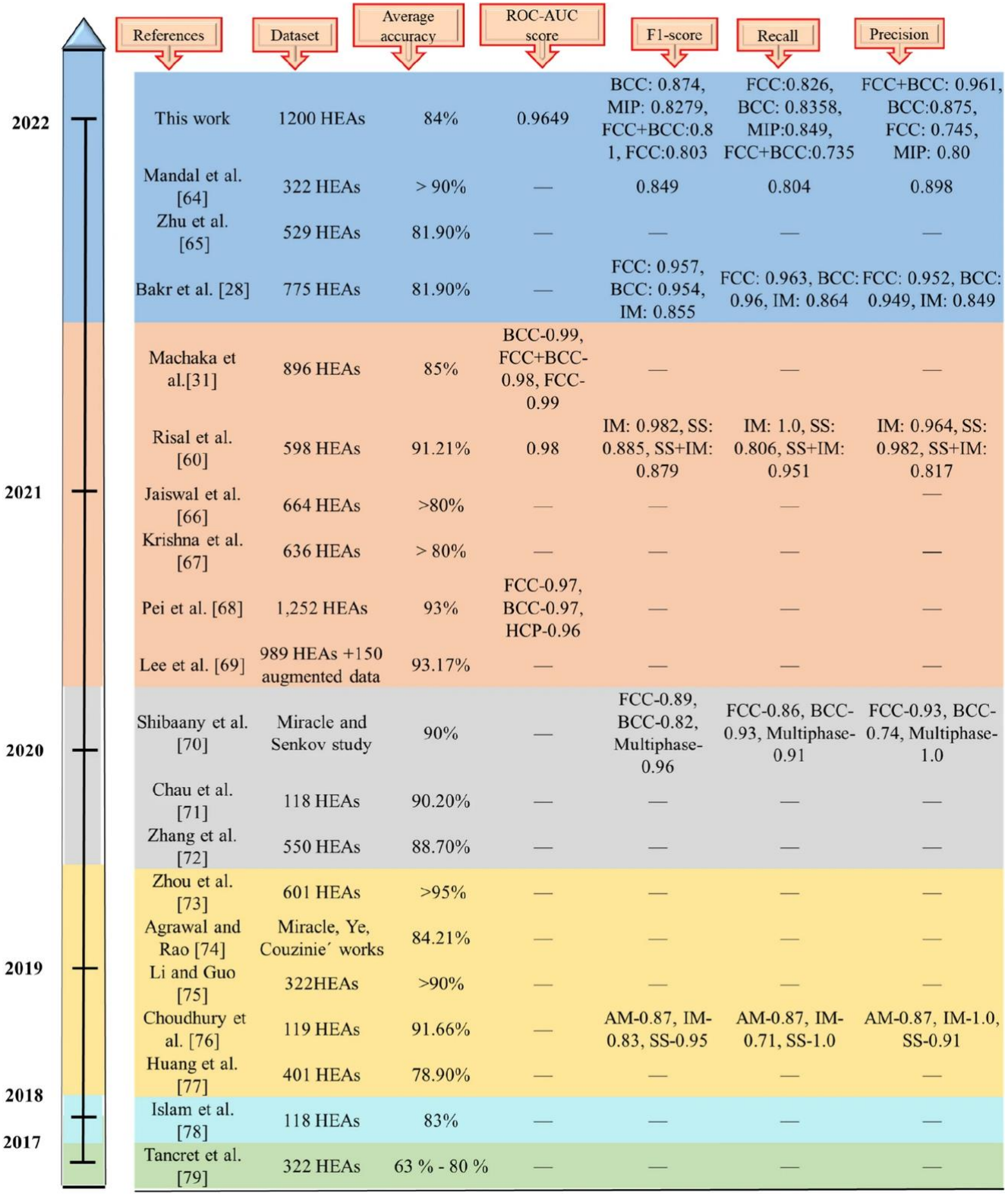

	References	Dataset	Average accuracy	ROC-AUC score	F1-score	Recall	Precision
2022	This work	1200 HEAs	84%	0.9649	BCC: 0.874, MIP: 0.8279, FCC+BCC:0.81, FCC:0.803	FCC:0.826, BCC: 0.8358, MIP:0.849, FCC+BCC:0.735	FCC+BCC: 0.961, BCC:0.875, FCC: 0.745, MIP: 0.80
	Mandal et al. [64]	322 HEAs	> 90%	—	0.849	0.804	0.898
	Zhu et al. [65]	529 HEAs	81.90%	—	—	—	—
	Bakr et al. [28]	775 HEAs	81.90%	—	FCC: 0.957, BCC: 0.954, IM: 0.855	FCC: 0.963, BCC: 0.96, IM: 0.864	FCC: 0.952, BCC: 0.949, IM: 0.849
2021	Machaka et al.[31]	896 HEAs	85%	BCC-0.99, FCC+BCC-0.98, FCC-0.99	—	—	—
	Risal et al. [60]	598 HEAs	91.21%	0.98	IM: 0.982, SS: 0.885, SS+IM: 0.879	IM: 1.0, SS: 0.806, SS+IM: 0.951	IM: 0.964, SS: 0.982, SS+IM: 0.817
	Jaiswal et al. [66]	664 HEAs	>80%	—	—	—	—
	Krishna et al. [67]	636 HEAs	> 80%	—	—	—	—
	Pei et al. [68]	1,252 HEAs	93%	FCC-0.97, BCC-0.97, HCP-0.96	—	—	—
	Lee et al. [69]	989 HEAs +150 augmented data	93.17%	—	—	—	—
2020	Shibaany et al. [70]	Miracle and Senkov study	90%	—	FCC-0.89, BCC-0.82, Multiphase-0.96	FCC-0.86, BCC-0.93, Multiphase-0.91	FCC-0.93, BCC-0.74, Multiphase-1.0
	Chau et al. [71]	118 HEAs	90.20%	—	—	—	—
	Zhang et al. [72]	550 HEAs	88.70%	—	—	—	—
2019	Zhou et al. [73]	601 HEAs	>95%	—	—	—	—
	Agrawal and Rao [74]	Miracle, Ye, Couzinie´ works	84.21%	—	—	—	—
	Li and Guo [75]	322HEAs	>90%	—	—	—	—
	Choudhury et al. [76]	119 HEAs	91.66%	—	AM-0.87, IM-0.83, SS-0.95	AM-0.87, IM-0.71, SS-1.0	AM-0.87, IM-1.0, SS-0.91
2018	Huang et al. [77]	401 HEAs	78.90%	—	—	—	—
	Islam et al. [78]	118 HEAs	83%	—	—	—	—
2017	Tancret et al. [79]	322 HEAs	63 % - 80 %	—	—	—	—

Figure 3.19. Performance comparison of proposed study with existing literature [12, 15-17, 73-78, 80-84, 86, 92, 93, 178]

3.11. Summary

This study developed a robust phase prediction framework for MPEAs, trained exclusively on high-quality experimental data restricted to alloys synthesized via the melting and casting route, thereby ensuring consistency and avoiding variability due to differing processing methods. A curated dataset of 1,200 HEA instances, spanning 3d-transition metal HEAs, refractory HEAs, precious metal-based systems, HEA brass/bronze, and low-density HEAs, was employed. Five commonly used classification algorithms, K-Nearest Neighbour (KNN), Support Vector Machine (SVM), Decision Tree (DT), Random Forest (RF), and Extreme Gradient Boosting (XGBoost) were implemented in their vanilla (base) forms. Among these, the vanilla Random Forest Classifier (V-RFC) demonstrated the best performance, achieving an average accuracy of 84%, a ROC-AUC score of 0.9649, a 10-fold cross-validation mean score of 0.9315, and superior Precision, Recall, and F1-score compared to the others.

Unlike most literature approaches, the framework consciously avoided synthetic data augmentation, which, although often reported to enhance model accuracy, risks compromising predictive reliability. To critically examine this practice, the SMOTE–Tomek Link method was applied to resample the dataset ($1200 + 192 = 1392$ instances). Using the RFC model (ST-RFC), an apparent increase in accuracy to 92% was observed. However, comparative analysis of confusion matrices and ROC curves revealed that the augmented model failed to provide reliable prediction. In contrast, the robustness of the V-RFC model, trained solely on experimental data, was further substantiated through experimental validation. A novel HEA composition, $Ni_{25}Cu_{18.75}Fe_{25}Co_{25}Al_{6.25}$, predicted by the model to form an FCC phase, was synthesized via vacuum arc melting and characterized using X-ray diffraction, which confirmed the FCC structure in agreement with the model's prediction. This demonstrated that accuracy alone is not a sufficient metric for an imbalanced dataset, and that augmenting experimental datasets with synthetic data may lead to misleading outcomes. These findings highlighted that robust classification performance could be achieved without resorting to synthetic data augmentation.

Major conclusions from this study can be summarised as follows:

a. Synthetic data augmentation, though capable of inflating model accuracy, compromises predictive reliability. Robust metrics such as ROC-AUC, Precision, Recall, and F1-score are essential for meaningful model assessment.

b. Reliable phase prediction can be achieved using only five key descriptors, Valence electron concentration (VEC), Electronegativity difference ($\Delta\chi$), Mixing entropy (ΔS_{mix}), Atomic size difference (δ), and Mixing enthalpy (ΔH_{mix}), provided that carefully screened experimental data are used.

c. The developed framework demonstrated strong performance in predicting solid-solution phases (FCC, BCC, FCC + BCC) and classifying multiphase HEAs as mixtures of intermetallic phases (MIPs). However, its ability to interpret the precise number and type of phases present in multiphase alloys remains limited. Future work could address this limitation by incorporating CALPHAD-derived phase-diagram descriptors (such as equilibrium phase fractions, Gibbs free energies, and phase-stability boundaries), which would supply thermodynamically grounded information on the number and identity of coexisting phases. In addition, unsupervised clustering techniques could be employed to reveal hidden composition–phase groupings that are not discernible from composition alone. Moreover, microstructure-based image analysis, leveraging SEM, EBSD, or TEM micrographs processed through convolutional neural networks (CNNs) or U-Net architectures, could extract phase-specific morphological features, enabling the model to infer the number, distribution, and nature of coexisting phases with significantly improved fidelity.

Building upon the development of a reliable framework for phase prediction in MPEAs, the subsequent stage of this research is directed toward the prediction of mechanical properties and the simultaneous optimization of competing attributes such as strength and ductility, with the objective of addressing the long-standing strength–ductility conundrum.

Chapter 4

Development of ML-Based Framework for Prediction and Optimization of Mechanical Properties of MPEAs

4.1. Introduction

This chapter presents a comprehensive machine learning framework for predicting and optimizing the mechanical properties of MPEAs. The initial focus is placed on predicting a key mechanical property i.e., yield strength, using a curated dataset comprising 700 experimentally characterized MPEAs. To achieve this, the study employs the Materials Simulation Toolkit for Machine Learning (MAST-ML), an open-source Python package specifically designed for materials informatics. Within the MAST-ML framework, three tree-based regression models, namely Decision Tree, Random Forest, and Extra Tree Regressor, were implemented. In contrast to approach adopted in the preceding chapter, where models were developed independently from scratch, MAST-ML was deliberately utilized here to investigate the extent to which an automated toolkit can streamline and facilitate mechanical property prediction. A critical assessment of MAST-ML's strengths and limitations is also provided in the context of mechanical property prediction of complex alloy systems such as MPEAs.

In view of the observed limitations of MAST-ML framework, custom ML framework was developed from scratch, utilizing Neural Network (NN), Random Forest Regressor (RFR), Extra Trees Regressor (ETR), Cat-Boost Regressor (CBR), and XGBoost Regressor (XGB), with the objective of simultaneously predicting multiple properties, including yield strength (YS), ultimate tensile strength (UTS), and elongation ($\mathcal{E}$). The best performing model was subsequently employed for the optimization of these properties through multi-objective optimization framework, achieved by integrating it with a nature-inspired Cuckoo Search Optimization algorithm coupled with the Non-Dominated Sorting Genetic Algorithm II (NSGA-II). This integrated framework enables the identification of Pareto-optimal alloy compositions, effectively balancing conflicting objectives and uncovering novel design pathways to overcome the long-standing strength-ductility conundrum.

4.2. Development of MAST-ML Based Model for Yield Strength Prediction

MAST-ML is a Python-based open-source toolkit developed by the Computational Materials Group at the University of Wisconsin–Madison [179] to automate and streamline machine-learning workflows in materials science. Unlike generic ML libraries, MAST-ML is specifically designed for materials datasets and aims to lower the entry barrier for researchers by automating key components of the ML pipeline and incorporating established best practices. Built on top of scikit-learn and integrated with materials-specific descriptor libraries such as MAGPIE and Matminer, MAST-ML provides an end-to-end workflow encompassing data import, cleaning, feature engineering, model selection, training, cross-validation, and uncertainty quantification.

In this work, MAST-ML was chosen over alternatives such as Matminer alone and generic AutoML frameworks (e.g., TPOT, H2O-AutoML) for several reasons. Matminer and MAGPIE function primarily as descriptor-generation tools and do not provide an integrated modelling pipeline. In contrast, MAST-ML extends these descriptors into a unified, end-to-end workflow, enabling efficient and reproducible model development. Furthermore, while generic AutoML systems are powerful for large-scale hyperparameter optimization, they typically lack materials-specific features, offer limited physical interpretability, and do not include built-in uncertainty estimation, capabilities essential for scientifically meaningful studies on alloy design. By incorporating materials-aware best practices, structured cross-validation routines, uncertainty estimation through bootstrap and k-fold methods, and feature-importance analysis, MAST-ML offers a domain-specific, interpretable, and reproducible modelling environment ideally suited for the small-to-medium experimental datasets characteristic of MPEA research. It is also compatible with other materials informatics toolkits such as pyMKS and AFLOW-ML, allowing flexible integration into broader research workflows. The MAST-ML framework follows straightforward machine learning workflow, as illustrated in Figure 4.1.

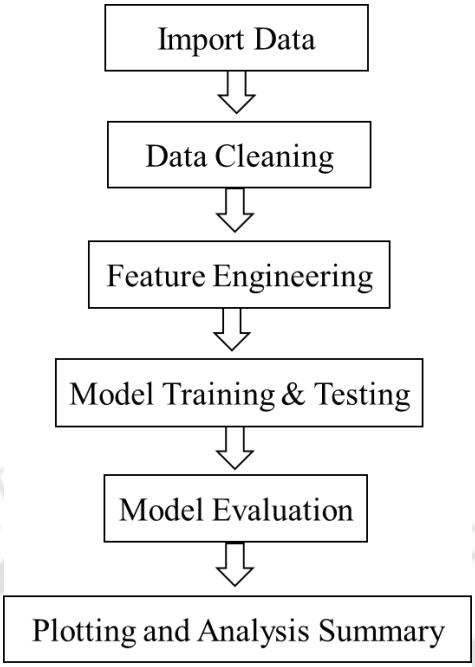

Figure 4.1.Workflow of MAST-ML toolkit

This study marks the first deployment of the MAST-ML toolkit for predicting mechanical property, specifically the yield strength of MPEAs. The steps involved are discussed in detail in subsequent sections.

4.2.1. Data Collection and Processing

The dataset employed in this study comprises 700 MPEA compositions with corresponding experimental yield strength values, curated from several published sources [119, 124, 180, 181]. Table 4.1 represent a subset of data imported for ML model development.

Table 4.1. Compiled database for yield strength prediction

	Compositions	Al(at%)	Co(at%)	Cr(at%)	Cu(at%)	Fe(at%)	Ni(at%)	Mn(at%)	Ti(at%)	V(at%)	C(at%)	Nb(at%)	Zr(at%)	Mo(at%)	YS(Mpa)
0	CrFeCoNiMo	0.0	20.000000	20.000000	0.0	20.000000	20.000000	0.0	0.0	0.0	0.0	0.0	0.0	20.000000	155
1	CrFeCoNiMo0.1	0.0	24.390244	24.390244	0.0	24.390244	24.390244	0.0	0.0	0.0	0.0	0.0	0.0	2.439024	198.8
2	CrFeCoNiMo0.2	0.0	23.809524	23.809524	0.0	23.809524	23.809524	0.0	0.0	0.0	0.0	0.0	0.0	4.761905	254.7
3	CrFeCoNiMo0.3	0.0	23.255814	23.255814	0.0	23.255814	23.255814	0.0	0.0	0.0	0.0	0.0	0.0	6.976744	305.3
4	CrFeCoNi	0.0	25.000000	25.000000	0.0	25.000000	25.000000	0.0	0.0	0.0	0.0	0.0	0.0	0.000000	140
5	CrMnFeCoNi	0.0	20.000000	20.000000	0.0	20.000000	20.000000	20.0	0.0	0.0	0.0	0.0	0.0	0.000000	215
6	(CrMnFeCoNi)93Al7	7.0	18.600000	18.600000	0.0	18.600000	18.600000	18.6	0.0	0.0	0.0	0.0	0.0	0.000000	242
7	(CrMnFeCoNi)89Al11	11.0	17.800000	17.800000	0.0	17.800000	17.800000	17.8	0.0	0.0	0.0	0.0	0.0	0.000000	832
8	(CrFeCoNi)94Ti2Al4	4.0	23.500000	23.500000	0.0	23.500000	23.500000	0.0	2.0	0.0	0.0	0.0	0.0	0.000000	200
9	AlNbTiV	25.0	0.000000	0.000000	0.0	0.000000	0.000000	0.0	25.0	25.0	0.0	25.0	0.0	0.000000	1000

The complete dataset was imported into the MAST-ML framework, which automatically handled data processing, including cleaning and organization, as part of its workflow (see Figure 4.1). Feature engineering was carried out through the MAGPIE elemental descriptor set embedded within MAST-ML, which systematically generates domain-related features based on fundamental elemental properties. This process resulted in an initial set of 300 independent features.

To reduce dimensionality and mitigate the risk of overfitting, SHAP (SHapley Additive exPlanations) values were computed within MAST-ML to evaluate feature importance. As shown in Figure 4.2, the lowest mean absolute error (MAE) was obtained when approximately 50 features were used. Therefore, this subset was selected as the optimal number of features, providing best trade-off between complexity and generalizability. Beyond this point, the inclusion of additional features provides little to no improvement in performance, while simultaneously increasing the risk of overfitting and unnecessary computational cost. Consequently, the final dataset consisted of 700 rows representing individual MPEA compositions, 50 independent feature columns, and one target column corresponding to yield strength.

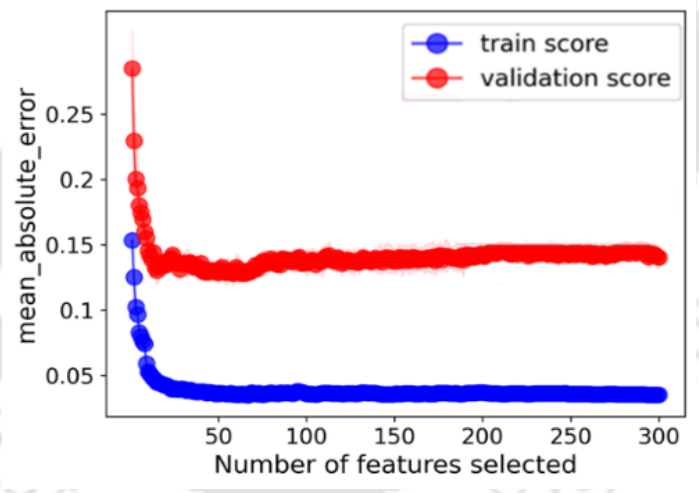

Figure 4.2. Feature selection by measuring MAE for 300 independent features

4.2.2. Model Training and Testing

The dataset was partitioned for training and testing three prominent tree-based regression algorithms: Decision Tree Regressor (DTR), Random Forest Regressor (RFR), and Extra Tree Regressor (ETR). In MAST-ML, this is achieved by defining the parameter n_splits, which specifies the number of folds for training and testing. For example, n_splits = 2 results in a 50:50 split, n_splits = 4 corresponds to a 75:25 split, and n_splits = 5 yields an 80:20 split. In the present investigation, n_splits = 5 was employed, thereby dividing the dataset into an 80:20 ratio for

training and testing.

In addition, MAST-ML enables the assessment of model robustness under both "best split" and "worst split" scenarios. These refer to the most and least favorable data partitions encountered during cross-validation. The "best split" highlights the model's maximum predictive capability, whereas the "worst split" reflects its limitation and generalizability.

4.2.3. Performance Assessment of Each Model

As the principles of Decision Tree and Random Forest algorithms have already been described in Chapter 3, in the context of classification, here they are discussed with respect to regression task. The Decision Tree Regressor (DTR) operates by recursively segmenting the feature space into progressively homogeneous subregions, thereby generating a hierarchical and interpretable model structure. While its transparency is advantageous for interpretability, the deterministic nature of DTR makes it highly vulnerable to overfitting, particularly when applied to noisy or high-dimensional datasets.

The Random Forest Regressor (RFR), on the other hand, constructs an ensemble of decision trees, each trained on randomly sampled subsets of the data and feature space. This bagging-based approach significantly enhances predictive robustness and generalization, resulting in more reliable estimates compared to those of any single tree. The Extra Tree Regressor (ETR) introduces an additional degree of randomness by selecting split thresholds at random, rather than optimizing them through a greed search. This further reduces variance and improves computational efficiency, as it avoids the computational cost associated with exhaustive split searches.

The performance of all three regression models was rigorously assessed using standard metrics: R^2 score (coefficient of determination), Mean Absolute Error (MAE)**,** and Root Mean Squared Error (RMSE)**,** applied to both the training and test sets, as summarized in Table 4.2 and Figure 4.3. A higher R^2 score indicates stronger explanatory power, while lower MAE and RMSE values reflect more accurate and consistent predictions.

Table 4.2. Performance evaluation of employed regression models

Dataset	**Split**	**Metrics**	**Algorithms**		
			DTR	**RFR**	**ETR**
	Best split	R2	0.998	0.974	0.997
		MAE	0.005	0.066	0.007
		RMSE	0.023	0.088	0.032

Training	Worst split	R2	0.994	0.964	0.995
		MAE	0.009	0.068	0.009
		RMSE	0.039	0.096	0.039
Testing	Best split	R2	0.825	0.897	**0.924**
		MAE	0.116	0.105	0.090
		RMSE	0.199	0.194	0.148
	Worst split	R2	0.520	0.799	**0.803**
		MAE	0.272	0.194	0.169
		RMSE	0.439	0.271	0.258

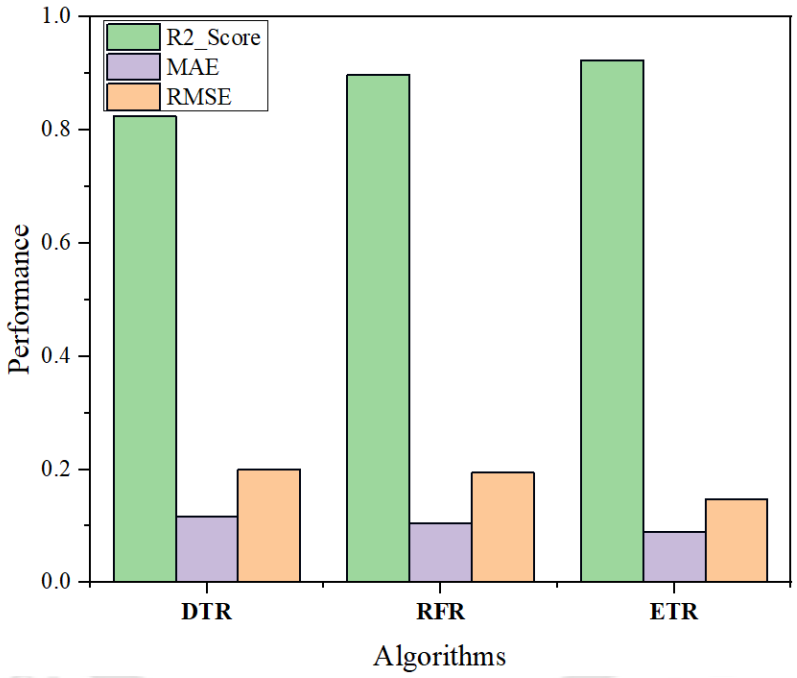

Figure 4.3. Bar chart comparing the performance of DTR, RFR and ETR for the best split of dataset.

Among the three models, ETR demonstrated superior performance across all metrics, with an R^2 score of 0.924**,** MAE of 0.090, and RMSE of 0.148 for the best split on the test set, distinguishing itself as robust. Even in the worst split, it retained a respectable R^2 score of 0.803, with MAE and RMSE values of 0.169 and 0.258, respectively, showcasing strong generalizability. Complementing these quantitative results, Figure 4.4 presents parity plots comparing the actual versus predicted yield strength values under both the best and worst data splits for testing data. These visualizations further corroborate the predictive fidelity of ETR relative to DTR and RFR, underscoring its suitability for yield strength prediction in MPEAs.

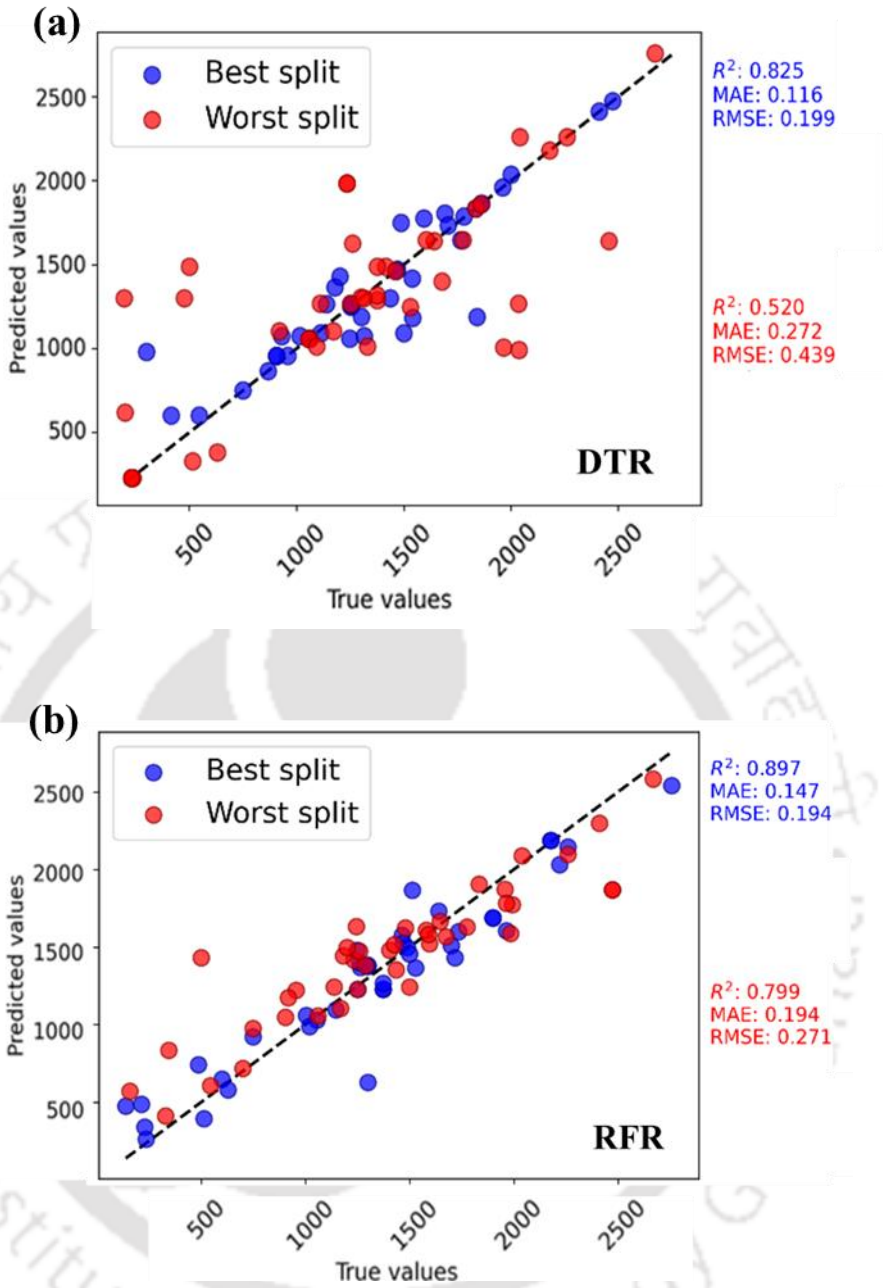
(a)
Best split
Worst split
R^2: 0.825
MAE: 0.116
RMSE: 0.199
R^2: 0.520
MAE: 0.272
RMSE: 0.439
DTR
Predicted values
True values
500
1000
1500
2000
2500
(b)
Best split
Worst split
R^2: 0.897
MAE: 0.147
RMSE: 0.194
R^2: 0.799
MAE: 0.194
RMSE: 0.271
RFR
Predicted values
True values

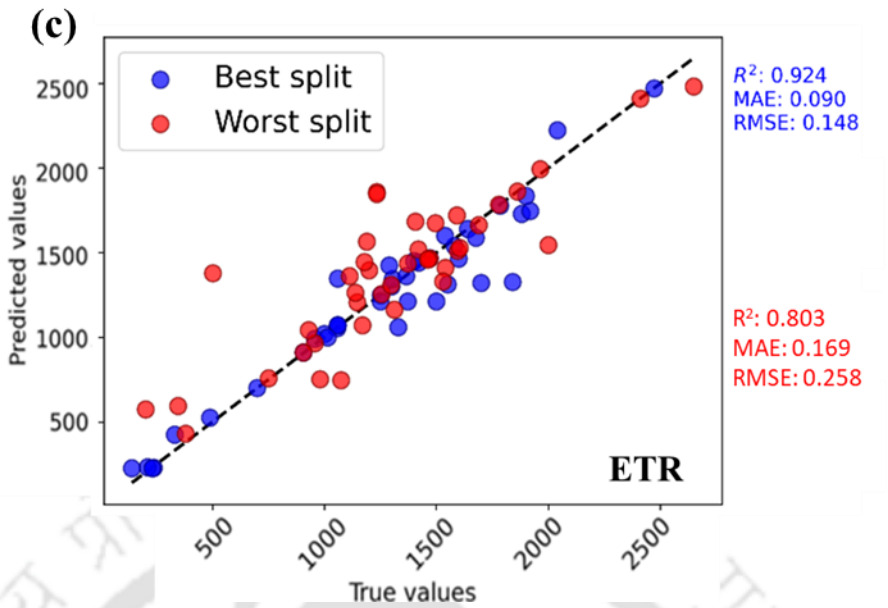

Figure 4.4. Parity plot comparing the true vs predicted yield strength values for **(a)** DTR, **(b)** RFR, and **(c)** ETR model for testing data

4.2.4. Validation of ETR Model Using Unseen Data

A fundamental measure of a machine learning model's utility lies in its ability to generalize to unseen data, which is a crucial requirement in predictive materials design. The ETR model consistently outperformed DTR and RFR, achieving higher R^2 scores and lower MAE and RMSE values across both the best and worst test set splits, highlighting its robustness and adaptability. To further validate its applicability, the ETR model was tested on unseen MPEA compositions sourced from the literature [120, 182-184] that were not included in the training or test sets. As detailed in Table 4.3, the predictions made by the ETR model for the new data showed good agreement, with an error margin of ± 20 MPa when compared to their actual (experimental) values. This high level of consistency confirms the reliability and extrapolative strength of the ETR model, demonstrating its potential as a powerful tool for generalizing to unseen data.

Table 4.3. ETR model validation for unseen compositions

Composition (unseen data for model)	Predicted Y. S	Actual Y. S	Error
$Al_{0.3}CoCrFeNi$ [182]	172.67	180	±7.33
$C_{2.2}(Co10Cr10Fe40Mn40)_{97.8}$ [183]	300.59	310	±9.4
$C_{4.4}(Co10Cr10Fe40Mn40)_{95.6}$ [183]	450.13	467	±16.8
$CoCuFeMnNiSn_{0.08}$ [184]	266.94	272	±5.06
$Al_{10}(CoCrFeMnNi)_{90}$ [120]	507.68	526	±18.3

4.2.5. Limitations of MAST-ML

MAST-ML demonstrates strong potential to accelerate materials research by streamlining machine learning workflows and enabling property predictions, such as yield strength, as demonstrated in this chapter. Its intuitive design makes it especially appealing for researchers new to machine learning, bridging the gap between domain expertise and data-driven modeling. While MAST-ML offers a powerful and user-friendly platform, several important limitations restrict its broader applicability. While the toolkit integrates well with scikit-learn for classical ML tasks, it does not currently support deep learning, GPU acceleration, or scalability to very large datasets. Additionally, it lacks integration with advanced optimization algorithms, such as metaheuristic approaches, that are essential for exploring vast and complex compositional spaces. Its design is largely batch-mode oriented, with diagnostic plots generated only after execution, limiting opportunities for interactive model refinement, real-time feedback, or iterative optimization.

Despite these limitations, MAST-ML remains a valuable platform for small- to medium-sized datasets and for researchers with limited coding experience. It's intuitive design and streamlined implementation make it particularly appealing for materials researcher new to Machine learning, as it allows them to build, validate and interpret predictive models with minimal programming expertise. However, it also limits opportunities for incorporation of deeper domain knowledge and customization.

The selection of algorithms within the MAST-ML environment was guided by both the capabilities of the toolkit and the characteristics of the dataset. MAST-ML primarily supports classical machine-learning models implemented in scikit-learn, with particular emphasis on tree-based and ensemble regressors. These methods are well suited for the moderate-sized, tabular dataset used in this study, offering strong performance, minimal tuning requirements, and interpretable feature-importance outputs. Kernel-based and deep-learning models were not selected as primary algorithms due to limited support within the current MAST-ML release and their typical requirement for larger datasets. Subsequent chapters extend beyond MAST-ML by incorporating advanced models, including neural networks, within a custom framework developed for multi-objective optimization.

4.3. Simultaneous Prediction and Optimization of Multiple Competing Properties

Building on the limitations of MAST-ML, a novel framework was developed for predicting and optimizing multiple properties simultaneously. The steps involved for achieving the proposed

objective are explained in Figure 4.5. The workflow begins with systematic collection of experimental data on MPEAs targeting YS, UTS and $\mathcal{E}$ simultaneously. Various regression algorithms including Neural Network (NN), Random Forest Regressor (RFR), Extra Trees Regressor (ETR), Cat-Boost Regressor (CBR), and XGBoost Regressor (XGB), were trained and tested using the curated data, and the best performing regression model was selected based on various evaluation metrics. In order to perform multi-objective optimization, the best-performing composition within the curated database was first identified and set as a benchmark reference. Building upon this foundation, the framework proceeds to multi-objective optimization, where the selected best-performing regression model was integrated with Cuckoo Search Optimization (CSO) and Non-Dominated Sorting Genetic Algorithm II (NSGA-II). This combined strategy enabled the exploration of vast compositional space to identify Pareto-optimal solutions which provide novel compositions that can surpass the benchmark, effectively providing novel design pathways for advanced alloy development, targeting strength-ductility trade-off. All these steps are explained in detail in the subsequent section.

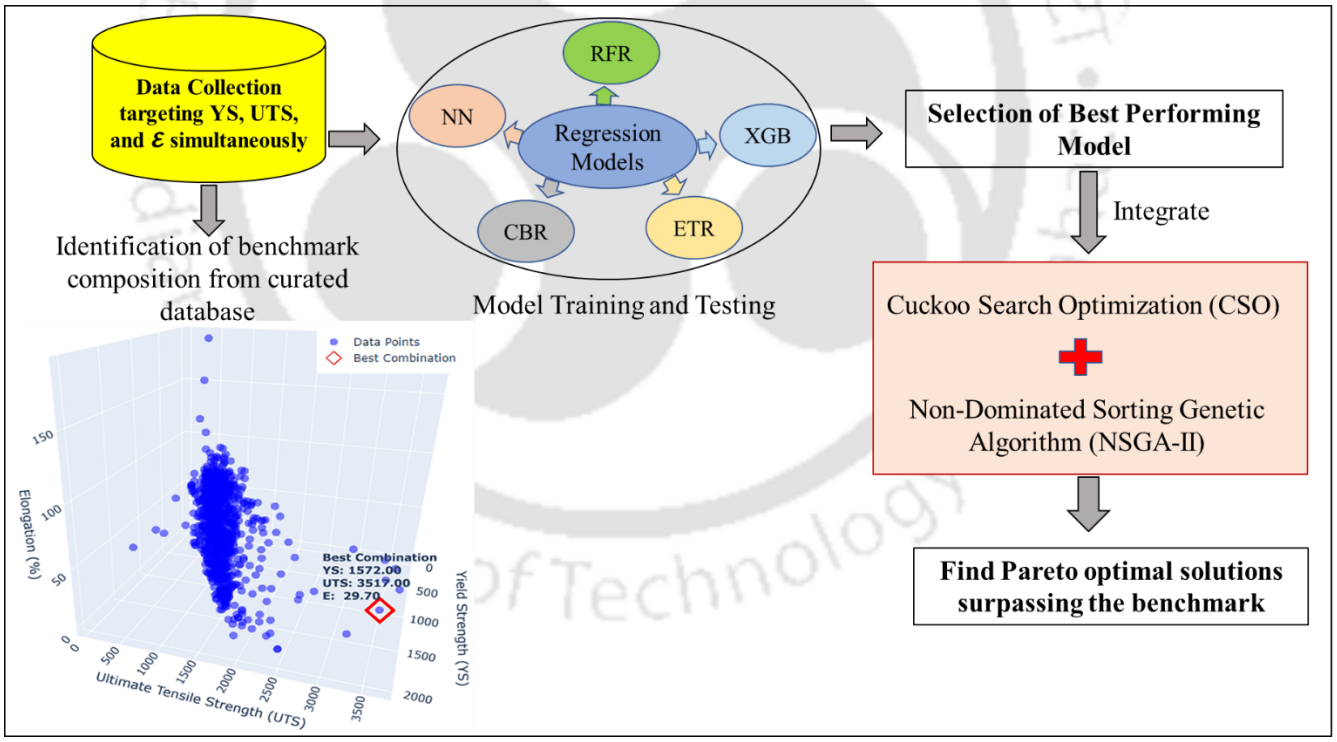

Figure 4.5. ML workflow for predicting and optimizing multiple properties simultaneously

4.3.1. Data Collection with a Focus on YS, UTS and, ε

A comprehensive dataset comprising 700 instances of MPEAs was meticulously curated from experimental literature. This dataset encompasses detailed compositional and mechanical property data, with the compositional information spanning 13 elements: Al, Co, Cr, Cu, Fe, Ni, Mn, Ti, V, C, Nb, Zr, and Mo. The mechanical properties recorded in the dataset include Yield Strength (YS), Ultimate Tensile Strength (UTS), and elongation (ε (%)). A snapshot of curated database is presented in Table 4.4.

Table 4.4. Curated database for predicting and simulataneously optimizing YS, UTS, and elongation

	Compositions	Al(at%)	Co(at%)	Cr(at%)	Cu(at%)	Fe(at%)	Ni(at%)	Mn(at%)	Ti(at%)	V(at%)	C(at%)	Nb(at%)	Zr(at%)	Mo(at%)	YS(Mpa)	UTS(Mpa)	El(%)
0	CrFeCoNiMo	0.0	20.000000	20.000000	0.0	20.000000	20.000000	0.0	0.0	0.0	0.0	0.0	0.0	20.000000	155	472.4	58.9
1	CrFeCoNiMo0.1	0.0	24.390244	24.390244	0.0	24.390244	24.390244	0.0	0.0	0.0	0.0	0.0	0.0	2.439024	198.8	479	51.1
2	CrFeCoNiMo0.2	0.0	23.809524	23.809524	0.0	23.809524	23.809524	0.0	0.0	0.0	0.0	0.0	0.0	4.761905	254.7	589.6	55.1
3	CrFeCoNiMo0.3	0.0	23.255814	23.255814	0.0	23.255814	23.255814	0.0	0.0	0.0	0.0	0.0	0.0	6.976744	305.3	709.7	49.3
4	CrFeCoNi	0.0	25.000000	25.000000	0.0	25.000000	25.000000	0.0	0.0	0.0	0.0	0.0	0.0	0.000000	140	488	83
5	CrMnFeCoNi	0.0	20.000000	20.000000	0.0	20.000000	20.000000	20.0	0.0	0.0	0.0	0.0	0.0	0.000000	215	491	71
6	(CrMnFeCoNi)93Al7	7.0	18.600000	18.600000	0.0	18.600000	18.600000	18.6	0.0	0.0	0.0	0.0	0.0	0.000000	242	529	47.2
7	(CrMnFeCoNi)89Al11	11.0	17.800000	17.800000	0.0	17.800000	17.800000	17.8	0.0	0.0	0.0	0.0	0.0	0.000000	832	1174	7.7
8	(CrFeCoNi)94Ti2Al4	4.0	23.500000	23.500000	0.0	23.500000	23.500000	0.0	2.0	0.0	0.0	0.0	0.0	0.000000	200	503	70
9	AlNbTiV	25.0	0.000000	0.000000	0.0	0.000000	0.000000	0.0	25.0	25.0	0.0	25.0	0.0	0.000000	1000	1280	5.2

4.3.2. Selection of the Optimal Composition from the Curated Database

To identify the best alloy composition that exhibits the most favorable combination of mechanical properties within the curated database, the Non-Dominated Sorting Genetic Algorithm II (NSGA-II) technique was employed. Through this analysis, the composition $AlCoCrFeNiZr_{0.008}$, characterized by YS, UTS, and elongation values of 1572 MPa, 3517 MPa, and 29.7%, respectively, was identified as the best composition within the database. The results are visually represented in a 3D plot, with YS, UTS, and elongation depicted on the three axes, providing a clear illustration of the relationship between these critical mechanical properties, see Figure 4.6. The best combination of mechanical properties is distinctly highlighted within a red square.

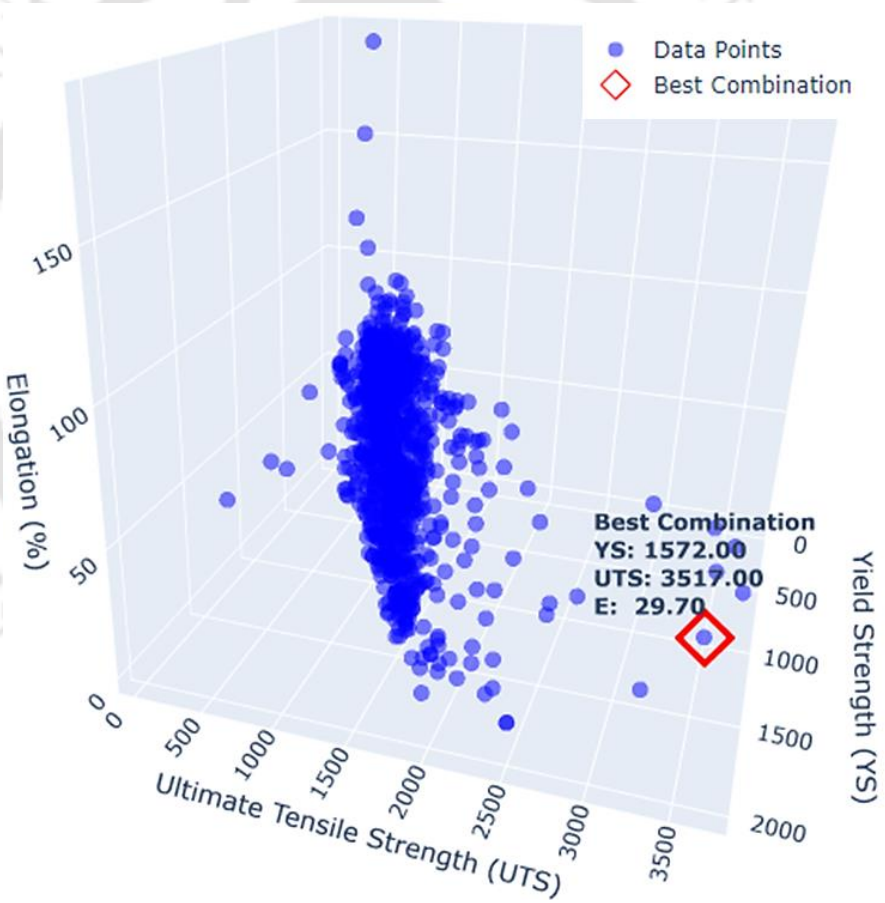

Figure 4.6. 3D plot illustrating the distribution of Yield Strength (YS), Ultimate Tensile Strength (UTS), and elongation (%) values for each data point in the dataset. The data point encircled within a red square represents the composition identified as having the optimal combination of these mechanical properties, as determined by the NSGA-II

4.3.3. Training and Testing ML Models

To predict the mechanical properties of MPEAs, several ML algorithms, including Neural Network (NN), Random Forest Regressor (RFR), Extra Trees Regressor (ETR), Cat-Boost Regressor (CBR), and XGBoost Regressor (XGB) were employed. The dataset was divided into an 80:20 ratio for training and testing the models. Standard scaling was applied to normalize the data. The performance of these models is depicted in Figure 4.7. Among all the regression models, the Cat-Boost Regressor (CBR) demonstrated superior performance, achieving the highest R^2 score of 0.91, along with the lowest Mean Squared Error (MSE) of 0.07 and Mean Absolute Error (MAE) of 0.16. Due to its exceptional performance, CBR was selected as the best model for subsequently performing multi-objective optimization.

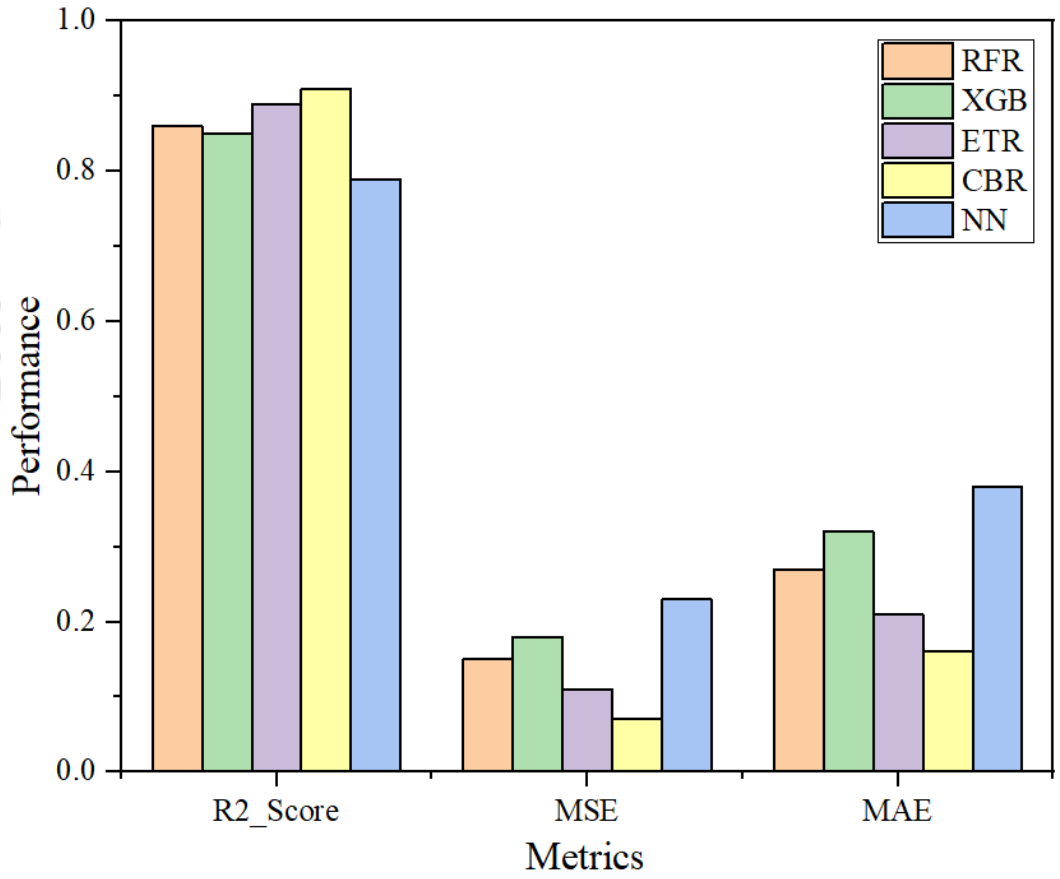

Figure 4.7. Performance evaluation of each algorithm based on R2_score, Mean Squared Error (MSE), and Mean Absolute Error (MAE)

4.3.4. Exploring Novel Compositions with Simultaneously Optimized YS, UTS, and, ε

Our objective is to find novel compositions that not only match but potentially surpass the mechanical properties of the benchmark composition $AlCoCrFeNiZr_{0.008}$ identified within the database. To achieve this goal, a hybrid model was developed by integrating Cuckoo Search

Optimization (CSO) and Non-Dominated Sorting Genetic Algorithm (NSGA-II) in the CBR model.

Cuckoo Search Optimization (CSO)

CSO is a metaheuristic algorithm based on the brood parasitism behavior of cuckoo birds. It strategically lay their eggs in the nests of other host birds. If the host bird detects the presence of alien eggs, it may either discard the foreign eggs or abandon the nest to build a new one. This natural behavior forms the basis of the CSO algorithm, which adeptly balances exploration and exploitation to solve complex optimization problems. The detailed workflow of the CSO process is illustrated in Figure 4.8.

CSO operates by mimicking Lévy flights, a random walk characterized by a series of long jumps, to explore the search space extensively. Simultaneously, it replaces the worst solutions with potentially better ones, thereby refining the solution set. This dual approach enables the CSO to navigate the expansive search space of MPEAs efficiently.

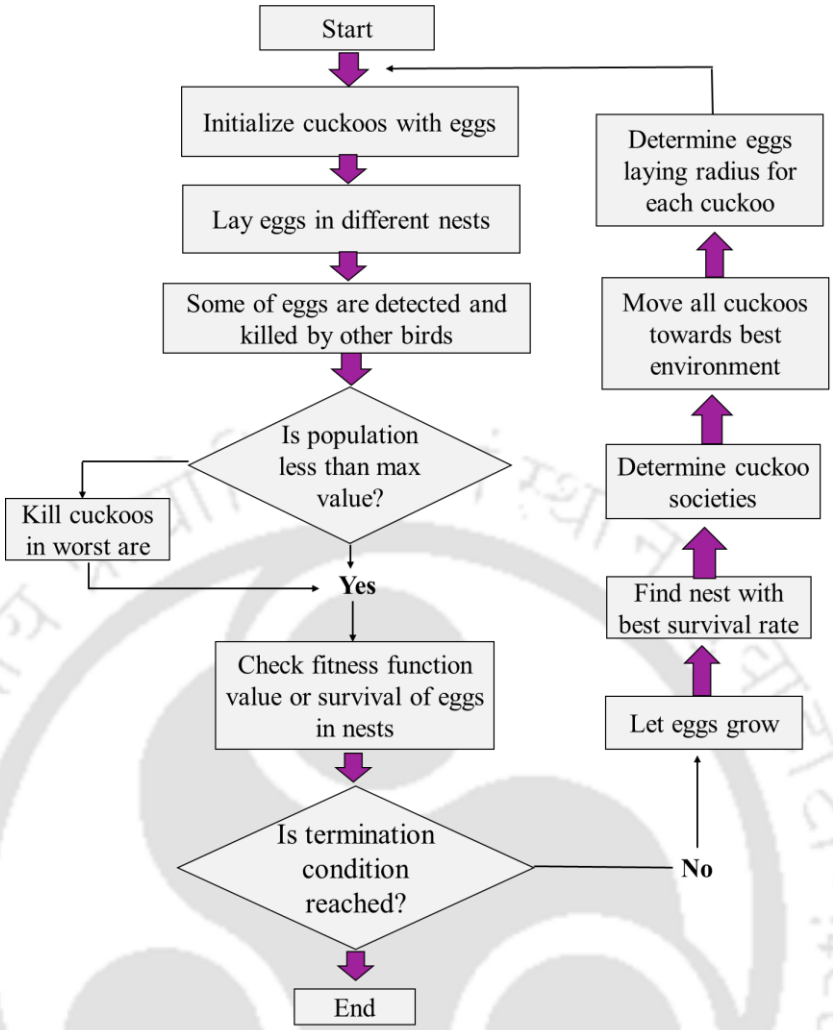

Figure 4.8. Workflow of cuckoo search optimization (CSO)

The compositional space was defined across 13 dimensions (13 elements within the curated database), with each dimension representing a distinct elemental component. To efficiently explore this high-dimensional space, key parameters within the CSO algorithm, including n (population size), α (step size of the Lévy flights), β (Lévy flight distribution), Pa (discovery rate of alien eggs), number of iterations and search space boundary were configured. The choice of CSO is particularly advantageous in this context due to its robustness and effectiveness in handling high-dimensional and nonlinear optimization problems.

Non-Dominated Sorting Genetic Algorithm (NSGA-II)

To navigate alloy compositions that offer the optimal combination of mechanical properties, the Non-Dominated Sorting Genetic Algorithm (NSGA-II) was employed. It is a highly regarded technique in the field of multi-objective optimization. The NSGA-II is particularly effective for problems where multiple objectives must be optimized simultaneously, and it is widely used due

to its ability to identify a diverse set of Pareto-optimal solutions. In the context of multi-objective optimization, the term "non-dominated" refers to solutions that are Pareto-optimal, meaning that no other solution in the search space is superior when all objectives are considered together. These solutions form what is known as the Pareto front, representing the best trade-offs between competing objectives.

NSGA-II improves upon the original NSGA (Non-Dominated Sorting Genetic Algorithm), an evolutionary algorithm designed to find a diverse set of solutions that are Pareto optimal, meaning no other solution is better in all objectives. It uses genetic operators (selection, crossover, mutation) just like other genetic algorithms, but it introduces advanced techniques such as:

(i) **Fast Non-Dominated Sorting**, where individuals in the population are sorted into different "fronts" based on Pareto dominance. The first front is completely non-dominated, the second front is dominated only by the first, and so on. NSGA-II improves the sorting algorithm to **$O(MN^2)$** complexity (where M is the number of objectives, N is population size), which is faster than the original NSGA.

(ii) **Crowding Distance**, which is a measure of solution density around a point. It helps to maintain diversity in the population by favouring solutions in less crowded areas of the front.

(iii) **Elitism** helps retains the best solutions found so far by combining parent and offspring populations (2N size), sorting them, and selecting the top N individuals for the next generation. This ensures better convergence and avoids losing good solutions.

(iv) **Binary Tournament Selection**, where individuals are being chosen based on rank (Pareto front) and crowding distance. If two individuals are in the same front, the one with a higher crowding distance is preferred.

NSGA-II is a faster**,** more efficient, and more robust version of the original NSGA. Its key innovations, such as elitism**,** crowding distance, and fast non-dominated sorting, make it more effective at finding diverse and high-quality Pareto fronts.

4.3.5. Identification and Validation of Pareto-Optimal Solutions

A list of identified Pareto-optimal solutions is presented in Table 4.5. Among these, the composition $Al_{0.84675}Co_{0.84675}Cr_1Fe_{0.9544}Ni_{0.84675}Zr_{0.00677}$ exhibited mechanical properties that closely matched those of the benchmark composition in the database, $AlCoCrFeNiZr_{0.008}$.

Furthermore, two additional compositions, MoNbTiVZr and MoNbTiV0.25Zr, were identified that surpass this benchmark, demonstrating mechanical properties of [YS = 1748 MPa, UTS = 3800 MPa, ε = 23%] and [YS = 1740 MPa, UTS = 3876 MPa, ε = 27%], respectively. Notably, these compositions have been previously reported in the literature but were not included in the original database collected for this study. Their experimentally derived YS, UTS, and elongation values are highlighted in red fonts in Table 4.5. A comparison of reported experimental values with those suggested by our developed ML framework, reveals close agreement for MoNbTiVZr [185] and $MoNbTiV_{0.25}Zr$ [186]. This consistency validates the predictive capability of the present study, and affirms the reliability and effectiveness of the developed framework.

Table 4.5. Identified Pareto-optimal solutions using the developed ML framework

S. No.	Alloy Composition	YS (MPa)	UTS (MPa)	ε (%)
1.	$Al_{0.7262}Co_{0.7785}Cr_{0.8063}Fe_{0.7027}Ni_1Mo_{0.0934}$	1209.976	3629.1116	19.9018
2.	$Al_{0.8225}Cr_1Ni_{0.8225}Zr_{0.4528}$	1229.609	3254.284	29.3906
3.	$AlCr_{0.9583}Fe_{0.675}Ni_{0.9264}Zr_{0.0058}$	1130.77	3158.11	25.85
4.	$Al_{0.84675}Co_{0.84675}Cr_1Fe_{0.9544}Ni_{0.84675}Zr_{0.00677}$	1572	3506.71	29.7
5.	$Al_1Cr_1Cu_{0.00937}Ni_{0.9409}Ti_{0.1028}V_{0.3879}$	1150.3729	2889.0830	27.8307
6.	$Al_1Cr_{0.556}Fe_{0.556}Ni_{0.5215}Ti_{0.2384}$	1226.918	2126.552	23.589
7.	$Al_{0.8247}Fe_{0.9693}Ni_1Zr_{0.0074}$	1017.25	3507.13	28.87
8.	★**$Mo_1Nb_1Ti_1V_1Zr_1$ [185]**	**1748 (1786)**	**3800 [3828]**	**23 [26]**
9.	$Al_{0.9756}Cr_1Fe_{0.8236}Ni_1Zr_{0.00747}$	1110.755	3821.219	29.175
10.	$Al_{0.9328}Co_1Cr_{0.9827}Fe_{0.8769}Zr_{0.0062}$	1043.51	3487.12	29.0895
11.	$Al_{0.9256}Cr_{0.752}Cu_{0.0987}Fe_{0.4703}Ni_1Mn_{0.0567}Ti_{0.1488}Nb_{0.1302}Zr_{0.0071}Mo_{0.0567}$	1087.4859	2693.45	17.719
12.	$Al_{0.9039}Co_1Cr_{0.9363}Fe_{0.9624}Zr_{0.00693}$	1655.31	3378.25	21.688
13.	★**$Mo_1Nb_1Ti_1V_{0.25}Zr_1$ [186]**	**1740 [1776]**	**3876 [3893]**	**27 [30]**
14.	$Al_1Cr_1Fe_{0.7356}Ni_1$	1146.430	3400.346	26.564
15.	$Al_1Co_{0.587}Cr_{0.18028}Ni_{0.767}Mn_{0.1734}V_{0.1802}C_{0.01469}$	1290.797	2580.7718	22.9337

4.4. Summary

This chapter presented a comprehensive, data-driven approach for predicting and optimizing the mechanical properties of MPEAs. The first part of this chapter focuses on predicting yield strength of MPEAs using the MAST-ML toolkit and a curated dataset of 700 experimentally synthesized MPEAs. Within the MAST-ML framework, three tree-based regression algorithms including Decision Trees Regressor (DTR), Random Forest Regressor (RFR) and Extra Trees Regressor (ETR) were employed. Among those three models, ETR demonstrated superior performance, achieving an R^2 score of 0.924, MAE of 0.09, and RMSE of 0.148 on test data. The ETR model also showed strong generalizability, as evidenced by its accurate predictions on unseen MPEA compositions, maintaining an error margin within ±20 MPa.

MAST-ML proved to be effective, particularly for researchers with limited programming experience and its good only for small- to medium-scale datasets in materials science. Currently, the toolkit integrates well with scikit-learn for classical ML tasks, but does not support deep learning, GPU acceleration, and real-time feedback. Additionally, it lacks integration with advanced optimization algorithms, such as metaheuristic approaches, that are essential for exploring vast and complex compositional spaces. Its design is largely batch-mode oriented, with diagnostic plots generated only after execution, limiting opportunities for interactive model refinement or real-time feedback. These limitations, offer clear avenues for future development and extension of the framework.

Building upon the limitations of MAST-ML, the second part of this chapter extend the study to develop a novel framework for multi-objective optimization. A database targeting yield strength (YS), ultimate tensile strength (UTS), and elongation ($\boldsymbol{\mathcal{E}}$), which are key properties often subject to competing trade-offs, was compiled from experimental literature. Various algorithms including Neural Network (NN), Random Forest Regressor (RFR), Extra Trees Regressor (ETR), Cat-Boost Regressor (CBR), and XGBoost Regressor (XGB) were employed for predicting the properties. Among all, CBR performed the best with highest R^2 score of 0.91, and the lowest MSE of 0.07 and MAE of 0.16, thus, CBR was selected for subsequently optimizing these three properties simultaneously.

A hybrid framework integrating CBR with Cuckoo Search Optimization (CSO) and the Non-Dominated Sorting Genetic Algorithm II (NSGA-II) was implemented for multi-objective optimization, where the objective was to explore the vast compositional space defined across 13 dimensions to find Pareto-optimal solutions. This newly developed approach successfully

identified several novel alloy compositions, including candidates that not only matched but surpassed the mechanical performance of the best-known benchmark alloy ($AlCoCrFeNiZr_{0.008}$) in the collected database. Notably, two compositions namely, MoNbTiVZr and $MoNbTiV_{0.25}Zr$ was utilized to validate the predictions of developed framework. The mechanical properties suggested via our developed framework was found in close agreement with their reported experimental values, thus validating the robustness of developed framework. This research underscores the potential of integrating ML models with metaheuristic optimization techniques to explore the vast compositional space of MPEAs, providing a reliable method for identifying alloys with superior mechanical properties. These findings not only demonstrate the effectiveness of our approach but also lay the groundwork for future experimental validation.

Building on the prediction and multi-objective optimization of mechanical properties, the subsequent focus of this research is directed toward minimizing reliance on critical raw materials (CRMs) or critical and strategic raw materials (C&SRMs) in the design of MPEAs through a dual strategy. The first approach establishes a hybrid ML–metaheuristic optimization framework that leverages ML-guided chemical tuning to systematically identify and design CRM-free or CRM-lean alloys without compromising mechanical performance. Complementing this, the second approach investigates strain engineering as a non-ML-based physical design strategy, drawing on theoretical analysis of literature evidence to evaluate its potential in enhancing mechanical properties while reducing dependence on C&SRMs. Together, these two complementary approaches aim to address challenges of material cost, supply risk, and long-term sustainability, thereby advancing the development of resource-efficient alloys aligned with Net Zero objectives.

Chapter 5

Design and Development of Critical Raw Materials (CRMs)-Free MPEAs Using ML Framework

5.1. Motivation to Reduce Reliance on Critical Raw Materials (CRMs)

Various refractory HEAs (RHEAs) such as NbMoTaW [124], $Ti_xNbMoTaW$ (x = 0, 0.25, 0.5, 0.75, 1) [124] $V_xNbMoTa$ (x = 0.25, 0.5, 0.75, 1.0) [125], $Nb_{40}Ti_{25}Al_{15}V_{10}Ta_5Hf_3W_2$ [126], $NbMoTaW(HfN)_x$ (x = 0, 0.3, 0.7, 1.0) [127], MoNbTaVW [128], HfNbTaZr [128], $Re_{0.1}Hf_{0.25}NbTaW_{0.4}$ [129]], along with several 3d transition metal HEAs such as $Al_{10.3}Co_{17}Cr_{7.5}Fe_9Ni_{48.6}Ti_{5.8}Ta_{0.6}Mo_{0.8}W_{0.4}$ [130], $Al_{10.2}Co_{16.9}Cr_{7.4}Fe_{8.9}Ni_{47.9}Ti_{5.8}Mo_{0.9}Nb_{1.2}W_{0.4}C_{0.4}$ [131] have been developed for high-temperature applications in aerospace, gas turbine, and nuclear power plants. Other MPEAs such as $CoCrFeNiTa_x$ (x = 0, 0.1, 0.2, 0.3, 0.4, 0.5, and 0.75) [132], $CoCrFeNiNb_x$ (x = 0, 0.103, 0.155, 0.206, 0.309 and 0.412) [133], and $CoCrFeNiNb_x$ (x = 0.1, 0.25, 0.5 and 0.8) [134] have also shown a remarkable combination of high strength and ductility, particularly in their eutectic counterparts such as $CoCrFeNiTa_{0.4}$ and $CrFeCoNiNb_{0.5}$. However, it is noticeable that these alloys are heavily reliant on the use of critical raw materials (CRMs) such as Ta, W, Nb and Hf [136].

Thus far, no efforts in the MPEA literature have been directed toward reducing or eliminating CRMs during alloy development. Rizzo et al. [136] emphasized the importance of ensuring a flawless supply chain of raw materials to maintain a sustainable circular economy. Therefore, the exigency of minimizing or completely eliminating the use of CRMs in the design of novel alloys is essential, not only to mitigate the excess of imports and curb the need for excessive mining, but also to accelerate the transition toward Net Zero goals. This forms the central focus of this chapter.

This chapter introduces a ML-based framework to design novel multicomponent alloy compositions, meticulously crafted to eliminate Critical Raw Materials (CRMs) while achieving hardness levels comparable to, or even surpassing, those of CRM-heavy MPEAs. Various metaheuristic optimization methods were explored to accomplish this goal.

5.2. Theoretical Background of Critical Raw Materials (CRMs)

5.2.1. Definition of CRMs

The modern pursuit of clean energy, digital innovation, and advanced manufacturing has rendered certain raw materials indispensable. Referred to as Critical Raw Materials (CRMs), elements such as tantalum (Ta), tungsten (W), niobium (Nb), hafnium (Hf), and others are vital to advanced technologies due to their unique properties. However, their supply is increasingly constrained by geopolitical, economic, and environmental factors [137]. Rizzo et al. emphasized the importance of maintaining a flawless raw material supply chain to support a sustainable circular economy [136]. Thus, CRMs are characterized by their technological importance, high supply risk, and the urgency to reduce their usage through limiting import dependency and minimizing excessive mining.

5.2.2. Classification of CRMs

Since 2011, the European Commission has published and regularly updated a list of CRMs every three years to support strategic planning and resource security within the European Union (EU). The classification of CRMs is a key distinction in the realization of this research. Accordingly, materials identified as critical in both past and recent reports were compiled and categorized into three groups, based on the frequency and continuity of their appearance on the CRM list. Figure 5.1, presents an overview of the materials listed in these reports from 2011 to 2023.

CRMs that appeared three or more times on the EU's critical materials list and remain a current concern were classified as 1st Tier. This category includes highly critical elements such as Be, Bi, Co, Ga, Ge, Hf, Mg, Nb, Sb, Sc, Si (metal), Ta, V and W. The 2nd Tier CRMs comprise elements such as Al, Cu, He, Li, Mn, Ni, P, Sr, and Ti, which have appeared more than once in recent listings but with less historical consistency. Elements such as Cr and In, excluded from the 2023 CRM list, were not considered critical (non-CRMs) in the context of this study.

Materials / Years	Al	Be	Bi	Co	Cr	Cu	Ga	Ge	He	Hf	In	Li	Mg	Mn	Nb	Ni	P	Sb	Sc	Sr	Si Metal	Ta	Ti	V	W
2011																									
2014																									
2017																									
2020																									
2023																									

Severity scale

1st Tier CRM	Appeared =>3 consecutive times and is of current concern
2nd Tier CRM	Appeared 1-2 times lately as CRM
Non-CRMs	Not recognised as CRM as of 2023

Figure 5.1. Severity scale of materials listed in category of CRMs by EU [187] [188] [189] [190] [191]

5.2.3. Attempts to Recover CRMs

Despite cobalt's inclusion in the 1st tier CRM category, its production is not a concern. The Democratic Republic of Congo (DRC) is the world's largest producer of Co, with its production projected to increase from 11,000 MT in the year 2000 to 98,000 MT by 2020 [192]. However, the market of Co presents a considerable risk due to supply chain complexities. China, which has limited domestic cobalt production has significantly increased its imports from the Democratic Republic of the Congo (DRC) and controls cobalt processing in the region through various Chinese firms. This initiative by China was aimed at securing a competitive advantage in regulating the electric vehicle market.

A potential remedy here would be to recover Co from waste batteries. Suriyanarayanan et al. [193] recently introduced an innovative and efficient approach for Co extraction with an extraction efficiency >97%, using a nonionic deep eutectic solvent (ni-DES) comprised of N-methylurea and acetamide. Zhang et al. [194] developed a supercritical fluid extraction process using supercritical CO_2 solvent with tributyl phosphate–nitric acid and hydrogen peroxide adduct to recover Li, Co, Mn and Ni with a 90% extraction efficiency. Moreover, Yang et al. [195] in 2024 estimated the sales volume of new energy passenger vehicle (NEPV) from 2023 to 2035 based on the historical NEPV sales data from 2013 to 2022. Utilizing Weibull distribution to analyze different sales scenarios, they estimated the potential of recycling Co for maintaining a balance between supply and demand. Their analysis predicted the peak potential of recycling of Co to be about 0.167 MT with an economic value ranging from 49.01 billion to 94.60 billion Chinese Yuan in 2035. Consequently, they concluded that recycling of Co is necessary to alleviate the supply risk pressure and taking the Co off of the CRM list.

Similarly, Petranikova at al. [196] summarized the efforts in the recovery of Vanadium by selecting more sustainable technologies with lower generation of harmful by-products. They highlighted the importance of combining hydrometallurgical and pyrometallurgical approaches to increase the material recovery rates. With ongoing strategic advancements in recovery and recycling, Cobalt (Co) and Vanadium (V) are expected to transition from their current status as CRMs to non-CRMs. As these management methods evolve, the associated risks related to these materials are anticipated to gradually decrease.

5.3. ML Framework Developed for Reducing Reliance on CRMs

Present chapter follows a systematic flow to design novel reduced CRM (CRM-lean) or CRM-free MPEAs, as demonstrated in Figure 5.2. Detailed description is provided in each respective section.

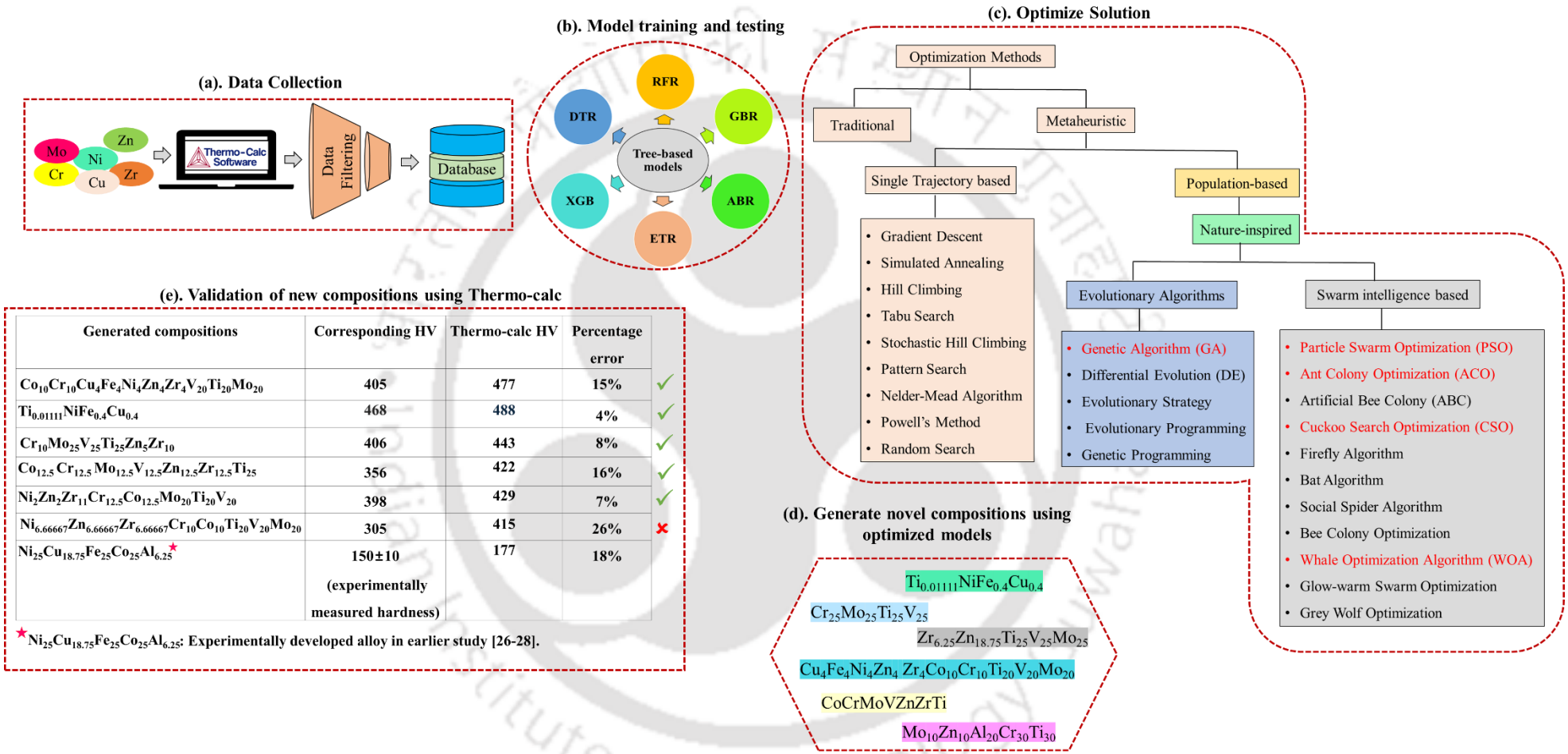

(e). Validation of new compositions using Thermo-calc

Generated compositions	Corresponding HV	Thermo-calc HV	Percentage error	
$Co_{10}Cr_{10}Cu_4Fe_4Ni_4Zn_4Zr_4V_{20}Ti_{20}Mo_{20}$	405	477	15%	✓
$Ti_{0.01111}NiFe_{0.4}Cu_{0.4}$	468	488	4%	✓
$Cr_{10}Mo_{25}V_{25}Ti_{25}Zn_5Zr_{10}$	406	443	8%	✓
$Co_{12.5}Cr_{12.5}Mo_{12.5}V_{12.5}Zn_{12.5}Zr_{12.5}Ti_{25}$	356	422	16%	✓
$Ni_2Zn_2Zr_{11}Cr_{12.5}Co_{12.5}Mo_{20}Ti_{20}V_{20}$	398	429	7%	✓
$Ni_{6.66667}Zn_{6.66667}Zr_{6.66667}Cr_{10}Co_{10}Ti_{20}V_{20}Mo_{20}$	305	415	26%	✗
$Ni_{25}Cu_{18.75}Fe_{25}Co_{25}Al_{6.25}$★	150±10 (experimentally measured hardness)	177	18%	

★$Ni_{25}Cu_{18.75}Fe_{25}Co_{25}Al_{6.25}$: Experimentally developed alloy in earlier study [26-28].

Figure 5.2. Workflow of present study

5.4. Data Collection

As noticed earlier, various MPEAs have been developed by utilizing elements such as Al, Cu, Cr, Ti, V, W, Ta, Hf, Nb, Mo, Zn, Zr, Si extensively, while certain precious metal HEAs incorporate elements such as Ag, Pt, Au, Ru, Rh, Pd and many of these elements (Hf, Nb, Ta, Pt, Pd, Ru, Rh, W) have been marked as critical and have reached an alarming stage [135]. Consequently, when considering MPEAs comprised solely of non-CRMs elements, the available experimental data in the literature is scarce which limits the training and testing of the machine learning models. Therefore, a fresh database has been extracted using Thermo-Calc 2024a software, which is based on a CALculation of PHAse Diagram (CALPHAD) approach.

In recent years, CALPHAD has played a crucial role in designing transition alloys from a completely serendipitous process to a well-established method seeking a thermodynamic rationale [123]. CALPHAD has been extensively utilized in literature for phase prediction and rapid screening of potential alloys by estimating their compositional and microstructural properties which are validated experimentally [123, 197]. However, no study can be seen in the literature with a focus on mechanical property prediction solely from the CALPHAD method. This is because predicting mechanical properties is not as straightforward as phase prediction. Phase prediction relies solely on the Gibbs free energy for lower-order compositions. For more complex or higher-order compositions, phases are predicted by extrapolating Gibbs free energy from the lower-order systems [198]. Unlike phase prediction, mechanical property prediction requires rigorous research into the manufacturing (processing) routes, processing parameters, post-processing treatments, testing parameters and extensive knowledge or expertise in the field. Thermo-Calc 2024a offers a property model calculator, which allows the prediction of yield strength and hardness of a composition based on the phases present at a particular temperature [199].

Currently, Thermo-Calc does not account for factors such as processing history, parameters, time and other crucial variables for accurately predicting mechanical properties under specific experimental conditions. However, its hardness prediction tool still provides a solid foundation for making informed estimations, hence the hardness prediction tool was utilized to collect database for this study. But first the Vickers hardness of various alloys, including medium- and high-entropy alloys, were extracted from experimental literature across different processing methods (casting, additive manufacturing, powder metallurgy, rolling, and severe plastic

deformation techniques such as High-Pressure Torsion (HPT) and Equal Channel Angular Pressing (ECAP)). These were then compared to Thermo-Calc predictions for respective alloys, as shown in Figure 5.3. This was done to assess the discrepancy between experimentally obtained hardness and Thermo-Calc predictions.

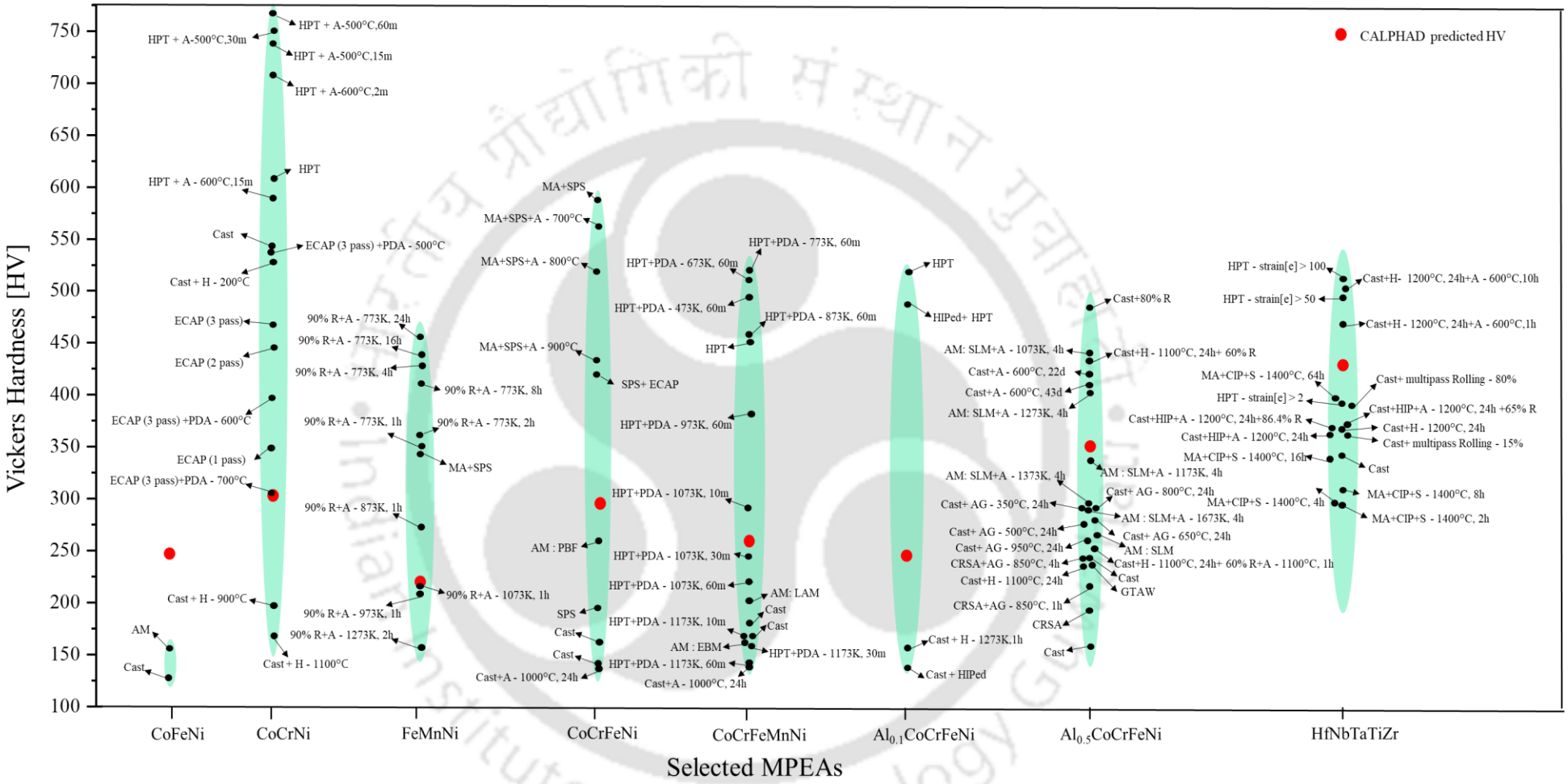

A: Annealing; AM: Additive Manufactured; AG: Aging; CIP: Cold isostatically pressing; CRSA: Casting+70% R +A-1200°C, 1h + Water quenching; d: days; EBM: Electron Beam melting; ECAP: Equal Channel Angular Pressing, GTAW: Gas-tungsten-arc-welding; H: Homogenization; HIP: Hot isostatic pressing; h: hours; High Pressure Torsion; LAM: Laser additive manufacturing; MA: Mechanical Alloying; PBF : Powder bed fusion; PDA: Post deformation annealing; R: Rolling; S:Sintering; SPS: Spark plasma sintering; SLM: Selective Laser Melting

Figure 5.3. Vickers hardness comparison for selective MPEAs based on the experimental results obtained from various manufacturing methods (black dots) vs. CALPHAD predicted values (in red dots)

A detailed comparison is provided in tabular form in Supplementary 5s. Thermo-Calc predictions were observed to be insensitive to the strain rate applied during the manufacturing process which can lead to different hardness values based on the manufacturing process. For a few compositions, the CALPHAD hardness value matched the experimental values, however, it is difficult to generalize which experiments led to the values that are closest to the CALPHAD predictions. For instance, the hardness values obtained from CALPHAD for CoCrNi match with the ECAP processed (for 3 passes) and post-deformation annealed (at 700 °C) samples. As for the FeMnNi medium entropy alloy, its CALPHAD value was closest to the alloy processed via rolling (90% rolled) and then annealed at 1073 K for 1 h (see Figure 5.3). Thus, generalizing which experimental processing route leads to hardness values that closely match those predicted by CALPHAD is arduous.

Database Prepared Using Thermo-Calc 2024a for Present Study

A large dataset comprising 3,608 instances with Vickers hardness values for unary and binary element-based compositions was computationally generated using the TCHEA7 database and the property model calculator in Thermo-Calc 2024a (Version 2024.1.132110-55). The dataset focuses on compositions containing the elements Al, Cr, Cu, Co, Fe, Ni, Ti, V, Mo, Mn, Sn, Zn and Zr. An exception was made while collecting data, as Co and V have also been included, which are although classed as 1st Tier CRMs were not treated as critical. This is due to the ongoing advances made in the recovery and recycling methods, moreover, its production is not a concern, and it is expected that the Co and V will become non-critical over time [193-195] [196]. Henceforth, Co and V were considered as non-CRM for the current investigation and included them in the database for current investigation. A total of 3,608 instances were recorded and no experimental data was incorporated to keep the database free from experimental uncertainty arising from the manufacturing process.

While extracting the data, it was observed that the property predictor module relies on certain assumptions. Those assumptions are as follows: (i) the material is homogeneous i.e., with no imperfections or defects (ii) it considers only local equilibrium and neglects long-range diffusion. Therefore, to calculate the mechanical properties, it uses simplified theoretical models and databases (containing thermodynamic and kinetic data), which do not capture the complexities related to processing (as-cast, heat-treated, homogenized, or severely deformed samples) and testing conditions (the amount of load and time required in hardness testing). Thermo-Calc predictions can therefore be expected to carry a certain percentage of error when compared to the experimentally synthesized specimen based on its processing history.

For determining the hardness value of a particular composition using Thermo-Calc, the phases present in the system were first identified using their corresponding phase diagram observed at a range of temperatures, computed using an equilibrium calculator. Based on the available features within the software, by considering the system size of 1 mol at a temperature of 300 K and 1 bar pressure, the hardness value was estimated. In some cases, the identified phases in the phase diagram could not be marked while calculating Vickers hardness due to their unavailability in the property model calculator, highlighting one of the several limitations of Thermo-Calc 2024a that needs to be improved.

Consequently, a total of 3,608 instances of different compositions were extracted. This database contains only compositional information and the hardness value of each instance. The highest hardness value obtained was in the range of 400–405 HV. Some of the interesting compositions with higher Vickers hardness values in the database were $Cr_{42}Ti_{58}$, $Ti_{74}Zn_{26}$, $Ni_{24}Ti_{76}$, $Cu_{16}Ti_{84}$ with a hardness value of 405HV, 404 HV, 403 HV and 402 HV respectively.

5.5. Data Processing

The compiled database was first carefully examined to remove duplicate entries. After cleaning, the final dataset was prepared for machine learning implementation. To facilitate model training and performance assessment, the dataset was partitioned into two subsets: 80% (2,886 instances) for training and model development, and 20% (722 instances) for evaluation and independent verification.

5.6. Description of Utilized ML Algorithms

Various tree-based regression algorithms such as Decision Tree Regressor (DTR), Random Forest Regressor (RFR), AdaBoost Regressor (ABR), Gradient Boost Regressor (GBR), XGBoost Regressor (XGBR) and Extra Tree Regressor (ETR) were employed. While some of these algorithms have been introduced in earlier chapters, their complete workflow has also been demonstrated in this chapter for clarity.

5.6.1. Decision Tree Regressor (DTR)

Decision tree is one tree structure which is based on if-else loop. The workflow of DTR is shown in Figure 5.4. A detailed description about DTR has already been discussed in Chapter 3 and 4.

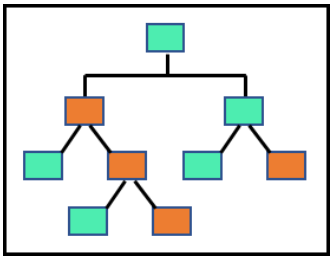

Figure 5.4. Workflow of Decision Tree Regressor

5.6.2. Random Forest Regressor (RFR)

RFR is an ensemble of various decision tree, based on bagging technique, where each tree is trained on a random subset of data and random subset of features. The final prediction is obtained by taking the average of predictions of each individual tree. The workflow of RFR is shown in Figure 5.5.

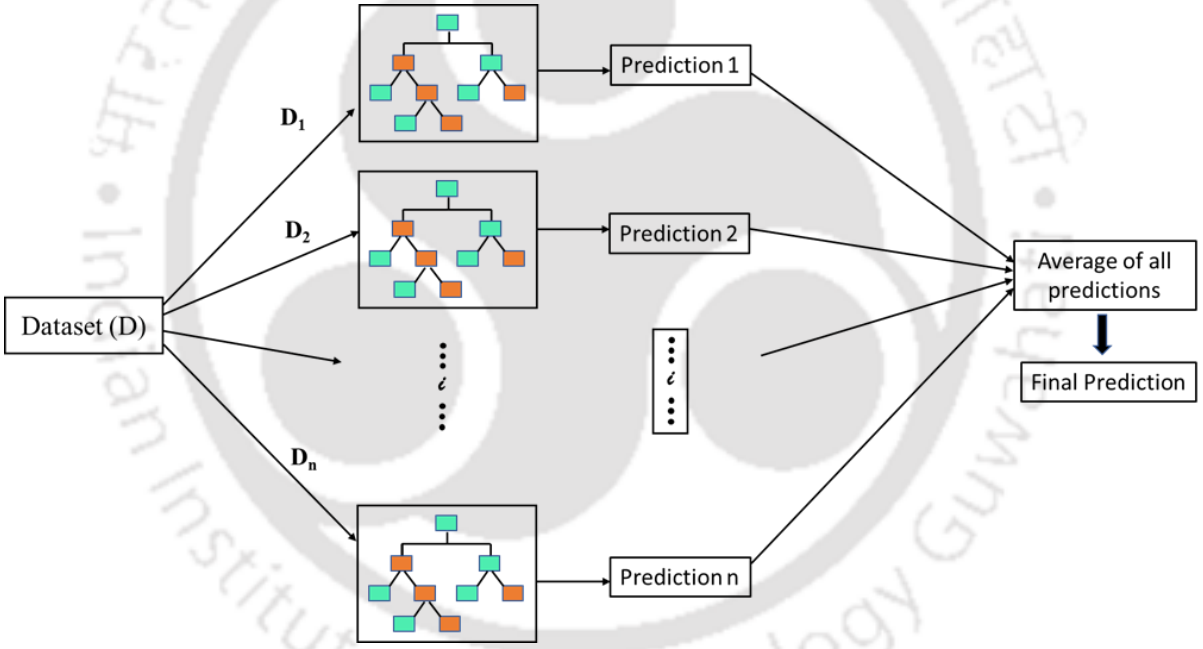

Figure 5.5. Workflow of Random Forest Regressor

5.6.3. Gradient Boosting Regressor (GBR)

GBR is also an ensemble of various decision tree, but it is based on boosting method. It combines multiple weak learners (typically decision trees) and build them sequentially where each subsequent tree tries to rectify the errors made by previous tree, thus create a robust predictive model. The workflow of GBR is shown in Figure 5.6.

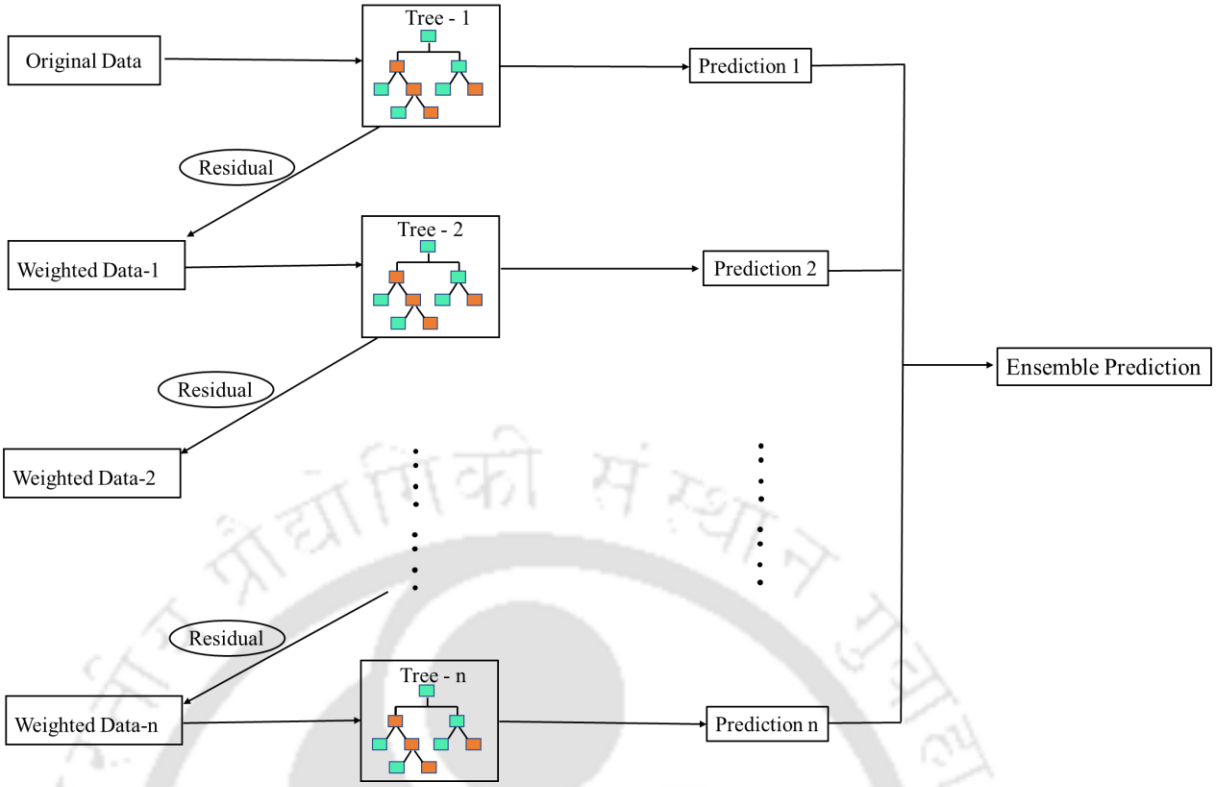

Figure 5.6. Workflow of Gradient Boosting Regressor

5.6.4. XGBoost Regressor (XGBR)

XGBoost (Extreme Gradient Boosting) is an optimized implementation of Gradient Boosting, which incorporates additional regularization, parallel processing and tree pruning. It is highly efficient and perform better compared to traditional Gradient Boosting. The workflow of XGBR is shown in Figure 5.7.

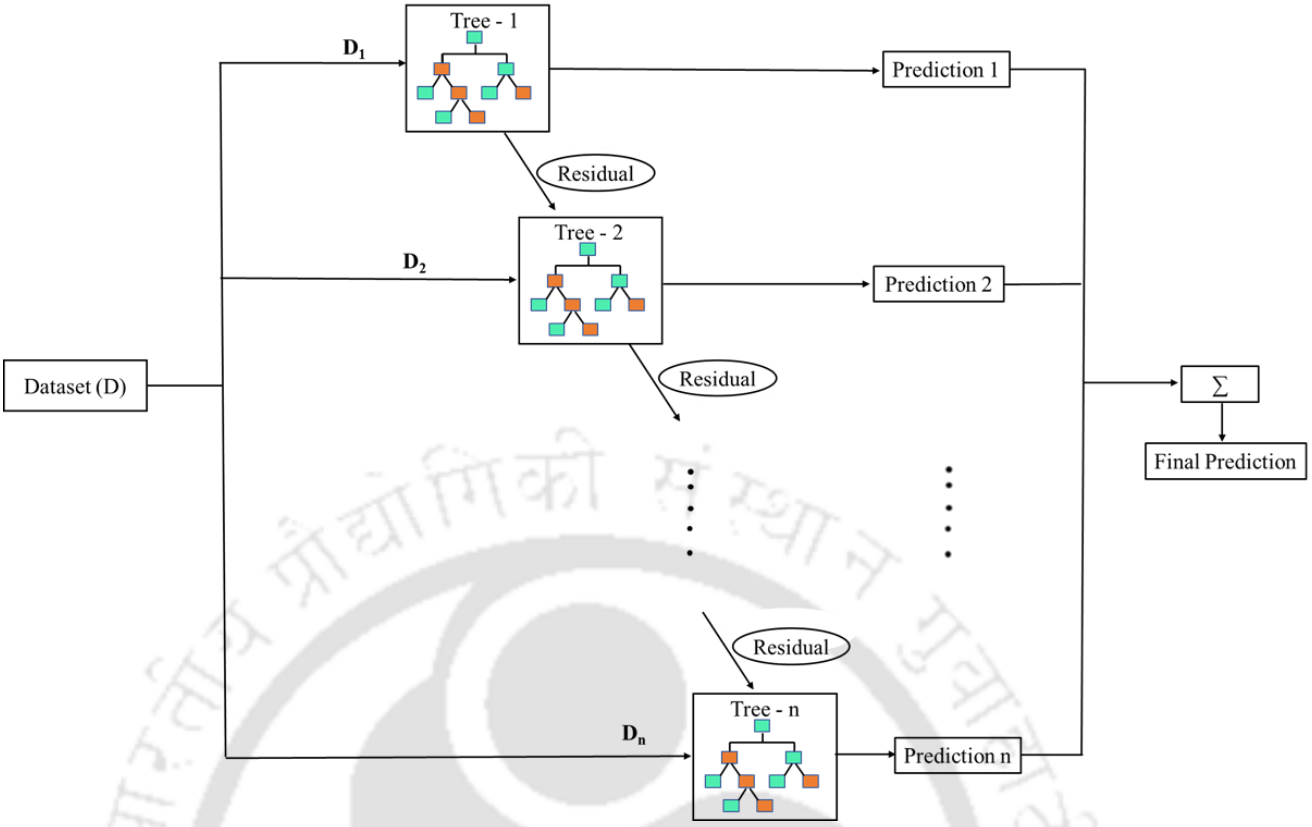

Figure 5.7. Workflow of XGBoost Regressor

5.6.5. AdaBoost Regressor (ABR)

ABR is also an ensemble learning algorithm that typically employs decision stumps, which are decision trees with a single split (one node and two leaves) as its weak learners, although deeper trees can also be used. In contrast, Random Forest (RF) constructs an ensemble of multiple decision trees of varying depths, each trained on random subsets of data and features. The workflow of ABR is illustrated in Figure 5.8.

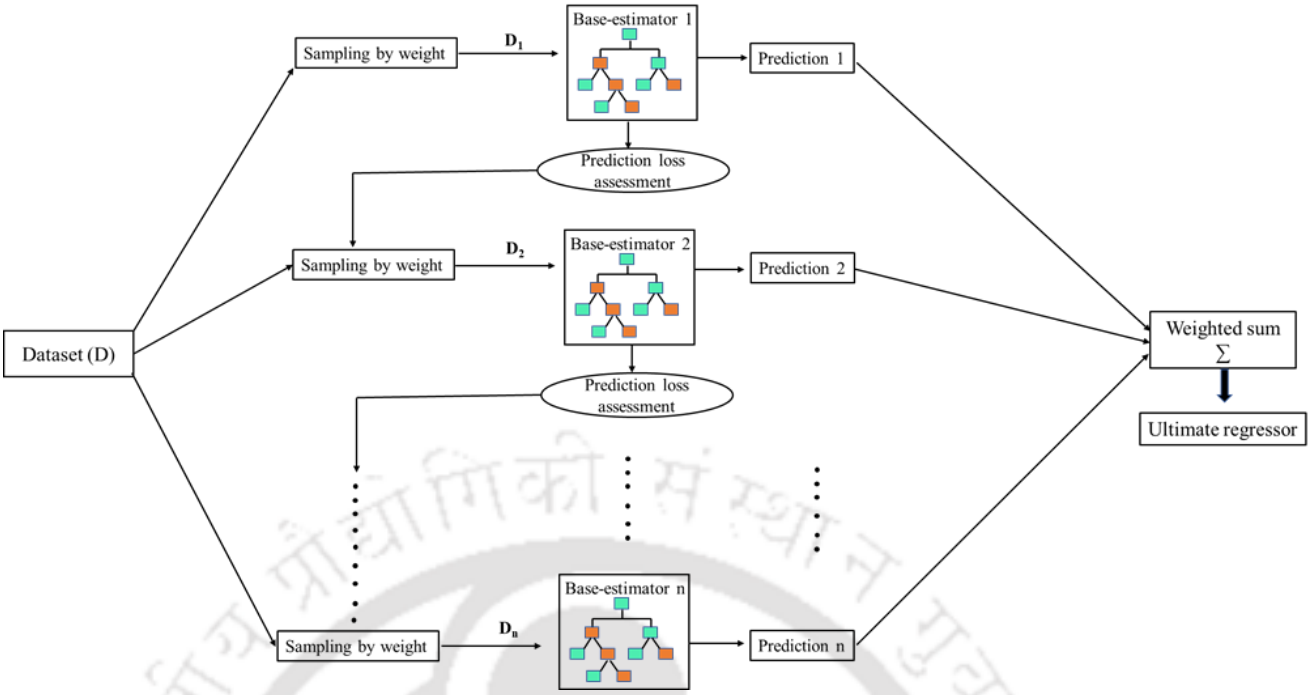

Figure 5.8. Workflow of AdaBoost Regressor

5.6.6. Extra Trees Regressor (ETR)

ETR also known as Extremely Randomized trees is an ensemble of various decision trees. It is quite similar to RFR as based on bagging method except for the random selection of split values. The workflow of ETR is shown in Figure 5.9.

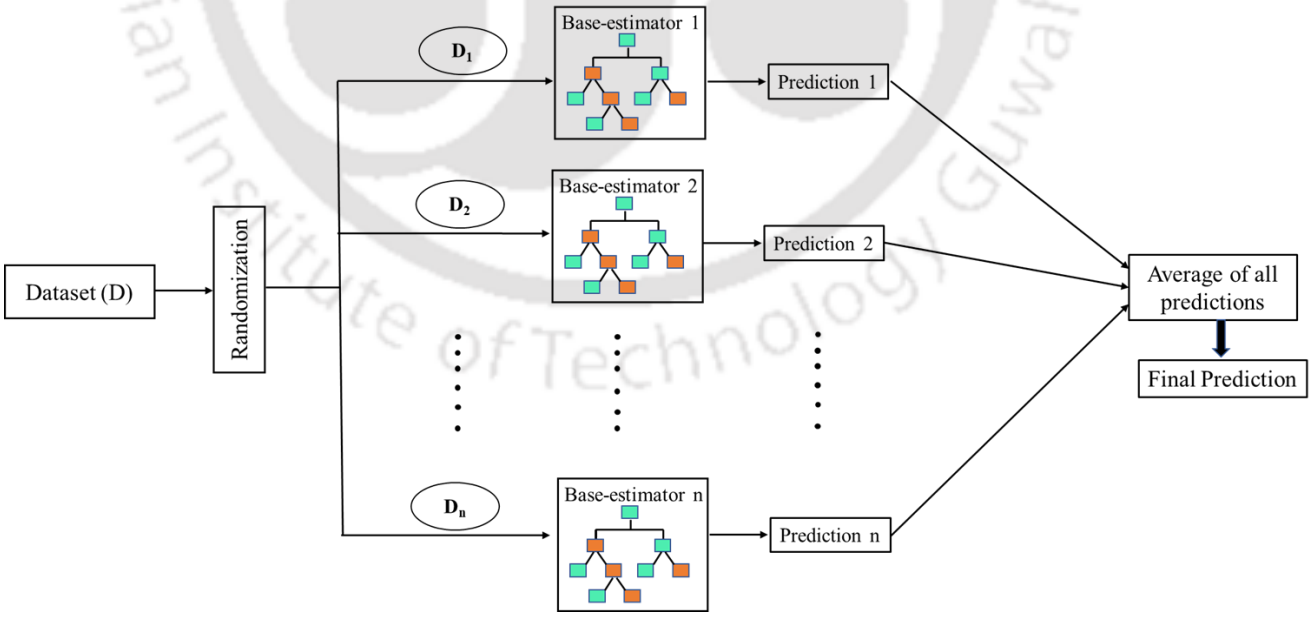

Figure 5.9. Workflow of Extra Trees Regressor

5.7. Hyperparameter Tuning of Utilized Algorithms

The performance of a ML model is influenced by its hyperparameters, which are adjustable settings that govern various aspects of the model's learning process, such as complexity, regularization, and convergence. Examples of hyperparameters include the maximum depth of trees in decision tree models, the number of trees in ensemble models like Random Forest and Gradient Boost, as well as the number of hidden layers in neural networks and the penalty term used in support vector machines. Proper tuning of these hyperparameters is essential for achieving an optimal balance between model accuracy and generalization.

To optimize the hyperparameters of the selected algorithms, Random Search CV was employed. Unlike Grid Search, which systematically evaluates all possible combinations of hyperparameter values, Random Search, samples a fixed number of hyperparameter combinations from a defined distribution. This approach significantly reduces computational costs while still allowing the exploration of a diverse range of values, making it particularly advantageous for complex models with many hyperparameters.

Each hyperparameter configuration was evaluated using a 5-fold cross-validation approach, where the dataset was divided into five subsets. Each subset was used once as a validation set while the others served as the training set, ensuring a thorough and unbiased assessment of the model's generalization capabilities.

The optimized hyperparameters for each regressor model are listed in Table 5.1. This methodology helped in identifying the best-performing hyperparameter settings, ensuring that the model would perform consistently across different data splits.

Table 5.1. Summary of the optimized hyperparameters for the chosen ML algorithms

Regression algorithm	**Hyperparameters**
Decision Tree Regressor (DTR)	min_samples_split: 4; min_sample_leaf: 3; max_features: None
Random Forest Regressor (RFR)	n_estimators: 651; min_samples_split: 2; min_sample_leaf: 1; max_depth: 70; bootstrap: True

	max_features: 'sqrt'
Gradient Boost Regressor (GBR)	Subsample: 0.97; n_estimators: 609; min_samples_split: 9; min_sample_leaf: 3; max_depth: 8; learning_rate: 0.042 max_features: 'log2'
AdaBoost Regressor (ABR)	learning_rate: 0.78; loss: linear; n_estimators: 280
XGBoost (XGB)	colsample_bytree: 0.87; gamma: 4.7; learning_rate: 0.22; max_depth: 7; min_child_weight: 5; n_estimators: 1738; subsample: 0.94
Extra Trees Regressor (ETR)	n_estimators: 1301; min_samples_split: 4; min_sample_leaf: 1; max_depth: None; bootstrap: False max_features: 'log2'

5.8. Performance Evaluation of Developed ML Models

The performance of each developed model was evaluated based on the coefficient of determination (R^2 score), mean absolute error (MAE), root mean squared error (RMSE), and mean absolute percentage error (MAPE), as detailed in Equation 5.1 to 5.4. These performance indicators were used to quantify the difference between predicted values and observed outcomes.

$$R^2\_score = \frac{\sum(y_i - \hat{y}_i)^2}{\sum(y_i - \mu)^2} \quad (5.1)$$

$$\text{MAPE} = \frac{1}{n}\sum_{i=1}^{n}\frac{|(y_i - \hat{y}_i)|}{(y_i)} \quad (5.2)$$

$$\text{MAE} = \frac{1}{n}\sum_{i=1}^{n}|y_i - \hat{y}_i| \quad (5.3)$$

$$\text{RMSE} = \sqrt{\frac{1}{n}\sum_{i=1}^{n}(y_i - \hat{y}_i)^2} \quad (5.4)$$

The results obtained from various regression models are presented in Figure 5.10 (a). The Extra Trees Regressor (ETR) demonstrated a superior performance and achieved an R^2 score of 0.82 and Mean Absolute Percentage Error (MAPE) of 0.17 (see the scatter plot in Figure 5.10 (b)), utilizing optimized hyperparameters determined through Random Search Cross-Validation.

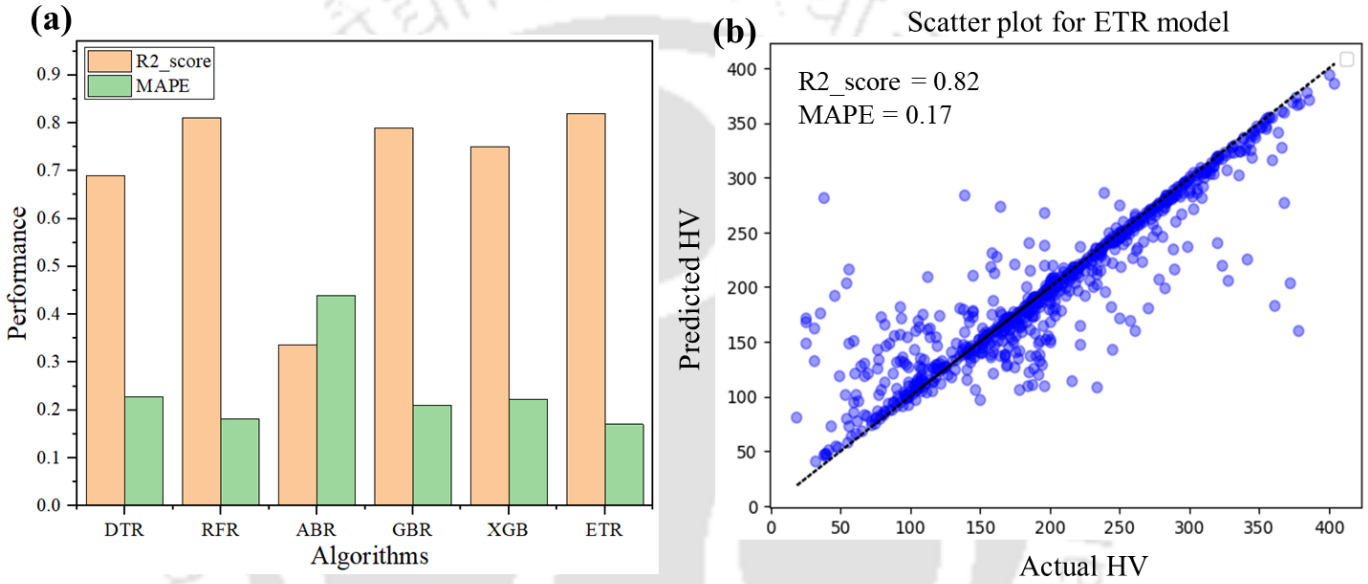

Figure 5.10. (a) Performance of various tree-based ML models: R2_score (in light orange), MAPE (in green), (b) actual vs. predicted hardness of test data for the ETR model

It is important to note that while several studies report even higher R^2 scores, those models typically incorporate numerous descriptors, such as atomic size difference (δ), electronegativity difference (Δχ), valence electron concentration (VEC), mixing enthalpy (ΔHmix), mixing entropy (ΔSmix), melting temperature (ΔT_m), Young's modulus (E), shear modulus (G), differences in shear modulus (δG), lattice distortion energy (μ), the Peierls-Nabarro factor (F), and other parameters (Ω-parameter, ϕ-parameter, and γ-parameter), which together enhance performance metrics. In contrast, this approach relies solely on compositional information and hardness values, achieving an R^2 score of 0.82. This underscores the model's robustness to predict hardness values without requiring any additional descriptors.

Among all the ML models evaluated, ETR demonstrated the superior performance across

the selected evaluation metrics. Owing to its predictive robustness, ETR was selected as the primary model for the subsequent stage of this study, i.e., the exploration of novel alloy compositions using metaheuristic optimization techniques. The details of compositional space defined for the curated dataset are presented in the subsequent section.

Compositional Space for the curated database

The compositional space of the curated database encompasses nearly 8,008 possible compositions (see Figure 5.11) as per combination theory while considering only ternary to decenary-based compositions derived from 13 elements. This space served as the search domain for evaluating the performance of optimization techniques in conjunction with the ETR model. Various metaheuristic optimization algorithms utilized to explore this compositional space is discussed below.

Possible compositions from 13 elements, while considering ternary to decenary based compositions, using combination theory formula:

C (n, k) = n! / (k! * (n-k)!)

C (13, 3) = 286,

C (13, 4) = 715,

C (13, 5) = 1287,

C (13, 6) = 1716,

C (13, 7) = 1716,

C (13, 8) = 1287,

C (13, 9) = 715,

C (13, 10) = 286.

Total sum of all combinations = 8,008 possible combinations.

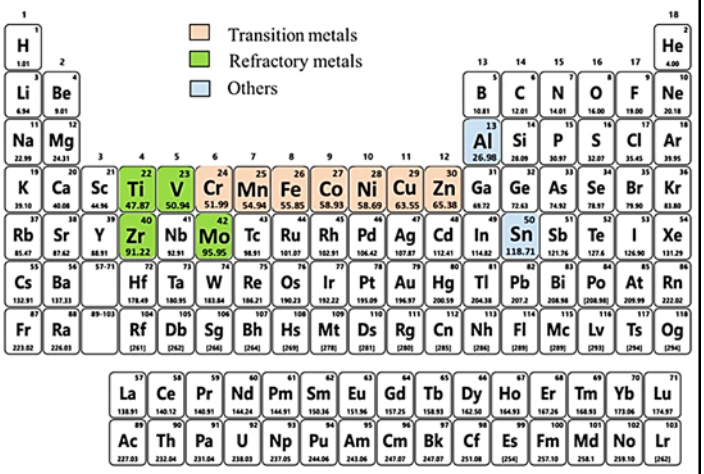

Figure 5.11. Total possible compositions from selected 13 elements

5.9. Need for Utilizing Optimization Methods

The vast compositional space of nearly 8,008 possible compositions presents not only an enormous opportunity for the development of novel materials but also a significant challenge in terms of efficient exploration. In particular, when the objective is to design alloys free of CRMs, the search becomes even more constrained, as compositions must both avoid elements with high supply risk and retain desirable mechanical performance. This necessitates the adoption of advanced optimization techniques capable of systematically navigating the large design space to identify promising candidates.

5.10. Types of Optimization Methods

The classification of various optimization methods is shown in Figure 5.12, with red fonts highlighting the algorithms used in this investigation. Traditional optimization techniques, which include general methods and non-general or specified methods tailored for specific types of problems, have certain limitations such as the requirement of the objective function to be differentiable and lack of ability to obtain a globally optimum solution. Some of the popular traditional optimization techniques such as Newton Raphson, Successive Quadratic Programming algorithm, Steepest Descent Algorithm, Stochastic Newton optimization method and Sequential Unconstrained Minimization technique [200] [201] are well known.

Recently, some non-traditional methods of optimization popularly known as meta-heuristic optimization techniques have gained increasing popularity in solving complex problems. The term metaheuristic combines meta and heuristic, both originated from Greek. Meta symbolizes higher or beyond, and heuristic signifies intelligent guesswork based on past experience or intuitive solution of a problem. Therefore, metaheuristic optimization can be considered as something beyond intuitive, combined with certain mathematical rules or higher-level frameworks. It can broadly be classified into two categories: single trajectory-based and population-based optimization as shown in Figure 5.12.

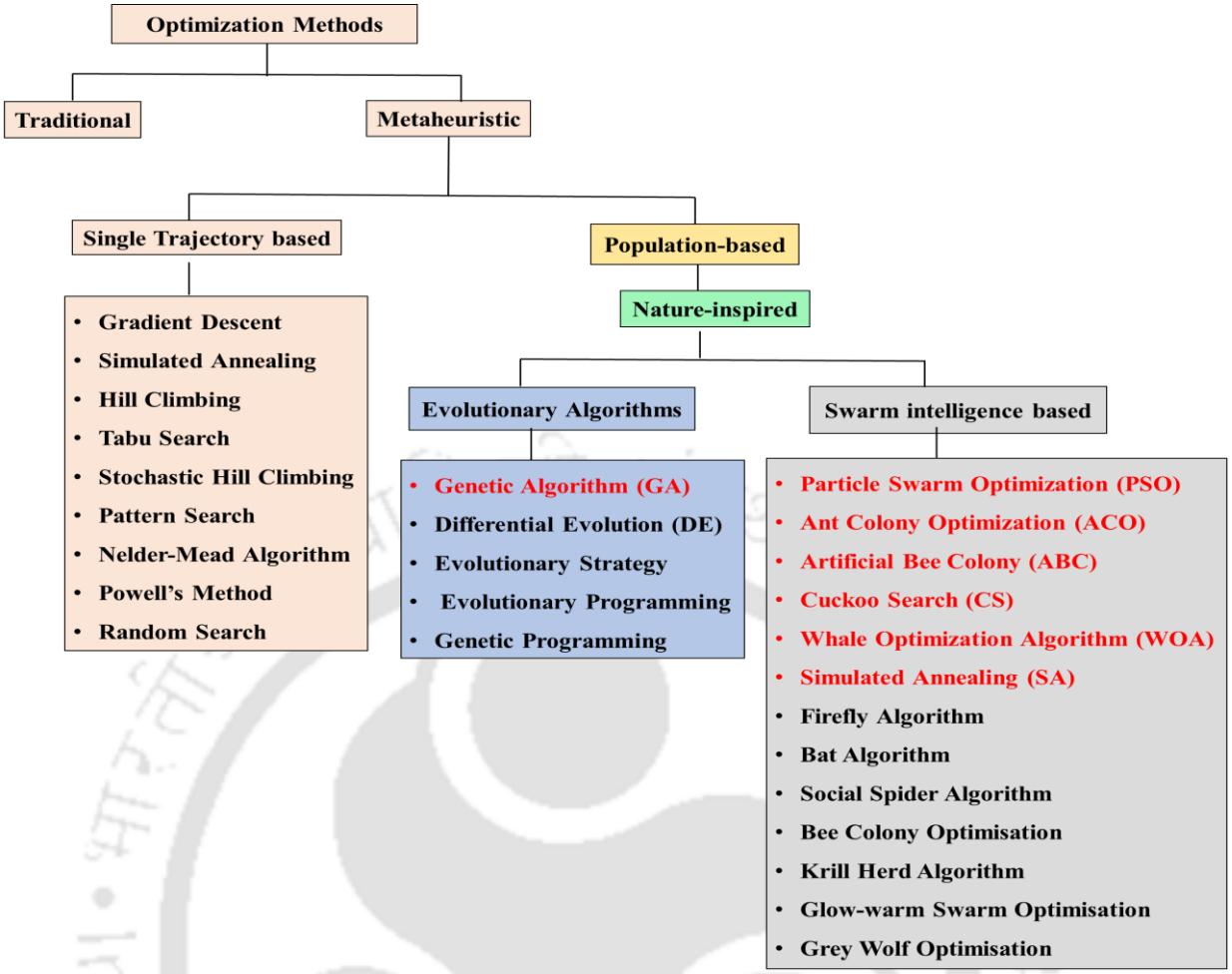

Figure 5.12. Classification of optimization methods

Single trajectory-based optimization (such as Hill Climbing, Gradient Descent, Tabu Search, Random Search etc.) starts with a single solution at each iteration, and the current solution is replaced by another best solution found in the neighborhood for that iteration. Contrarily, population-based optimization techniques are inspired by natural-selection and biological evolution, where a set of solutions are randomly initialized and updated through an iterative process. Genetic algorithm, Differential evolution and others belong to evolutionary optimization techniques, while Particle swarm optimization, Ant colony optimization, Cuckoo search and others are examples of swarm-intelligence-based optimization techniques [201, 202]. These techniques are exploration-and-exploitation oriented, which introduces diversification in the search space, resulting in the attainment of global optimum solutions by avoiding local optimum solutions for complex real-world problem [203].

Among all available various nature-inspired metaheuristic optimization techniques, genetic algorithms, particle swarm optimization, Cuckoo search and a few others have been proven to successfully solve a wide range of complex real-world problems. However, some of

the recently introduced metaheuristic optimization techniques such as Ant colony optimization, Artificial Bee Colony optimization, Spotted Hyena optimization, whale optimization need substantiation for their convergence. Rao [204], in his book chapter, emphasized that these methods share the same fundamental principles, despite being referred to by different names.

5.11. Metaheuristic Optimization Methods Utilized in this Work

The five most popular and well-studied metaheuristic optimization techniques used to identify novel MPEA compositions with minimized CRM content are shown in Figure 5.13. The description of each optimization method along with its flowchart is described in the subsequent section. By employing these metaheuristic optimization methods in combination with ETR, the search for optimal compositions can be carried out efficiently, striking a balance between sustainability (by eliminating CRMs) and performance, thereby ensuring that the designed alloys are both technologically viable and environmentally responsible.

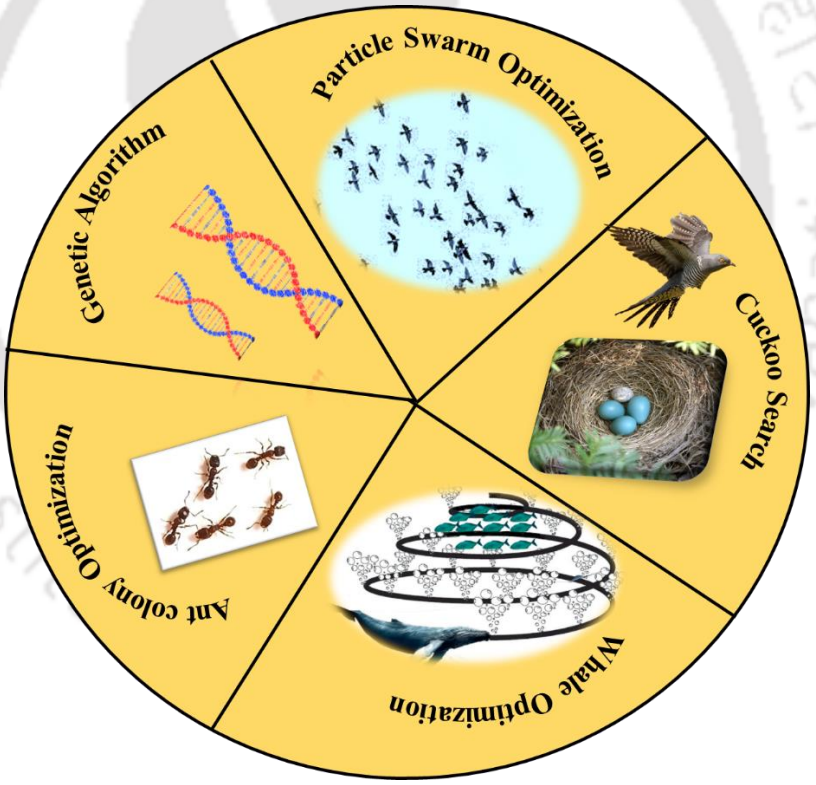

Figure 5.13.Various metaheuristic optimization models applied in this study: Genetic Algorithm (GA), Particle Swarm Optimization (PSO), Cuckoo Search Optimization (CSO), Whale Optimization Algorithm (WOA) and Ant Colony Optimization (ACO)

5.11.1. Genetic Algorithm (GA)

GA is one of the most popular evolutionary algorithms based on the principle of Darwin's theory of survival of the fittest. It includes random initialization of population, selection, crossover, mutation to generate new population with improved fitness. In this method, the variables (or compositional elements in particular for our objective) corresponds to the chromosomes of population, and based on the best fitness value (i.e., the highest hardness value), they are selected for recombination and mutation to generate new population with better fitness for the next generation (i.e., compositions corresponding to higher hardness than the previous generation). The optimal or near-optimal solution obtained after several generations represents the best solution of the problem. Complete description of working principle of genetic algorithm is shown in Figure 5.14. Table 5.2, presents the range of hyperparameters used in GA for present study.

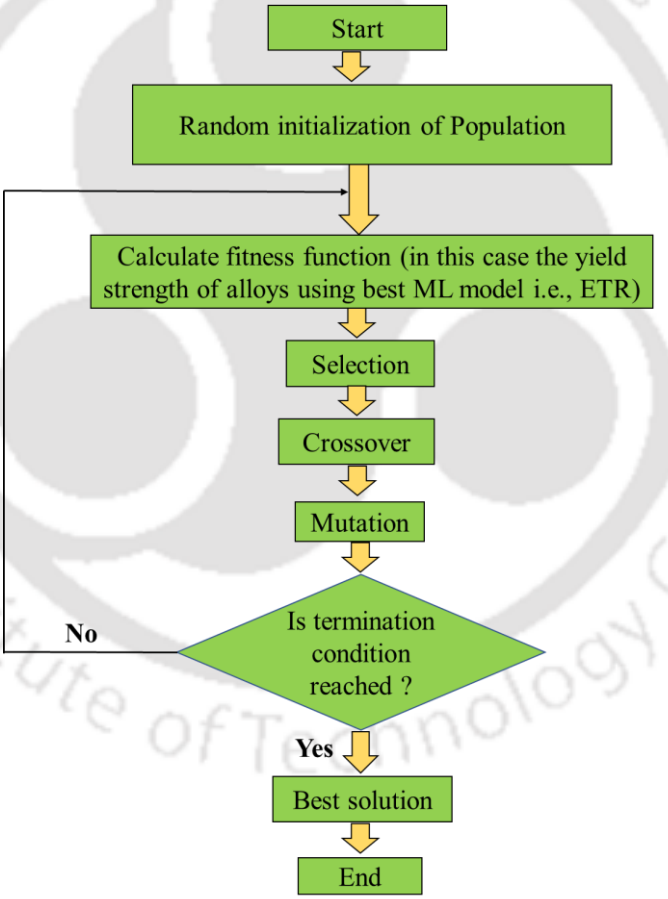

Figure 5.14. Flowchart of working principle of Genetic Algorithm

Table 5.2. Range of hyperparameters used for GA

GA Parameters	Values
Population size	Range of 50-1000.
Crossover rate	Range of 0.6 - 0.9.
Mutation rate	Range of 0.01 - 0.1.
Selection method	Tournament wheel selection.
Number of generations	Range of 1000-5000.

5.11.2. Particle Swarm Optimization (PSO)

Particle swarm optimization (PSO) technique is a nature-inspired technique based on social behavior of bird flocking and fish schooling. It is a robust stochastic optimization technique based on the movement and intelligence of swarms, useful to solve difficult optimization problems. Here, each particle represents a potential solution, which move in search space based on individual and group experience. Each particle adjusts its position by considering its personnel best-known position and global best position. One notable drawback of swarm algorithms is the need for subjective parameter tuning. Incorrect parameter setting can cause the algorithm to converge prematurely [93], resulting in suboptimal solutions. An effective approach to address this issue is to find methods that reduce or, if possible, eliminate the need for parameter tuning. Complete description of working principle of PSO is shown in Figure 5.15. A range of hyperparameters used in PSO is shown in Table 5.3.

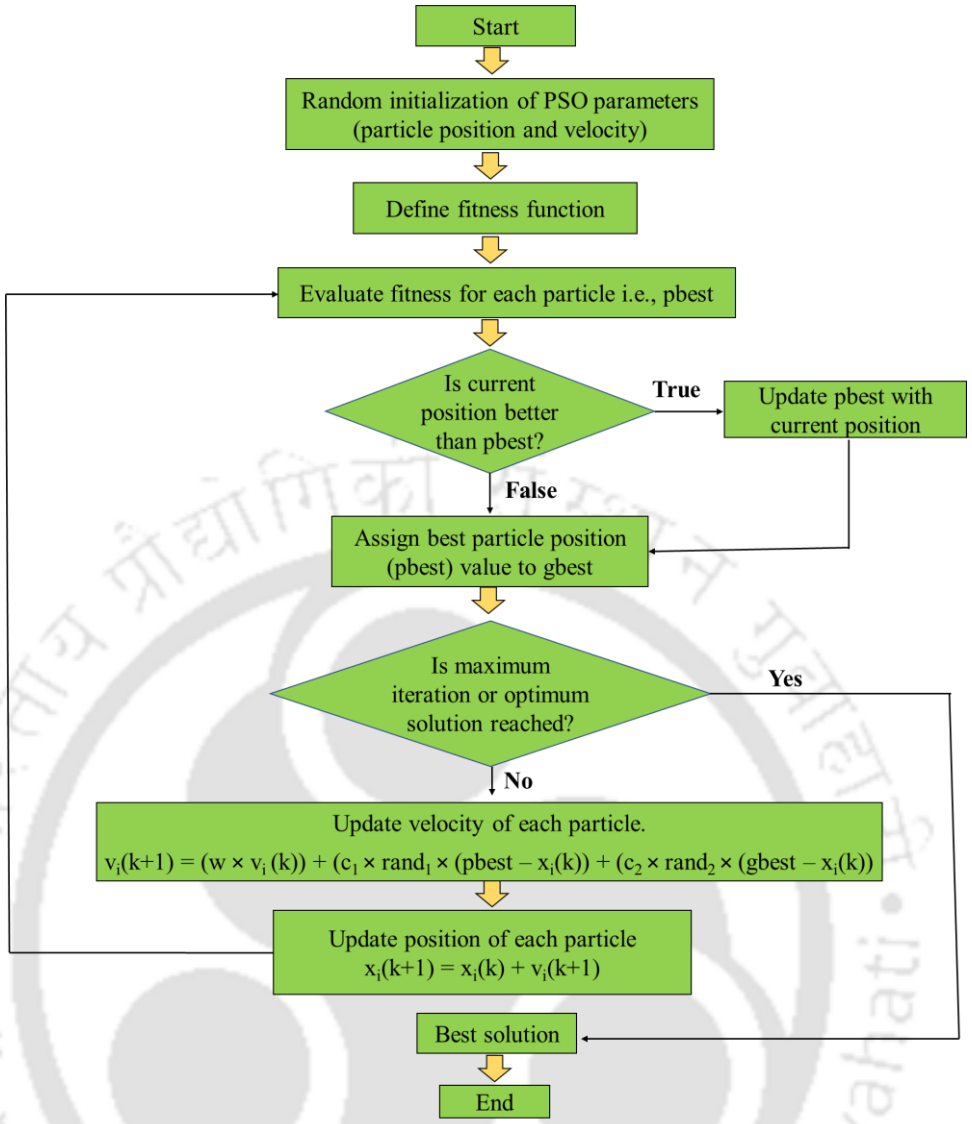

Figure 5.15. Flowchart of working principle of Particle swarm optimization

Table 5.3. Range of hyperparameters used for PSO

PSO Parameters	Values
Swarm size (population size)	Range of 50-100.
Cognitive coefficient (c1)	Range of 1.5 - 2.0.
Social coefficient (c2)	Range of 1.5 - 2.0.
Inertia weight (w)	Range of 0.7 - 1.5.
Maximum number of iterations	Range of 100-5000.

5.11.3. Whale Optimization Algorithm (WOA)

WOA is inspired by the foraging behavior of Humpback whales. Humpback whales hunt schools of krills or small fishes close to the surface by creating distinctive bubbles along a spiral path and this strategy is known as bubble-net hunting strategy of humpback whales. The working principle of WOA is shown in Figure 5.16. A range of hyperparameters used in WOA is illustrated in Table 5.4.

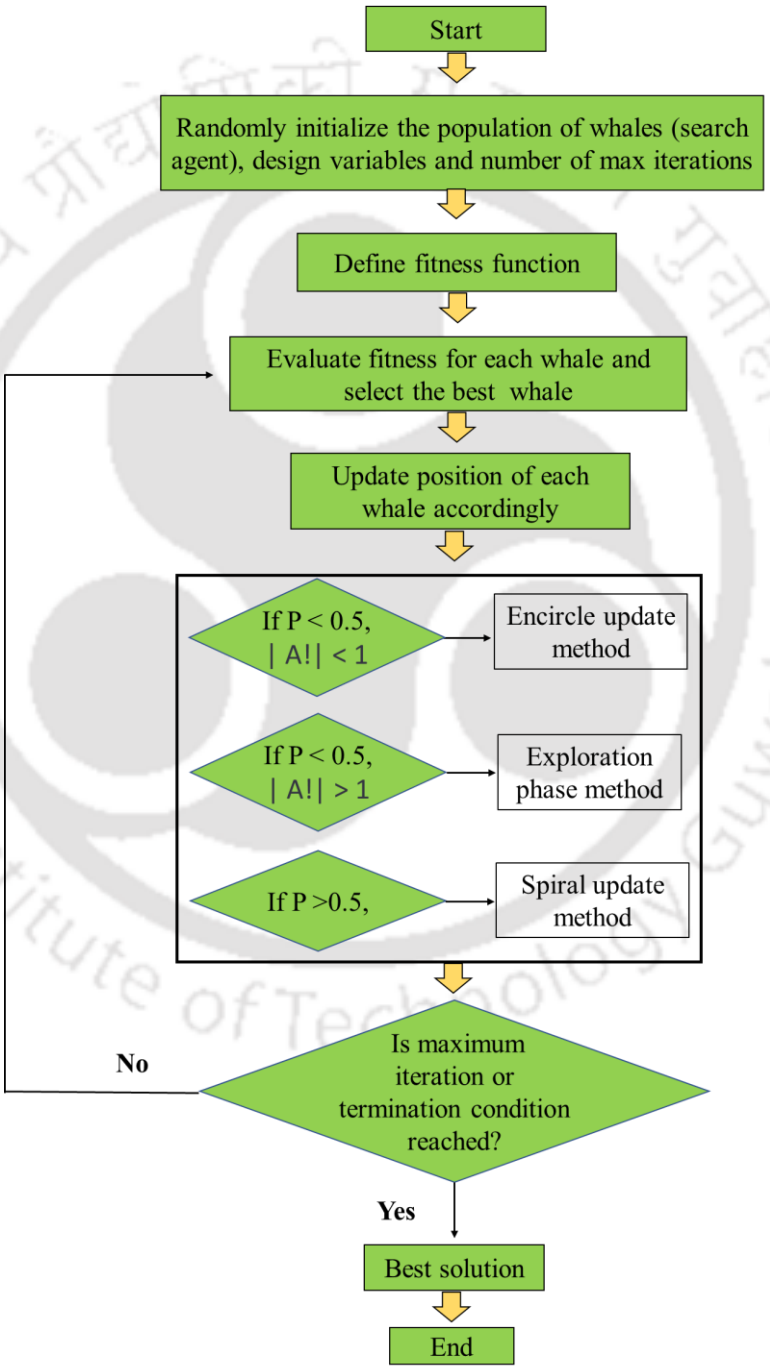

Figure 5.16. Flowchart of working principle of Whale optimization Algorithm

Table 5.4. Range of hyperparameters used for WOA

WOA Parameters	Values
Population size (Number of whales)	Range of 20-300.
Exploration and exploitation control parameter (a)	Linearly decreasing from 2 to 0 during iterations.
Convergence control parameter (b)	Range of 0.5-1.0.
Maximum number of iterations	Range of 20-1000.

5.11.4. Ant Colony Optimization (ACO)

Ant colony optimization is based on the cooperative behavior of real ant colonies which enables them to find the shortest path from the nest to the food source. Ants are social insects and as many as several millions live together in a colony or nest or anthill. They use pheromone as a means of communication. The ant colony optimization mimics the foraging behavior of ants. Initially, ants wander randomly in different directions. Once any one or more ants find food source, they return to their colony (with food) while leaving pheromone trails. The pheromone is made of certain chemicals produced by a living organism to send messages or signals to other members of the same species. If other ants find such a path, they follow the trail to the food source instead of wandering randomly. When they return to their colony, they too leave pheromone reinforcing the existing pheromone intensity. With time, pheromone evaporates, thus reducing the strength of the pheromone. Eventually, the ants adjust and find the shortest path to the food source. The working principle of ant colony optimization algorithm is shown in Figure 5.17. Table 5.5 highlights the range of hyperparameters used in ACO.

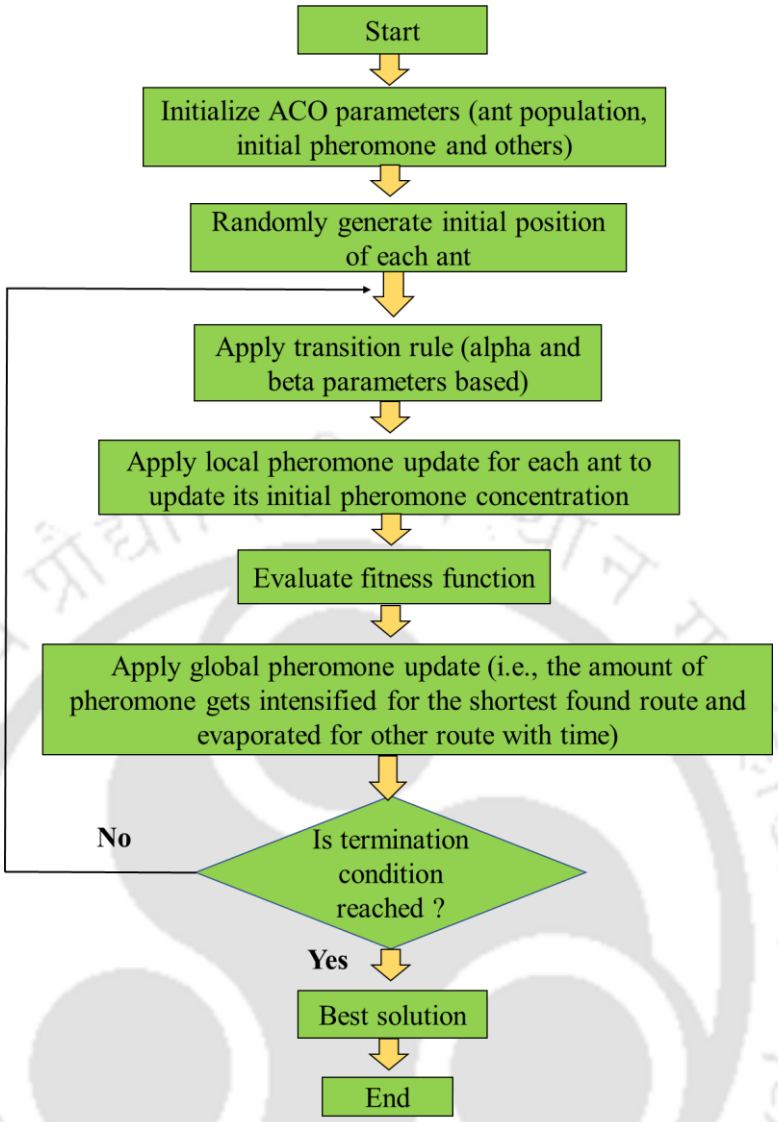

Figure 5.17. Flowchart of working principle of Ant Colony optimization

Table 5.5. Range of hyperparameters used for ACO

ACO Parameters	Values
Number of ants	Range of 10-200.
Pheromone evaporation rate (ρ)	Range of 0.1-0.5.
Pheromone influence (α)	Range of 1-5.
Heuristic influence (β)	Range of 1-10.
Maximum number of iterations	Range of 10-500.

5.11.5. Cuckoo Search Algorithm

Cuckoo search optimization is based on the brood parasitism of certain cuckoo species, as discussed earlier in chapter 4. This algorithm is enhanced by the use of Lévy flights [21], rather than simple isotropic random walks. CSO employs a balanced combination of a local random

walks and global explorative random walks, controlled by a switching parameter. It offers two distinct advantages over other algorithms such as GA and Simulated Annealing: efficient random walks and balanced mixing. Since Lévy flights are generally more effective than other random-walk-based randomization techniques, CSO can be highly efficient in global search. In fact, recent studies have shown that CSO can achieve guaranteed global convergence [27]. Additionally, the similarity between eggs can lead to better new solutions, which essentially represents fitness-proportional generation with strong mixing capability. In other words, CSO incorporates varying mutation through Lévy flights, while the fitness-proportional generation of new solutions based on similarity acts as a subtle form of crossover. Several studies have highlighted that CSO may be significantly more efficient than PSO and GA [11,12,40,41,26]. A flowchart of its working principle is demonstrated in Figure 5.18. The range of hyperparameters used in CSO is shown in Table 5.6.

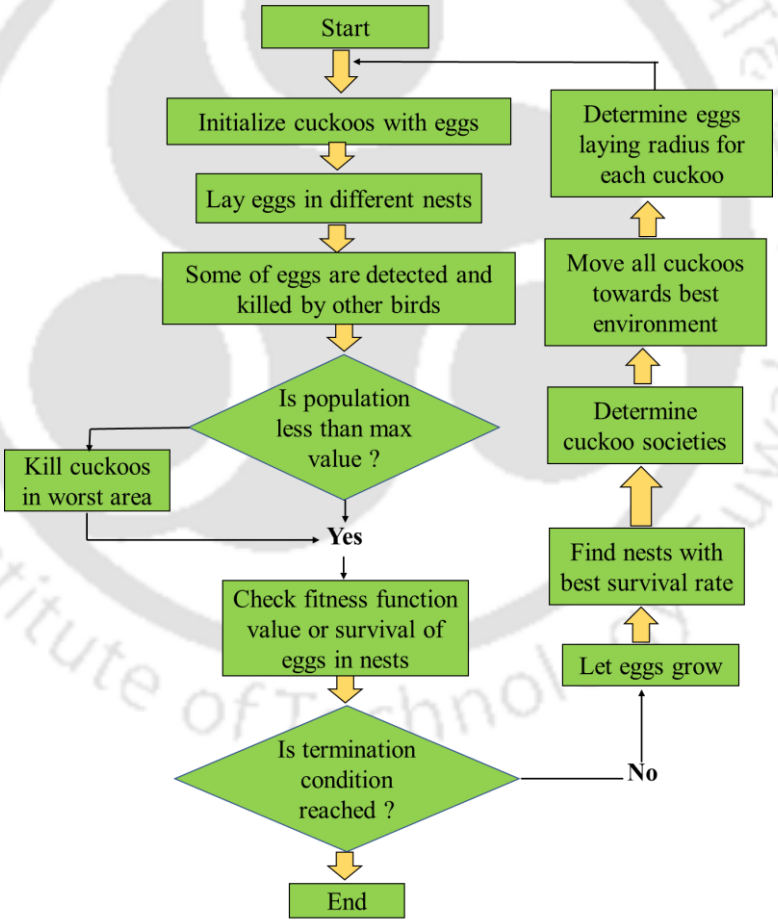

Figure 5.18. Flowchart of working principle of Cuckoo Search Optimization (CSO)

Table 5.6. Range of hyperparameters used for CSO

CSO Parameters	Values
Population Size (n)	Range of 500-5000
Discovery Rate of Alien Eggs/Probability of Abandonment (pa)	Range of 0.1 to 0.3
Maximum Number of Generations/Iterations	Range of 100-1000
Step Size Control Parameter (α)	Range of 0.01 to 1
Lévy Flight Distribution	1.5

A consolidated comparison of the five metaheuristic optimization algorithms, GA, PSO, ACO, WOA, and CSO, is presented in Table 5.7**.** This comparative summary outlines their underlying core mechanisms, key strengths, limitations, and specific performance observations within the context of CRM-free alloy design. The comparative structure facilitates a systematic evaluation of their relative performance and optimization behavior across the high-dimensional, multi-objective design space addressed in this work.

Table 5.7. Description of various algorithms used in this study

Algorithm	Mechanism	Strengths	Limitations	Observation (in context of CRM-free alloy design)
Genetic Algorithm (GA)	Based on Darwinian evolution; uses selection, crossover, mutation	Strong global exploration; well-established	Slower convergence; parameter-sensitive	Provided initial diversity but showed slow convergence for multi-objective design space
Particle Swarm Optimization (PSO)	Inspired by flocking behavior of birds	Fast convergence; easy implementation	May stagnate in local minima; requires tuning	Performed well initially but showed early convergence and limited exploration
Ant Colony Optimization (ACO)	Simulates pheromone trail-based path finding of ants	Good for discrete combinatorial problems	Computationally heavy for continuous problems	Less suitable for continuous composition optimization in alloy design
Cuckoo Search Optimization (CSO)	Based on brood parasitism of cuckoo birds with Lévy flight randomization	Strong balance between exploration and exploitation; few parameters; fast convergence	May need tuning of Lévy flight step size	Demonstrated most stable and rapid convergence with high accuracy for hardness prediction
Whale Optimization Algorithm (WOA)	Cooperative bubble-net hunting of humpback whales	Good balance between exploration and	May oscillate near global optimum; tuning sensitive	Competitive accuracy but inconsistent convergence across runs

		exploitation; adaptive		

5.12. Exploration of Defined Compositional Space Using GA, PSO, WOA, ACO and CSO

To explore novel multi-component compositions, the five metaheuristic optimization strategies described above were employed with the objective of generating alloys exhibiting superior hardness compared to those in the training and testing datasets, which consisted exclusively of unary and binary compositions (extracted using Thermo-Calc 2024a). The optimization function was designed to identify novel multi-principal element alloys (MPEAs) with Vickers hardness values exceeding 400 HV. A compositional constraint was applied such that the sum of 3, 4, 5, 6, 7, 8, 9, or 10 selected elements equals 100 atomic percent, while maintaining equal or near-equal proportions of each element to ensure the formation of multicomponent compositions. The ternary to decenary MPEA compositions obtained through GA, PSO, WOA, ACO and CSO, are presented in Tables 5.8, 5.9, 5.10, 5.11, and 5.12, respectively. The predicted hardness values of the newly optimized MPEAs were also compared with Thermo-Calc estimates using the Property Model Calculator, as detailed for each composition in the respective tables.

Table 5.8. Compositions generated using GA optimization, along with corresponding Thermo-Calc (TC) evaluations and assessed percentage errors in hardness values

No. of elements	Composition suggested from GA	Corresponding HV	Thermo-Calc HV	Percentage Error (%)
3	$Mn_{23.41682}Sn_{23.41682}Ti_{53.16636}$	387	421	8%
3	$Cu_{9.10794325}Mo_{9.10794325}Ti_{81.7841135}$	392	364	8%
4	$Cu_{6.11253929}Ni_{6.11253929}Cr_{32.1722748}Ti_{55.60264661}$	399	425	6%
4	$Cr_{11.11111}Co_{22.22222}Ti_{22.22222}Mo_{22.22222}V_{22.22222}$	377	423	11%
5	$Ni_{5.79651873}Zn_{5.79651873}Mo_{5.79651873}Mn_{30.09710402}Ti_{53.2668911}$	388	391	0.8%
5	$Mo_{20}Mn_{20}Ti_{20}Sn_{20}V_{20}$	399	350	14%
6	$Ti_{6.66667}Cr_{16.66667}Co_{16.66667}Mo_{20}V_{20}Zr_{20}$	381	414	8%
6	$Cr_{10}Zr_{10}Mo_{20}Ti_{20}Sn_{20}V_{20}$	368	397	7%
7	$Cu_5Zr_5Co_{15}Cr_{15}Ti_{20}Mo_{20}V_{20}$	382	393	3%
7	$Zn_5Zr_5Co_{10}Ti_{20}Cr_{20}Mo_{20}V_{20}$	324	414	22%
8	$Ni_5Zr_5Cr_{10}Co_{10}Zn_{10}Ti_{20}V_{20}Mo_{20}$	310	413	25%
8	$Co_{10}Sn_{10}V_{10}Zn_{10}Zr_{10}Cr_{12.5}Ti_{17.5}Mo_{20}$	398	370	8%

9	$Cu_5Ni_5Zn_5Zr_5Co_{12}Cr_{12}Mo_{13}V_{13}Ti_{30}$	367	398	8%
9	$Cu_5Co_5Ni_5Zr_5Cr_8Mo_{10}Ti_{10}V_{10}Sn_{42}$	391	308	27%
10	$Mn_2Sn_2Zr_4Cu_6Zn_6Cr_{10}Co_{10}Ti_{20}V_{20}Mo_{20}$	319	409	22%
10	$Cu_3Ni_3Fe_3Zn_3Zr_3Co_5Cr_5Mo_{25}Ti_{25}V_{25}$	350	444	21%

Table 5.9. Compositions generated using PSO optimization, along with corresponding Thermo-Calc (TC) evaluations and assessed percentage errors in hardness values

No. of elements	**Composition suggested from PSO**	**Corresponding HV**	**Thermo-Calc HV**	**Percentage Error (%)**
4	$Mo_{5.55556}Zn_{5.55556}Mn_{44.44444}V_{44.44444}$	306	339	10%
4	$Fe_{6.25}Ni_{6.25}Cr_{43.75}\ Zn_{43.75}$	303	397	24%
5	$Ni_{5.88235}Zr_{5.88235}Mn_{5.88235}Cr_{41.17647}Ti_{41.17647}$	330	394	16%
5	$Cr_{4.76190}Ni_{4.76190}Co_{4.76190}Mn_{42.85714}Ti_{42.85714}$	335	372	10%
6	$Cu_{4.54545455}Mn_{4.54545455}Sn_{4.54545455}Fe_{4.54545455}$ $Cr_{40.90909091}Ti_{40.90909091}$	349	308	13%
6	$V_{4.16667}Ni_{4.16667}Fe_{4.16667}Mo_{4.16667}Cr_{41.66667}$ $Ti_{41.66667}$	326	395	17%
7	$Cu_8Zr_8Co_{12}Cr_{12}Ti_{20}Mo_{20}V_{20}$	304	394	23%
7	$Co_4Cu_4Fe_4Mn_4Ni_4Cr_{40}Ti_{40}$	340	310	10%
7	$Co_5V_5Zn_5Zr_5Cr_{10}Mo_{20}Ti_{50}$	311	364	14%
8	$Ni_{6.66667}Zn_{6.66667}Zr_{6.66667}Cr_{10}Co_{10}Mo_{20}\ Ti_{20}V_{20}$	305	415	26%
8	$Cu_5Zn_5Zr_5Co_{12}Cr_{12}Mo_{13}V_{13}Ti_{35}$	298	378	21%
9	$Cu_5Ni_5Co_5Zn_5Ti_{10}V_{10}Cr_{10}Mo_{10}Sn_{40}$	316	325	3%
9	$Cu_5Ni_5Zn_5Zr_5Co_{10}Cr_{10}Mo_{15}V_{15}Ti_{30}$	290	411	29%
10	$Al_{4.16666667}Cu_{4.16666667}Cr_{4.16666667}Fe_{4.16666667}$ $Mn_{4.16666667}Ti_{4.16666667}Zn_{4.16666667}Zr_{4.16666667}$ $Mo_{33.33333333}V_{33.33333333}$	315	424	26%
10	$Co_{10}Cr_{10}Cu_{10}Fe_{10}Ni_{10}Mo_{10}Ti_{10}V_{10}Zr_{10}Zn_{10}$	343	296	16%

Table 5.10. Compositions generated using WOA optimization, along with corresponding Thermo-Calc (TC) evaluations and assessed percentage errors in hardness values

No. of elements	**Composition suggested from WOA**	**Corresponding HV**	**Thermo-Calc HV**	**Percentage Error (%)**
3	$Cu_{11.2}Mn_{36.8}Ti_{52}$	391	419	7%
4	$Mo_{5.92105}Al_{13.81579}Co_{17.10526}Ti_{63.15789}$	363	192	89%

4	$Fe_{10}Zn_{20}Cr_{30}Ti_{40}$	355	325	9%
5	$Ni_{3.41880}Mn_{4.27350}Zn_{10.25641}V_{29.05983}Mo_{52.99145}$	346	375	8%
5	$Cr_{9.09091}Mn_{9.09091}Zr_{9.09091}Mo_{36.36364}V_{36.36364}$	324	400	19%
6	$Fe_{5.55556}Mn_{5.55556}V_{5.55556}Zn_{5.55556}Ti_{38.88889}Cr_{38.88889}$	333	382	13%
6	$Cr_{7.14286}Mn_{7.14286}Ti_{7.14286}Zr_{7.14286}Mo_{35.71429}V_{35.71429}$	322	445	28%
7	$Co_{4.34783}Cr_{4.34783}Ni_{4.34783}Ti_{4.34783}Zn_{4.34783}Mo_{39.13043}V_{39.13043}$	337	414	18%
7	$Co_5Cr_{10}V_{10}Zn_{10}Zr_{10}Mo_{20}Ti_{35}$	323	409	21%
8	$Al_5Co_5Cu_5Fe_5Mn_5Ni_5Mo_{35}V_{35}$	319	390	18%
8	$Al_{12.5}Co_{12.5}Cr_{12.5}Mo_{12.5}Ti_{12.5}V_{12.5}Zn_{12.5}Zr_{12.5}$	312	379	18%
9	$Fe_{4.34783}Ni_{4.34783}Mo_{4.34783}Sn_{4.34783}Ti_{4.34783}Zn_{4.34783}Zr_{4.34783}Cu_{34.78261}V_{34.78261}$	281	296	5%
9	$Cu_5Ni_5Zn_5Zr_5Co_6Cr_6Mo_9V_9Ti_{50}$	326	413	21%
10	$Al_{3.57143}Co_{3.57143}Cr_{3.57143}Cu_{3.57143}Fe_{3.57143}Ni_{3.57143}Ti_{3.57143}Zr_{3.57143}Mo_{35.71429}V_{35.71429}$	314	420	25%
10	$Al_5Co_5Cr_5Fe_5Mn_5Ti_5Zr_5Zn_5Mo_{30}V_{30}$	315	365	14%

Table 5.11. Compositions generated using ACO optimization, along with corresponding Thermo-Calc (TC) evaluations and assessed percentage errors in hardness values

No. of elements	**Composition suggested from ACO**	**Corresponding HV**	**Thermo-Calc HV**	**Percentage Error (%)**
3	$Co_{13}Al_{20}Cu_{67}$	168	196	14%
4	$Fe_{10}Zn_{20}Cr_{30}Ti_{40}$	278	325	14%
5	$Fe_4Co_{15}V_{24}Sn_{28}Cr_{29}$	273	352	22%
6	$Sn_4Mn_7Ti_{13}Ni_{21}Al_{26}Zr_{29}$	150	235	36%
6	$Cr_8Cu_8Mn_9Sn_{16}Al_{18}Zn_{41}$	167	272	39%
6	$Cu_6Mo_6Ni_6Zr_{20}Sn_{30}Cr_{32}$	258	332	22%
7	$Fe_3Mo_4Mn_8Cu_9Zn_{19}Cr_{25}Co_{32}$	269	348	23%
7	$Ti_2V_6Fe_{14}Mn_{15}Cr_{17}Zr_{18}Mo_{28}$	244	376	35%

Table 5.12. Compositions generated using CSO optimization, along with corresponding Thermo-Calc (TC) evaluations and assessed percentage errors in hardness values

No. of elements	Composition suggested from CSO	Corresponding HV	Thermo-Calc HV	Percentage Error (%)
4	$Mo_{25}Sn_{25}Ti_{25}V_{25}$	397	383	4%
4	$Cr_{25}Mo_{25}Ti_{25}V_{25}$	401	424	5%
4	**$Ti_{0.01111}NiFe_{0.4}Cu_{0.4}$**	**468**	**488**	**4%**
5	$Co_{12.5}Cr_{12.5}Mo_{25}Ti_{25}V_{25}$	398	416	4%
5	$Mo_{10}Zn_{10}Al_{20}Cr_{30}Ti_{30}$	400	398	0.5%
5	$Co_{11.11111}Cr_{11.11111}Mo_{22.22222}V_{22.22222}Ti_{33.33333}$	404	430	6%
5	$Zn_{6.25}Cr_{18.75}Mo_{25}Ti_{25}V_{25}$ (similar to novel one)	402	415	3%
5	$Zr_{6.25}Zn_{18.75}Ti_{25}V_{25}Mo_{25}$ (similar to novel one	404	434	7%
6	$Zn_5Cr_{10}Zr_{10}Mo_{25}Ti_{25}V_{25}$	406	443	8%
6	$Co_{16.66667}Cr_{16.66667}Mo_{16.66667}Ti_{16.66667}V_{16.66667}Zr_{16.66667}$	395	427	7%
7	CoCrMoVZnZrTi	356	422	16%
7	$Cu_5Zr_5Co_{12}Cr_{12}Mo_{13}V_{13}Ti_{40}$	382	411	7%
8	$Co_{10}Mn_{10}V_{10}Zn_{10}Zr_{10}Cr_{12.5}Ti_{17.5}Mo_{20}$	396	416	5%
8	$Co_{12.5}Cu_{12.5}Cr_{12.5}Mo_{12.5}Ti_{12.5}V_{12.5}Zn_{12.5}Zr_{12.5}$	385	427	10%
8	$Ni_2Zn_2Zr_{11}Cr_{12.5}Co_{12.5}Mo_{20}Ti_{20}V_{20}$	398	429	7%
9	$Cu_5Ni_5Zn_5\ Zr_5Co_8Cr_8Mo_{10}V_{10}Ti_{44}$	403	432	7%
10	$Co_{3.57143}Cr_{3.57143}Cu_{3.57143}Fe_{3.57143}Ni_{3.57143}Zn_{3.57143}Zr_{3.57143}Mo_{25}Ti_{25}V_{25}$ OR $(CoCrCuFeNiZnZr)_{0.1428572}MoTiV$	404	448	10%
10	$Cu_4Fe_4Ni_4Zn_4\ Zr_4Co_{10}Cr_{10}Ti_{20}V_{20}Mo_{20}$	405	477	15%

By comparing the hardness values of the newly generated compositions to those evaluated by Thermo-Calc (TC), it is evident that the CSO algorithm produced the most reliable multicomponent compositions, with a prediction error of less than ±20% (see Table 5.12). Furthermore, compositions generated by CSO exhibited superior hardness compared to those derived from other optimization methods. For instance, CSO successfully generated compositions such as $Cu_4Fe_4Ni_4Zn_4Zr_4Co_{10}Cr_{10}V_{20}Ti_{20}Mo_{20}$ (10 elements), $Zn_5Cr_{10}Zr_{10}Mo_{25}Ti_{25}V_{25}$ (6 elements), $Zr_{6.25}Zn_{18.75}Ti_{25}V_{25}Mo_{25}$ (5 elements), $Ti_{0.01111}NiFe_{0.4}Cu_{0.4}$ (4 elements), which achieved hardness values of 477 HV, 443 HV, 434 HV and 488 HV respectively. In contrast, while GA, PSO, and WOA demonstrated consistency in their predictions for several compositions, they often failed to accurately predict compositions with higher hardness values. Notably, these algorithms became increasingly erroneous with the inclusion of more elements in the alloy design.

ACO method proved to be reliable for ternary and quaternary compositions, yielding relatively low prediction errors. However, as the complexity escalated from quinary to decenary compositions, the percentage error substantially increased, and ACO was unable to generate viable compositions with more than seven elements. As a result, CSO emerged as the most reliable algorithm among those tested, capable of generating multicomponent compositions with reduced CRM content and enhanced hardness values.

Recent literature also suggests that the CSO performs better than PSO, GA, ACO, ABC and WOA [205-208]. Gandomi et al. [205] provided an extensive comparison and concluded that CSO performs better than GA and PSO, as GA requires a higher number of iterations and its implementation is computationally expensive [207]. On the other hand, PSO requires less computational effort but considerable execution time to find a solution from a large space for a complex optimization problem. Civicioglu and Desdo [8] suggested that CSO provides more robust results than PSO and ABC. Bhargava et al. [209] showed that CSO offers a reliable method for solving thermodynamic calculations for complex phase equilibrium applications.

Figure 5.19 illustrates the hardness values generated by each optimization method in comparison to those evaluated by Thermo-Calc (TC) for ternary to decenary based compositions, providing a comprehensive overview of model performance across varying levels of compositional complexity.

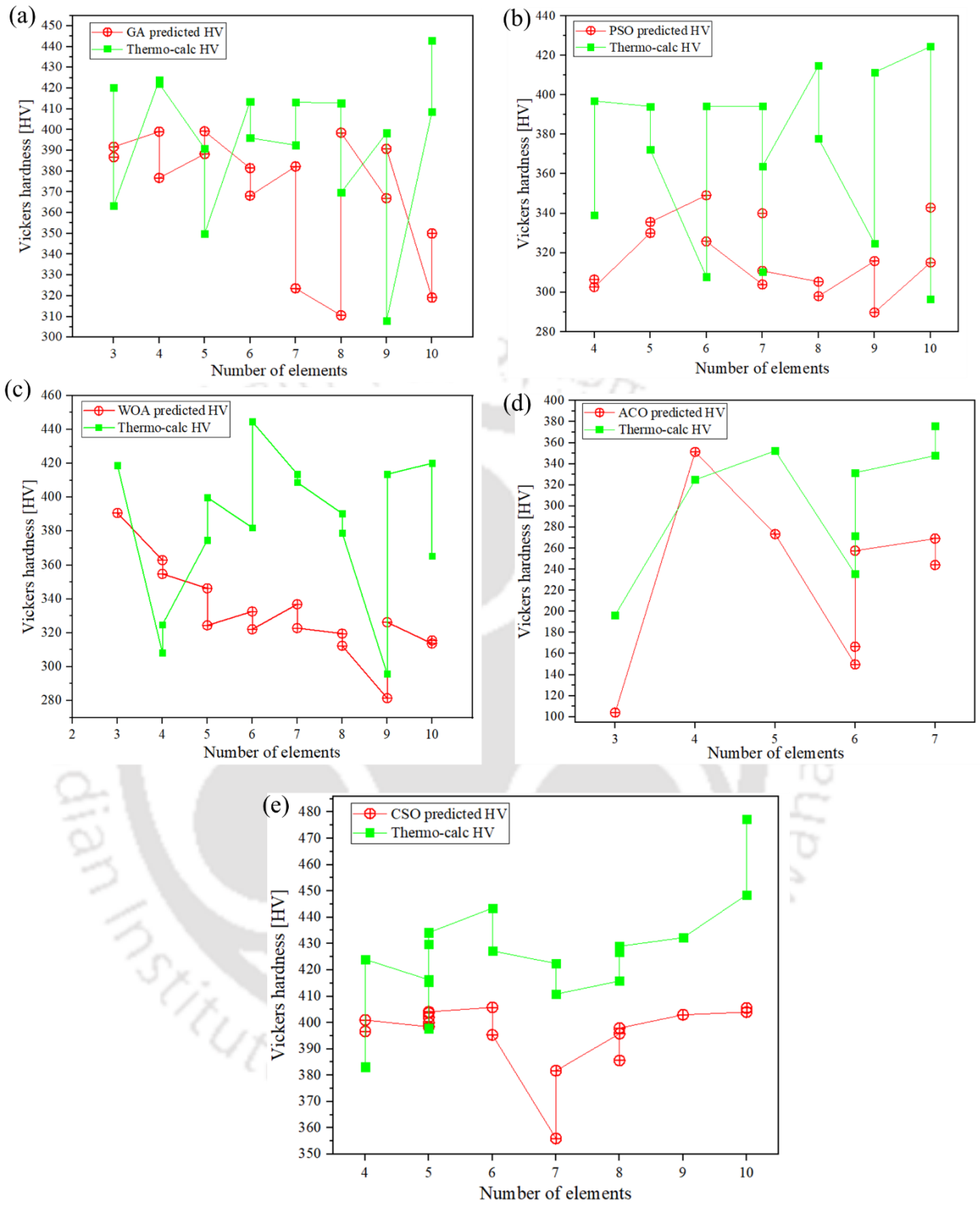

Figure 5.19. Comparison of hardness value for newly generated MPEA compositions with Thermo-Calc evaluations using various optimization techniques: (a) Genetic algorithm (GA), (b) Particle swarm optimization (PSO), (c) Whale optimization (WOA), (d) Ant colony optimization (ACO), (e) Cuckoo search optimization (CSO)

The reduced-CRM MPEA (R-CRM-MPEA) compositions generated using Cuckoo Search Optimization (CSO) were found to be in close agreement with their corresponding Thermo-Calc (TC) evaluated hardness values for each composition, as presented in Table 5.11 and Figure 5.19(e). Based on this agreement, the newly generated compositions were selected for further investigation. To assess the novelty and relevance of the optimized alloys, the MPEA compositions generated via CSO in this study were compared with CRM-rich MPEA compositions reported in the literature, thereby highlighting the differences and potential improvements.

5.13. Hardness Comparison of CRM-Heavy (from Literature) vs. R-CRM-MPEA

The hardness values of the newly generated R-CRM-MPEAs were compared with those of CRM-heavy MPEAs reported in the literature to assess the feasibility of partially or fully substituting CRMs. Figure 5.20 presents a comparison of the mechanical properties between experimentally synthesized CRM-heavy alloys from the literature and the newly predicted R-CRM-MPEAs developed in this study.

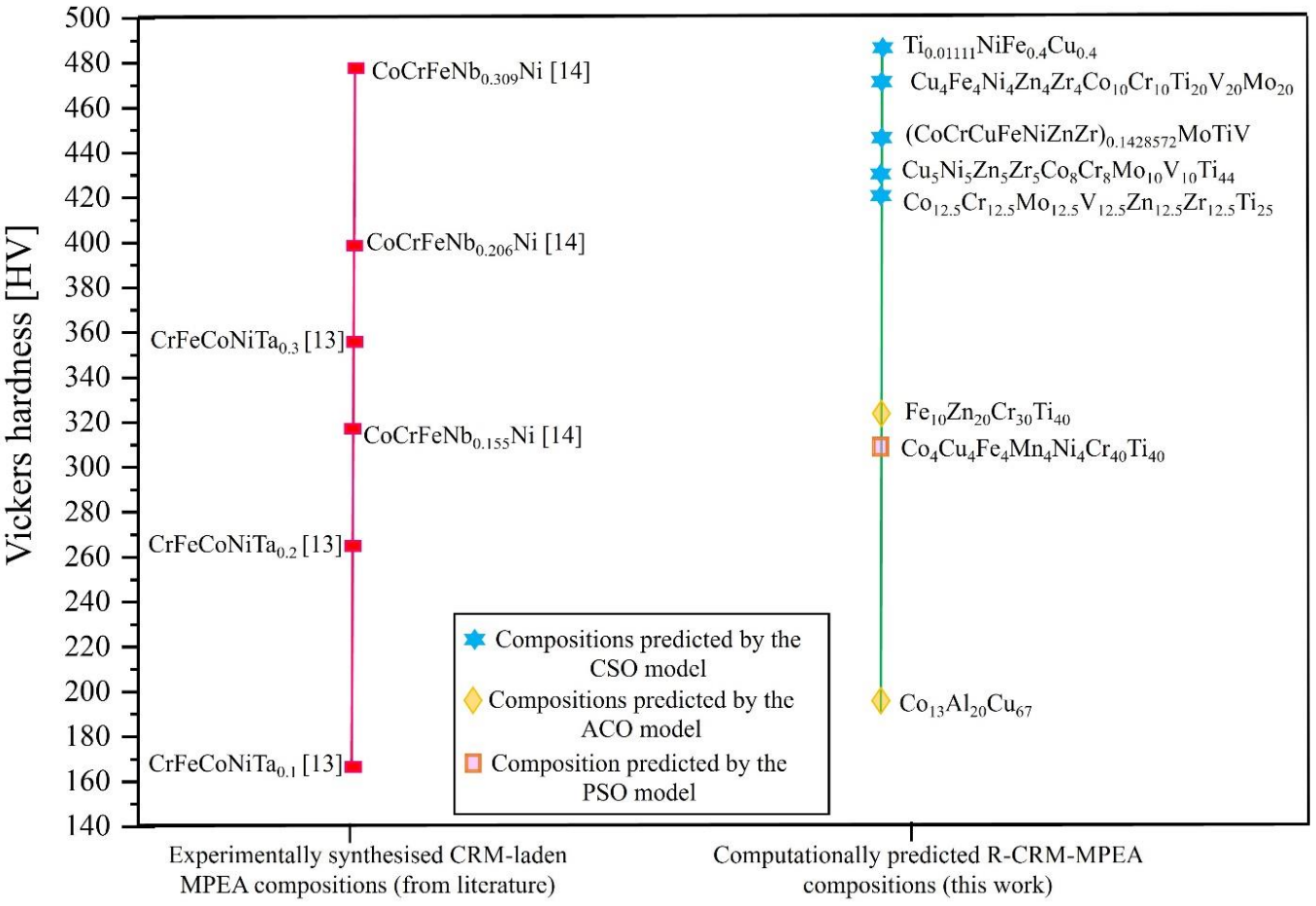

Figure 5.20. Comparison of R-CRM-MPEA with CRM-heavy MPEAs to demonstrate the feasibility of partially or fully substituting CRMs with readily available elements while attaining comparable mechanical properties

The results demonstrate that the proposed computational approach can yield alloy compositions with hardness values comparable to, or even exceeding, those of CRM-heavy counterparts. For instance, the composition $CoCrFeNb_{0.309}Ni$, which contains 1st-Tier CRM, cobalt (Co) and niobium (Nb), exhibits a hardness of 480 HV. In contrast, the CSO-generated novel composition $Ti_{0.0111}NiFe_{0.4}Cu_{0.4}$, incorporating only a 2nd-Tier CRM (titanium, Ti), achieves a superior hardness of 488 HV, without the inclusion of any 1st-Tier CRM. These findings highlight the strong potential of the employed optimization framework in designing reduced-CRM or CRM-free MPEAs.

5.14. Experimental Validation of CSO-Generated Novel MPEA: $Ti_{0.0111}NiFe_{0.4}Cu_{0.4}$

The CSO-generated novel composition $Ti_{0.0111}NiFe_{0.4}Cu_{0.4}$, was selected for experimental validation and synthesized using a vacuum arc melting setup at IIT Kanpur (refer to Figure 3.17, Chapter 3). The resulting alloy was subjected to Vickers hardness testing using a Wilson hardness testing apparatus under an applied load of 0.1 kgf (Figure 5.21). The reported hardness values

represents the average of ten independent indents performed on a meticulously polished sample surface to ensure measurement accuracy.

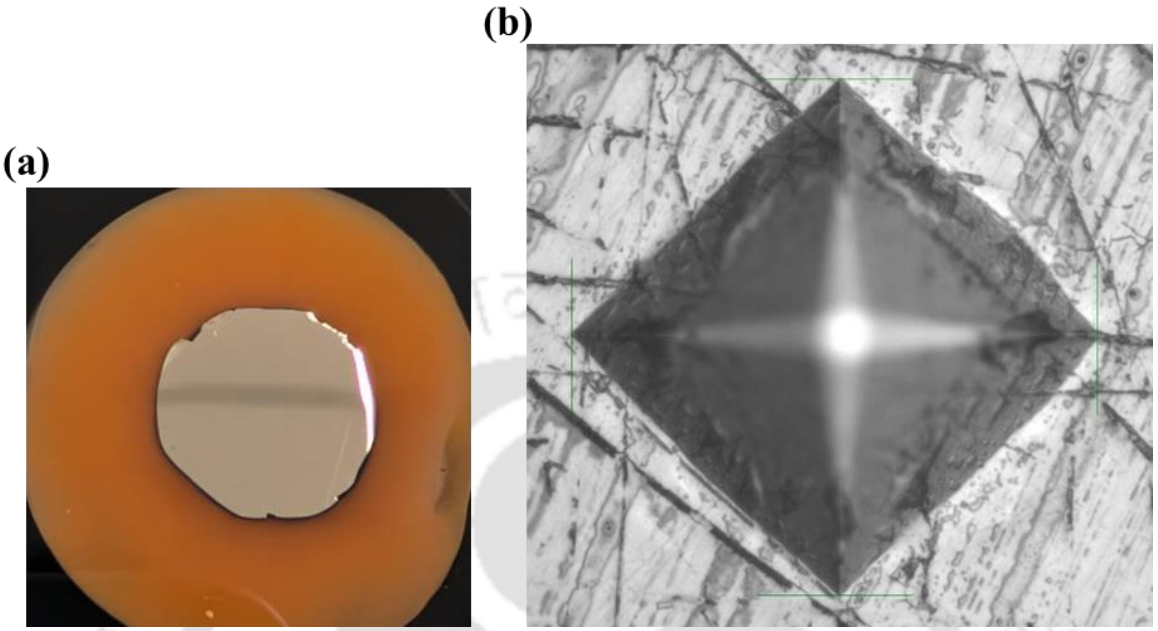

Figure 5.21. (a) Synthesized and polished $Ti_{0.0111}NiFe_{0.4}Cu_{0.4}$ alloy sample, (b) Vickers hardness indent used for hardness measurement

The experimentally measured Vickers hardness of the $Ti_{0.0111}NiFe_{0.4}Cu_{0.4}$ composition was compared with the values predicted by the CSO and those evaluated using Thermo-Calc (TC) (refer to Table 5.12). The measured hardness was 394 ± 20 HV, which is lower than both the CSO-predicted value of 468 HV and the TC-evaluated value of 488 HV, corresponding to percentage errors of 16% and 19%, respectively. This discrepancy can be attributed to the limited post-processing applied to the alloy. The synthesis involved only vacuum arc melting, casting, and homogenization, without any subsequent deformation or thermomechanical treatments, processes known to significantly enhance mechanical properties such as hardness.

As illustrated in Figure 5.3, most TC-evaluated hardness values closely align with experimental values for alloys that have undergone post-processing techniques such as equal channel angular pressing (ECAP) or rolling followed by annealing. For instance, the TC-evaluated hardness value for the CoCrNi alloy closely matches that of an experimentally processed sample subjected to three ECAP passes, followed by annealing at 700 °C. Similarly, for the FeMnNi medium entropy alloy, the TC-predicted hardness corresponds well with the experimental value of a sample that was 90% cold-rolled and subsequently annealed at 1073 K for 1 hour.

These trends suggest that applying appropriate post-processing techniques, such as thermomechanical treatments or severe plastic deformation, to the $Ti_{0.0111}NiFe_{0.4}Cu_{0.4}$ alloy may enhance its hardness and align it more closely with the CSO-predicted and TC-evaluated values. This represents a key direction for future investigation.

Table 5.7. Comparison of experimentally measured hardness with TC and CSO-predicted hardness

Alloy	**Experimentally evaluated [$HV_{0.1}$]**	**Predicted HV [TC and ML]**		**Percentage error (%)**
$Ti_{0.0111}NiFe_{0.4}Cu_{0.4}$	**Mean**	**TC-evaluated**	488 HV	19%
	394 ± 20 HV	**CSO-predicted**	468 HV	16%

Microstructural Characterization

Detailed microstructural observations were carried out using scanning electron microscopy (SEM) to assess phase uniformity and grain morphology. The microstructural examination of the $Ti_{0.0111}NiFe_{0.4}Cu_{0.4}$ alloy (Figure 5.22) reveals a dense and homogeneous matrix composed of uniformly distributed, nearly equiaxed grains, with no observable porosity, cracking, or coarse secondary phases. The absence of phase contrast or signs of segregation supports the formation of a single-phase solid solution structure. The experimentally observed microstructure and hardness of the $Ti_{0.0111}NiFe_{0.4}Cu_{0.4}$ alloy provide preliminary validation of the CRM-free alloy design framework developed in this study. These findings demonstrate a promising alignment between experimental outcomes and computational predictions, supporting the practical feasibility of the integrated CALPHAD + ML + metaheuristic optimization methodology.

(a)

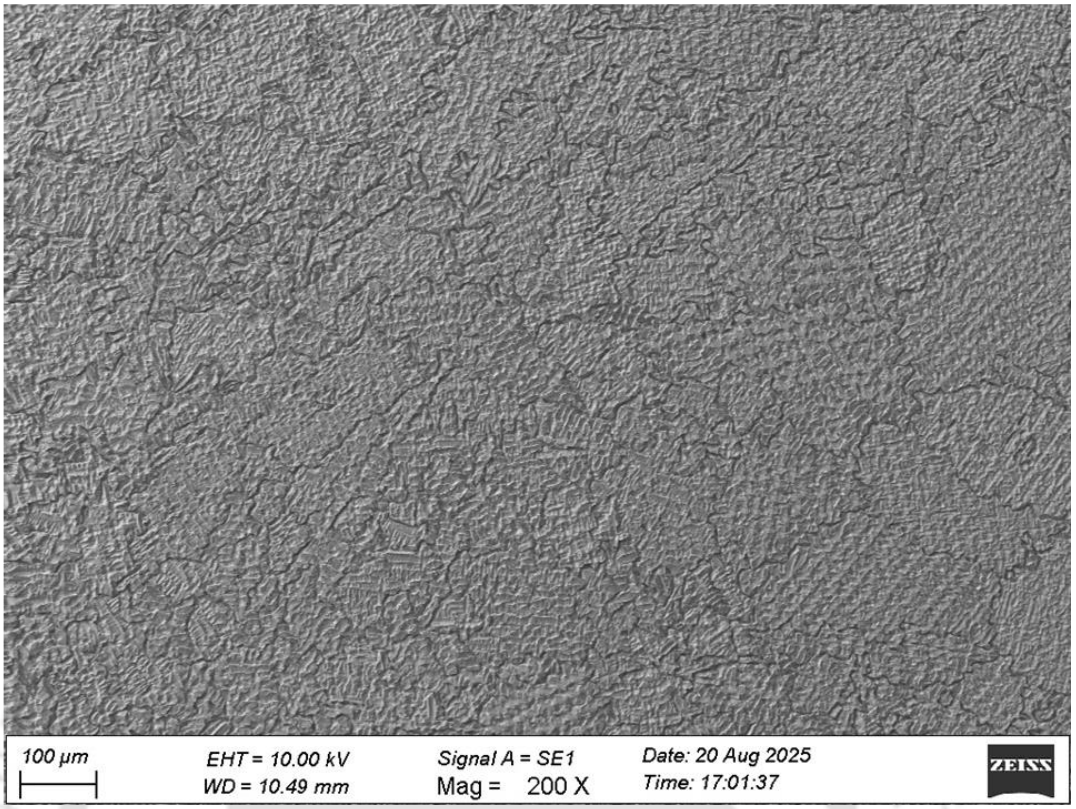
100 µm
EHT = 10.00 kV
WD = 10.49 mm
Signal A = SE1
Mag = 200 X
Date: 20 Aug 2025
Time: 17:01:37
ZEISS

(b)

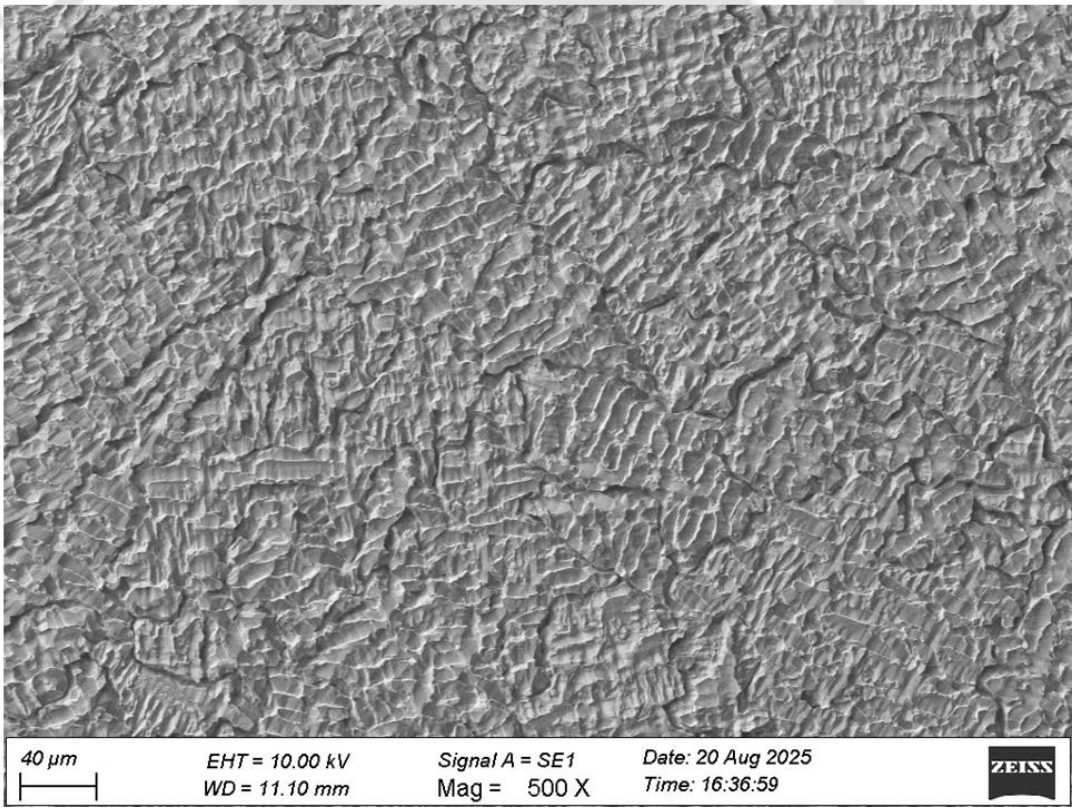
40 µm
EHT = 10.00 kV
WD = 11.10 mm
Signal A = SE1
Mag = 500 X
Date: 20 Aug 2025
Time: 16:36:59
ZEISS

(c)

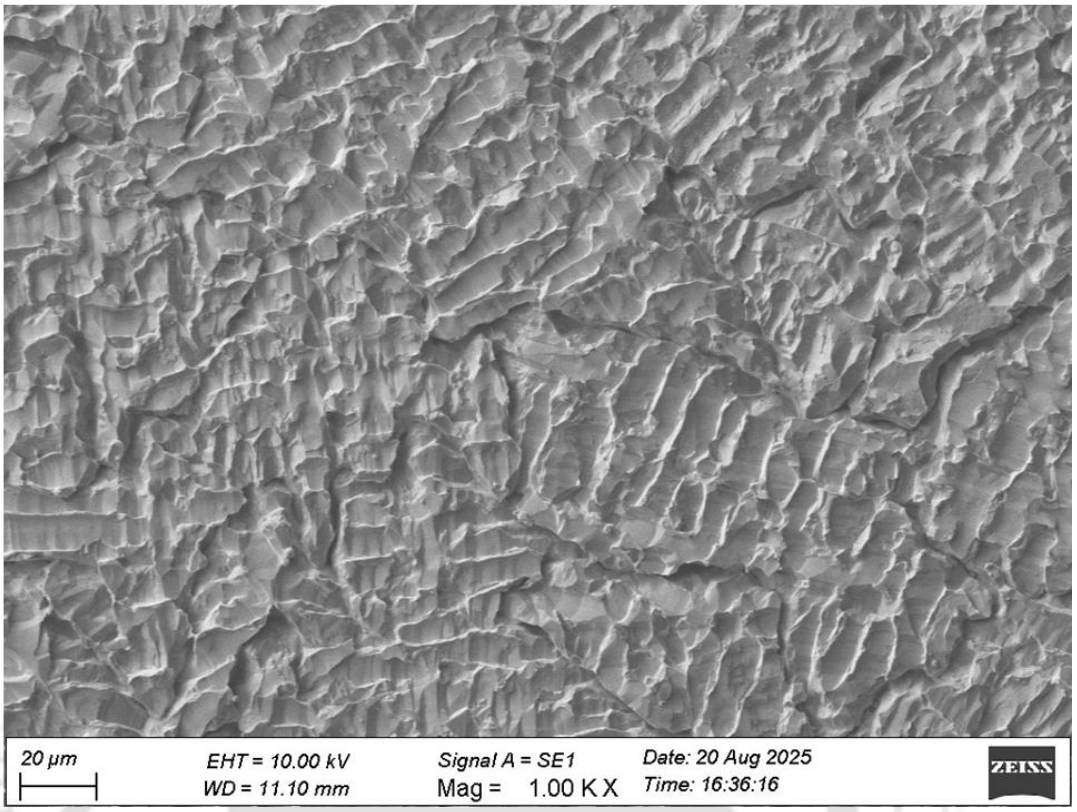

Figure 5.22. SEM micrographs of the $Ti_{0.0111}NiFe_{0.4}Cu_{0.4}$ alloy at different magnifications: (a) 200X, (b) 500X, and (c) 1000X

5.15. Summary

This study represents a significant step toward supporting Net-Zero initiatives by enabling the design of novel alloy compositions with reduced dependence on critical raw materials (CRMs). A hybrid machine learning (ML)–metaheuristic optimization framework was developed, utilizing a dataset of Vickers hardness values for unary and binary compositions generated using Thermo-Calc 2024a (TCHEA7 database with the Property Model Calculator). This dataset was employed to train ML models for hardness prediction and to guide the discovery of complex alloy compositions with minimized CRM content, without compromising mechanical performance.

Among the tree-based regression models evaluated, Decision Tree Regressor (DTR), Random Forest Regressor (RFR), AdaBoost Regressor (ABR), Gradient Boosting Regressor (GBR), Extreme Gradient Boosting Regressor (XGBR), and Extra Trees Regressor (ETR), the ETR exhibited the best performance, achieving an R^2 score of 0.82 and a MAPE of 0.17 on the test data. To identify novel multicomponent CRM-free or CRM-lean alloys, several metaheuristic optimization techniques were employed, including Genetic Algorithm (GA), Particle Swarm Optimization (PSO), Whale Optimization Algorithm (WOA), Ant Colony Optimization (ACO),

and Cuckoo Search Optimization (CSO). Among these, CSO proved particularly effective, generating compositions that demonstrated strong agreement with their corresponding Thermo-Calc (TC) predictions, with an average deviation of less than ±20%. The hardness of CSO-generated one such composition, **$Ti_{0.01111}NiFe_{0.4}Cu_{0.4}$**, containing a single 2nd-Tier CRM, (Ti), was compared against a literature-reported CRM-heavy composition, **$CoCrFeNb_{0.309}Ni$,** which contains two 1st-Tier CRMs (Co and Nb). While $CoCrFeNb_{0.309}Ni$ exhibited a hardness of 480 HV, the CSO-generated $Ti_{0.01111}NiFe_{0.4}Cu_{0.4}$ achieved a superior hardness of 488 HV, thereby demonstrating the feasibility of reducing CRM content without compromising, and potentially surpassing mechanical performance.

The validity of the proposed framework was further reinforced by experimentally synthesizing $Ti_{0.01111}NiFe_{0.4}Cu_{0.4}$ using vacuum arc melting and casting, and its measured hardness was compared with CSO-predicted and TC-evaluated values. The experimentally measured hardness of 394 ± 20 HV was lower than both the CSO-predicted value (468 HV) and the TC-evaluated value (488 HV). This discrepancy is attributed to the fact that most TC-evaluated hardness values exhibit close agreement with experimental measurements for alloys that had undergone post-processing treatments such as ECAP or rolling (as discussed in the data collection section, refer to Figure 5.3). Since all the ML and metaheuristic models were trained on a dataset dominated by post-processed compositions, their predictions inherently reflect the influence of these strengthening mechanisms. Thus, the CSO-predicted values derived from this database, are also biased toward post-processed compositions. In contrast, the synthesized $Ti_{0.01111}NiFe_{0.4}Cu_{0.4}$ sample was evaluated in the as-cast condition, without any subsequent deformation or thermomechanical treatment. Therefore, it is anticipated that the application of suitable post-processing techniques could enhance its hardness to levels more consistent with the CSO predictions and TC evaluations. Accordingly, such processing forms an important direction for future work.

Moreover, it is acknowledged that Thermo-Calc's property model does not explicitly account for processing-induced variations such as cooling rate or deformation history. However, its use was deemed appropriate for generating a high-fidelity, compositionally driven hardness database based on unary and binary systems, especially given the scarcity of experimental data for CRM-free alloys. These systems are well-supported by validated CALPHAD-based models, making them suitable for equilibrium hardness estimation. The predicted values were used comparatively, rather than absolutely, to rank candidate compositions under consistent thermodynamic assumptions.

This investigation thus provides valuable insight into the design of multi-principal element alloys with reduced reliance on CRMs, contributing to sustainable materials innovation in alignment with Net-Zero objectives. The proposed approach can be further leveraged to minimize or eliminate CRM usage in a wide range of applications, including catalysis, semiconductor devices, transportation, and other carbon-intensive industrial sectors.

While the hybrid ML–metaheuristic framework demonstrates the promise of ML-guided chemical tuning to reduce CRM dependency without compromising performance, the next phase of this research explores a complementary, non-ML-based strategy. Specifically, strain engineering is investigated as a sustainable physical design approach aimed at reducing reliance on critical and strategic raw materials (C&SRMs) through microstructural refinement induced by mechanical deformation, with its effectiveness supported by evidence from the literature.

Chapter 6

Theoretical Investigation of Strain Engineering to Minimize the Use of Critical and Strategic Raw Materials (C&SRMs) without Resorting to Chemical Modification

6.1. Introduction

As part of the broader pursuit of sustainable alloy design, and in continuation of the previous chapter which established a hybrid ML–metaheuristic optimization framework for designing novel MPEAs with reduced reliance on critical raw materials (CRMs) through ML-guided chemical tuning, the present chapter investigates a complementary non-ML-based approach. Specifically, strain engineering is examined as an alternative pathway to the same objective, minimizing dependence on critical and strategic raw materials (C&SRMs) while preserving or enhancing mechanical performance. Unlike chemical alloying strategies that depend on compositional modifications guided by ML predictions, strain engineering represents a purely physical design route, enabling property modulation through strain-induced microstructural modifications such as dislocation density enhancement, ultrafine grain formation, and activation of deformation mechanisms including twinning-induced plasticity (TWIP) and transformation-induced plasticity (TRIP). The central premise is that carefully applied strain engineering can suppress the use of scarce C&SRMs while still achieving, or even surpassing, the mechanical properties of conventional C&SRM-rich alloys.

In this context, the chapter presents a comprehensive data-driven analysis (non-ML-based) of both MPEAs and pure elements, drawing from literature evidence to evaluate the effectiveness of strain engineering as a sustainable physical design strategy. Through systematic comparison, it highlights the differences in mechanical performance between strain-engineered and conventionally synthesized materials, underscoring the potential of strain engineering not only to deliver mechanical robustness but also to enable significant material savings. In doing so, the study positions strain engineering as a cost-effective and sustainable pathway for alloy development, aligning with global priorities of resource efficiency and Net Zero targets.

6.2. Critical and Strategic Raw Materials (C&SRMs)

Chapter 5 examined the implications of Critical Raw Materials (CRMs), which are essential to modern technologies yet constrained by high supply risk and environmental impacts. Building on that foundation, this chapter broadens the focus to include Strategic Raw Materials (SRMs), a subset of raw materials deemed vital not only for economic security but also for advancing green energy transitions, digital technologies, and defense capabilities. Collectively, CRMs and SRMs form the class of Critical and Strategic Raw Materials (C&SRMs), many of which, such as Hf, Nb, Ta, W, Co, and rare-earth elements, are heavily used in advanced alloy systems. However, their scarcity, geopolitical concentration, and mining-related emissions present significant barriers to achieving Net Zero goals. To ensure sustainable innovation, alloy development must prioritize the use of readily available and non-critical elements.

The European Commission plays a key role in the identification and periodic revision of the list of CRMs and SRMs. Since 2011, it has released triennial reports that reflect evolving supply–demand dynamics and geopolitical considerations. Based on these assessments (from 2011 to 2023), CRMs and SRMs were classified based on the frequency and continuity of their inclusion in these reports (see Figure 6.1), following an approach similar to that employed in Chapter 5. Materials that have appeared in three or more reports and are still of concern in 2023 are categorized as "1st Tier CRMs." Recently identified materials, having appeared in two or fewer reports, are classified as "2nd Tier CRMs." Additionally, materials such as Cr and indium (In), which are absent from the 2023 report, are classified as "non-CRMs." Figure 6.1 also integrates SRMs, with hatched elements indicating those that are both CRMs and SRMs. These include B/Borate, Bi, Co, Cu, Ga, Ge, Li, Mg, Mn, Ni, Si metal, Ti, and W. Natural graphite, platinum group metals, and rare earth elements are also classified as both CRMs and SRMs, though they are absent from Figure 6.1. Moreover, arsenic, baryte, coking coal, feldspar, fluorspar, strontium, and phosphate rock are also categorized as CRMs, but are likewise omitted from Figure 6.1 [210].

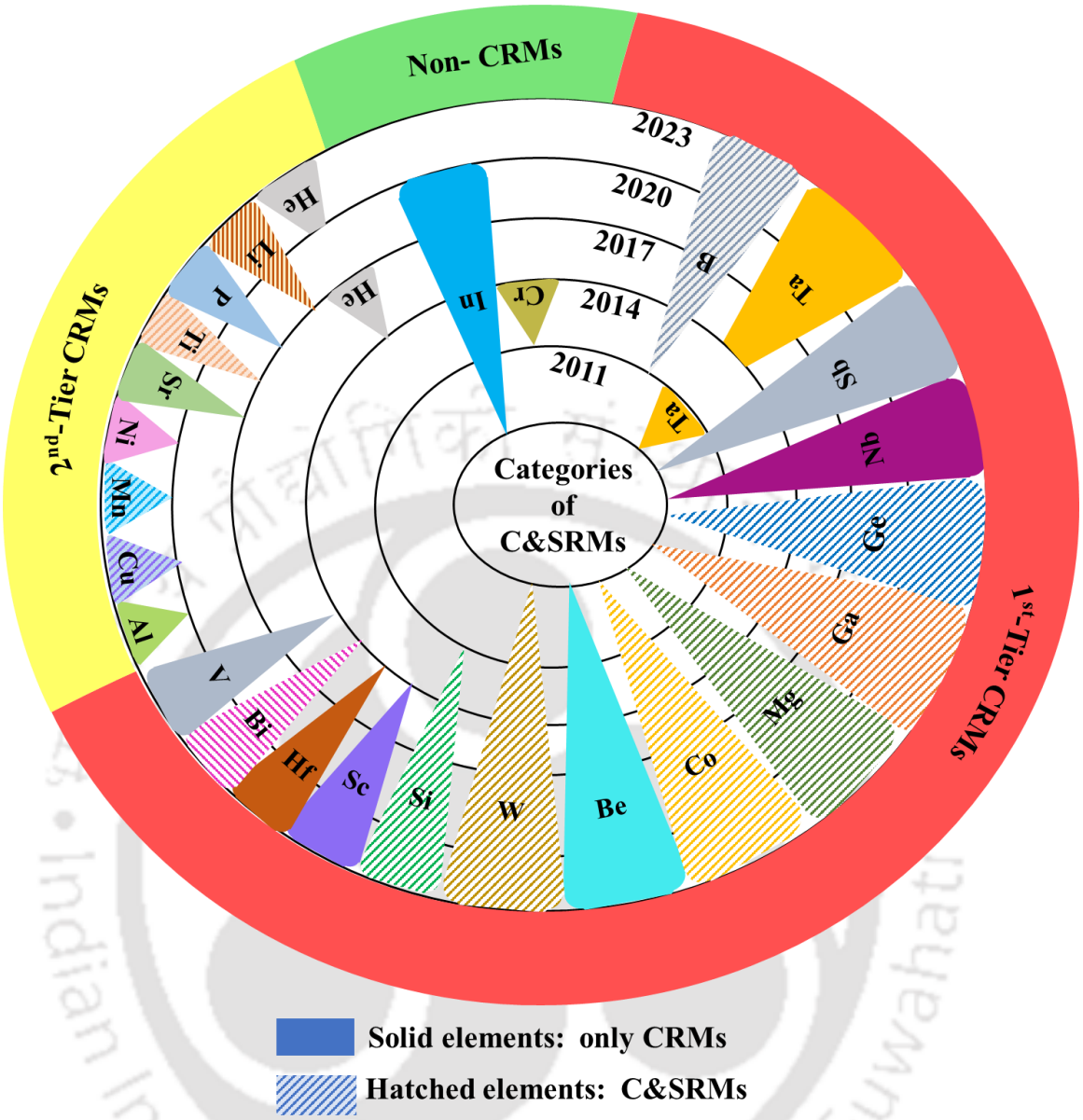

Figure 6.1. Classification of various Critical and Strategic Raw Materials (C&SRMs) [187-191, 210]

6.3. Strain-Engineering

Strain engineering refers to the process of deforming materials to induce changes in their microstructure, such as increasing dislocation density, promoting twinning, forming ultra-fine grained (UFG) or nano-crystalline (NC) structures, and in some cases, triggering phase transformations like transformation-induced plasticity (TRIP) and twinning-induced plasticity (TWIP) to enhance its properties. This encompasses conventional thermo-mechanical processing (TMP) methods, including rolling, forging, extrusion, and drawing, as well as advanced techniques commonly referred to as severe plastic deformation (SPD), such as High-Pressure Torsion (HPT), Equal Channel Angular Pressing (ECAP), Friction Stir Processing (FSP), and Twist Extrusion (TE). Other manufacturing processes include

casting, powder metallurgy (P/M), and additive manufacturing (AM), which are outside the scope of strain engineering [211, 212].

6.4. Severe Plastic Deformation (SPD)

Severe Plastic Deformation (SPD) refers to a group of metal processing techniques used to introduce extremely high strains into materials without significantly altering their macroscopic shape. The primary objective of SPD is to refine the grain structure down to the ultrafine-grained (UFG) or even nanocrystalline (NC) scale, thereby enhancing mechanical properties such as hardness, yield strength, and fatigue resistance, often via the Hall–Petch relationship[213].

Unlike conventional deformation processes (e.g., rolling or extrusion), SPD techniques impose large shear strains while maintaining the sample's overall dimensions, making them ideal for materials research and for producing bulk nanostructured materials. SPD methods function by introducing intense plastic shear deformation through repetitive pressing, torsion, or extrusion. As the deformation progresses: dislocation density increases sharply, dislocation cells evolve into subgrains and then into equiaxed ultrafine grains, grain boundaries increase in number and transform from low-angle to high-angle grain boundaries, and the structure transitions from coarse-grained to ultrafine or nanograined, which boosts strength while retaining reasonable ductility [214, 215].

6.5. Major SPD Techniques

This section outlines the most widely adopted SPD methods, including Equal Channel Angular Pressing (ECAP), High-Pressure Torsion (HPT), Twist Extrusion (TE), and Accumulative Roll Bonding (ARB), each offering unique advantages for microstructural refinement and property enhancement [216, 217].

6.5.1. High-Pressure Torsion (HPT)

HPT, imposes intense compressive and torsional stresses by subjecting the material to high pressure while rotating, resulting in extreme grain refinement, particularly near the sample's edges.

6.5.2. Equal Channel Angular Pressing (ECAP)

ECAP applies shear stress uniformly as the material passes through a die composed of two channels intersecting at an angle (typically 90°). The material undergoes shear deformation

at the channel intersection but retains its original cross-section, enabling repetitive processing. It induces more homogeneous deformation across larger samples.

6.5.3. Friction Stir Processing (FSP)

FSP is derived from Friction Stir Welding (FSW). It uses a rotating, non-consumable tool that plunges into the workpiece and stirs the material. The intense plastic flow and frictional heat result in dynamic recrystallization of the microstructure.

6.5.4. Twist Extrusion (TE)

The material is extruded through a die with a twisted channel, which imposes intense shear strain as the material flows through the helical path.

6.5.5. Accumulative Roll Bonding (ARB)

Metal sheets are stacked, rolled together under high pressure, then cut, restacked, and rolled again. This is repeated over several cycles to achieve ultrafine grain sizes.

6.6. Effect of Various Synthesis Routes on Mechanical Property of MPEAs

Figure 6.2 presents a comparison of yield strength (YS) of four popular MPEAs CoCrNi, CoCrFeMnNi, $Al_{0.1}$CoCrFeNi and HfNbTaTiZr, showcasing different mechanical properties based on the synthesis route. A detailed description of the manufacturing process, crystal structure, hardness, yield strength (YS), ultimate tensile strength (UTS), and elongation, as reported in the literature, can be found in Supplementary 6s. Although the YS of post-processed (heat-treated) samples are included in Supplementary Table 6s, they were excluded from the preparation of Figure 6.2. This is because the heat-treated samples typically exhibit increased ductility at the expense of strength.

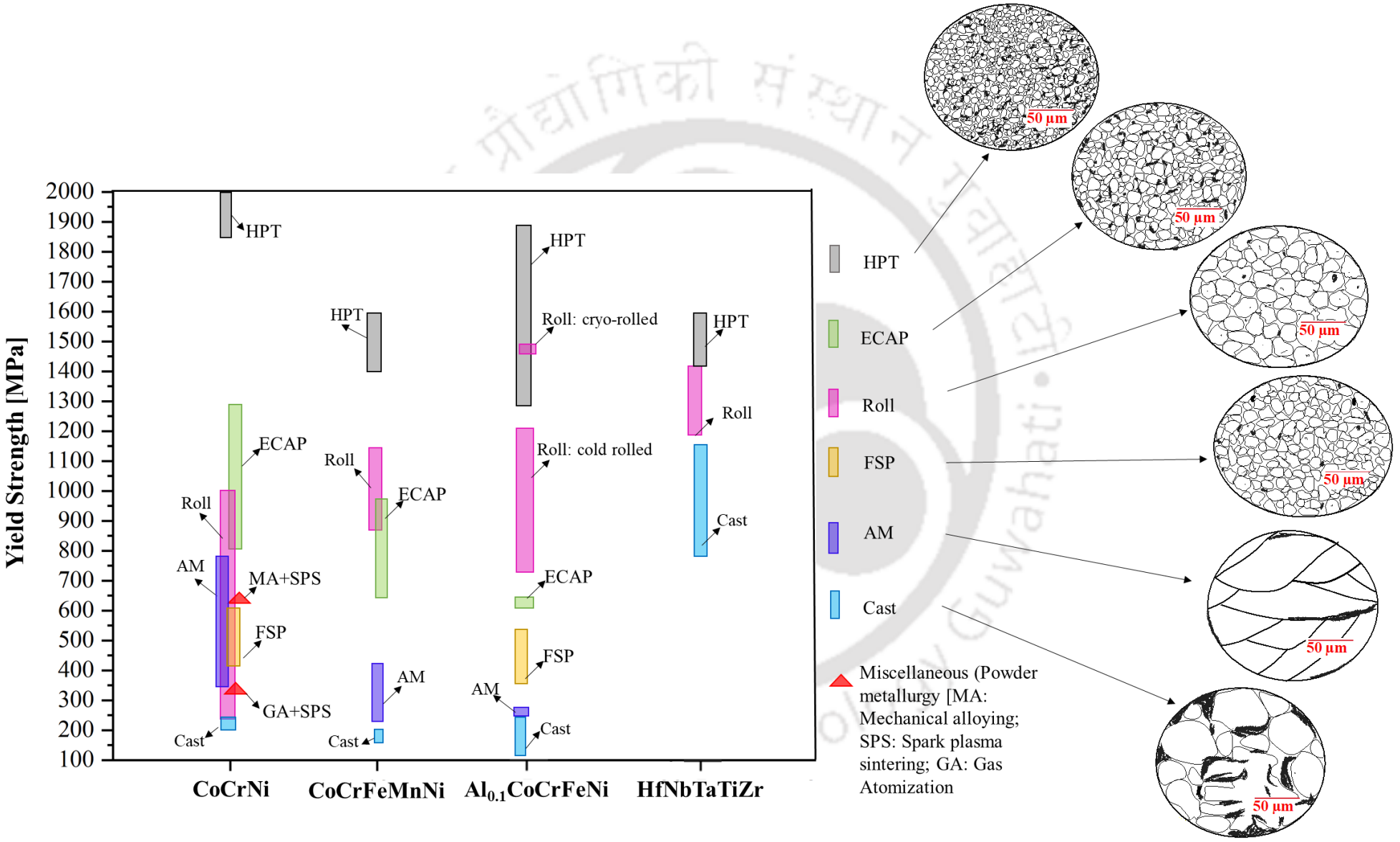

Figure 6.2. Yield strength of four representative MPEAs showing the influence of processing route on the grain structure

Moreover, in certain experimental studies, tensile testing was not conducted, leading to missing information in the literature, and as a result, some data is unavailable for comparison in Figure 6.2. For instance, the tensile test results of HfNbTaTiZr HEA processed through FSP, ECAP, AM and P/M have not been reported. Consequently, further experimental investigation of a wide range of MPEA compositions synthesized via diverse processing routes is indispensable to initiate a full-fledged exploration of strain engineering approaches in the synthesis of MPEAs/HEAs/CCAs.

As illustrated in Figure 6.2, all four MPEAs processed via HPT exhibit higher YS, indicating that strain engineering can have a more pronounced effect on the mechanical properties (yield strength in this case). This suggests that strain rate can be used to control the resulting mechanical properties in MPEAs, providing a compelling alternative to eliminate the need for the change of chemical composition.

CoCrFeMnNi HEA crystallizes in an FCC phase, and it was the first reported MPEA/HEA with excellent room-temperature ductility (~ 61.7% - 71%) but relatively low YS (~ 209 - 215 MPa) and UTS (~ 491- 496 MPa). The grain size in this state typically ranges from approximately ~300-400 μm [120, 218]. In contrast, when processed via High-Pressure Torsion (HPT), the CoCrFeMnNi alloy demonstrate a significantly higher YS (~1400 MPa) and UTS (~1740 MPa) at the expense of ductility, which dropped to 4% with an ultra-fine grain (UFG) size of ~10 nm [219]. Post-deformation annealing (PDA) at 1073K for 1h of the HPT-processed CoCrFeMnNi HEA resulted in 80% recovery of ductility, albeit, with a corresponding reduced YS of 530 MPa and UTS of 680 MPa and a grain size of ~4 μm.

The CoCrNi a medium entropy alloy (MEA) exhibits superior mechanical properties compared to its parent alloy, CoCrFeMnNi a high entropy alloy, irrespective of the processing route (see Figure 6.2). When processed via HPT, the CoCrNi MEA demonstrates an exceptionally high YS of ~1880 MPa and UTS of around ~2170 MPa and a moderate ductility of ~9% with a grain size of ~660 nm [220]. Schuh et al. [221] reported similar high YS (1901±114 MPa) and UTS (2067±153 MPa), though with a lower ductility (3.9 ±1.5%) for the HPT-processed CoCrNi MEA. Moreover, under cryogenic conditions, the HPT-processed CoCrNi alloy exhibit excellent strength and ductility (YS = 1975 MPa, UTS= 2054 MPa, and ductility= 27%), outperforming its mechanical properties at room temperature (YS = 1435MPa, UTS= 1580 MPa, and ductility= 24%) [222]. This demonstrates that exceptional mechanical properties can be achieved with fewer constituent elements, indicating the potential for reduced

use of chemical elements without negating the performance. CoCrNi contains less C&SRMs than its parent alloy CoCrFeMnNi and still exhibit superior mechanical properties, highlighting the scope of reduced use of C&SRMs.

The superior strength-ductility synergy of CoCrNi MEA compared to CoCrFeMnNi HEA has been attributed to its low stacking fault energy (SFE). The wider separation between Shockley partials in CoCrNi results in lower SFE, thereby enabling the activation of nano-twinning at significantly lower strains, both at room temperature and at cryogenic temperature. It is widely recognized that twin boundaries can enhance mechanical properties by increasing the strain hardening rate and delaying the onset of necking [122]. It should be noted that both CoCrFeMnNi and CoCrNi MPEA show strong temperature-dependent strength and ductility phenomena [222]. Otto et al. [223] highlighted the influence of temperature on the mechanical properties of CoCrFeMnNi HEA. They observed an improvement in strength from 763 MPa at room temperature to 1280 MPa at a cryogenic temperature (77K), along with an enhanced ductility from 50% to 70% for cold-rolled (~87%) CoCrFeMnNi HEA.

Gludovatz et al.[224] reported improved strength and ductility (YS = 657 MPa, UTS = 1311 MPa, ductility = 0.9) for cold-forged and cross-rolled CoCrNi alloy at a reduced temperature of 77K. At room temperature, the YS and fracture toughness of CoCrFeMnNi HEA and CoCrNi MEA were found to be comparable, while the UTS and ductility of CoCrNi MEA were significantly higher than those of the CoCrFeMnNi HEA by 15% and 30%, respectively. However, at a cryogenic temperature of 77K, the UTS of both CoCrFeMnNi HEA and CoCrNi MPEA was comparable (~1300 MPa), but CoCrNi exhibited 27% higher ductility and 25% greater fracture toughness. Thus, it can be noticed that at room-temperature, the CoCrFeMnNi HEA suffers from a strength-ductility tradeoff. Post-processing heat treatment, such as annealing of ultrafine-grained (UFG) or nano-crystalline (NC) materials, help achieve a desirable balance of mechanical properties. However, this raises a key question: “Can the strength-ductility synergy be improved without heat treatment? To address this strength-ductility tradeoff, various strategies have been explored over the past few decades, including generating bimodal or heterogeneous microstructure [225], introducing nanotwins [226] [227], and controlling twinning /transformation induced plasticity (TWIP/TRIP) mechanism [228]. Picak et al. [229] demonstrated the formation of a desirable heterogeneous microstructure in the CoCrFeMnNi MPEA after two passes of ECAP at both high and medium temperatures, thereby eliminating the need for subsequent heat treatments. The resulting microstructure exhibited a bimodal/ heterogeneous grain size distribution, characterized by two distinct regions: one with large,

elongated grains, and the other consisting of recrystallized ultrafine grains (UFG). This heterogeneous structure facilitated a composite effect during plastic deformation, with the large grains enabling extended plasticity, while the smaller grains contributed to strengthening. Transmission Electron Microscopy (TEM) investigation revealed elongated UFGs, along with deformation twinning and ε-martensite lamellae, even after high-temperature deformation. Typically, dislocation plasticity serves as the primary deformation and strengthening mechanism in CoCrFeMnNi HEAs at room temperature. However, ECAP demonstrated significant potential for strengthening these materials by promoting grain refinement and increasing dislocation density. Notably, ECAP was shown to activate both Twinning-Induced Plasticity (TWIP) and Transformation-Induced Plasticity (TRIP), which substantially enhances the resistance to dislocation motion. The authors attributed the observed enhancement in strength and ductility to the simultaneous activation of twinning (TWIP) and ε-martensite (TRIP) mechanisms. This simultaneous activation of TWIP and TRIP in severely plastically deformed CoCrFeMnNi HEA was reported for the first time, warrants a more detailed investigation.

Furthermore, a superior combination of strength and ductility can be achieved in compositions exhibiting low stacking fault energy, primarily through the activation of nano-twinning mechanism, as previously demonstrated in the case of CoCrNi MEA. Thus, by processing materials to induce bimodal or heterogeneous microstructures, promoting nanotwins, controlling TWIP and TRIP mechanisms, or utilizing materials with inherently low SFE, eliminates the necessity of additional post-processing to achieve high strength-ductility synergy.

Moreover, akin to CoCrNi, which contains reduced C&SRMs compared to its parent CoCrFeMnNi, exhibiting superior mechanical properties, newer compositions without C&SRMs can be developed. Strain engineering approach inducing low-mobility defects, ultrafine grained structure (either homogeneous or heterogeneous, depending upon the specific requirements) and activating TWIP and TRIP mechanisms can be used. However, these strategies are primarily effective under ambient conditions. Achieving a similar strength-ductility synergy in hydrogen-rich environments presents a significant challenge due to the susceptibility to hydrogen embrittlement. To address this issue, Mohammadi et al. [230] conducted HPT deformation on $Al_{0.1}$CoCrFeNi alloy, an FCC-phase alloy noted for its sluggish hydrogen lattice diffusion. The HPT processing resulted in an impressive combination of high strength (YS = 1960 MPa) and ductility (10%) through the generation of low-mobility lattice defects, such as nanotwins and Lomer-Cottrell locks. These defects act as hydrogen trapping sites, mitigating hydrogen-enhanced localized plasticity and minimizing stress concentration. Similarly, CoCrFeMnNi HEA

processed via cold-rolling and annealing exhibited an excellent strength-ductility combination in hydrogen environments, with a significant improvement in resistance to hydrogen embrittlement due to grain refinement, which inhibited grain boundary decohesion [231]. Thus, by introducing various lattice defects, particularly low-mobility defects, and refining grain structures during TMP or SPD techniques, a desirable strength-ductility synergy can be achieved. This effect holds true in both ambient and hydrogen-exposed environments, especially for FCC-structured materials, which are known for their slow hydrogen lattice diffusion.

Aside from the study by Mohammadi et al. [230], there is a notable absence of research on the mechanical properties of HPT-processed $Al_{0.1}CoCrFeNi$ alloy in the literature. Therefore, it is crucial to conduct further experimental investigations on this alloy under HPT processing in absence of hydrogen to fully understand the unique influence of HPT processing on $Al_{0.1}CoCrFeNi$ alloy.

Similar to other compositions presented in Figure 6.2, HPT processed HfNbTaTiZr HEA subjected to a shear strain (Υ) > 40, exhibit a remarkable increase in strength, rising significantly from 830 MPa in its as-received state to 1900 MPa after deformation, primarily due to grain refinement. Surprisingly, despite substantial gain in strength, the specimen retained a notable degree of ductility, with only a minor reduction in total elongation at failure (from 9.2% to 7.9%). This retention of ductility was attributed to the dynamic deformation and recovery processes occurring at $\Upsilon > 40$, establishing a dynamic equilibrium of generation and annihilation of defects. This equilibrium resulted in a homogenous microstructure characterized by nanocrystalline, equiaxed grains. However, no conclusive evidence was found to attribute this enhancement to commonly known mechanisms, such as twinning or a bimodal grain size distribution, which are typically employed to achieve strength-ductility synergy. The underlying cause of the simultaneous improvement in strength and ductility remains unexplored, presenting a promising avenue for future research [232].

6.7. Effect of Various Synthesis Routes on Mechanical Property of Pure Elements

Given the high YS observed in HPT-deformed MPEAs across various compositions, it becomes imperative to investigate whether similar trends extend to pure elements or if this observation is exclusive to MPEAs. To address this question, more data was extracted from literature for several pure elements (Al, Cu, Mg, Ni, Ta, Ti, Fe). A comprehensive description of each element's processing conditions, crystal structure, hardness, yield strength, ultimate tensile strength, and elongation, as reported in the literature, is provided

in Supplementary 6s. However, only a limited number of studies report YS for specific pure elements across all processing routes (see Figure 6.3).

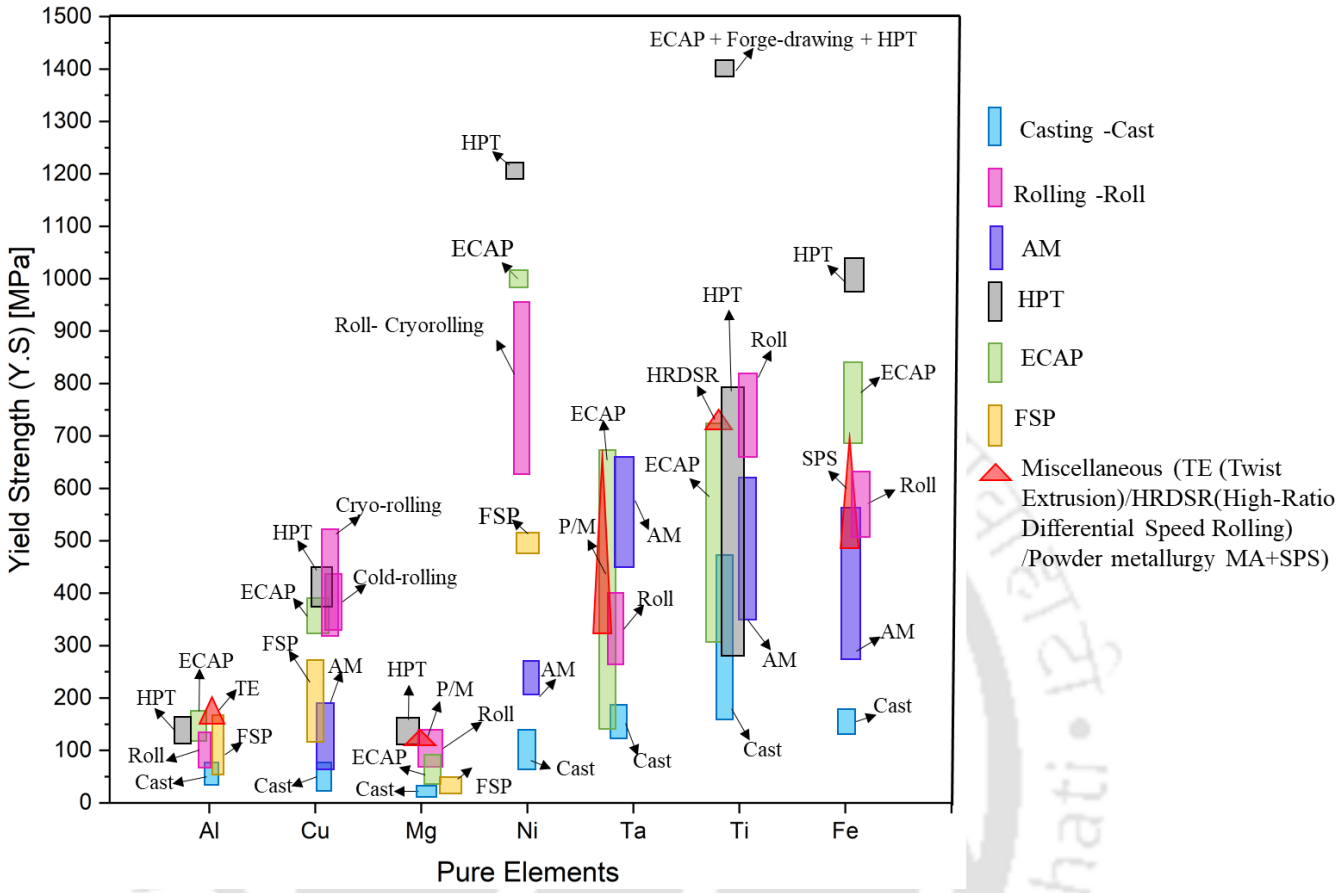

Figure 6.3. Yield strength of pure elements obtained from various manufacturing processes

Except for Al and Cu, a similar trend to that observed in MPEAs was also noted for pure elements, where the YS of samples processed via high-pressure torsion (HPT) consistently exceeded that of samples produced through other processing methods (see Figure 6.3). Notably, ECAP processed Al exhibited a slightly higher YS of 173 MPa after 10 ECAP passes, compared to 146 MPa for HPT-processed Al at an equivalent strain of 25.1. This may be attributed to the higher stresses exerted during ECAP compared to HPT.

In the case of pure Cu, the YS of HPT-deformed samples vary in the range of 370-474 MPa, the highest among all processing methods, except for cryo-rolled pure Cu, which exhibits YS ranging from 336 to 520 MPa. The increase in YS could be linked to the operating temperature, where rolling was carried out at cryogenic temperature, which enhances material's strength. Regarding pure Ta, the YS of HPT-processed samples could not be displayed in Figure 6.3, as only a single study provided data on the UTS of HPT-processed Ta without corresponding YS data [233]. For commercially pure (cp) Ti, the YS of HPT-processed samples ranged from

280 to 790 MPa [26-28]. However, the strength increased up to 1400 MPa when ECAP was performed at 450°C (with an angle of 90°, route Bc, n=8), followed by additional forge-drawing at 300°C, reducing the diameter from 24 mm to 16 mm, prior to HPT. This combination of processes before HPT facilitated grain refinement and enhanced structural homogeneity, resulting in improved mechanical properties [214].

Achieving a balance of strength and ductility in MPEAs has been demonstrated through the creation of heterogeneous microstructure, combining ultrafine-grained (UFG) and larger elongated grains, or by inducing nanotwins and others [229]. Similarly, it has been proposed that the ductility of pure Cu can be enhanced by generating a bimodal microstructure (a combination of UFG and coarse grains) or by introducing twin boundaries [213]. Additionally, pure Mg processed via HPT also exhibits a bimodal microstructure both at 293K and 423K across 1/8, 1 and 10 turns. After 10 turns, the dislocation density was of the order of 3.26×10^{15} and 2.96×10^{14} at 293K and 423K respectively. This discrepancy arises from dislocation entanglements after rotations of 1/8 and 1 turn, with dynamic recrystallization initiating after 10 turns for the 293K sample. In contrast, continuous dynamic recrystallization (CDRx) was evident throughout all turns for samples processed at 423 K. Consequently, samples produced at 293 K exhibit higher YS with moderate uniform elongation, while the samples produced at 423K showed relatively lower strength but large uniform elongation after 10 HPT turns [234].

It is important to note that the extent of strength enhancement produced by severe plastic deformation (SPD) techniques cannot be universally generalized across all alloys, as the magnitude of refinement-induced strengthening strongly depends on alloy chemistry, stacking-fault energy, deformation mode, die geometry, strain path, and specific processing parameters (e.g., number of passes, rotation angle, temperature). For this reason, a single comparative plot ranking SPD method in terms of strengthening potential would be scientifically misleading. Instead, alloy-specific comparisons, as presented in Figures 6.2 and 6.3, provide a more accurate and meaningful visualization of SPD-induced strengthening behaviour across different materials systems. These figures already capture the comparative trends by illustrating the yield-strength ranges achieved by various SPD routes for multiple alloys without imposing an oversimplified universal hierarchy.

6.8. Fundamentals of Microstructural Evolution During Plastic Deformation

Figure 6.4 highlights the effect of TMP/SPD processing on microstructure of an alloy/element. A more fundamental question at this stage to answer is “How does the microstructure evolve during SPD or conventional TMP?” Clearly, answering this question requires a fundamental

materials science approach. Typically, when a material undergoes plastic deformation, a substantial number of dislocations are generated, leading to an increase of dislocation density. These dislocations then rearrange or annihilate, depending on the prevalent restoration mechanism.

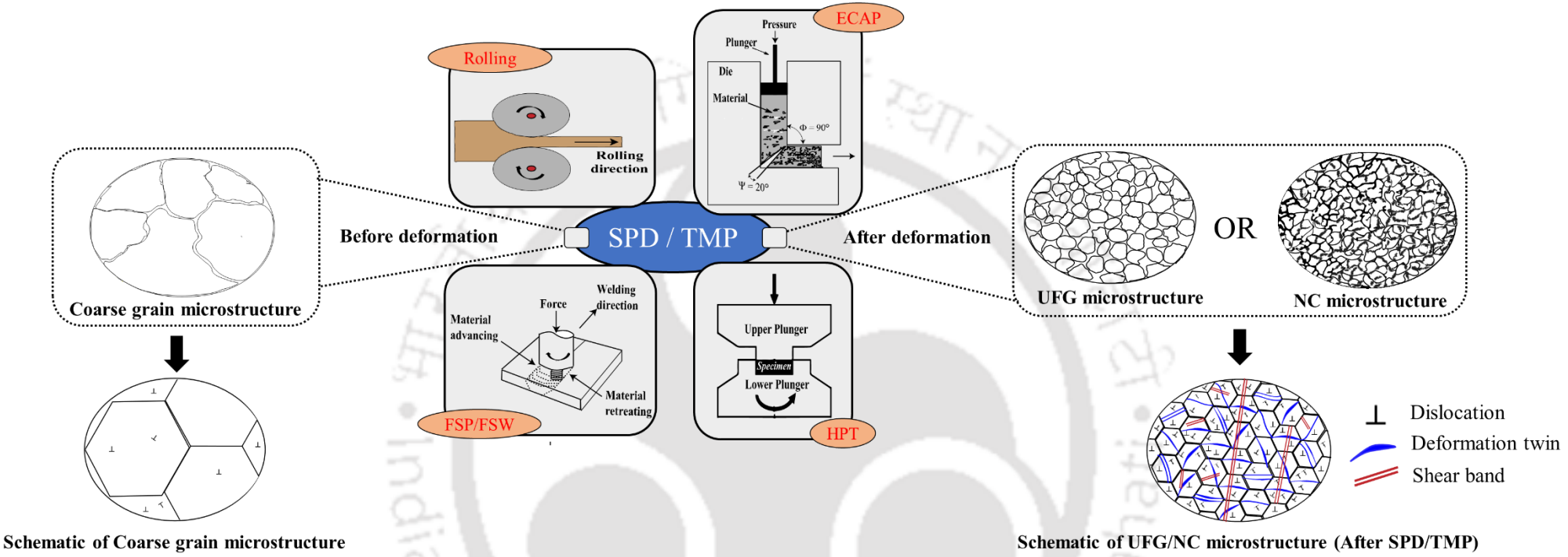

Figure 6.4. Effect of TMP or SPD processes on the microstructure of an alloy

6.8.1. Types of Restoration Mechanism Involved During Plastic Deformation

Dynamic recovery (DRV) and dynamic recrystallization (DRx) are the two crucial restoration mechanisms, which help to modify the microstructure by arranging dislocations during deformation. The three most critical microstructural features that define the microstructural evolution during deformation are grain size, grain shape (equiaxed or elongated/columnar) and grain boundary character distribution, such as low-angle grain boundaries (LAGBs) and high-angle grain boundaries (HAGBs). During DRV, the mechanical properties of a deformed material are partially restored through rearrangement and annihilation of dislocations. As strain is experienced by the material, dislocation generation becomes more pronounced, leading to an increase in the dislocation density. Eventually, a steady state is reached whereby dislocation generation and annihilation balance each other, resulting in the formation of subgrains surrounded by low-angle grain boundaries (LAGBs). DRV primarily involves the migration of LAGBs inside the deformed grains and is typically observed in materials with high stacking fault energy (SFE) or those processed at lower temperatures (approximately 0.4×Tm), facilitating the restoration of material properties.

Dynamic recrystallization (DRx) can be categorized into three types:

i. Discontinuous Dynamic Recrystallization (DDRx)
ii. Continuous Dynamic Recrystallization (CDRx)
iii. Geometric Dynamic Recrystallization (GDRx)

The specific recrystallization mechanism depends on factors such as stacking fault energy (SFE), initial grain size and processing conditions. DDRx is prevalent in materials with low stacking fault energy (SFE) during hot deformation, where nucleation of new strain-free grains occurs heterogeneously due to bulging of dislocations at grain-boundaries. In materials with low SFE, dislocations are unable to easily cross-slip, leading to the formation of a necklace-like structure at the grain boundaries. As deformation progresses, the strain-free nucleates start to grow at the expense of dislocations, migrating across the grain boundaries [235]. In certain cases, particularly during hot deformation, if the strain is halted after reaching a critical value without a reduction in temperature, the nuclei continue to grow using the stored energy. This phenomenon is referred to as post-dynamic recrystallization (PDRx) or metadynamic recrystallization (MDRx). In contrast to PDRx/MDRx, CDRx does not involve distinct nucleation and growth phases. Instead, it evolves the microstructure progressively, with subgrains surrounded by LAGBs transforming into grains

enclosed by HAGBs as subgrains boundary misorientation increases at higher levels of deformation. CDRx is particularly prevalent in materials with high SFE, and can occur over a broad range of temperatures, from low to high-temperature deformation. GDRx is generally observed in materials with high SFE, undergoing deformation at elevated temperatures and large strain. During this process, HAGBs migrate, forming serrations with a wavelength comparable to the subgrain size. Significant grain elongation and thinning take place, and once the grain thickness reduces to below 1-2 subgrain sizes, the developed serrations pinch off, resulting in the formation of equiaxed grains with HAGBs. GDRx is especially common in materials with high SFE and is frequently observed during deformation to large strains with significant reduction in one direction, such as in hot rolling, where the original grains become elongated and refined [236]. The effect of other factors such as initial grain size and processing conditions has not been extensively studied for CDRx and GDRx, as these mechanisms of restoration of microstructure and mechanical properties were introduced later with the advent of SPD processes, hence not addressed in this study. However, it is important to emphasize that no definitive rule exists to determine which type of dynamic recrystallization (DDRx, CDRx, or GDRx) will dominate under specific processing conditions [235]. For instance, CDRx can dominate in low SFE materials, as observed during the rolling of fine-grained 304 austenitic stainless steel [237]. Conversely, DDRx may occur in high-SFE materials, as reported in high-purity aluminum [238]. Moreover, depending on the processing conditions and initial grain size, these mechanisms can transition from one to another (e.g., from DDRx to CDRx) or even coexist simultaneously, as seen with the coexistence of CDRx and GDRx in Zircaloy-4 [239]. Consequently, generalizing the dominant restoration mechanism under given conditions remains a complex challenge.

6.8.2. Influence of Microstructural Evolution on Mechanical Properties

As the microstructure of a material evolves under plastic deformation, its mechanical properties also exhibit corresponding changes. The Hall-Petch relationship has long substantiated the influence of ultra-fine grained (UFG) and nano-crystalline (NC) structures on the mechanical properties of alloys. Materials deformed via SPD have consistently demonstrated enhanced YS (as shown in Figure 6.2 and 6.3), primarily due to their fine-grained structures (with grain sizes ranging from 200 nm to 1 μm), high dislocation density, and presence of nano-twins. Notably, HPT-processed materials exhibit exceptional strength, characterized by a significant fraction of HAGBs and grain sizes below 100 nm. Grain-boundary strengthening is well-described by the Hall-Petch relationship (see equation 6.1) [240]. Kumar et al. [241], attributed the increased

strength of FSP-processed $Al_{0.1}CoCrFeNi$ to a combination of grain boundary strengthening and lattice friction stress (commonly referred to as 'Peierls stress'), which is the force required to move a dislocation within the atomic plane of a unit cell [242, 243]). Their observations of the gauge section of the tensile sample in the FSP-processed alloy revealed a distinct polycrystalline behavior, characterized by a significantly small grain size of 14 ± 10 μm, compared to the as-received sample's grain size of 500 μm. The reduction in grain size accommodated a larger number of grains, thereby amplifying the effectiveness of lattice friction stress and grain boundary strengthening mechanisms. In contrast, for the as-received sample, only the lattice friction stress contributed to YS, as the influence of grain boundaries was deemed negligible. It was further suggested that the contribution of dislocation strengthening to the YS could be considered negligible, given the low dislocation density present in the nugget microstructure after FSP [241].

Effect of Dislocation Density on Materials Strength

Dislocation density plays a pivotal role in material strengthening, in contrast to the earlier notions that dislocations tend to weaken a material. In reality, a high dislocation density is highly desirable for improving strength. The strengthening due to dislocations can be quantitatively described using Taylor's equation, which correlates the increase in strength with dislocation density (see eq 6.2) [240].

$$\sigma_y = \sigma_o + kd^{-1/2} \tag{6.1}$$

$$\sigma_y = \sigma_o + \alpha GbM\sqrt{\rho} \quad \text{where } \rho = \rho_0+\rho_b \tag{6.2}$$

where σ_o is friction stress, k is the locking parameter, d is grain size, α is dislocation strength parameter, G is shear modulus, M is Taylor factor, b is Burgers vector, ρ is total dislocation density, ρ_0 is the dislocations present between the boundaries, and ρ_b is the GNDs contained within low angle boundaries.

In this context, dislocations can be categorized into two types: statistically stored dislocations (SSD) and geometrically necessary dislocations (GND). SSDs arise from random trapping during plastic deformation, while GNDs emerge in regions with high strain gradients ensuring geometrical compatibility and preventing the formation of overlaps and voids. GNDs are critical for accommodating localized deformation within the crystal structure. The presence of GNDs plays a significant role in influencing the flow stress of material, as described by the

Taylor's model.

Effect of Mechanical Twinning on Materials Strength

In addition to the dislocations, mechanical twinning or deformation-induced twinning provides an alternative mechanism for accommodating plastic deformation in materials. Deformation twinning involves formation of mirror-image regions, known as twins, within a grain in response to shear stress. These twins introduce twin boundaries, acting as barriers to dislocation motion, thereby contributing to strengthening through grain refinement as described by the Hall-Petch hardening rule. Mechanical twinning was observed in HPT-deformed CoCrFeMnNi HEA [217], where the propensity of deformation caused an increase in twin density, along with the formation of new twin variants (micron-sized blocks of twin lamellae). At much higher strains ($\boldsymbol{\gamma}$ ranging from ~4.0 to ~50), the twin lamellae transformed, gradually diffusing into a homogeneous nano-crystalline (NC) structure. This demonstrated that deformation twinning can serve as a dominant mechanism for grain refinement (down to ~50 nm), resulting in exceptionally high strength accompanied by moderate ductility. Similarly, during plane-strain multi-pass rolling (ε = 80%), conducted at both room and liquid nitrogen temperatures, deformation twinning was observed to be the primary strengthening mechanism. This led to a significant increase in UTS from 440 MPa to 1500 MPa at 77K and 1200 MPa at 293K, though at the cost of reduced ductility from original 71% down to 12% at 77K and 14% at 293K [244].

Other Factors Affecting Materials Strength

To understand the reasons why HPT leads to superior mechanical properties compared to other processing techniques, it's indispensable to understand the response of material under deformation or loading. In the subsequent section, the influence of crucial factors involved in different synthesis routes, the response of material under different deformation conditions and the mechanisms causing strengthening of materials have been discussed extensively.

The microstructure and mechanical properties of an alloy synthesized through various routes are influenced by several key factors. These include **cooling rate,** which is crucial in both casting and additive manufacturing (AM); the **applied pressure and temperature** during Hot-isostatic pressing (HIP) in powder metallurgy, where both parameters play a crucial role in determining density, porosity and microstructure. Conversely, in spark-plasma sintering (SPS), **temperature** predominantly governs the consolidation of powders. HIP typically results in higher density and finer microstructure compared to conventional sintering methods and is particularly advantageous

for materials that are difficult to sinter. Additionally, factors such as **applied strain and processing temperature** during conventional-TMP and SPD techniques significantly influence the resulting microstructure and mechanical properties of an alloy.

The YS of additively manufactured alloys has demonstrated superior performance compared to cast samples, regardless of the elemental composition (see Figure 6.2 and 6.3). This enhancement can be attributed to the rapid cooling rate during AM, which inhibits grain growth and promotes a finer microstructure. The typical cooling rates involved in casting and AM are presented in Table 6.1. However, despite the improved properties compared to as-cast alloys, the strength of additively manufactured alloys remains lower than those produced through conventional TMP and SPD methods. This disparity can be ascribed to several factors such as the formation of dendritic or columnar structures during layer-by-layer deposition, the introduction of residual stresses due to thermal gradients and rapid solidification, anisotropic mechanical properties, microstructural inhomogeneities, and porosity, particularly in powder-bed fusion techniques such as selective laser melting (SLM) and electron beam melting (EBM).

Table 6.1. Cooling rate during different processing techniques

Processing route	**Cooling Rate (**K/s**)**
Casting	10^1 to10^2 K/s [245-247]
Additive Manufacturing	10^2 to10^8 K/s [182, 245, 248]

High-pressure torsion (HPT), Equal channel angular pressing (ECAP), Friction stir processing (FSP) and Twist extrusion (TE) are examples of SPD techniques, all of which fall under the “Top-down” approach, alongside conventional TMP methods such as rolling, forging and others. During “top-down” approach, bulk samples with a relatively coarse grain are subjected to substantial strain in order to refine the grain size, ultimately yielding ultrafine-grained (UFG) or a nanocrystalline (NC) structure [249]. Notably, this method mitigates the introduction of contaminants or porosity, common issues encountered during powder metallurgy (P/M) processes. Powder metallurgy itself contrarily employs a "bottom-up" approach; wherein bulk samples are fabricated by consolidating individual particles. This typically involves high-energy ball milling followed by consolidation techniques such as spark plasma sintering (SPS) or hot isostatic pressing (HIP) [249]. While this approach offers the advantage of producing fine microstructures, its applicability is often limited by challenges such as small size of finished

products, the introduction of contaminants and residual porosity.

Conventional TMP methods, such as rolling, extrusion, drawing and forging are typically conducted at warm to hot temperatures to impart large strains while minimizing the risk of introducing defects such as cracks. This is because these processes primarily apply uniaxial compressive stress, which at ambient temperatures often lead to formation of various defects. In contrast, non-conventional TMP or SPD methods impart significant strain without inducing cracking by utilizing a combination of compressive stress (to prevent cracking) and shear stress (to introduce large strain). Furthermore, one of the key advantages of SPD techniques is their ability to impose large plastic strains on a material without altering its overall shape; that is, the material retains its initial geometry after the SPD process [250]. Strains of several hundred to thousands of percent can be achieved during SPD processes. For instance, during ECAP, a material is subjected to multiple passes through a die with intersecting channels, leading to cumulative strain with each pass. Similarly, in HPT, the material undergoes torsional deformation under high pressure, resulting in substantial strain accumulation. Table 6.2 provides an overview of the typical strain rates (sec^{-1}) associated with various manufacturing processes. Table 6.3 highlights effective plastic strain associated with various manufacturing processes.

Table 6.2. Strain rate during different processing techniques

Processing route	**Strain rate (sec^{-1})**
Rolling (Plane strain compression)	10^1 to 8×10^2 (depending on the working temperature and thickness reduction) [251]
ECAP	10^{-3} to 10^0 (depending on the corner and channel angle) [252]
HPT	10^{-2} to 2×10^1 (depending on the pressure, rotation speed and number of turns) [212]
Powder metallurgy	--

Strain rate ($\dot{\varepsilon}$) refers to the time dependent strain or the rate at which deformation occurs in a material. Though, it quantifies the rate of deformation but does not reflect the cumulative strain or deformation imparted to the material during processing.

Table 6.3. Effective plastic strain during different processing techniques.

Processing route	Effective plastic strain
Uniaxial compression (UC)	0.69 (50% reduction in height) - 2.30 (90% reduction in height) [213]
Rolling (Plane strain compression)	0.80 (50% reduction in height) - 2.66 (90% reduction in height) [213]
ECAP	1.15 (Φ (oblique angle (or channel angle)) = 90 degrees and Ψ (corner angle) = 0 degrees). For more common angle of Φ = 90 degrees and Ψ = 20 degrees $\varepsilon_{eff} = 1$; for N such passes, the total ε_{eff} will be N. [213]
HPT	effective plastic strains of about 8-10, and in some cases up to 20. [213]
Powder Metallurgy (P/M)	effective plastic strains of about 0.01 to 0.1 per pass during powder compaction. [253]

Effective plastic strain ($\mathcal{E}_{eff}$) is a key parameter that quantifies the cumulative permanent deformation that the material experiences during its deformation process. Unlike strain rate, which is measured in sec^{-1}, effective plastic strain is a dimensionless quantity and is calculated by integrating the plastic strain over the entire deformation cycle. The calculation of $\mathcal{E}_{eff}$ is governed by Equation 6.3, with specific formulations for the ECAP and HPT processes represented by Equations 6.4 and 6.5, respectively [213].

$$\mathcal{E}_{eff} = \left\{\frac{2}{9}[(\mathcal{E}_{11} - \mathcal{E}_{22})^2 + (\mathcal{E}_{22} - \mathcal{E}_{33})^2 + (\mathcal{E}_{33} - \mathcal{E}_{11})^2] + \frac{1}{3}(\gamma_{12}^2 + \gamma_{23}^2 + \gamma_{31}^2)\right\}^{0.5} \quad (6.3)$$

$$\mathcal{E}_{eff} = \frac{1}{\sqrt{3}}\left[2\ \cot\left(\frac{\Phi+\Psi}{2}\right) + \Psi\ cosec\left(\frac{\Phi+\Psi}{2}\right)\right] \quad (6.4)$$

$$\boldsymbol{\gamma} = \frac{2\pi r N}{t} \quad (6.5)$$

where Φ is the inner angle/ oblique angle/ channel angle, Ψ is the outer angle/ corner angle, $\boldsymbol{\gamma}$ is the shear strain along the radius (r), *N* is the number of rotations and *t* is thickness of the disk.

Table 6.3 illustrates the extent of effective plastic strain induced in various manufacturing

processes. During rolling, which is a conventional TMP method, the effective plastic strain of 0.8 results in 50% reduction in height, while it reaches 2.66 for a 90% reduction in height [213].

For the most common inner angle (Φ = 90°) and outer angle (Ψ = 20°) in a single ECAP pass, the effective plastic strain value is 1. For N such passes, the total imposed effective plastic strain becomes N. By varying the inner and outer angles, the amount of effective plastic strain induced can be adjusted. For instance, with Φ = 90° and Ψ = 0°, the effective plastic strain per pass increases to 1.15 [213]. The HPT process induces a broad range of effective plastic strain, from a minimum of 8 to a maximum of 20. This significant capacity for imparting high levels of effective plastic strain is a key factor contributing to the superior YS of materials processed via HPT, compared to those subjected to other manufacturing techniques. The extent of effective plastic strain across various manufacturing processes is schematically represented in Figure 6.5.

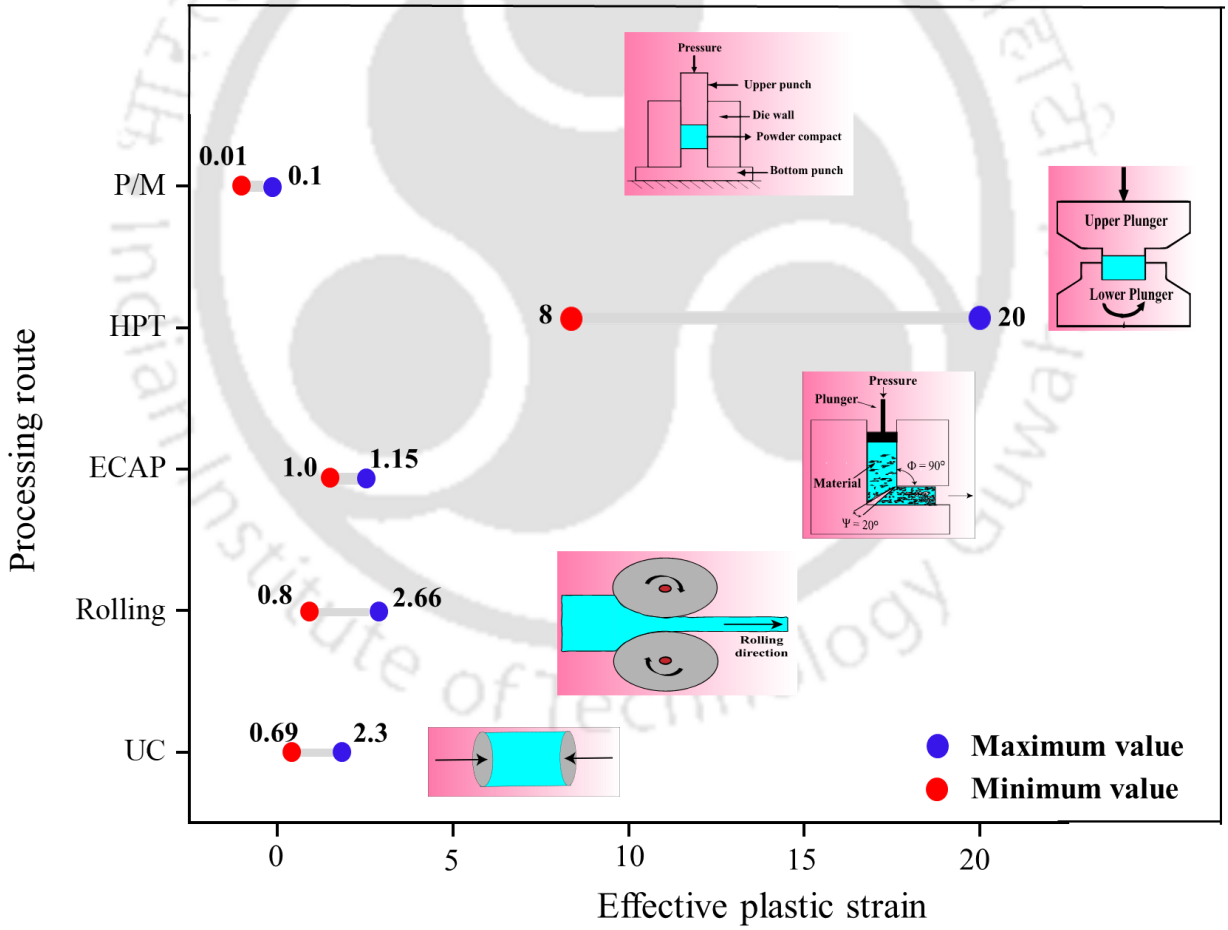

Figure 6.5. Effective plastic strain during different processing techniques. P/M: Powder Metallurgy; HPT: High Pressure Torsion; ECAP: Equal Channel Angular Pressing; UC: Uniaxial Compression

6.9. Mechanical and Environmental Advantages of SPD Over Conventional Methods

Figure 6.6 demonstrates the effectiveness of employing SPD processing over conventional methods. SPD-processed components have been observed to offer exceptional mechanical properties such as increased strength and toughness. For instance, Sadasivan & Balasubramanian [254] reviewed various SPD techniques used for processing tubular materials, which are among the most widely used industrial products. They emphasized that SPD-processed tubes, with strengthened walls, can be produced with reduced thickness, leading to material savings and contributing to sustainability. Moreover, components processed via SPD demonstrate improves fatigue life, corrosion resistance, and wear resistance compared to those produced through conventional methods. This can reduce the frequency of replacements and repairs, resulting in cost savings and supporting the development of more sustainable products with lower carbon emissions. SPD techniques have also been employed to fabricate high-strength components, such as micro-bolts from UFG carbon steel [255], turbine blades from AA6063 [256], and high-strength bolts from AA6061 [257], using hybrid processes such as drawing, ECAP, and rolling.

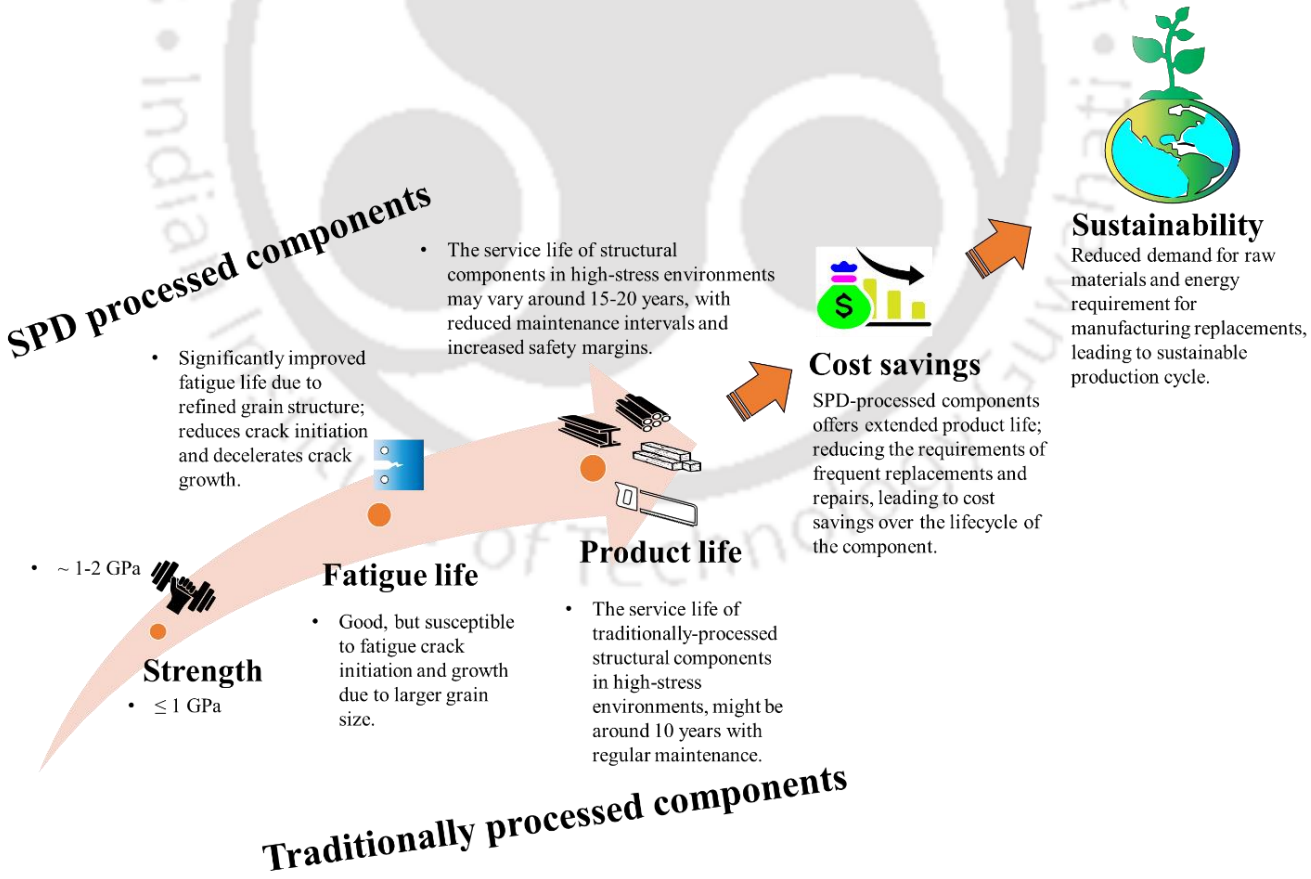

Figure 6.6. Cost-effectiveness of using SPD over traditional-processing routes

6.10. Summary

This chapter underscores the critical role of strain engineering as a timely and effective non-ML-based physical design strategy for reducing dependence on critical and strategic raw materials (C&SRMs) in the development of high-performance metallic alloys. Unlike chemical tuning approaches that require compositional modification, often involving the addition of scarce or environmentally burdensome elements, strain engineering achieves significant enhancement of mechanical properties through microstructural refinement alone, eliminating the need for additional C&SRMs. Strain engineering enables precise control over key microstructural parameters, including grain size, grain structure, nanotwin formation, and the activation of deformation mechanisms such as twinning- and transformation-induced plasticity (TWIP/TRIP). These microstructural modifications improve strength, ductility, fatigue resistance, and other performance metrics that would traditionally necessitate the use of expensive or critical alloying elements.

Experimental evidence from the literature supports the effectiveness of this approach and have shown that strain engineering provides a viable path for creating sustainable alloys, particularly for demanding applications. For instance, hydrogen storage materials processed via high-pressure torsion (HPT) to achieve ultrafine-grained (UFG) structures outperform those fabricated through conventional methods such as thermal annealing, groove rolling, and high-energy ball milling [258]. Similarly, UFG pure titanium exhibits superior fatigue resistance and biocompatibility compared to conventional Ti-6Al-4V alloys, making it a promising candidate for biomedical applications [259-262]. Additionally, the incorporation of nanotwins through severe plastic deformation (SPD) enhances strength without sacrificing electrical conductivity, offering viable alternatives to copper-based alloys in high-strength electrical components. These findings suggest that SPD techniques could pave the way for a new class of high-performance, sustainable materials suited to various industrial applications, including bioimplants, electrical components, and structural engineering.

Beyond property improvements, strain-engineered materials frequently allow for reduced component thickness due to their superior mechanical properties, leading to weight reduction, lower fuel consumption in transportation, and minimized material usage in storage systems. Their superior fatigue life, corrosion resistance, and wear resistance extend longevity and minimise the need for frequent repairs and replacements. These outcomes align directly with sustainability

goals and contribute to the reduction of carbon emissions, an essential step toward achieving Net-Zero targets. Moreover, literature-based lifecycle assessments indicate that high-risk elements such as Co, W, and Nb exhibit approximately 4–10× higher CO_2 emissions per kilogram during mining, extraction, and refining compared to earth-abundant elements such as Fe, Al, and Cu. By intentionally avoiding these critical raw materials, the proposed C&SRM-free alloy design approach has the potential to substantially reduce embodied carbon, lower energy consumption during raw-material production, and decrease dependence on volatile or geopolitically sensitive supply chains. Although a full lifecycle assessment (LCA) lies beyond the scope of the present work, these quantitative indicators highlight the potential for significant environmental and resource-efficiency gains through C&SRM-free alloy design.

In conclusion, this study establishes strain engineering as a sustainable and scalable alternative to composition-based design strategies, offering a path to developing C&SRM-free or C&SRM-lean alloys suitable for diverse industrial sectors, including biomedical devices, electronics, energy systems, and structural applications. By minimizing the need for rare-earth and other critical elements, thereby reducing the environmental and energy burdens associated with their extraction, strain engineering supports more sustainable metal processing. This study not only showcases the current capabilities of strain engineering but also underscores its potential to transform material design, sustainability, and technological innovation steps that needs to be initiated across industries around the world.

This work highlights the transformative potential of strain-induced microstructural design in reducing material criticality while enhancing alloy performance, independent of machine learning or chemical modification. Together with the findings from the earlier ML–metaheuristic framework, these insights lay the foundation for the overarching conclusions of this research and define promising directions for future studies, as discussed in the next chapter.

Chapter 7

Conclusions and Future Scope

7.1. Overview

The primary objective of the present work was to study MPEAs using machine learning (ML). In view of this, robust ML frameworks were developed for predicting phases, mechanical properties, as well as optimizing multiple competing mechanical properties, and targeting the reduction of Critical Raw Materials (CRMs) while developing novel MPEAs. Moreover, it introduces a physical engineering approach to develop high-performing materials without the need of chemical tuning to minimize reliance on Critical and Strategic Raw Materials (C&SRMs).

Supervised learning algorithms were employed to predict phase formation using an experimental database extracted from the literature, with model validation performed through the experimental synthesis of a novel MPEA. The widespread use of synthetic data augmentation methods in the literature to improve model accuracy was critically evaluated, and their shortcomings were demonstrated through a comparative analysis between models trained exclusively on pure experimental data and those trained on synthetically augmented datasets. Mechanical property prediction was carried out using the open-source Python toolkit MAST-ML, rather than developing a new framework from scratch. MAST-ML was specifically designed for materials researchers with limited expertise in machine learning, providing automated workflows that streamline model development with minimal coding requirements. In this work, it was applied for the first time to complex alloy systems such as MPEAs. While the toolkit demonstrated efficiency in predicting mechanical properties, it was not without limitations. Due to limitations of MAST-ML, a novel ML framework was subsequently developed from scratch to predict and optimize multiple mechanical properties simultaneously. This framework was designed to identify alloy compositions that concurrently optimize yield strength (YS), ultimate tensile strength (UTS), and elongation ($\mathcal{E}$), thereby providing an effective solution to the long-standing strength–ductility trade-off.

To promote material sustainability and advance Net Zero objectives, this work adopted a dual strategy to minimize dependence on critical raw materials (CRMs) and critical and strategic raw materials (C&SRMs). First, a novel ML framework was developed to

design high-performance MPEAs that are either completely free of CRMs or contain them in reduced amounts. This was achieved through ML-guided chemical tuning using a large computational database of unary and binary compositions generated via CALPHAD-based Thermo-Calc (TC) simulations. The framework systematically explored the compositional space to suppress costly elements such as Co, Nb, Ta, and W while maintaining mechanical performance, thereby enabling the discovery of sustainable, high-performance alloys. Complementing this ML-based chemical tuning approach, a second pathway was introduced in the form of strain engineering, a non-ML-based physical design strategy that reduces reliance on C&SRMs without requiring chemical modification. By leveraging strain-induced microstructural modifications, such as dislocation accumulation, ultrafine grain refinement, and the activation of TWIP and TRIP mechanisms, strain engineering provides a powerful means of tuning alloy properties while offering additional sustainability benefits such as weight reduction and resource efficiency. Together, these two complementary approaches provide a holistic pathway toward the development of sustainable next-generation alloys aligned with global Net Zero priorities.

The overall research work has been carried out in the following major stages.

- Phase prediction of MPEAs considering the high-quality experimental database, extracted by focusing on melting and casting methods, without resorting to synthetic data augmentation, a practice frequently employed in the literature to improve model accuracy.
- Mechanical property prediction through the first systematic application of an MPEA database within the MAST-ML toolkit for yield strength (YS) prediction. Recognizing the limitations of MAST-ML, a novel ML framework was subsequently developed from scratch to perform multi-objective optimization, simultaneously targeting YS, ultimate tensile strength (UTS), and elongation ($\boldsymbol{\mathcal{E}}$).
- Sustainable alloy design through ML-guided compositional tuning by developing a hybrid ML–metaheuristic optimization framework, aimed at minimizing the use of CRMs. This was achieved using a computational database comprising unary and binary compositions with corresponding compositional and Vickers hardness data generated via CALPHAD-based simulations.
- A non-ML-based physical design strategy to minimize or eliminate reliance on C&SRMs, through a theoretical framework that leverages strain-induced microstructural

modifications, to enhance mechanical properties while avoiding compositional tuning or the use of costly C&SRMs.

7.2. Conclusions and Research Contributions

Important conclusions drawn from the thesis work and specific research contributions are listed in the following sub section:

7.2.1. Development of a Robust and Reliable Phase Prediction Framework

In this work, a robust and reliable machine learning framework for phase prediction in MPEAs/HEAs was developed using a carefully curated high-quality experimental dataset comprising 1,200 alloy instances. The dataset covered a broad spectrum of alloy families, including 3d-transition metal HEAs, refractory HEAs, precious metal–based systems, HEA brass/bronze, and low-density HEAs, ranging from ternary to higher-order compositions. To ensure consistency and avoid variability introduced by mixed synthesis methods, only alloys synthesized via the melting and casting route were considered, thereby eliminating spurious effects from heterogeneous processing conditions. Five widely used classification algorithms, K-Nearest Neighbour (KNN), Support Vector Machine (SVM), Decision Tree Classifier (DTC), Random Forest Classifier (RFC), and XGBoost (XGB) were trained and tested on this curated dataset. Among these, the vanilla Random Forest Classifier (V-RFC) demonstrated the best performance, achieving an average accuracy of 84%, a ROC-AUC score of 0.9649, a 10-fold cross-validation mean score of 0.9315, and higher Precision, Recall, and F1-score compared to the other models.

To critically examine the reliability of synthetic data augmentation, the V-RFC was compared against a Random Forest model trained on an augmented dataset generated using the SMOTE–Tomek Link method (ST-RFC). While the augmented model achieved a higher accuracy of 92% on the expanded dataset (1200 original + 192 synthetic = 1392 entries), comparative analysis of confusion matrices and ROC curves revealed that its predictions are not reliable. In contrast, the V-RFC trained solely on experimental data provided robust and consistent performance, highlighting the limitations of synthetic augmentation for complex alloys such as HEAs. The robustness of the V-RFC model was further substantiated through experimental validation. A novel HEA composition, $\mathbf{Ni_{25}Cu_{18.75}Fe_{25}Co_{25}Al_{6.25}}$, predicted by the model to form an FCC phase, was synthesized via vacuum arc melting and characterized using X-ray diffraction, which confirmed the FCC phase in agreement with the model's prediction.

The following conclusions can be drawn from this study:

1. Synthetic data merged into the real-world experimental data can lead to spurious outcomes when feeding to the ML models. An attempt like this (which is routinely done in literature) may although help achieve higher model accuracy, but it can compromise the quality of prediction, particularly, when inferring complex phases of high entropy alloys. Moreover, accuracy alone is not a reliable measure for evaluating ML models on imbalanced datasets. Various other evaluation metrics such as ROC-AUC score, Precision, Recall, and F1-score are robust for classifying an imbalanced dataset.
2. This study revealed that reliable predictions of HEA phase formation are achievable using only five key parameters: valence electron concentration (VEC), electronegativity difference ($\Delta\chi$), mixing entropy (ΔS_{mix}), atomic size difference (δ), and mixing enthalpy (ΔH_{mix}). However, care must be taken to ensure input data are consistently derived from controlled synthesis methods (in this case, melting and casting).
3. The developed framework performed robustly in predicting solid-solution phases (FCC, BCC, FCC + BCC) and complex multiphase HEAs classified as mixtures of intermetallic phases (MIP). However, the framework was found to be limited in its ability to accurately predict the number and types of phases present within MIP systems.

7.2.2. Mechanical Property Prediction and Development of a Multi-Objective Optimization Framework

This part of the work integrates two key components: (i) the development of predictive models for yield strength using an open-source machine learning toolkit, and (ii) the establishment of a novel multi-objective optimization framework for identifying MPEA compositions with superior combination of competing mechanical properties, such as YS, UTS, and $\mathcal{E}$.

First, the Materials Simulation Toolkit for Machine Learning (MAST-ML), an open-source Python package specifically tailored for materials researchers with limited or no prior coding expertise, was systematically applied for the first time to complex concentrated alloys (CCAs) or multi-principal element alloys (MPEAs) to predict yield strength (YS). Unlike prior applications of such open-source toolkits to problems such as perovskite oxide stability, electromigration charge, or dilute solute diffusion, its use in modeling mechanical properties of complex alloys had remained largely unexplored. A curated dataset of 700 experimentally reported MPEA compositions with corresponding yield strength values was employed to benchmark the toolkit. Three regression models, Decision Tree Regressor (DTR), Random Forest

Regressor (RFR), and Extra Trees Regressor (ETR), were implemented and evaluated under MAST-ML's specialized train/test division strategies ("best split" and "worst split"), designed to test generalizability beyond conventional random splits or k-fold cross-validation. Among them, the ETR model consistently outperformed the others, achieving higher R^2 scores and lower MAE and RMSE across both split strategies. When tested on previously unseen compositions, the ETR model predicted yield strength values in close agreement with experimental reports, with an average error margin of ±20 MPa, thereby confirming its predictive robustness.

The following conclusions were drawn from this study:

1. MAST-ML offers a powerful, user-friendly platform that lowers the entry barrier for researchers new to machine learning.
2. While MAST-ML provides a streamlined pipeline for supervised regression tasks, several limitations persist**.** Its scope is largely confined to classical ML models and lacks integration with advanced techniques such as deep learning or GPU acceleration. Crucially, the toolkit does not incorporate advanced optimization algorithms, which are essential for systematically exploring the vast and complex compositional space of MPEAs. Moreover, its batch-oriented design produces diagnostic plots only after execution, restricting opportunities for interactive model refinement, real-time feedback, or iterative optimization.
3. Current capabilities for parallelization and handling very large datasets remain limited compared to modern ML platforms such as TensorFlow or PyTorch.

Recognizing the limitations of MAST-ML, the second component of this work developed a novel ML framework from scratch to address the long-standing strength–ductility trade-off by simultaneously optimizing yield strength (YS), ultimate tensile strength (UTS), and elongation ($\mathcal{E}$). Unlike most prior studies that performed only bi-objective optimization, this framework represents one of the first systematic attempts at true multi-objective optimization in MPEAs. A curated experimental dataset of 700 MPEA compositions was employed, and various regression algorithms including Neural Networks (NN), Random Forest Regressor (RFR), Extra Trees Regressor (ETR), Cat-Boost Regressor (CBR), and XGBoost Regressor (XGB) were trained and evaluated. Among these, the CBR model demonstrated the most consistent performance and was therefore selected for integration with Cuckoo Search Optimization (CSO) and the Non-Dominated Sorting Genetic Algorithm II (NSGA-II). CSO enabled efficient global exploration of the compositional space, while NSGA-II facilitated Pareto-front based optimization across competing objectives.

The proposed framework successfully identified novel alloy compositions with superior mechanical property combinations compared to those in the curated database. Notably, two predicted compositions, MoNbTiVZr and MoNbTiV0.25Zr, though absent from the training dataset, have been independently reported in experimental studies [185, 186], with predicted properties closely matching experimental values. This provides compelling evidence of the framework's reliability and real-world generalizability. The conclusions drawn from this study are as follows:

1. The framework provides a simple yet powerful approach to identify high-performance, multi-objective optimized alloys, relying solely on compositional data.
2. The integration of ML with metaheuristic algorithms (CSO and NSGA-II) enables systematic navigation of the vast compositional space, uncovering alloys with superior mechanical properties.
3. The successful prediction of alloys absent from the training dataset but validated by prior experimental studies underscores the framework's robustness, generalizability, and practical utility in alloy design.
4. It effectively resolves the strength–ductility trade-off by enabling simultaneous optimization of YS, UTS, and ε.

7.2.3. Development of a Hybrid ML-Metaheuristic Optimization Framework for Reducing Reliance on CRMs in High-Performance MPEAs

A hybrid ML–metaheuristic optimization framework was established to design novel, high-performance MPEAs with minimal or no reliance on Critical Raw Materials (CRMs). The framework employed ML-guided chemical tuning to reduce dependence on costly elements such as Co, Nb, Ta, and W, while maintaining mechanical performance. To address the scarcity of CRM-free or CRM-lean HEA data in the literature, a new computational database comprising 3,608 entries was generated using Thermo-Calc 2024a (TCHEA7 database with the property model calculator). This database included unary and binary alloys with Vickers hardness values targeting non-CRM elements. Among several regression algorithms employed, Decision Tree Regressor (DTR), Random Forest Regressor (RFR), AdaBoost Regressor (ABR), Gradient Boost Regressor (GBR), XGBoost Regressor (XGBR), and Extra Tree Regressor (ETR), the ETR model exhibited the best predictive performance. It was subsequently integrated with metaheuristic optimization methods such as Genetic Algorithm (GA), Particle Swarm Optimization (PSO), Cuckoo Search Optimization (CSO), Whale Optimization Algorithm (WOA), and Ant Colony

Optimization (ACO) to identify candidate compositions for reduced-CRM MPEAs (R-CRM-MPEAs) or CRM-free MPEAs. Among these, CSO-generated compositions demonstrated the highest level of agreement with their respective Thermo-Calc (TC)-evaluated hardness values, with an average deviation of less than ±20%.

Furthermore, a literature-sourced CRM-heavy composition, $CoCrFeNb_{0.309}Ni$ (containing two 1st-Tier CRMs, Co and Nb), with a hardness of 480 HV, was compared with the CSO-generated alloy **$Ti_{0.01111}NiFe_{0.4}Cu_{0.4}$**, containing only a single 2nd-Tier CRM (Ti), which exhibited a hardness of 488 HV. This comparison highlighted the potential to substantially reduce CRM usage in MPEAs without compromising, or even surpassing, mechanical performance. The reliability of this framework was further reinforced by experimentally synthesizing the CSO-generated R-CRM-MPEA composition, $Ti_{0.0111}NiFe_{0.4}Cu_{0.4}$ using vacuum arc melting and casting, followed by hardness testing. The experimentally measured hardness observed for $Ti_{0.0111}NiFe_{0.4}Cu_{0.4}$ was lower than both the CSO-predicted and the TC-evaluated values. This discrepancy was attributed to the fact that most TC-evaluated hardness values closely matched experimental measurements for alloys that had undergone post-processing treatments such as rolling or ECAP. As CSO predictions are derived from this database, they are inherently biased toward post-processed compositions. In contrast, $Ti_{0.0111}NiFe_{0.4}Cu_{0.4}$ was assessed in the as-cast state, without deformation or thermomechanical treatment. It is therefore anticipated that appropriate post-processing could yield hardness values more consistent with CSO predictions and TC evaluations.

Overall, this study confirms the feasibility of the developed hybrid ML–metaheuristic optimization framework for designing sustainable MPEAs with reduced CRM reliance, while offering valuable insights into pathways for advancing resource-efficient alloy development in alignment with Net Zero objectives. Following conclusions can be drawn from this work:

1. It is possible to obtain CRM-free or CRM-lean multicomponent compositions from the developed framework that has been trained only on unary and binary based compositions.
2. The hybrid ML–metaheuristic optimization framework enables the design of high-performance MPEAs with reduced CRM content, while simultaneously addressing challenges related to supply chain vulnerabilities, cost, import dependence, and environmental sustainability.
3. This framework establishes a transferable methodology that can be extended beyond hardness optimization to other mechanical and functional properties (e.g., strength, ductility, corrosion resistance), thereby broadening its utility for sustainable alloy design

7.2.4. Strain-Engineering as a Non-ML-Based Physical Design Strategy to Minimize Reliance on C&SRMs

A systematic data-driven analysis was carried out to evaluate strain engineering as an alternative, non-ML-based pathway for minimizing the use of Critical and Strategic Raw Materials (C&SRMs). Mechanical performance data for both pure elements and well-established MPEAs processed through different synthesis routes were critically examined. Among these, severe plastic deformation (SPD) techniques, particularly High-Pressure Torsion (HPT), were found to significantly enhance mechanical properties in both pure metals and complex alloys. The study also established the theoretical basis of property enhancement through strain engineering, emphasizing the role of microstructural evolution induced by processing conditions. Overall, this work positions strain engineering as a viable physical design strategy, independent of ML-guided chemical tuning, for developing sustainable alloys with minimal reliance on costly C&SRMs while maintaining high mechanical performance. The conclusions drawn from this study are as follows:

1. Strain engineering through SPD induces profound microstructural modifications, including increased dislocation density, ultrafine-grained (UFG) and nanocrystalline (NC) structures, and, in certain cases, activation of transformation-induced plasticity (TRIP) and twinning-induced plasticity (TWIP) mechanisms. These changes collectively lead to substantial improvements in mechanical performance.
2. Processing conditions also play a critical role, for instance, parameters such as the number of passes, corner angle, and channel angle in Equal Channel Angular Pressing (ECAP), and pressure, rotation speed, and number of turns in High-Pressure Torsion (HPT) significantly influence the resulting microstructure and properties.
3. Strain-engineered materials not only demonstrate superior mechanical performance but also improved resistance to fatigue, corrosion, and wear. These enhancements enable reductions in component thickness and weight, offering significant sustainability benefits such as reduced material consumption and fuel savings in transportation applications. Furthermore, their extended durability contributes to longer product lifespans, reducing lifecycle costs and environmental impact.

7.3. Scope for Future Work

The comprehensive computational and experimental investigations presented in this thesis have laid a solid foundation for data-driven MPEAs design. Nevertheless, several promising directions remain open for future studies:

- Important microstructural descriptors such as grain size, dislocation density, and twinning can be extracted from metallographic images using advanced image analysis and deep learning approaches (e.g., Convolutional Neural Networks (CNNs), U-Net, DenseNet). This would enable improved phase identification, particularly in multiphase alloys, and allow correlations with mechanical properties to be more systematically established. However, challenges such as inconsistent magnification scales (e.g., 100×, 500×, 1000×) and variations in image quality across literature sources remain to be addressed. Developing standardized and annotated datasets would be essential to support robust and scalable microstructure-informed ML frameworks.
- Future ML frameworks can be developed to simultaneously optimize multiple functional properties, including creep resistance, thermal stability, corrosion resistance, oxidation resistance, and irradiation tolerance. Such comprehensive optimization would make MPEAs more attractive for critical applications in aerospace, energy, and defense.
- Strategies for CRM/C&SRM minimization can be further extended to incorporate recyclability, life-cycle assessment (LCA), and environmental impact evaluation, thereby offering a more comprehensive approach to sustainable alloy development. Integrating economic factors such as cost–performance trade-offs and supply-chain risk assessments would also be worth investigating to ensure industrial scalability and adoption.
- Future work could benefit from integrating Explainable AI (XAI) and Active Learning to enhance alloy discovery in data-scarce regimes. Techniques like SHAP (SHapley Additive exPlanations) or LIME (Local Interpretable Model-Agnostic Explanations) can uncover interpretable links between elemental features and target properties such as hardness or cost, improving transparency and trust in ML predictions. Active Learning, in turn, enables models to selectively prioritize unexplored compositions where uncertainty is high, reducing reliance on expensive CALPHAD simulations or experiments. Together, XAI and Active Learning offer a scalable, adaptive extension to the current framework, well-suited for navigating the complex design space of CRM-free multi-principal element alloys.
- Developing inverse design tools that recommend feasible alloy compositions and processing

parameters for a targeted set of mechanical or functional properties would be highly beneficial. Such an “inverse property calculator” could accelerate alloy screening and guide experimental development, thereby bridging the gap between computational predictions and practical applications.

References

1. Cantor, B., et al., *Microstructural development in equiatomic multicomponent alloys.* Materials Science and Engineering: A, 2004. **375**: p. 213-218.
2. Yeh, J.W., et al., *Nanostructured high-entropy alloys with multiple principal elements: novel alloy design concepts and outcomes.* Advanced engineering materials, 2004. **6**(5): p. 299-303.
3. Zhang, Y., et al., *Microstructures and properties of high-entropy alloys.* Progress in materials science, 2014. **61**: p. 1-93.
4. Ye, Y., et al., *High-entropy alloy: challenges and prospects.* Materials Today, 2016. **19**(6): p. 349-362.
5. Miracle, D.B. and O.N. Senkov, *A critical review of high entropy alloys and related concepts.* Acta Materialia, 2017. **122**: p. 448-511.
6. Jien-Wei, Y., *Recent progress in high entropy alloys.* Ann. Chim. Sci. Mat, 2006. **31**(6): p. 633-648.
7. Li, Z., et al., *Ab initio assisted design of quinary dual-phase high-entropy alloys with transformation-induced plasticity.* Acta Materialia, 2017. **136**: p. 262-270.
8. Li, Z., et al., *Metastable high-entropy dual-phase alloys overcome the strength–ductility trade-off.* Nature, 2016. **534**(7606): p. 227-230.
9. Cantor, B., *Multicomponent and high entropy alloys.* Entropy, 2014. **16**(9): p. 4749-4768.
10. Katiyar, N.K., et al., *A perspective on the catalysis using the high entropy alloys.* Nano Energy, 2021. **88**: p. 106261.
11. Jose, R. and S. Ramakrishna, *Materials 4.0: Materials big data enabled materials discovery.* Applied Materials Today, 2018. **10**: p. 127-132.
12. Huang, W., P. Martin, and H.L. Zhuang, *Machine-learning phase prediction of high-entropy alloys.* Acta Materialia, 2019. **169**: p. 225-236.
13. Zhang, Y., S. Yang, and J. Evans, *Revisiting Hume-Rothery's Rules with artificial neural networks.* Acta Materialia, 2008. **56**(5): p. 1094-1105.
14. Nong, Z.-S., et al., *Stability and structure prediction of cubic phase in as cast high entropy alloys.* Materials Science and Technology, 2014. **30**(3): p. 363-369.
15. Islam, N., W. Huang, and H.L. Zhuang, *Machine learning for phase selection in multi-principal element alloys.* Computational Materials Science, 2018. **150**: p. 230-235.
16. Choudhury, A., et al., *Structure prediction of multi-principal element alloys using ensemble learning.* Engineering Computations, 2019.
17. Li, Y. and W. Guo, *Machine-learning model for predicting phase formations of high-entropy alloys.* Physical Review Materials, 2019. **3**(9): p. 095005.
18. Wen, C., et al., *Machine learning assisted design of high entropy alloys with desired property.* Acta Materialia, 2019. **170**: p. 109-117.
19. Kim, G., et al., *First-principles and machine learning predictions of elasticity in severely lattice-distorted high-entropy alloys with experimental validation.* Acta Materialia, 2019. **181**: p. 124-138.
20. Bhandari, U., et al., *Yield strength prediction of high-entropy alloys using machine learning.* Materials Today Communications, 2021. **26**: p. 101871.
21. Vilalta, P.C., et al., *Machine learning for predicting the critical yield stress of high entropy alloys.* Journal of Engineering Materials and Technology, 2021. **143**(2): p. 021005.
22. Choi, S., et al., *High-entropy alloys properties prediction model by using artificial neural network algorithm.* Metals, 2021. **11**(10): p. 1559.
23. Debnath, B., et al. *Designing fe-based high entropy alloy–a machine learning approach*. in *IOP Conference Series: Materials Science and Engineering*. 2020. IOP Publishing.
24. Rickman, J.M., et al., *Materials informatics for the screening of multi-principal elements and high-entropy alloys.* Nature Communications, 2019. **10**(1): p. 2618.
25. Chang, Y.-J., et al., *Prediction of the composition and hardness of high-entropy alloys by machine learning.* Jom, 2019. **71**(10): p. 3433-3442.

26. George, E.P., W. Curtin, and C.C. Tasan, *High entropy alloys: A focused review of mechanical properties and deformation mechanisms.* Acta Materialia, 2020. **188**: p. 435-474.
27. George, E.P., D. Raabe, and R.O. Ritchie, *High-entropy alloys.* Nature reviews materials, 2019. **4**(8): p. 515-534.
28. Chen, J., et al., *A review on fundamental of high entropy alloys with promising high–temperature properties.* Journal of Alloys and Compounds, 2018. **760**: p. 15-30.
29. Li, Z., et al., *A TRIP-assisted dual-phase high-entropy alloy: grain size and phase fraction effects on deformation behavior.* Acta Materialia, 2017. **131**: p. 323-335.
30. Huang, H., et al., *Phase-transformation ductilization of brittle high-entropy alloys via metastability engineering.* Advanced Materials, 2017. **29**(30): p. 1701678.
31. Huang, P.K., et al., *Multi-principal-element alloys with improved oxidation and wear resistance for thermal spray coating.* Advanced Engineering Materials, 2004. **6**(1-2): p. 74-78.
32. Chen, S.Y., et al., *Microstructures and crackling noise of AlxNbTiMoV high entropy alloys.* Entropy, 2014. **16**(2): p. 870-884.
33. Yeh, J.-W., *Alloy design strategies and future trends in high-entropy alloys.* Jom, 2013. **65**(12): p. 1759-1771.
34. Murty, B.S., et al., *High-entropy alloys*. 2019: Elsevier.
35. Gaskell, D.R., *Introduction to the Thermodynamics of Materials.* MRS BULLETIN, 2004. **975**.
36. Porter, D.A. and K.E. Easterling, *Phase transformations in metals and alloys (revised reprint)*. 2009: CRC press.
37. Mehta, A. and Y.H. Sohn, *Fundamental core effects in transition metal high-entropy alloys:"High-entropy" and "sluggish diffusion" effects.* Diffusion Foundations, 2021. **29**: p. 75-93.
38. Divinski, S.V., et al., *A mystery of" sluggish diffusion" in high-entropy alloys: the truth or a myth?* Diffusion foundations, 2018. **17**: p. 69-104.
39. Bi, X., et al., *Improvement of mechanical properties at cryogenic temperature of CoCrNi medium entropy alloy fabricated by hybrid additive manufacturing technology.* Materials Characterization, 2023. **205**: p. 113351.
40. Jiang, J., W. Sun, and N. Luo, *Atomic insights into effects of temperature and grain diameter on the micro-deformation mechanism, mechanical properties and sluggish diffusion of nanocrystalline high-entropy alloys.* Materials Today Communications, 2022. **33**: p. 104224.
41. Tong, Y., et al., *Severe local lattice distortion in Zr-and/or Hf-containing refractory multi-principal element alloys.* Acta Materialia, 2020. **183**: p. 172-181.
42. Yang, D., et al., *Effect of local lattice distortion on the core structure of edge dislocation in NbMoTaW multi-principal element alloys and the subsystems.* Materials Science and Engineering: A, 2022. **855**: p. 143869.
43. Nagini, M. and B. Murty, *Advanced high-entropy alloys: A next generation materials.* Transactions of the Indian National Academy of Engineering, 2024. **9**(3): p. 541-557.
44. Cantor, B., *Multicomponent high-entropy Cantor alloys.* Progress in Materials Science, 2021. **120**: p. 100754.
45. Kim, J., A. Wakai, and A. Moridi, *Materials and manufacturing renaissance: Additive manufacturing of high-entropy alloys.* Journal of Materials Research, 2020. **35**(15): p. 1963-1983.
46. Agrawal, A. and A. Choudhary, *Perspective: materials informatics and big data: realization of the ''fourth paradigm''of science in materials science. APL Mater 4: 053208*. 2016.
47. Science, N. and T. Council, *Materials genome initiative for global competitiveness*. 2011: Executive Office of the President, National Science and Technology Council.
48. Hohenberg, P. and W. Kohn, *Inhomogeneous electron gas.* Physical review, 1964. **136**(3B): p. B864.
49. Kohn, W. and L.J. Sham, *Self-consistent equations including exchange and correlation effects.* Physical review, 1965. **140**(4A): p. A1133.
50. Alder, B.J. and T.E. Wainwright, *Studies in molecular dynamics. I. General method.* The Journal of Chemical Physics, 1959. **31**(2): p. 459-466.
51. Rahman, A., *Correlations in the motion of atoms in liquid argon.* Physical review, 1964.

136(2A): p. A405.
52. Baumgärtner, A., et al., *The Monte Carlo method in condensed matter physics*. Vol. 71. 2012: Springer Science & Business Media.
53. Saunders, N. and A.P. Miodownik, *CALPHAD (calculation of phase diagrams): a comprehensive guide*. Vol. 1. 1998: Elsevier.
54. Kresse, G., *Ab initio molecular dynamics: recent progresses and limitations.* Journal of non-crystalline solids, 2002. **312**: p. 52-59.
55. Zhang, C. and Y. Yang, *The CALPHAD approach for HEAs: Challenges and opportunities.* MRS Bulletin, 2022. **47**(2): p. 158-167.
56. Samuel, A.L., *Some studies in machine learning using the game of checkers.* IBM Journal of research and development, 1959. **3**(3): p. 210-229.
57. Vamathevan, J., et al., *Applications of machine learning in drug discovery and development.* Nature reviews Drug discovery, 2019. **18**(6): p. 463-477.
58. Rana, C., *Artificial intelligence based object detection and traffic prediction by autonomous vehicles–A review.* Expert Systems with Applications, 2024. **255**: p. 124664.
59. Zhou, T., Z. Song, and K. Sundmacher, *Big data creates new opportunities for materials research: a review on methods and applications of machine learning for materials design.* Engineering, 2019. **5**(6): p. 1017-1026.
60. Schleder, G.R., et al., *From DFT to machine learning: recent approaches to materials science–a review.* Journal of Physics: Materials, 2019. **2**(3): p. 032001.
61. Ayodele, T.O., *Types of machine learning algorithms.* New advances in machine learning, 2010. **3**(19-48): p. 5-1.
62. Singh, A., N. Thakur, and A. Sharma. *A review of supervised machine learning algorithms*. in *2016 3rd international conference on computing for sustainable global development (INDIACom)*. 2016. Ieee.
63. Naeem, S., et al., *An unsupervised machine learning algorithms: Comprehensive review.* International Journal of Computing and Digital Systems, 2023.
64. AlMahamid, F. and K. Grolinger. *Reinforcement learning algorithms: An overview and classification*. in *2021 IEEE Canadian Conference on Electrical and Computer Engineering (CCECE)*. 2021. IEEE.
65. Jafary-Zadeh, M., et al., *Applying a machine learning interatomic potential to unravel the effects of local lattice distortion on the elastic properties of multi-principal element alloys.* Journal of Alloys and Compounds, 2019. **803**: p. 1054-1062.
66. Guo, T., L. Wu, and T. Li, *Machine learning accelerated, high throughput, multi-objective optimization of multiprincipal element alloys.* Small, 2021. **17**(42): p. 2102972.
67. Zhang, L., et al., *The microstructure and high-temperature properties of novel nano precipitation-hardened face centered cubic high-entropy superalloys.* Scr. Mater, 2018. **146**: p. 226-230.
68. Guo, S., *Phase selection rules for cast high entropy alloys: an overview.* Materials Science and Technology, 2015. **31**(10): p. 1223-1230.
69. Ren, M.-x., B.-s. Li, and H.-z. Fu, *Formation condition of solid solution type high-entropy alloy.* Transactions of Nonferrous Metals Society of China, 2013. **23**(4): p. 991-995.
70. Tsai, M.-H. and J.-W. Yeh, *High-entropy alloys: a critical review.* Materials Research Letters, 2014. **2**(3): p. 107-123.
71. Poletti, M.G. and L. Battezzati, *Electronic and thermodynamic criteria for the occurrence of high entropy alloys in metallic systems.* Acta materialia, 2014. **75**: p. 297-306.
72. Jiang, L., et al., *Formation rules of single phase solid solution in high entropy alloys.* Materials Science and Technology, 2016. **32**(6): p. 588-592.
73. Pei, Z., et al., *Machine-learning informed prediction of high-entropy solid solution formation: Beyond the Hume-Rothery rules.* npj Computational Materials, 2020. **6**(1): p. 1-8.
74. Chau, N.H., et al. *Phase Prediction of Multi-principal Element Alloys Using Support Vector Machine and Bayesian Optimization*. 2021. Cham: Springer International Publishing.
75. Agarwal, A. and A. Prasada Rao, *Artificial intelligence predicts body-centered-cubic and face-centered-cubic phases in high-entropy alloys.* Jom, 2019. **71**(10): p. 3424-3432.

76. Zhou, Z., et al., *Machine learning guided appraisal and exploration of phase design for high entropy alloys.* npj Computational Materials, 2019. **5**(1): p. 1-9.
77. Jaiswal, U.K., et al., *Machine learning-enabled identification of new medium to high entropy alloys with solid solution phases.* Computational Materials Science, 2021. **197**: p. 110623.
78. Krishna, Y.V., U.K. Jaiswal, and M. Rahul, *Machine learning approach to predict new multiphase high entropy alloys.* Scripta Materialia, 2021. **197**: p. 113804.
79. Zeng, Y., et al., *Revealing high-fidelity phase selection rules for high entropy alloys: A combined CALPHAD and machine learning study.* Materials & design, 2021. **202**: p. 109532.
80. Mandal, P., et al., *Phase Prediction in High Entropy Alloys by Various Machine Learning Modules Using Thermodynamic and Configurational Parameters.* Metals and Materials International, 2022: p. 1-15.
81. Machaka, R., et al., *Machine learning-based prediction of phases in high-entropy alloys: A data article.* Data in brief, 2021. **38**.
82. Risal, S., et al., *Improving phase prediction accuracy for high entropy alloys with machine learning.* Computational Materials Science, 2021. **192**: p. 110389.
83. Lee, S.Y., et al., *Deep learning-based phase prediction of high-entropy alloys: Optimization, generation, and explanation.* Materials & Design, 2021. **197**: p. 109260.
84. Bakr, M., J. Syarif, and I.A.T. Hashem, *Prediction of phase and hardness of HEAs based on constituent elements using machine learning models.* Materials Today Communications, 2022. **31**: p. 103407.
85. Qu, N., et al., *The phase selection via machine learning in high entropy alloys.* Procedia Manufacturing, 2019. **37**: p. 299-305.
86. Tancret, F., et al., *Designing high entropy alloys employing thermodynamics and Gaussian process statistical analysis.* Materials & Design, 2017. **115**: p. 486-497.
87. Jiang, X., et al., *Fast prediction of the quasi phase equilibrium in phase field model for multicomponent alloys based on machine learning method.* Calphad, 2019. **66**: p. 101644.
88. Kaufmann, K. and K.S. Vecchio, *Searching for high entropy alloys: A machine learning approach.* Acta Materialia, 2020. **198**: p. 178-222.
89. Qi, J., A. Cheung, and S. Poon, *High entropy alloys mined from binary phase diagrams. Sci. Rep. 9, 1–10 (2019)*.
90. Wu, Q., et al., *Uncovering the eutectics design by machine learning in the Al–Co–Cr–Fe–Ni high entropy system.* Acta Materialia, 2020. **182**: p. 278-286.
91. Dai, D., et al., *Using machine learning and feature engineering to characterize limited material datasets of high-entropy alloys.* Computational Materials Science, 2020. **175**: p. 109618.
92. Zhang, Y., et al., *Phase prediction in high entropy alloys with a rational selection of materials descriptors and machine learning models.* Acta Materialia, 2020. **185**: p. 528-539.
93. Al-Shibaany, Z.Y.A., et al. *Deep learning-based phase prediction of high-entropy alloys*. in *IOP Conference Series: Materials Science and Engineering*. 2020. IOP Publishing.
94. Zhang, L., et al., *Machine learning reveals the importance of the formation enthalpy and atom-size difference in forming phases of high entropy alloys.* Materials & Design, 2020. **193**: p. 108835.
95. Roy, A., et al., *Machine learned feature identification for predicting phase and Young's modulus of low-, medium-and high-entropy alloys.* Scripta Materialia, 2020. **185**: p. 152-158.
96. Nassar, A. and A. Mullis, *Rapid screening of high-entropy alloys using neural networks and constituent elements.* Computational Materials Science, 2021. **199**: p. 110755.
97. Lee, K., et al., *A comparison of explainable artificial intelligence methods in the phase classification of multi-principal element alloys.* Scientific Reports, 2022. **12**(1): p. 11591.
98. Jin, T., et al., *Accelerated crystal structure prediction of multi-elements random alloy using expandable features.* Scientific reports, 2021. **11**(1): p. 5194.
99. Bundela, A.S. and M. Rahul, *Machine learning-enabled framework for the prediction of mechanical properties in new high entropy alloys.* Journal of Alloys and Compounds, 2022. **908**: p. 164578.
100. Zhou, Q., et al., *Machine learning-assisted mechanical property prediction and descriptor-property correlation analysis of high-entropy ceramics.* Ceramics International, 2023. **49**(4): p.

5760-5769.
101. Yang, C., et al., *A machine learning-based alloy design system to facilitate the rational design of high entropy alloys with enhanced hardness.* Acta Materialia, 2022. **222**: p. 117431.
102. Klimenko, D., et al., *Machine learning-based strength prediction for refractory high-entropy alloys of the Al-Cr-Nb-Ti-V-Zr system.* Materials, 2021. **14**(23): p. 7213.
103. Khakurel, H., et al., *Machine learning assisted prediction of the Young's modulus of compositionally complex alloys.* Scientific reports, 2021. **11**(1): p. 17149.
104. Bhandari, U., et al., *Deep learning-based hardness prediction of novel refractory high-entropy alloys with experimental validation.* Crystals, 2021. **11**(1): p. 46.
105. Buranich, V., et al. *Predicting the properties of the refractory high-entropy alloys for additive manufacturing-based fabrication and mechatronic applications*. in *2020 IEEE 10th International Conference Nanomaterials: Applications & Properties (NAP)*. 2020. IEEE.
106. Ren, W., et al., *Prediction and design of high hardness high entropy alloy through machine learning.* Materials & Design, 2023. **235**: p. 112454.
107. Roy, A., et al., *Rapid discovery of high hardness multi-principal-element alloys using a generative adversarial network model.* Acta Materialia, 2023. **257**: p. 119177.
108. Hastings, T., et al., *Accelerated Multi-Objective Alloy Discovery Through Efficient Bayesian Methods: Application to the FCC High Entropy Alloy Space.*
109. Menou, E., et al., *Evolutionary design of strong and stable high entropy alloys using multi-objective optimisation based on physical models, statistics and thermodynamics.* Materials & Design, 2018. **143**: p. 185-195.
110. Menou, E., et al., *Computational design of light and strong high entropy alloys (HEA): Obtainment of an extremely high specific solid solution hardening.* Scripta Materialia, 2018. **156**: p. 120-123.
111. Dai, F.-Z., et al., *Theoretical prediction on thermal and mechanical properties of high entropy (Zr0. 2Hf0. 2Ti0. 2Nb0. 2Ta0. 2) C by deep learning potential.* Journal of Materials Science & Technology, 2020. **43**: p. 168-174.
112. Li, L., et al., *Machine learning approach to design high entropy alloys with heterogeneous grain structures.* Metallurgical and Materials Transactions A, 2021. **52**(2): p. 439-448.
113. Zhang, L., et al., *Molecular dynamics simulation and machine learning of mechanical response in non-equiatomic FeCrNiCoMn high-entropy alloy.* Journal of Materials Research and Technology, 2021. **13**: p. 2043-2054.
114. Li, J., et al., *High-throughput simulation combined machine learning search for optimum elemental composition in medium entropy alloy*. Journal of Materials Science & Technology, 2021. **68**: p. 70-75.
115. Zhao, D., et al., *Structure prediction in high-entropy alloys with machine learning.* Applied physics letters, 2021. **118**(23).
116. Zheng, T., et al., *Tailoring nanoprecipitates for ultra-strong high-entropy alloys via machine learning and prestrain aging.* Journal of Materials Science & Technology, 2021. **69**: p. 156-167.
117. Qin, G., et al., *Microstructures and mechanical properties of Nb-alloyed CoCrCuFeNi high-entropy alloys.* Journal of Materials Science & Technology, 2018. **34**(2): p. 365-369.
118. Zhang, K., et al., *Microstructure and mechanical properties of CoCrFeNiTiAlx high-entropy alloys.* Materials Science and Engineering: A, 2009. **508**(1-2): p. 214-219.
119. Zhu, Z., et al., *Compositional dependence of phase formation and mechanical properties in three CoCrFeNi-(Mn/Al/Cu) high entropy alloys.* Intermetallics, 2016. **79**: p. 1-11.
120. He, J., et al., *Effects of Al addition on structural evolution and tensile properties of the FeCoNiCrMn high-entropy alloy system.* Acta Materialia, 2014. **62**: p. 105-113.
121. Wu, Z., et al., *Temperature dependence of the mechanical properties of equiatomic solid solution alloys with face-centered cubic crystal structures.* Acta Materialia, 2014. **81**: p. 428-441.
122. Xu, D., et al., *A critical review of the mechanical properties of CoCrNi-based medium-entropy alloys.* Microstructures, 2022. **2**(1): p. 2022001.
123. Agarwal, R., et al., *Understanding the deformation behavior of CoCuFeMnNi high entropy alloy by investigating mechanical properties of binary ternary and quaternary alloy subsets.* Materials

& Design, 2018. **157**: p. 539-550.
124. Han, Z., et al., *Microstructures and mechanical properties of TixNbMoTaW refractory high-entropy alloys.* Materials Science and Engineering: A, 2018. **712**: p. 380-385.
125. Wang, M., et al., *Designing VxNbMoTa refractory high-entropy alloys with improved properties for high-temperature applications.* Scripta Materialia, 2021. **191**: p. 131-136.
126. Pang, J., et al., *A ductile Nb40Ti25Al15V10Ta5Hf3W2 refractory high entropy alloy with high specific strength for high-temperature applications.* Materials Science and Engineering: A, 2022. **831**: p. 142290.
127. Wan, Y., et al., *A Nitride-Reinforced NbMoTaWHfN Refractory High-Entropy Alloy with Potential Ultra-High-Temperature Engineering Applications.* Engineering, 2023.
128. Dixit, S., et al., *Refractory High-Entropy Alloy Coatings for High-Temperature Aerospace and Energy Applications.* Journal of Thermal Spray Technology, 2022. **31**(4): p. 1021-1031.
129. He, H., et al., *Carbide-reinforced Re0. 1Hf0. 25NbTaW0. 4 refractory high-entropy alloy with excellent room and elevated temperature mechanical properties.* International Journal of Refractory Metals and Hard Materials, 2023. **116**: p. 106349.
130. Tsao, T.K., et al., *On the superior high temperature hardness of precipitation strengthened high entropy Ni-based alloys.* Advanced Engineering Materials, 2017. **19**(1): p. 1600475.
131. Tsao, T.-K., et al., *The high temperature tensile and creep behaviors of high entropy superalloy.* Scientific reports, 2017. **7**(1): p. 12658.
132. Jiang, H., et al., *Effects of Ta addition on the microstructures and mechanical properties of CoCrFeNi high entropy alloy.* Materials Chemistry and Physics, 2018. **210**: p. 43-48.
133. Liu, W., et al., *Effects of Nb additions on the microstructure and mechanical property of CoCrFeNi high-entropy alloys.* Intermetallics, 2015. **60**: p. 1-8.
134. He, F., et al., *Designing eutectic high entropy alloys of CoCrFeNiNbx.* Journal of Alloys and Compounds, 2016. **656**: p. 284-289.
135. Rivera-Díaz-del-Castillo, P.E. and H. Fu, *Strengthening mechanisms in high-entropy alloys: Perspectives for alloy design.* Journal of Materials Research, 2018. **33**(19): p. 2970-2982.
136. Rizzo, A., et al., *The critical raw materials in cutting tools for machining applications: A review.* Materials, 2020. **13**(6): p. 1377.
137. Dobbelstein, H., et al., *Laser metal deposition of refractory high-entropy alloys for high-throughput synthesis and structure-property characterization.* International Journal of Extreme Manufacturing, 2020. **3**(1): p. 015201.
138. He, J., et al., *Machine learning-assisted design of high-entropy alloys with superior mechanical properties.* Journal of Materials Research and Technology, 2024.
139. Liu, S., K. Lee, and P.V. Balachandran, *Integrating machine learning with mechanistic models for predicting the yield strength of high entropy alloys.* Journal of Applied Physics, 2022. **132**(10).
140. Precker, C.E.G.C., Andrea; Muíños Landín, Santiago, *Materials for Design Open Repository. High Entropy Alloys.* 2021.
141. Martin, P., et al., *HEAPS: A user-friendly tool for the design and exploration of high-entropy alloys based on semi-empirical parameters.* Computer Physics Communications, 2022. **278**: p. 108398.
142. Zhang, Y., et al., *Solid-Solution Phase Formation Rules for Multi-component Alloys.* 2008. **10**(6): p. 534-538.
143. Takeuchi, A. and A. Inoue, *Quantitative evaluation of critical cooling rate for metallic glasses.* Materials Science and Engineering: A, 2001. **304**: p. 446-451.
144. Sheng, G. and C.T. Liu, *Phase stability in high entropy alloys: Formation of solid-solution phase or amorphous phase.* Progress in Natural Science: Materials International, 2011. **21**(6): p. 433-446.
145. Katrutsa, A. and V. Strijov, *Comprehensive study of feature selection methods to solve multicollinearity problem according to evaluation criteria.* Expert Systems with Applications, 2017. **76**: p. 1-11.
146. Cuartas, M., et al., *Machine learning algorithms for the prediction of non-metallic inclusions in steel wires for tire reinforcement.* Journal of Intelligent Manufacturing, 2021. **32**(6): p. 1739-

1751.
147. Fan, C., et al., *A Review on Data Preprocessing Techniques Toward Efficient and Reliable Knowledge Discovery From Building Operational Data.* Frontiers in Energy Research, 2021. **9**.
148. Famili, A., et al., *Data preprocessing and intelligent data analysis.* Intelligent Data Analysis, 1997. **1**(1): p. 3-23.
149. Cunningham, P. and S.J. Delany, *k-Nearest Neighbour Classifiers - A Tutorial.* ACM Comput. Surv., 2021. **54**(6): p. Article 128.
150. Cover, T. and P. Hart, *Nearest neighbor pattern classification.* IEEE transactions on information theory, 1967. **13**(1): p. 21-27.
151. Salam Patrous, Z., *Evaluating XGBoost for User Classification by using Behavioral Features Extracted from Smartphone Sensors*, in *TRITA-EECS-EX*. 2018.
152. Jakkula, V., *Tutorial on support vector machine (svm).* School of EECS, Washington State University, 2006. **37**(2.5): p. 3.
153. Song, Y.Y. and Y. Lu, *Decision tree methods: applications for classification and prediction.* Shanghai Arch Psychiatry, 2015. **27**(2): p. 130-5.
154. Izza, Y., A. Ignatiev, and J. Marques-Silva, *On explaining decision trees.* arXiv preprint arXiv:2010.11034, 2020.
155. Breiman, L., *Random forests.* Machine learning, 2001. **45**(1): p. 5-32.
156. Biau, G., *Analysis of a random forests model.* The Journal of Machine Learning Research, 2012. **13**(1): p. 1063-1095.
157. Chen, T., et al., *Xgboost: extreme gradient boosting.* R package version 0.4-2, 2015. **1**(4): p. 1-4.
158. Pedregosa, F., et al., *Scikit-learn: Machine learning in Python.* the Journal of machine Learning research, 2011. **12**: p. 2825-2830.
159. Hossin, M. and M.N. Sulaiman, *A review on evaluation metrics for data classification evaluations.* International journal of data mining & knowledge management process, 2015. **5**(2): p. 1.
160. Yacouby, R. and D. Axman. *Probabilistic extension of precision, recall, and F1 score for more thorough evaluation of classification models*. in *Proceedings of the first workshop on evaluation and comparison of NLP systems*. 2020.
161. Goutte, C. and E. Gaussier. *A probabilistic interpretation of precision, recall and F-score, with implication for evaluation*. in *European conference on information retrieval*. 2005. Springer.
162. Bewick, V., L. Cheek, and J. Ball, *Statistics review 13: receiver operating characteristic curves.* Critical care, 2004. **8**(6): p. 1-5.
163. Varpa, K., et al., *Applying one-vs-one and one-vs-all classifiers in k-nearest neighbour method and support vector machines to an otoneurological multi-class problem*, in *User Centred Networked Health Care*. 2011, IOS Press. p. 579-583.
164. Akosa, J. *Predictive accuracy: A misleading performance measure for highly imbalanced data*. in *Proceedings of the SAS global forum*. 2017.
165. Luque, A., et al., *The impact of class imbalance in classification performance metrics based on the binary confusion matrix.* Pattern Recognition, 2019. **91**: p. 216-231.
166. Gu, Q., L. Zhu, and Z. Cai. *Evaluation measures of the classification performance of imbalanced data sets*. in *International symposium on intelligence computation and applications*. 2009. Springer.
167. Kulkarni, A., D. Chong, and F.A. Batarseh, *Foundations of data imbalance and solutions for a data democracy*, in *data democracy*. 2020, Elsevier. p. 83-106.
168. Thölke, P., et al., *Class imbalance should not throw you off balance: Choosing classifiers and performance metrics for brain decoding with imbalanced data.* bioRxiv, 2022.
169. Batista, G.E., A.L. Bazzan, and M.C. Monard. *Balancing Training Data for Automated Annotation of Keywords: a Case Study*. in *WOB*. 2003.
170. Yi, J., et al., *A novel Al0. 5CrCuNiV 3d transition metal high-entropy alloy: Phase analysis, microstructure and compressive properties.* Journal of Alloys and Compounds, 2020. **846**: p. 156466.
171. Sohn, S., et al., *Noble metal high entropy alloys.* Scripta Materialia, 2017. **126**: p. 29-32.
172. Zhou, Y., et al., *Microstructure and compressive properties of multicomponent Alx*

(TiVCrMnFeCoNiCu) 100− x high-entropy alloys. Materials Science and Engineering: A, 2007. **454**: p. 260-265.
173. Chuang, M.-H., et al., *Microstructure and wear behavior of AlxCo1. 5CrFeNi1. 5Tiy high-entropy alloys.* Acta Materialia, 2011. **59**(16): p. 6308-6317.
174. Fazakas, E., et al., *Experimental and theoretical study of Ti20Zr20Hf20Nb20X20 (X= V or Cr) refractory high-entropy alloys.* International Journal of Refractory Metals and Hard Materials, 2014. **47**: p. 131-138.
175. Pi, J.-H., et al., *Microstructure and property of AlTiCrFeNiCu high-entropy alloy.* Journal of Alloys and Compounds, 2011. **509**(18): p. 5641-5645.
176. Jiao, Z., et al., *Superior mechanical properties of AlCoCrFeNiTi x high-entropy alloys upon dynamic loading.* Journal of Materials Engineering and Performance, 2016. **25**(2): p. 451-456.
177. Ma, S. and Y. Zhang, *Effect of Nb addition on the microstructure and properties of AlCoCrFeNi high-entropy alloy.* Materials Science and Engineering: A, 2012. **532**: p. 480-486.
178. Zhu, W., et al., *Phase formation prediction of high-entropy alloys: a deep learning study.* Journal of Materials Research and Technology, 2022. **18**: p. 800-809.
179. Jacobs, R., et al., *The Materials Simulation Toolkit for Machine learning (MAST-ML): An automated open source toolkit to accelerate data-driven materials research.* Computational Materials Science, 2020. **176**: p. 109544.
180. Gorsse, S., et al., *Database on the mechanical properties of high entropy alloys and complex concentrated alloys.* Data in brief, 2018. **21**: p. 2664-2678.
181. Zuo, T., et al., *Effects of Al and Si addition on the structure and properties of CoFeNi equal atomic ratio alloy.* Journal of magnetism and magnetic materials, 2014. **371**: p. 60-68.
182. Cheng, P., et al., *Microstructural evolution and mechanical properties of Al0. 3CoCrFeNiSix high-entropy alloys containing coherent nanometer-scaled precipitates.* Materials Science and Engineering: A, 2020. **772**: p. 138681.
183. Chen, L., et al., *Heavy carbon alloyed FCC-structured high entropy alloy with excellent combination of strength and ductility.* Materials Science and Engineering: A, 2018. **716**: p. 150-156.
184. Liu, L., et al., *Microstructure and tensile properties of FeMnNiCuCoSnx high entropy alloys.* Materials & Design, 2013. **44**: p. 223-227.
185. Wu, Y., et al., *Phase composition and solid solution strengthening effect in TiZrNbMoV high-entropy alloys.* Materials & Design, 2015. **83**: p. 651-660.
186. Zhang, Y., X. Yang, and P. Liaw, *Alloy design and properties optimization of high-entropy alloys.* Jom, 2012. **64**: p. 830-838.
187. Commission, E., *Tackling the challenges in commodity markets and on raw materials.* Brussels: European Commission, 2011.
188. Commission, E., *On the Review of the List of Critical Raw Materials for the EU and the Implementation of the Raw Materials Initiative.* Ad-hoc Working Group on Defining Critical Raw Minerals of the Raw Materials Supply Group, 2014.
189. Commission, E., *List of critical raw materials for the EU.* Online verfügbar unter, 2017.
190. Commission, E., *Critical Raw materials resilience: charting a path towards greater security and sustainability.* Communication from the Commission to the European Parliament, the Council, the European Economic and Social Committee and the Committee of the regions, 2020.
191. Grohol, M. and C. Veeh, *Study on the Critical Raw Materials for the EU 2023*. 2023: Publications Office of the European Union.
192. Gulley, A.L., *China, the Democratic Republic of the Congo, and artisanal cobalt mining from 2000 through 2020.* Proceedings of the National Academy of Sciences, 2023. **120**(26): p. e2212037120.
193. Suriyanarayanan, S., et al., *Highly Efficient Recovery and Recycling of Cobalt from Spent Lithium-Ion Batteries Using an N-Methylurea–Acetamide Nonionic Deep Eutectic Solvent.* ACS omega, 2023. **8**(7): p. 6959-6967.
194. Zhang, J. and G. Azimi, *Recycling of lithium, cobalt, nickel, and manganese from end-of-life lithium-ion battery of an electric vehicle using supercritical carbon dioxide.* Resources, Conservation and Recycling, 2022. **187**: p. 106628.

195. Yang, L., et al., *Recycling potential of cobalt metal from end-of-life new energy passenger vehicles in China.* Waste Management & Research, 2024: p. 0734242X231219650.
196. Petranikova, M., et al., *Vanadium sustainability in the context of innovative recycling and sourcing development.* Waste Management, 2020. **113**: p. 521-544.
197. Mahmoud, E.R., et al., *Phase Prediction, Microstructure and Mechanical Properties of Fe–Mn–Ni–Cr–Al–Si High Entropy Alloys.* Metals, 2022. **12**(7): p. 1164.
198. Lukas, H., S.G. Fries, and B. Sundman, *Computational thermodynamics.* (No Title), 2007: p. 104.
199. Walbrühl, M., et al., *Modelling of solid solution strengthening in multicomponent alloys.* Materials Science and Engineering: A, 2017. **700**: p. 301-311.
200. Ahmed, Z.E., et al., *Optimizing energy consumption for cloud internet of things.* Frontiers in Physics, 2020. **8**: p. 358.
201. Janga Reddy, M. and D. Nagesh Kumar, *Evolutionary algorithms, swarm intelligence methods, and their applications in water resources engineering: a state-of-the-art review.* h2oj, 2020. **3**(1): p. 135-188.
202. Kumar, A. and S. Bawa, *A comparative review of meta-heuristic approaches to optimize the SLA violation costs for dynamic execution of cloud services.* Soft Computing, 2020. **24**(6): p. 3909-3922.
203. Dhiman, G. and A. Kaur, *Optimizing the design of airfoil and optical buffer problems using spotted hyena optimizer.* Designs, 2018. **2**(3): p. 28.
204. Rao, S.S., *Engineering optimization: theory and practice*. 2019: John Wiley & Sons.
205. Gandomi, A.H., X.-S. Yang, and A.H. Alavi, *Cuckoo search algorithm: a metaheuristic approach to solve structural optimization problems.* Engineering with computers, 2013. **29**: p. 17-35.
206. Gandomi, A.H., et al., *Design optimization of truss structures using cuckoo search algorithm.* The structural design of tall and special buildings, 2013. **22**(17): p. 1330-1349.
207. Katiyar, S., *A comparative study of genetic algorithm and the particle swarm optimization.* International Journal of Technology, 2010. **2**(2): p. 21-24.
208. Yang, X.-S. and S. Deb, *Cuckoo search: recent advances and applications.* Neural Computing and applications, 2014. **24**: p. 169-174.
209. Bhargava, V., S.-E.K. Fateen, and A. Bonilla-Petriciolet, *Cuckoo search: a new nature-inspired optimization method for phase equilibrium calculations.* Fluid Phase Equilibria, 2013. **337**: p. 191-200.
210. Manfredi, S., et al., *Raw Materials Information System (RMIS): towards v2. 0.* 2017.
211. Singh, S., et al., *Strain engineering: A sustainable alternative to avoid using strategic and critical raw materials in developing high-performance alloys.* Materials Today Advances, 2024. **24**: p. 100538.
212. Edalati, K., et al., *Significance of strain rate in severe plastic deformation on steady-state microstructure and strength.* Materials Science and Engineering: A, 2022. **859**: p. 144231.
213. Kapoor, R., *Severe plastic deformation of materials*, in *Materials Under Extreme Conditions*. 2017, Elsevier. p. 717-754.
214. Islamgaliev, R., et al., *Microstructure and mechanical properties of titanium (Grade 4) processed by high-pressure torsion.* Materials Science and Engineering: A, 2008. **493**(1-2): p. 190-194.
215. Stolyarov, V., et al., *A two step SPD processing of ultrafine-grained titanium.* Nanostructured Materials, 1999. **11**(7): p. 947-954.
216. Shahmir, H., et al., *Microstructure and properties of a CoCrFeNiMn high-entropy alloy processed by equal-channel angular pressing.* Materials Science and Engineering: A, 2017. **705**: p. 411-419.
217. Schuh, B., et al., *Mechanical properties, microstructure and thermal stability of a nanocrystalline CoCrFeMnNi high-entropy alloy after severe plastic deformation.* Acta Materialia, 2015. **96**: p. 258-268.
218. Salishchev, G., et al., *Effect of Mn and V on structure and mechanical properties of high-entropy alloys based on CoCrFeNi system.* Journal of Alloys and Compounds, 2014. **591**: p. 11-21.

219. Shahmir, H., et al., *Effect of annealing on mechanical properties of a nanocrystalline CoCrFeNiMn high-entropy alloy processed by high-pressure torsion.* Materials Science and Engineering: A, 2016. **676**: p. 294-303.
220. Sathiyamoorthi, P., et al., *Effect of annealing on microstructure and tensile behavior of CoCrNi medium entropy alloy processed by high-pressure torsion.* Entropy, 2018. **20**(11): p. 849.
221. Schuh, B., R. Pippan, and A. Hohenwarter, *Tailoring bimodal grain size structures in nanocrystalline compositionally complex alloys to improve ductility.* Materials Science and Engineering: A, 2019. **748**: p. 379-385.
222. Sathiyamoorthi, P., et al., *Superior cryogenic tensile properties of ultrafine-grained CoCrNi medium-entropy alloy produced by high-pressure torsion and annealing.* Scripta Materialia, 2019. **163**: p. 152-156.
223. Otto, F., et al., *The influences of temperature and microstructure on the tensile properties of a CoCrFeMnNi high-entropy alloy.* Acta Materialia, 2013. **61**(15): p. 5743-5755.
224. Gludovatz, B., et al., *Exceptional damage-tolerance of a medium-entropy alloy CrCoNi at cryogenic temperatures.* Nature communications, 2016. **7**(1): p. 10602.
225. Wang, Y., et al., *High tensile ductility in a nanostructured metal.* nature, 2002. **419**(6910): p. 912-915.
226. Zhao, Y.H., et al., *Simultaneously increasing the ductility and strength of ultra-fine-grained pure copper.* Advanced Materials, 2006. **18**(22): p. 2949-2953.
227. Lu, L., et al., *Ultrahigh strength and high electrical conductivity in copper.* Science, 2004. **304**(5669): p. 422-426.
228. Tian, Y., et al., *Enhanced strength and ductility in an ultrafine-grained Fe-22Mn-0.6 C austenitic steel having fully recrystallized structure.* Metallurgical and Materials Transactions A, 2014. **45**: p. 5300-5304.
229. Picak, S., H. Yilmaz, and I. Karaman, *Simultaneous deformation twinning and martensitic transformation in CoCrFeMnNi high entropy alloy at high temperatures.* Scripta Materialia, 2021. **202**: p. 113995.
230. Mohammadi, A., et al., *High strength and high ductility of a severely deformed high-entropy alloy in the presence of hydrogen.* Corrosion Science, 2023. **216**: p. 111097.
231. Koyama, M., K. Ichii, and K. Tsuzaki, *Grain refinement effect on hydrogen embrittlement resistance of an equiatomic CoCrFeMnNi high-entropy alloy.* International Journal of Hydrogen Energy, 2019. **44**(31): p. 17163-17167.
232. Schuh, B., et al., *Thermodynamic instability of a nanocrystalline, single-phase TiZrNbHfTa alloy and its impact on the mechanical properties.* Acta Materialia, 2018. **142**: p. 201-212.
233. Maury, N., et al., *A critical examination of pure tantalum processed by high-pressure torsion.* Materials Science and Engineering: A, 2015. **638**: p. 174-182.
234. Li, Z., et al., *An Evaluation of the Mechanical Properties, Microstructures, and Strengthening Mechanisms of Pure Mg Processed by High-Pressure Torsion at Different Temperatures.* Advanced Engineering Materials, 2022. **24**(10): p. 2200799.
235. Huang, K. and R.E. Logé, *A review of dynamic recrystallization phenomena in metallic materials.* Materials & Design, 2016. **111**: p. 548-574.
236. Sakai, T., et al., *Dynamic and post-dynamic recrystallization under hot, cold and severe plastic deformation conditions.* Progress in materials science, 2014. **60**: p. 130-207.
237. Yanushkevich, Z., A. Belyakov, and R. Kaibyshev, *Microstructural evolution of a 304-type austenitic stainless steel during rolling at temperatures of 773–1273 K.* Acta Materialia, 2015. **82**: p. 244-254.
238. Yamagata, H., et al., *Nucleation of new grains during discontinuous dynamic recrystallization of 99.998 mass% Aluminum at 453 K.* Scripta Materialia, 2001. **45**(9): p. 1055-1061.
239. Chauvy, C., P. Barberis, and F. Montheillet, *Microstructure transformation during warm working of β-treated lamellar Zircaloy-4 within the upper α-range.* Materials Science and Engineering: A, 2006. **431**(1-2): p. 59-67.
240. Lanjewar, H., L.A. Kestens, and P. Verleysen, *Damage and strengthening mechanisms in severely deformed commercially pure aluminum: Experiments and modeling.* Materials Science and Engineering: A, 2021. **800**: p. 140224.

241. Kumar, N., et al., *Friction stir processing of a high entropy alloy Al 0.1 CoCrFeNi.* Jom, 2015. **67**: p. 1007-1013.
242. Nabarro, F.R.N., *Theoretical and experimental estimates of the Peierls stress.* Philosophical Magazine A, 1997. **75**(3): p. 703-711.
243. Joos, B. and M. Duesbery, *The Peierls stress of dislocations: an analytic formula.* Physical Review Letters, 1997. **78**(2): p. 266.
244. Stepanov, N., et al., *Effect of cryo-deformation on structure and properties of CoCrFeNiMn high-entropy alloy.* Intermetallics, 2015. **59**: p. 8-17.
245. Shakil, S., et al., *Additive manufactured versus cast AlSi10Mg alloy: Microstructure and micromechanics.* Results in Materials, 2021. **10**: p. 100178.
246. Pawlik, P., K. Pawlik, and A. Przybył, *Investigation of the cooling rate in the suction casting process.* Rev. Adv. Mater. Sci, 2008. **18**(1): p. 81.
247. Zhao, J.-C. and M.R. Notis, *Continuous cooling transformation kinetics versus isothermal transformation kinetics of steels: a phenomenological rationalization of experimental observations.* Materials Science and Engineering: R: Reports, 1995. **15**(4-5): p. 135-207.
248. Chen, B., et al., *Strength and strain hardening of a selective laser melted AlSi10Mg alloy.* Scripta Materialia, 2017. **141**: p. 45-49.
249. Kecskes, L., et al., *Grain size engineering of bcc refractory metals: Top-down and bottom-up—Application to tungsten.* Materials Science and Engineering: A, 2007. **467**(1-2): p. 33-43.
250. Wongsa-Ngam, J., M. Kawasaki, and T.G. Langdon, *A comparison of microstructures and mechanical properties in a Cu–Zr alloy processed using different SPD techniques.* Journal of Materials Science, 2013. **48**: p. 4653-4660.
251. YADA, H., et al., *Strength and structural changes under high strain-rate hot deformation of C steels.* Transactions of the Iron and Steel Institute of Japan, 1983. **23**(2): p. 100-109.
252. Kim, H.S., *Evaluation of strain rate during equal-channel angular pressing.* Journal of Materials Research, 2002. **17**(1): p. 172-179.
253. Akhmetshin, L., I.Y. Smolin, and S.P. Buyakova. *Numerical study of hard-metal powder compaction*. in *IOP Conference Series: Materials Science and Engineering*. 2021. IOP Publishing.
254. Sadasivan, N. and M. Balasubramanian, *Severe plastic deformation of tubular materials–Process methodology and its influence on mechanical properties–A review.* Materials Today: Proceedings, 2021. **46**: p. 3460-3468.
255. Yanagida, A., K. Joko, and A. Azushima, *Formability of steels subjected to cold ECAE process.* Journal of Materials Processing Technology, 2008. **201**(1-3): p. 390-394.
256. Salcedo, D., et al., *Manufacturing of nanostructured blades for a Francis turbine by isothermal forging of AA6063.* Journal of Manufacturing Science and Engineering, 2014. **136**(1): p. 011009.
257. Kim, J.H., et al., *High-strength bolt-forming of fine-grained aluminum alloy 6061 with a continuous hybrid process.* Materials Science and Engineering: A, 2012. **552**: p. 316-322.
258. Edalati, K., E. Akiba, and Z. Horita, *High-pressure torsion for new hydrogen storage materials.* Science and Technology of advanced MaTerialS, 2018. **19**(1): p. 185-193.
259. Fattahi, M., et al., *Severe plastic deformation: Nanostructured materials, metal-based and polymer-based nanocomposites: A review.* Heliyon, 2023.
260. Valiev, R.Z., *Superior strength in ultrafine-grained materials produced by SPD processing.* Materials Transactions, 2014. **55**(1): p. 13-18.
261. Medvedev, A., et al., *Comparison of laboratory-scale and industrial-scale equal channel angular pressing of commercial purity titanium.* Materials Letters, 2015. **145**: p. 308-311.
262. Elias, C.N., et al., *Ultrafine grained titanium for biomedical applications: An overview of performance.* Journal of Materials Research and Technology, 2013. **2**(4): p. 340-350.

Appendix

Appendix 1.1

Permissions for figure 2.2 (only first page of the license agreement)

SPRINGER NATURE LICENSE
TERMS AND CONDITIONS

Aug 22, 2025

This Agreement between Swati Singh, Research Scholar, IIT Guwahati ("You") and Springer Nature ("Springer Nature") consists of your license details and the terms and conditions provided by Springer Nature and Copyright Clearance Center.

License Number	6094070785136
License date	Aug 22, 2025
Licensed Content Publisher	Springer Nature
Licensed Content Publication	Journal of Materials Research
Licensed Content Title	Materials and manufacturing renaissance: Additive manufacturing of high-entropy alloys
Licensed Content Author	Jinyeon Kim et al
Licensed Content Date	Aug 1, 2020
Type of Use	Thesis/Dissertation
Requestor type	academic/university or research institute
Format	print and electronic
Portion	figures/tables/illustrations
Number of figures/tables/illustrations	1